Advancing the Matter Bispectrum Estimation in Large-Scale Structure

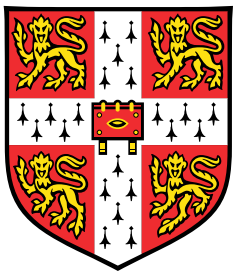

Johnathan Man Chiu Hung

Department of Applied Mathematics and Theoretical Physics
University of Cambridge

This dissertation is submitted for the degree of
Doctor of Philosophy

St. Catharine's College

August 2019

This thesis is dedicated to my parents for their undying love and support over all these years.

Declaration

I hereby declare that except where specific reference is made to the work of others, the contents of this dissertation are original and have not been submitted in whole or in part for consideration for any other degree or qualification in this, or any other university. This dissertation is my own work and contains nothing which is the outcome of work done in collaboration with others, except as specified in the text and Acknowledgements. Chapters 2 and 3 contain work published in [1] done in collaboration with James Fergusson and Paul Shellard. The codes to calculate α_n^Q coefficients and γ_{mn} were first written by James Fergusson, and the code to calculate β_n^Q coefficients were first written by Marcel Schmittfull, and subsequently made massively parallel by James Briggs and John Pennycook. All further testing of the various algorithms, including the discovery of numerical inaccuracies when directing calculating γ_{mn} on the tetrapyd, its subsequent replacement with Fourier methods for small grids, consistency checks of the estimated bispectra at different grid sizes, all scaling and numerical accuracy checks, and aliasing tests, as well as improvements such as the introduction of extra modes and restructuring and refactoring of the code base, was my own work. Chapter 4 is based on results done with Marc Manera and Paul Shellard published in [2], all of which is entirely my own work.

Johnathan Man Chiu Hung
August 2019

Acknowledgements

First and foremost I would like to acknowledge my supervisor, Paul Shellard, for his unstinting guidance and wisdom, without which this work would never have been possible. I am greatly indebted to him for the opportunity to work with numerous wonderful people at this prestigious institution.

I am hugely grateful to James Fergusson for his persistence, patience and numerical expertise, allowing us to make huge advances on the `MODAL-LSS` method and great strides in our analysis of the dark matter bispectrum. I would also like to thank Marc Manera for lending us his profound insight in halo phenomenology, allowing us to make breakthroughs in the development of fast methods to produce halo mock catalogues.

My sincere gratitude extends to Tobias Baldauf for his sagely advice, both professionally and personally, which has significantly enriched my life. The computationally intensive work behind this Thesis could not have been completed without the abundant technical support of James Briggs, Juha Jäykkä and especially Kacper Kornet. A special mention goes to Amelia Drew and Julija Markevičiūtė for their company when work is slow in the office.

My PhD was generously funded by the Cambridge Commonwealth, European and International Trust and the Croucher Foundation. I have additionally received invaluable financial assistance from St. Catharine's College, Cambridge, the Cambridge Philosophical Society, the Department of Applied Mathematics and Theoretical Physics, and the Centre for Theoretical Cosmology in my final year.

Abstract

The ΛCDM model for the Universe is highly successful in explaining cosmological observations to date, and its parameters tightly constrained by Cosmic Microwave Background (CMB) experiments such as Planck. Higher-order statistics, like the three-point correlation function or bispectrum in Fourier space, will be indispensable for furthering our understanding of the Universe. While these methodologies have been developed over the years and applied to CMB analyses, similar work on large-scale structure is still in its infancy. Additionally, information from future galaxy surveys such as LSST and Euclid will soon exceed that available from the CMB, demonstrating a pressing need for such tools.

The theoretical modelling of non-linear gravitational interactions is difficult beyond the perturbative regime, necessitating large, expensive N-body dark matter simulations to understand the small-scale dynamics. Additionally, the direct numerical computation of the matter bispectrum is intractable due to the multiplicity of triangular configurations. In this Thesis, we make breakthroughs in both of these problems. First, we present the newly rewritten `MODAL-LSS` formalism that enables efficient and optimal estimation of the full bispectrum for any matter density field to unprecedented accuracy, as well as demonstrating rapid convergence which makes it ideal for the analysis of large datasets. This has allowed us to benchmark fast dark matter codes (e.g. particle-mesh or L-PICOLA) against `GADGET-3` using the bispectrum, showing quantitatively how the mismatch at large k can be improved with a simple boosting technique in the power spectrum. We have also estimated the non-Gaussian contribution to the dark matter bispectrum covariance, which cannot be computed analytically in the non-linear regime. This will be vital for the extraction of cosmological parameters from data in the future.

In preparation for the analysis of future galaxy datasets we have also investigated the non-trivial problem of linking the underlying dark matter density field to the observed galaxy distribution. As an important milestone we have investigated the effects of the halo profile, the Halo Occupation Distribution (HOD) model, and multivariate assembly bias models of the halo occupation and concentration on the power spectrum and full bispectrum of a subhalo catalogue derived from the `ROCKSTAR` halo finder. These fast, phenomenological methods allow us to pave the way for the efficient generation of mock galaxy catalogues.

Table of contents

List of figures

List of tables

Chapter 1

Introduction

1.1 The story so far

Though people had an understanding of our place in the Universe by the end of the 19th century, the scientific study of Cosmology is relatively young. Newton's Law of Universal Gravitation, proposed in the 1600s, was the first breakthrough in understanding celestial mechanics, but it was Einstein's Theory of General Relativity in 1915 that truly revolutionised the field. Combined with the *Cosmological Principle*, which states that the Universe is homogeneous and isotropic on large scales [19], this allowed Friedmann, Lemaître, Robertson and Walker [20–23] to independently write down the mathematical model for the whole Universe, right from the beginning after the Big Bang and up to the present day. Amazingly Einstein's theory has been successful in explaining all the phenomena we have observed so far, surviving a wide range of tests from the weak field limit in the Solar System [24] to demanding strong field tests such as binary black-hole mergers [25]. Nevertheless modified gravity theories remain an active research area [26] in an attempt to explain puzzling aspects in our theoretical understanding, such as the dark components of our Universe and the cosmological constant problem.

The Universe is mind-bogglingly big, but it is also ancient: in the ΛCDM model of Cosmology the age of the Universe is estimated to be 13.8 billion years old. Along with the key observations of the Cosmic Microwave Background (CMB) by Penzias and Wilson in 1964 [27] and the accelerated expansion of the Universe through Type Ia Supernovae (SNe) in the '90s [28, 29], one quickly sees the need to incorporate new ingredients into our story line. This is what makes Cosmology exciting: it is the study of extremes, from the most microscopic Quantum Field Theories to the most macroscopic Theories of Gravitation. We learn that the two are deeply intertwined, culminating in the development of Inflation which

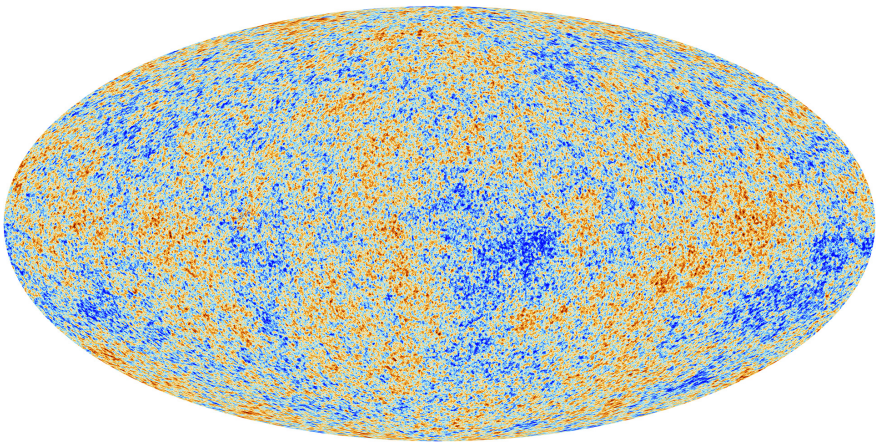

Fig. 1.1 The temperature anisotropies of the Cosmic Microwave Background as seen by the ESA *Planck* satellite [3].

almost completes our modern picture [30]. The postulation of Dark Matter and Dark Energy, driven by the necessity to explain seemingly unobservable matter and the expansion of the Universe respectively, gives us the 6-parameter ΛCDM model [31] which is taken as the standard by most practitioners. The most successful scientific probe of our Universe to date is the ESA Planck mission which made extensive maps of the CMB at 8 frequency bands, and its final data release in 2018 [32, 33] has given us extremely precise measurements of these parameters. Figure 1.1 shows a detailed map of the temperature anisotropies in the CMB based on data from the Legacy data release of Planck.

The success of Planck has propelled Cosmology into a high precision era, with further CMB missions, ground- [34], balloon- [35] and space-based [36], to follow. Despite the sophistication of our cosmological models, however, many long-standing questions, e.g. the nature of early-Universe physics [37], remain in the field, especially concerning the formation of large-scale structure (LSS). For example, we know that the visible galaxies are biased tracers of the underlying dark matter field because the spatial clustering of the two do not precisely match [38]. The gravitational collapse of matter is a highly non-linear process and difficult to understand from a theoretical standpoint. This is additionally complicated by small-scale baryonic physics, which can feedback onto the formation of dark matter haloes [39]. Other important issues include the discrepant measurements of the Hubble constant H_0 by supernovae-type [40] and CMB [33] experiments, as well as the nature of Dark Matter and Dark Energy.

The next generation of galaxy surveys, such as Dark Energy Survey (DES) [41, 42], the Large Synoptic Survey Telescope (LSST) [43], the ESA Euclid Satellite [44] and the Dark Energy Spectroscopic Instrument (DESI) [45], is certain to bring in a wealth of observational

data and help resolve these outstanding problems. But in order to take advantage of this additional source of cosmological information we must first make theoretical advances in LSS [46].

1.2 Standard Cosmological Model

Any cosmological theory must involve a theory for gravity, which we take to be Einstein's General Relativity. We will use the sign convention $(-,+,+,+)$ for the metric g_{ab}, and natural units such that $c = 1$.

1.2.1 Cosmological Field Equations

In his 1915 seminal paper [47] Einstein wrote down for the first time the tensorial gravitational field equations. Later in 1917 [48] he further introduced the cosmological constant Λ, giving rise to these equations in their familiar form:

$$G_{ab} = 8\pi G T_{ab} + \Lambda g_{ab}, \tag{1.1}$$

where G_{ab} is the Einstein tensor which depends on the geometric properties of spacetime, G is the Newtonian Gravitational Constant and T_{ab} is the energy-momentum tensor given by the types of matter in consideration, and finally g_{ab} is the metric tensor which encapsulates the geometry of the spacetime in question.

To understand the physical meaning of this terse equation we first need to express the Einstein tensor with the spacetime metric of our choosing. It can be shown the Levi-Civita connection is the unique connection on a Riemannian manifold that is both torsion-free and metric-compatible [49]. In this case the connection coefficients Γ^a_{bc} are given by the Christoffel symbols:

$$\Gamma^a_{bc} = \frac{1}{2} g^{ad} (\partial_b g_{dc} + \partial_c g_{bd} - \partial_d g_{bc}). \tag{1.2}$$

This allows us to further define the Riemann curvature tensor $R_{abc}{}^d$:

$$R_{abc}{}^d = -\partial_a \Gamma^d_{bc} + \partial_b \Gamma^d_{ac} + \Gamma^e_{ac}\Gamma^d_{be} - \Gamma^e_{bc}\Gamma^d_{ae}, \tag{1.3}$$

and its contractions the Ricci tensor R_{ab} and Ricci scalar R:

$$R_{ab} \equiv R_{acb}{}^{c} = -\partial_a \Gamma^c_{cb} + \partial_c \Gamma^c_{ab} + \Gamma^e_{ab}\Gamma^c_{ce} - \Gamma^e_{cb}\Gamma^c_{ae}, \tag{1.4}$$

$$R \equiv R^a_a. \tag{1.5}$$

Finally the Einstein tensor can be expressed in terms of these quantities as follows:

$$G_{ab} \equiv R_{ab} - \frac{1}{2} R g_{ab}. \tag{1.6}$$

To incorporate the Cosmological principle into our theory we find the most general homogeneous and isotropic metric in an expanding universe, also known as the FLRW metric after Friedmann, Lemaître, Robertson and Walker:

$$ds^2 \equiv g_{ab} dx^a dx^b = -dt^2 + a(t)^2 \left[\frac{dr^2}{1-kr^2} + r^2 (d\theta^2 + \sin^2\theta d\phi^2) \right], \tag{1.7}$$

where $a(t)$ is the scale factor which controls the expansion history, and k is a constant which determines the geometry of the Universe. The geometry is closed, flat, and open for positive, zero, and negative curvature respectively. With this choice of metric the non-vanishing elements in the Ricci tensor and the Ricci scalar can be calculated with Equation (1.4):

$$R_{00} = -3\frac{\ddot{a}}{a}, \tag{1.8}$$

$$R_{ij} = \left[\frac{\ddot{a}}{a} + 2\left(\frac{\dot{a}}{a}\right)^2 + 2\frac{k}{a^2} \right] g_{ij}, \tag{1.9}$$

$$R = 6\left[\frac{\ddot{a}}{a} + \left(\frac{\dot{a}}{a}\right)^2 + \frac{k}{a^2} \right]. \tag{1.10}$$

Next we turn our attention to T_{ab} which is encoded by the matter content. We model all forms of matter as perfect fluids which are completely determined by their isotropic density $\rho(t)$ and pressure $P(t)$, such that their energy-momentum tensor takes the form:

$$T_{ab} = (\rho + P) U_a U_b + P g_{ab}, \tag{1.11}$$

Component	Contributions	Equation of state	Energy density
Matter	Cold dark matter Baryons	$w = 0$	$\rho \propto a^{-3}$
Radiation	Photons Neutrinos Gravitons	$w = \frac{1}{3}$	$\rho \propto a^{-4}$
Dark energy	Vacuum energy Modified gravity Something else?	$w = -1$	$\rho \propto a^{0}$

Table 1.1 The cosmic inventory.

where U_a is the 4-velocity of the fluid. For a comoving observer the energy-momentum tensor takes a particularly simple form:

$$T^a_b = \begin{pmatrix} -\rho & 0 & 0 & 0 \\ 0 & P & 0 & 0 \\ 0 & 0 & P & 0 \\ 0 & 0 & 0 & P \end{pmatrix}. \tag{1.12}$$

Additionally, conservation of the energy-momentum tensor:

$$\nabla_a T^a_b \equiv \partial_a T^a_b + \Gamma^a_{ac} T^c_b - \Gamma^c_{ab} T^a_c = 0, \tag{1.13}$$

implies the continuity equation for the cosmological fluid:

$$\dot{\rho} = -3\frac{\dot{a}}{a}(\rho + P), \tag{1.14}$$

since the spatial components of the conservation equation are identically zero. If we assume a constant equation of state $P = w\rho$ we can rewrite the continuity equation as

$$\frac{\dot{\rho}}{\rho} = -3(1+w)\frac{\dot{a}}{a} \Rightarrow \rho = \rho_0 \left(\frac{a}{a_0}\right)^{-3(1+w)}. \tag{1.15}$$

The ΛCDM model of the Universe is the most successful model in explaining our observations to date, and within the model all known (or theorised) particles are divided into three categories: matter, radiation and dark energy (Table 1.1).

Collecting these ingredients together allows us to reduce the 10 equations in Equation (1.1) to the two Friedmann equations:

$$\left(\frac{\dot{a}}{a}\right)^2 = \frac{8\pi G}{3}\rho - \frac{k}{a^2}, \tag{1.16}$$

$$\frac{\ddot{a}}{a} = -\frac{4\pi G}{3}(\rho + 3P). \tag{1.17}$$

Here ρ and P denotes the *total* energy density and pressure in the universe. We further define the Hubble parameter H as

$$H = \frac{\dot{a}}{a}. \tag{1.18}$$

Alternatively we can define the conformal Hubble parameter $\mathcal{H}$ in terms of conformal time $d\tau = \frac{dt}{a(t)}$:

$$\mathcal{H} = \frac{a'}{a} = aH, \tag{1.19}$$

where we use a dot to denote differentiation with respect to coordinate time, and a prime for conformal time.

1.2.2 Kinematics

All cosmological observations so far have been based on light of various forms, including radio waves as in the CMB [27, 50, 51], Infrared [52], X-rays [53], and most importantly for LSS surveys, optical rays [54, 55, 41, 43, 44]. With the recent detection of gravitational waves [56–61] we will enter a new era in cosmology. Nevertheless the technology is still in its infancy, and though it may become competitive or even surpass constraints from light-based observations as more detectors get built and hence detections made [62, 63], optical surveys will remain the primary source of cosmological information in the near future, especially in the context of LSS.

Due to the expansion of the Universe as well as the intrinsic movement of objects in the sky, photons that we observe are typically *redshifted*. To see this we first need to derive the geodesic equations which govern the motion of freely moving photons. We begin with the relativistic action $\mathcal{S}$ of a *massive* particle following a path $x^a(\lambda)$ parameterised by λ:

$$\mathcal{S} = \int ds = \int \sqrt{g_{ab}(x)\dot{x}^a\dot{x}^b}\,d\lambda \equiv \int \mathcal{L}(\lambda, x, \dot{x})\,d\lambda, \tag{1.20}$$

where the overdots denote differentiation with respect to λ. To extremise the action we invoke the Euler-Lagrange equations for the Lagrangian $\mathcal{L}$:

$$\frac{\partial \mathcal{L}}{\partial x^a} = \frac{d}{d\lambda}\left(\frac{\partial \mathcal{L}}{\partial \dot{x}^a}\right), \tag{1.21}$$

which, after some manipulations, give

$$\ddot{x}^a + \frac{1}{2}g^{ad}(\partial_b g_{dc} + \partial_c g_{bd} - \partial_d g_{bc})\dot{x}^b\dot{x}^c = \frac{\ddot{s}}{\dot{s}}\dot{x}^a, \tag{1.22}$$

and using the definition of the Christoffel symbols (Equation (1.2)) we obtain

$$\ddot{x}^a + \Gamma^a_{bc}\dot{x}^b\dot{x}^c = \frac{\ddot{s}}{\dot{s}}\dot{x}^a. \tag{1.23}$$

The term on the right hand side arises from the general choice of parameter λ. If λ is chosen to be an *affine* parameter such that $s = a\lambda + b$ then the right hand side vanishes, and identifying the 4-momentum vector of the massive particle as $P^a = \dot{x}^a$ we finally obtain its geodesic equation:

$$\frac{dP^a}{d\lambda} + \Gamma^a_{bc}P^bP^c = 0. \tag{1.24}$$

Although we have derived this equation for time-like geodesics (i.e. for massive particles), it can be shown that the same equation applies to null geodesics as well [49], and therefore can be used as the geodesic equation for photons.

1.2.3 Redshift

Before we use the FLRW metric (Equation (1.7)) to evaluate the geodesic equation we first rewrite the derivative term as:

$$\frac{dP^a}{d\lambda} = \frac{dx^b}{d\lambda}\frac{\partial P^a}{\partial x^b} = P^b\frac{\partial P^a}{\partial x^b}, \tag{1.25}$$

and due to spatial homogeneity, which implies $\partial_i P^a = 0$, the geodesic equation becomes

$$P^0\frac{\partial P^a}{\partial t} + \Gamma^a_{bc}P^bP^c = 0. \tag{1.26}$$

For a general photon 4-momentum $P^a = (p, \mathbf{p})$, where p is the magnitude of the 3-momentum: $p^2 = g_{ij}P^iP^j$, the 0th component of the geodesic equation gives

$$\frac{\dot{p}}{p} = -\frac{\dot{a}}{a} \qquad \Rightarrow \qquad p \propto \frac{1}{a}, \tag{1.27}$$

i.e. the physical momentum, and hence frequency, of photons decay as the Universe expands. This is known as redshifting simply because the low frequency of the visible spectrum appears red to us.

For a photon with wavelength λ_1 emitted from a distant galaxy at time t_1, and received by us at time t_0 with wavelength λ_0, we define the redshift parameter as the fractional change in the wavelength:

$$z \equiv \frac{\lambda_0 - \lambda_1}{\lambda_1} = \frac{a(t_0)}{a(t_1)} - 1. \tag{1.28}$$

It is conventional to define the scale factor at current time to be 1, i.e. $a(t_0) \equiv 1$, so we can also write

$$1 + z = \frac{1}{a(t_1)}. \tag{1.29}$$

Since the scale factor is a monotonically increasing function of time[1], the redshift parameter is a convenient label for events in the past, as well as the positions of galaxies in the sky. It is standard practice in galaxy surveys to represent the full 3D positions of galaxies with their angular position in the field of view, complimented by the distance information given by the redshift (Figure 1.2).

1.2.4 Hubble's law

For nearby galaxies we can Taylor expand the scale factor around the present day to find

$$a(t_1) = a(t_0)[1 + (t_1 - t_0)H_0 + \cdots], \tag{1.30}$$

where we define the Hubble constant, i.e. the present-day value of the Hubble parameter, as

$$H_0 \equiv \frac{\dot{a}(t_0)}{a(t_0)}. \tag{1.31}$$

[1] As we will see in Section 1.3 this is only true after the hot Big Bang.

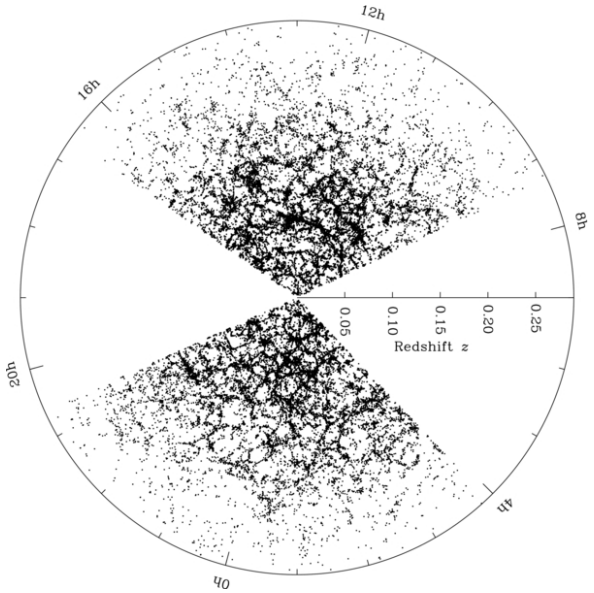

Fig. 1.2 The redshift distribution of galaxies in the Sloan Digital Sky Survey Data Release 7 (SDSS DR7) [4].

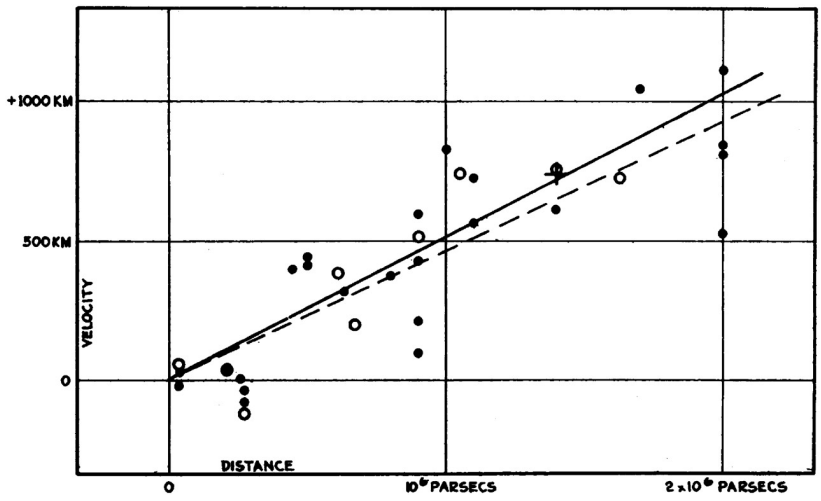

Fig. 1.3 Hubble's original work on the velocity-distance relationship of nearby galaxies [5]. Note that the y-axis should have velocity units of km/s.

For galaxies that are sufficiently close by the exact details of our cosmological model does not matter, and we can identify $t_1 - t_0$ as the distance d of the galaxy from us. Using Equation (1.28) this means the redshift of these galaxies are proportional to their distance away:

$$z \simeq H_0 d. \tag{1.32}$$

Lemaître [64] and Hubble [5] pioneered the measurement of the Hubble constant, and although the values they obtained are out by an order of magnitude from modern measurements it is the comprehensive work of the latter (Figure 1.3) that led this equation to be named Hubble's law. It is conventional to define

$$H_0 \equiv 100\,h\,\mathrm{km\,s^{-1}\,Mpc^{-1}}, \tag{1.33}$$

where h is a dimensionless parameter. The value of h given by the 2018 data release of the Planck Collaboration [33] is

$$h = 67.66 \pm 0.42. \tag{1.34}$$

This measurement of the Hubble constant with the CMB relies on the cosmological history of our entire Universe, in contrast to the work of Lemaître and Hubble which depends only on the local expansion history. The current state-of-the-art experiment that measures H_0 directly using our local environment is the Supernovae, H_0, for the Equation of State of Dark Energy (SHoES) collaboration, which utilises the standard candle property of Type Ia supernovae to reconstruct the Hubble diagram. Currently there is a significant disparity between these two methods: the latest results from SHoES reports a value of $h = 74.03 \pm 1.42$ which is in tension with the above value from Planck to more than 4σ [65]. This disagreement is quite possibly the most interesting puzzle in cosmology right now, prompting some unorthodox proposals to extend the base ΛCDM model (e.g. [66, 67]). The authors of [68] have outlined the requirements that any such modifications must satisfy, demonstrating the non-trivial task at hand.

1.2.5 ΛCDM

We conclude this section with the latest developments on the ΛCDM model. First we define the critical density parameter as present day as

$$\rho_{crit,0} \equiv \frac{3H_0^2}{8\pi G} = 1.878 \times 10^{-26} h^2 \,\mathrm{kg\,m^{-3}}, \tag{1.35}$$

where the subscript '0' denotes present day quantities, and use this to define the dimensionless density parameter for each cosmological component I:

$$\Omega_I \equiv \frac{\rho_{I,0}}{\rho_{crit,0}}. \tag{1.36}$$

The Friedmann equation (Equation (1.16)) can now be expressed as

$$\frac{H^2}{H_0^2} = \Omega_r a^{-4} + \Omega_m a^{-3} + \Omega_k a^{-2} + \Omega_\Lambda, \tag{1.37}$$

where we define the curvature density parameter as $\Omega_k \equiv -k/(a_0 H_0)^2$, and have normalised $a_0 = 1$. The FIRAS instrument on COBE gave a highly precise measurement of the black-body temperature of the CMB at $T = 2.72548 \pm 0.00057\,\mathrm{K}$ [69], which corresponds to $\Omega_r = 9.140 \times 10^{-5}$. The 2018 Planck data release, combined with measurements from CMB lensing and baryon acoustic oscillations (BAOs), gives [33]

$$\Omega_m = 0.3111 \pm 0.0056, \quad \Omega_k = 0.0007 \pm 0.0037, \quad \Omega_\Lambda = 0.6889 \pm 0.0056.$$

The matter density is further split into the cold dark matter component $\Omega_c = 0.04897$ and the baryon component $\Omega_b = 0.2607$. The consistency of Ω_k with 0 shows that our Universe is currently very flat. Since the energy contribution from curvature increases as a^{-2}, this rather astonishing result implies that the geometry of the early Universe was even flatter. This 'Flatness Problem', first raised by Dicke [70], was seen as a serious theoretical issue due to the belief that it is unnatural for fundamental physical parameters to be finely-tuned to special values [71]. This is one of the primary motivations behind the development of Cosmic Inflation, which we address in the next section.

1.3 Inflation

The statistical isotropy and homogeneity of our Universe is an empirical fact that we use to build our cosmological models. However the lack of a theoretical basis for this observation

has led many to search for a solution to this fine-tuning problem, in addition to the flatness problem mentioned above. In particular, this homogeneity implies that different, vastly separated, parts of the Universe must have been in causal contact with each other earlier in time, even though this could not happen in the cosmological model presented above without significant fine-tuning. This is known as the 'Horizon Problem' which we will elucidate here.

1.3.1 Horizon Problem

First we need to define the *horizon* of an observer, i.e. the regions in the spacetime that the observer can be in causal contact with. Since information travels at the speed of light we start by looking at photon geodesics, which is most convenient using conformal time. We consider radially travelling photons for simplicity[2], so that their line element can be written as

$$ds^2 = -a(\tau)^2(d\tau^2 - d\chi^2), \tag{1.38}$$

where we use χ here to denote the comoving radial coordinate in flat space, and $r = a\chi$ for the physical one. Since photons travel on null geodesics $ds^2 = 0$, their paths are given simply by

$$\Delta\chi = \pm\Delta\tau, \tag{1.39}$$

where positive denotes future-directed paths and negative past-directed ones. On a spacetime diagram of τ and χ the light cones therefore lie at 45° to either axis, and remain undistorted by the expansion of the Universe. We can then define the Particle Horizon as the greatest distance that an observer could have been influenced by past events:

$$\chi_{ph} = \tau - \tau_i = \int_{t_i}^{t} \frac{dt}{a(t)}, \tag{1.40}$$

where $\tau = \tau_i$ is some space-like surface in the past.

We further define the comoving Hubble radius as $(aH)^{-1} = \mathcal{H}^{-1}$, which is related to the particle horizon as follows:

$$\chi_{ph} = \int_{t_i}^{t} \frac{dt}{a(t)} = \int_{\ln(a_i)}^{\ln(a)} \frac{d\ln(a)}{aH}. \tag{1.41}$$

[2] We can do this due to the isotropy of spacetime.

Another way to understand the comoving Hubble radius is that it represents the distance at which objects appear to be moving away at the speed of light. To see this relationship consider the *Hubble velocity* of an object, which is its apparent speed driven purely by the expansion of the Universe:

$$v_{hub} = \frac{dr}{d\tau} = \frac{d(a\chi)}{d\tau} = a'\chi = \mathcal{H}r. \tag{1.42}$$

Note that we set $\chi' = 0$ here as we are not interested in the intrinsic, or peculiar, motion of the object. If the object appears to travel at $v_{hub} = 1$ we find that $r = \mathcal{H}^{-1}$, therefore $\mathcal{H}^{-1}$ roughly denotes the greatest distance an observer can communicate with at the current time.

For a perfect fluid with equation of state w the scale factor grows as $t^{2/3(1+w)}$, and if we assume it obeys the strong energy condition such that $1+3w > 0$, then we can evaluate the particle horizon:

$$\chi_{ph} = \frac{2}{1+3w}(aH)^{-1}, \tag{1.43}$$

i.e. for a conventional matter source the particle horizon and the Hubble radius both grow as the Universe expands. This immediately presents us with a problem: if we suppose that the Universe started at $a = \tau = 0$ then we find that the CMB is made up of many disconnected regions, which is difficult to reconcile with the uniformity of the CMB to one part in 10^5. This is illustrated in Figure 1.4. At the time of Recombination τ_{rec} when the CMB was formed, both the particle horizon and comoving Hubble radius were much smaller, therefore the sky is partitioned into many regions which have never been in causal contact. Given that the redshift of Recombination is $z_{rec} = 1100$, which is during the matter domination era such that $\chi_{ph} \propto \sqrt{a}$, the number of disconnected regions is

$$N = \left(\frac{r_0}{r_{rec}}\right)^2 = \frac{a_0}{a_{rec}} = 1 + z \approx 1100. \tag{1.44}$$

The statistical unlikelihood for these regions to all have almost the same temperature was a major theoretical problem.

1.3.2 Solution to the Horizon Problem

A solution to the Horizon Problem emerged in the early 1980s and marked a radical departure to the then conventional understanding of our Universe. This *Inflationary* model, while by no means without flaws, nor the only candidate solution (see e.g. [72]), has since become the most widely accepted theory to explain the early Universe. First proposed by Starobinsky

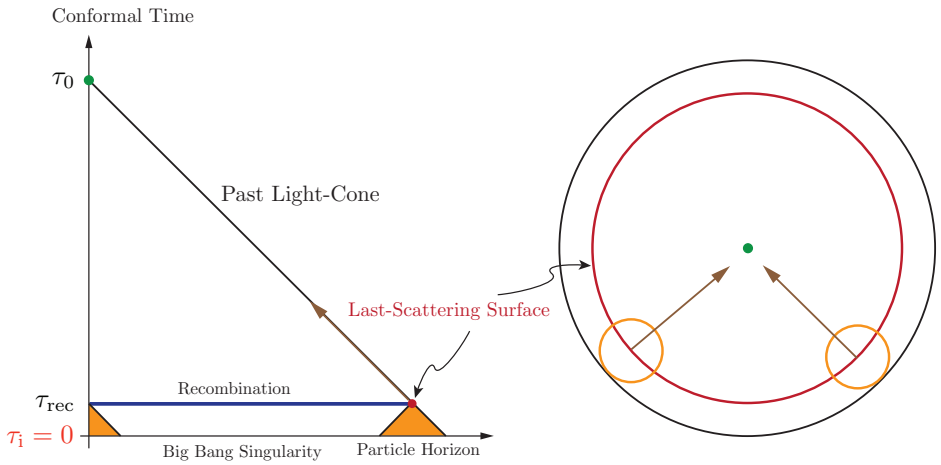

Fig. 1.4 Diagram illustrating the Horizon Problem [6]. Back at the time of Recombination the comoving Hubble radius and particle horizon were much smaller, which meant that many CMB photons could never have been in causal contact with each other, despite observations of the CMB showing a remarkable uniformity of one part in 10^5.

[73], Guth [74], Albrecht and Steinhardt [75], among others, the theory postulated a phase of accelerated expansion in the early Universe so that the comoving Hubble radius *shrank* with time:

$$\frac{d}{dt}(aH)^{-1} < 0. \tag{1.45}$$

This means that $\tau = 0$ is no longer the Big Bang singularity; there is a lot more conformal time than we previously thought. By pushing the singularity to negative conformal time we allow the whole Universe to communicate with itself (Figure 1.5), thus resolving the Horizon Problem.

However appealing the simplicity of this idea, a moment's reflection on the physical implications of a shrinking comoving Hubble radius highlights a significant drawback of the theory. An accelerated expansion requires a fluid that violates the strong energy condition such that $1+3w < 0$, a property shared by Dark Energy in order to explain the accelerated expansion at present day. This also implies that the Big Bang singularity is pushed to:

$$\tau_i = \int^{a_i} \frac{dt}{a(t)} = \frac{2H_0^{-1}}{1+3w} a_i^{(1+3w)/2} \to -\infty \tag{1.46}$$

for $a_i \to 0$. So far there has not been a satisfactory theoretical candidate for either. Nevertheless, it is a convenient conjecture motivated by observational data which provides a respite from the issues we have discussed above.

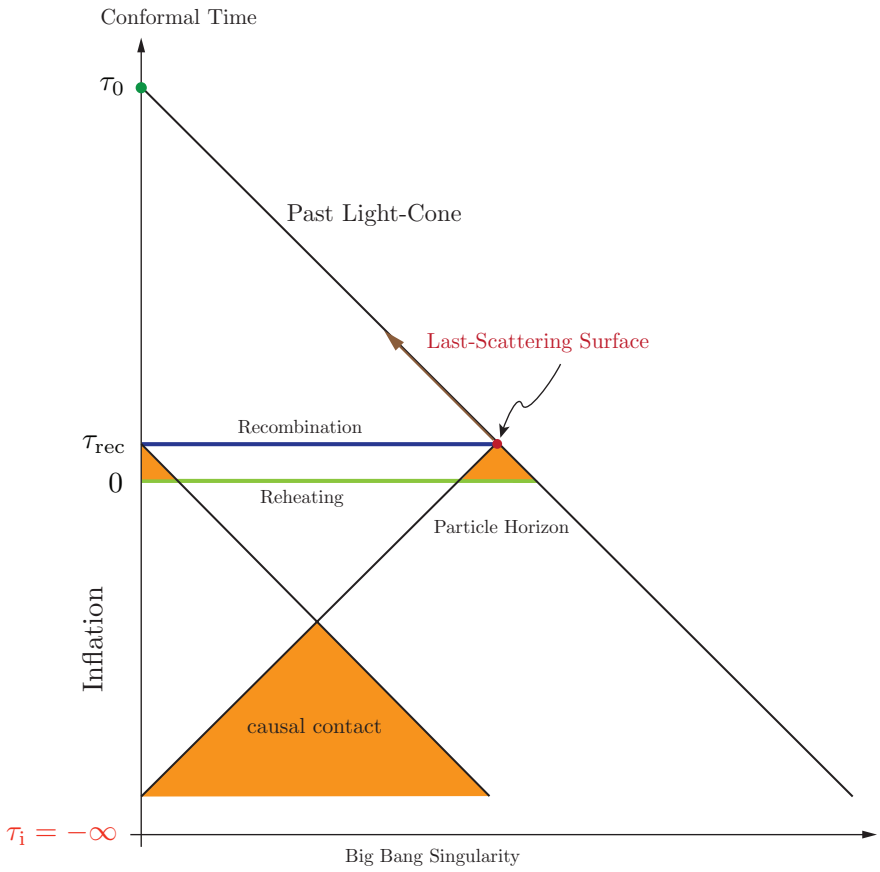

Fig. 1.5 Inflationary solution to the Horizon Problem [6]. By demanding a period of accelerated expansion we allow much more conformal time between the Big Bang singularity and Recombination, thus bringing all the disconnected regions in the CMB into causal contact.

Finally we conclude this discussion of the Horizon Problem by calculating the length of inflation required to solve the problem. To answer this question we must determine the energy scale at which inflation ended, which is yet another outstanding question. A number of theoretical considerations in theories beyond the Standard Model (SM) of particle physics, such as proton decay and Grand Unification Theories (GUT), point to a special mass scale of 10^{16} GeV [76], and it seems reasonable to adopt this as our gauge for the end of inflation. To solve the Horizon Problem we require the observable universe today to fit within the comoving Hubble radius at the beginning of inflation, i.e.

$$(a_I H_I)^{-1} \sim (a_0 H_0)^{-1}. \tag{1.47}$$

Assuming the Universe has been radiation-dominated since the end of inflation such that $H \propto a^{-2}$, the change in comoving Hubble radius is

$$\frac{a_0 H_0}{a_E H_E} \sim \frac{a_0}{a_E}\frac{a_E^2}{a_0^2} = \frac{a_E}{a_0} \sim \frac{T_{\gamma,0}}{T_{\gamma,E}} \sim 10^{-29}. \tag{1.48}$$

Since photons are relativistic their energy density is related to their temperature by $\rho_\gamma \propto T_\gamma^4$, and using $\rho_\gamma \propto a^{-4}$ we deduce $a \propto T_\gamma^{-1}$. The numerical value for $T_{\gamma,E}$ is 10^{16} GeV as argued above, and $T_{\gamma,0} = 2.725\,\mathrm{K} \sim 10^{-4}$ eV. As we shall see below we require the Hubble parameter to be roughly constant during inflation, therefore

$$\frac{a_E H_E}{a_I H_I} \sim \frac{a_E}{a_I} \sim 10^{29} \Rightarrow \ln\left(\frac{a_E}{a_I}\right) \gtrsim 60, \tag{1.49}$$

i.e. about 60 e-folds of inflation will solve the Horizon Problem.

1.3.3 The Mechanics of Inflation

Here we first write down the conditions for inflation to happen, and then discuss how we can achieve the 60 e-folds we need. A shrinking comoving Hubble radius implies

$$\frac{d}{dt}(aH)^{-1} = -\frac{\dot{a}H + a\dot{H}}{(aH)^2} = -\frac{1}{a}(1-\varepsilon) < 0 \Rightarrow \varepsilon \equiv -\frac{\dot{H}}{H^2} < 1. \tag{1.50}$$

Furthermore, for inflation to last we need ε to remain small over a number of e-folds. We can quantify this with a new parameter η, where

$$\eta \equiv \frac{d\ln(\varepsilon)}{dN} = -\frac{\dot{\varepsilon}}{H\varepsilon}, \tag{1.51}$$

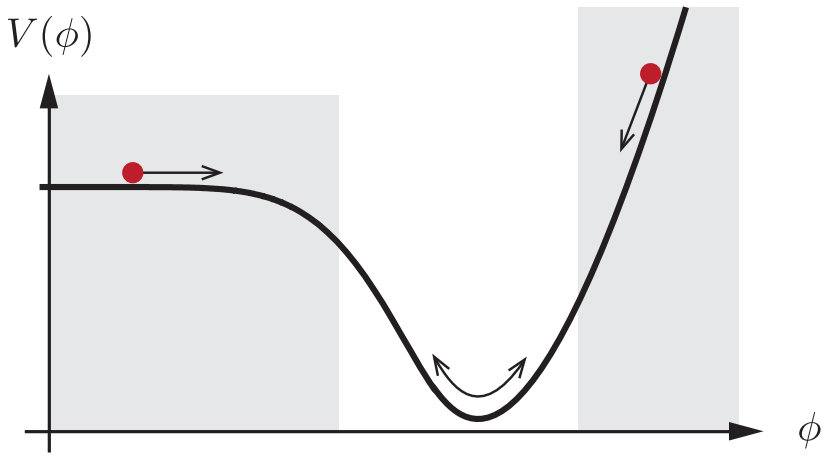

Fig. 1.6 Example of a potential that would allow slow-roll inflation. Inflation can occur in the parts of the potential that are shaded [7].

and we have defined $dN \equiv d\ln a = Hdt$. $|\eta| < 1$ therefore ensures inflation will persist. ε and η are examples of *slow-roll* parameters, for reasons we shall see below.

Due to the high energy scales involved we have no direct probe of inflationary physics, which has led to a proliferation of models in the literature. Here as a simple model: we consider inflation with a single scalar field, the inflaton $\phi(t,\mathbf{x})$, to illustrate the general principles. Even with this restriction there are hundreds of candidate theories [77], and many more for multi-field inflation. Assuming the inflaton is minimally coupled to gravity we can write down the action and its associated Lagrangian $\mathcal{L}$ of the theory as:

$$S \equiv \int dt\, d^3x \sqrt{-g}\mathcal{L} = \int dt\, d^3x \sqrt{-g}\left(-\frac{1}{2}\partial_a\phi\,\partial^a\phi - V(\phi)\right), \tag{1.52}$$

where g is the determinant of the metric, and $V(\phi)$ is the potential of the field that controls its dynamics. It is convenient to split the inflaton field into the background value $\bar{\phi}(t)$, which does not vary with position due to statistical isotropy, and its fluctuations around the mean, $\delta\phi(t,\mathbf{x})$. In this case we use the background FRW metric for which $g = -a^6$, and the Euler-Lagrange equations for $\bar{\phi}$ give

$$\frac{\partial\mathcal{L}}{\partial\bar{\phi}} = \partial_a\left(\frac{\partial\mathcal{L}}{\partial(\partial_a\bar{\phi})}\right) \Rightarrow \ddot{\bar{\phi}} + 3H\dot{\bar{\phi}} + V'(\bar{\phi}) = 0, \tag{1.53}$$

where $V'(\bar{\phi}) \equiv \frac{dV}{d\phi}|_{\phi=\bar{\phi}}$. This is the Klein-Gordon equation for the background inflaton which determines its evolution with time.

While the interactions of ϕ, which is encoded by the potential $V(\phi)$, is far from understood we can put constraints on it by making the *slow-roll* approximation, i.e. that $\varepsilon, |\eta| \ll 1$ such that the inflaton slowly rolls down the potential well. To see this we first evaluate the energy-momentum tensor for $\bar{\phi}$ from the action:

$$T_{ab} = \partial_a\bar{\phi}\partial_b\bar{\phi} - g_{ab}\left(\frac{1}{2}\partial_c\bar{\phi}\,\partial^c\bar{\phi} + V(\bar{\phi})\right), \tag{1.54}$$

which gives the energy density and pressure of the inflaton as

$$\rho_{\bar{\phi}} = \frac{1}{2}\dot{\bar{\phi}}^2 + V, \tag{1.55}$$

$$P_{\bar{\phi}} = \frac{1}{2}\dot{\bar{\phi}}^2 - V, \tag{1.56}$$

by using Equation (1.12). The Friedmann equation (Equation (1.16)) then gives

$$H^2 = \frac{1}{3M_p^2}\left(\frac{1}{2}\dot{\bar{\phi}}^2 + V\right), \tag{1.57}$$

where $M_p \equiv (8\pi G)^{-1/2}$ is the reduced Planck mass. This allows us to calculate the slow-roll parameters to be

$$\varepsilon = \frac{\dot{\bar{\phi}}^2}{2M_p^2H^2}, \tag{1.58}$$

$$\eta = 2\left(\varepsilon + \frac{\ddot{\bar{\phi}}}{H\dot{\bar{\phi}}}\right). \tag{1.59}$$

With $\varepsilon \ll 1$ the Friedmann equation becomes $H^2 \approx V/3M_p^2$, i.e. the Hubble parameter stays roughly constant, and if further $|\eta| \ll 1$ then the Klein-Gordon equation simplifies to $3H\dot{\bar{\phi}} = -V'(\bar{\phi})$, which differentiates to $3\dot{H}\dot{\bar{\phi}} + 3H\ddot{\bar{\phi}} = -V''\dot{\bar{\phi}}$. Substituting these back into the definition of ε and η implies

$$\varepsilon \approx \frac{M_p^2}{2}\left(\frac{V'}{V}\right)^2 \tag{1.60}$$

$$4\varepsilon - \eta \approx 2M_p^2\frac{V''}{V}. \tag{1.61}$$

This clearly shows that provided that the potential is flat enough the slow-roll approximation applies, as illustrated in the left part of Figure 1.6.

1.3.4 Statistics

All physical theories require concrete predictions, but two major difficulties arise if we were to test inflationary models. First of all due to the high energy scales involved ($\sim 10^{16}\,\text{GeV}$ as previously discussed) we likely will never be able to directly probe inflationary physics with terrestrial experiments, given that even in the 'far' future accelerators will still be confined to energy scales of $\sim 10^{6}\,\text{GeV}$ [78]. Cosmological observations allow us to indirectly probe the inflaton interactions, but we would have to first understand the full evolution history of our Universe is obviously a non-trivial task in itself.

Second, and more importantly, inflation is a quantum theory and as such is inherently unpredictable, i.e. the exact configuration of the inflaton field at the end of inflation cannot be known. Instead we are given the statistics of the field, and to test theory against observations we must measure the statistical properties of the Universe and compare them with the predictions evaluated from the model.

While it seems most appropriate to calculate the statistics of the inflaton fluctuations $\delta\phi$, the most convenient variable is actually the comoving curvature perturbation ζ. This is because it can also be shown that for adiabatic primordial perturbations (which are predicted by simple inflationary models [6]) ζ is conserved on super-Hubble scales where $k \ll \mathcal{H}$. This means that modes that exit the horizon during inflation due to the shrinking Hubble sphere are frozen and do not evolve, and retain the same value until they re-enter the horizon at late times. This is a powerful way to connect predictions from primordial theories and late-time observables, especially since the physics between those times is not always completely well understood.

Metric perturbations

Before we confront the relationship between $\delta\phi$ and ζ we must first discuss the perturbations to the metric, which couple to $\delta\phi$ via the action (Equation (1.52)). This will be useful for our discussion of observational constraints on inflation at the end of this section.

For a flat FLRW metric $ds^2 = a^2(\tau)\left(-d\tau^2 + \delta_{ij}dx^i dx^j\right)$ we write the perturbed metric as

$$ds^2 = a^2(\tau)\left[-(1+2A)d\tau^2 + 2B_i d\tau dx^i + (\delta_{ij} + h_{ij})dx^i dx^j\right]. \tag{1.62}$$

We can decompose these perturbations into scalar, vector and tensorial (SVT) contributions, which at linear order do not mix with each other. The vector B_i can be split into a scalar part $\partial_i B$ and a divergence-free vector $\hat{B}_i$ such that $\partial^i \hat{B}_i = 0$. Similarly the symmetric tensor h_{ij} can be written as the sum of a scalar part $2C\delta_{ij} + 2\partial_{\langle i}\partial_{j\rangle}E$, a divergence-free vector part

$2\partial_{(i}\hat{E}_{j)}$, and a divergence- and trace-free tensorial part $2\hat{E}_{ij}$, where

$$\partial_{\langle i}\partial_{j\rangle}E \equiv \left(\partial_i\partial_j - \frac{1}{3}\delta_{ij}\nabla^2\right)E, \tag{1.63}$$

$$\partial_{(i}\hat{E}_{j)} \equiv \frac{1}{2}\left(\partial_i\hat{E}_j + \partial_j\hat{E}_i\right). \tag{1.64}$$

This then gives a total of $4+4+2=10$ degrees of freedom comprised of the scalars A, B, C, E, vectors $\hat{B}_i, \hat{E}_i$ and tensor $\hat{E}_{ij}$.

However, not all these are physical degrees of freedom. In GR we always have a freedom in our choice of coordinates, giving rise to fictitious, *gauge* degrees of freedom that can be dealt with either by using gauge-invariant quantities that do not change under coordinate transformations, or by eliminating them through fixing the gauge. For a general coordinate transformation $x^a \to \tilde{x}^a = x^a + \xi^a$ we can similarly apply the SVT decomposition: $\xi^a = (\xi^0, \partial_i\xi + \hat{\xi}_i)$. This allows us to eliminate 2 scalar degrees of freedom through ξ^0 and ξ, and 2 vector ones through $\hat{\xi}_i$. A suitable choice of gauge typically greatly simplifies calculations, and here we adopt the *spatially-flat* gauge such that $C = E = 0$. In this gauge the relationship between $\delta\phi$ and ζ takes a remarkably simple form:

$$\zeta = -\frac{aH}{\dot{\phi}}\delta\phi. \tag{1.65}$$

Power Spectrum

The simplest statistic for ζ is the one-point correlation function, or ensemble mean, $\langle\zeta\rangle$. Since $\delta\phi$ measures deviations from the mean by Equation (1.65) it is clear that $\langle\zeta\rangle = 0$. For convenience when we discuss late time observables we will similarly use quantities with an ensemble average of zero. Throughout the thesis we shall adopt the following Fourier convention:

$$\zeta(\mathbf{k}) = \int d^3x\,\zeta(\mathbf{x})e^{-i\mathbf{k}\cdot\mathbf{x}}, \tag{1.66}$$

$$\zeta(\mathbf{x}) = \int \frac{d^3k}{(2\pi)^3}\,\zeta(\mathbf{k})e^{i\mathbf{k}\cdot\mathbf{x}}. \tag{1.67}$$

The lowest order statistic of practical use is therefore the two-point correlation function, also known as the power spectrum in Fourier space:

$$\left\langle\zeta(\mathbf{k})\zeta(\mathbf{k}')\right\rangle = (2\pi)^3\delta_D(\mathbf{k}+\mathbf{k}')P_\zeta(k). \tag{1.68}$$

$P_\zeta(k)$ depends only on the wavenumber k due to statistical isotropy and homogeneity. We further define the dimensionless power spectrum as

$$\Delta^2_\zeta(k) \equiv \frac{k^3}{2\pi^2} P_\zeta(k). \tag{1.69}$$

Since we switch from $\delta\phi$ to ζ at horizon crossing $k = aH$ we use Equation (1.65) to write

$$\Delta^2_\zeta(k) = \left(\frac{aH}{\dot{\phi}}\right)^2 \Delta^2_{\delta\phi}\bigg|_{k=aH} = \frac{1}{2\varepsilon M_p^2}\Delta^2_{\delta\phi}\bigg|_{k=aH}, \tag{1.70}$$

where we used the definition of ε in Equation (1.58), and for single field slow-roll inflation it can be shown that in the super-horizon limit $\Delta^2_{\delta\phi} = \left(\frac{H}{2\pi}\right)^2$. Since H and ε are slowly varying variables during inflation, and because we evaluate the $\Delta^2_\zeta(k)$ at horizon crossing $k = aH$, we expect the primordial power spectrum to be *nearly scale-invariant*, i.e. almost independent of k. It can therefore be parameterised in this form:

$$\Delta^2_\zeta(k) \equiv A_s \left(\frac{k}{k_*}\right)^{n_s - 1}, \tag{1.71}$$

where A_s is the amplitude measured at a reference scale k_* (also known as the pivot scale, typically chosen to be $0.05\,\mathrm{Mpc}^{-1}$), and n_s is the spectral tilt which characterises the k-dependence of $\Delta^2_\zeta(k)$. For single field slow-roll inflation we can evaluate n_s as

$$n_s - 1 \equiv \frac{d\ln\Delta^2_\zeta}{d\ln k} = -2\varepsilon - \eta, \tag{1.72}$$

so a small deviation from exact scale-invariance is predicted.

While single field slow-roll inflation gives a nearly scale-invariant power spectrum for scalar perturbations, an even more generic prediction from inflation is the existence of *primordial gravitational waves* from the tensorial perturbations in the metric $\hat{E}_{ij}$. We can similarly define a power spectrum for these tensorial modes:

$$\Delta^2_t(k) \equiv 2 \times \Delta^2_{\hat{E}}(k), \tag{1.73}$$

and for single field slow-roll inflation it again takes a nearly scale-invariant form:

$$\Delta^2_t(k) = \frac{2}{\pi^2}\frac{H^2}{M_p^2}\bigg|_{k=aH} \equiv A_t \left(\frac{k}{k_*}\right)^{n_t}, \tag{1.74}$$

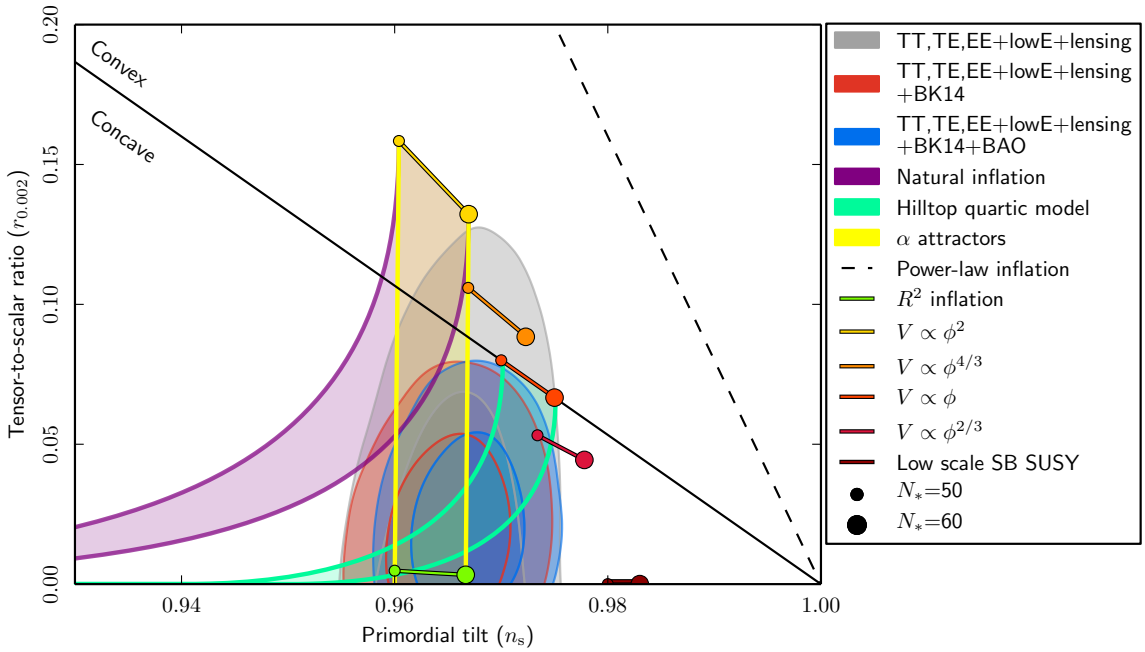

Fig. 1.7 Joint marginalised constraints for n_s and r evaluated at $k_* = 0.002\,\mathrm{Mpc}^{-1}$, using various data sources [8]. Also shown are predictions of selected inflationary models. While there is still much to learn about inflation, we are finally able to distinguish between competing models, and in particular rule out some of them, e.g. ϕ^2 inflation.

where A_t is the amplitude of the tensor perturbations and n_t is the tensor spectral index. A common measure for the amplitude of tensor modes is via the tensor-to-scalar index $r \equiv A_t/A_s$, which is equal to 16ε for single field slow-roll inflation.

Finally to conclude this discussion on the primordial power spectra we present the latest constraints on inflation from the Planck 2018 data release [33]. Combining Planck, CMB lensing, and BAO data gives an scalar amplitude of $A_s = (2.105 \pm 0.030) \times 10^{-9}$, and further incorporating data from the BICEP2/Keck Array (BK14) data gives the scalar spectral index as $n_s = 0.9670 \pm 0.0037$. To date primordial gravitational waves have not yet been observed, and the tensor-to-scalar ratio is constrained to be $r_{0.002} < 0.065$. Joint constraints on n_s and r are shown in Figure 1.7; it is truly an impressive feat to be able to put such tight bounds on these parameters and rule out inflationary theories, in spite of the seemingly insurmountable difficulties.

Bispectrum

A special class of primordial perturbations are known as *Gaussian* random fields as they are fully described by their power spectrum. However, interactions encoded in the inflaton potential can source higher order statistics. Measurements of higher order correlation functions thus serve as a probe of inflaton interactions since the power spectrum only constrains the free theory [7]. These correlators, which quantify the deviation from Gaussianity, or *non-Gaussianity*, of the distribution function are of popular interest as they are powerful ways to constrain non-linear interactions in any primordial theory.

The lowest order non-linear statistic is the three-point correlation function, or in Fourier space, the bispectrum:

$$\langle \zeta(\mathbf{k}_1)\zeta(\mathbf{k}_2)\zeta(\mathbf{k}_3)\rangle = (2\pi)^3 \delta_D(\mathbf{k}_1+\mathbf{k}_2+\mathbf{k}_3) B_\zeta(k_1,k_2,k_3). \tag{1.75}$$

Due to statistical isotropy and homogeneity the bispectrum only depends on the 3 wavenumbers k_i. Additionally the delta function, arising from momentum conservation, imposes the triangle condition on the wavevectors so the three k_i, when taken as lengths, must be able to form a triangle.

Unlike the power spectrum, which is a one-dimensional object, bispectra are inherently three-dimensional. The particular dependence of a bispectra on the three k_i is known as its shape. The primordial bispectrum is often written in terms of the shape function S_ζ:

$$S_\zeta(k_1,k_2,k_3) \equiv \frac{(k_1k_2k_3)^2}{(2\pi^2\Delta^2_\zeta)^2} B_\zeta(k_1,k_2,k_3), \tag{1.76}$$

and it is useful to further define the amplitude of this non-Gaussian contribution in the equilateral configuration via the f_{nl} parameter:

$$f_{nl} \equiv \frac{5}{18} S_\zeta(k_1,k_2,k_3). \tag{1.77}$$

This somewhat odd definition is a historical accident. We shall consider a simple non-Gaussian model by Komatsu and Spergel [79] to illustrate these concepts. A obvious way to generate non-linear effects is by Taylor expanding around a Gaussian field. The *local* template has an additional term proportional to the square of the Gaussian field ζ_G:

$$\zeta_{\text{local}}(\mathbf{x}) = \zeta_G(\mathbf{x}) + \frac{3}{5} f_{nl,loc}(\zeta^2_G(\mathbf{x}) - \langle \zeta^2_G \rangle), \tag{1.78}$$

where we have put in $f_{nl,loc}$ explicitly to quantify the amplitude of non-Gaussianity, and the term in angle brackets is added to ensure $\zeta_{\rm local}$ has zero mean. The factor of 3/5 comes from the fact that the model was first written down in terms of the Newtonian gauge metric perturbation, which is related to the comoving curvature perturbation by $\Phi = -\frac{3}{5}\zeta$ during the matter-dominant era.

In Fourier space squaring becomes a self-convolution operation:

$$\zeta_{\rm local}(\mathbf{k}) = \zeta_G(\mathbf{k}) + \frac{3}{5} f_{nl,loc} \int \frac{d^3q}{(2\pi)^3}\, \zeta_G(\mathbf{q})\zeta_G(\mathbf{k}-\mathbf{q}), \tag{1.79}$$

so that the three-point correlator of $\zeta_{\rm local}(\mathbf{k})$ is

$$\begin{aligned}
&\langle \zeta_{\rm local}(\mathbf{k}_1)\zeta_{\rm local}(\mathbf{k}_2)\zeta_{\rm local}(\mathbf{k}_3)\rangle \\
&= \frac{3}{5} f_{nl,loc} \left\langle \zeta_G(\mathbf{k}_1)\zeta_G(\mathbf{k}_2) \int \frac{d^3q}{(2\pi)^3}\, \zeta_G(\mathbf{q})\zeta_G(\mathbf{k}_3-\mathbf{q}) \right\rangle + 2\,\text{perms.} \\
&\quad + \frac{27}{125} f_{nl,loc}^3 \Big\langle \int \frac{d^3q_1}{(2\pi)^3} \int \frac{d^3q_2}{(2\pi)^3} \int \frac{d^3q_3}{(2\pi)^3} \\
&\qquad \times \zeta_G(\mathbf{q}_1)\zeta_G(\mathbf{k}_1-\mathbf{q}_1)\zeta_G(\mathbf{q}_2)\zeta_G(\mathbf{k}_2-\mathbf{q}_2)\zeta_G(\mathbf{q}_3)\zeta_G(\mathbf{k}_3-\mathbf{q}_3) \Big\rangle \\
&\approx \frac{6}{5} f_{nl,loc} (2\pi)^3 \delta_D(\mathbf{k}_1+\mathbf{k}_2+\mathbf{k}_3) \left[P_\zeta(k_1)P_\zeta(k_2) + P_\zeta(k_2)P_\zeta(k_3) + P_\zeta(k_3)P_\zeta(k_1) \right].
\end{aligned} \tag{1.80}$$

In going from the first to second line we used the Gaussianity of ζ_G so that odd correlators of ζ vanish, and that Wick's theorem can be applied to expand the even correlators in the second line to products of the two-point correlator and hence power spectrum P_ζ. We also used the fact that some terms in the Wick expansion only contribute to the zero mode $\mathbf{k} = 0$ and hence become irrelevant, e.g.

$$\begin{aligned}
&\langle \zeta_G(\mathbf{k}_1)\zeta_G(\mathbf{k}_2)\rangle \left\langle \int \frac{d^3q}{(2\pi)^3}\, \zeta_G(\mathbf{q})\zeta_G(\mathbf{k}_3-\mathbf{q}) \right\rangle \\
&= (2\pi^3)\delta_D(\mathbf{k}_1+\mathbf{k}_2)P(k_1) \int d^3q\, \delta_D(\mathbf{k}_3)P(q).
\end{aligned} \tag{1.81}$$

It is worth noting that a similar calculation shows that the power spectrum of $\zeta_{\rm local}$, $P_{\rm local}$, is the same as P_ζ, demonstrating that the power spectrum is insensitive to the non-linear interactions in this model.

Through Equation (1.80) we can identify the bispectrum of $\zeta_{\rm local}$ as

$$B_{\rm local}(k_1,k_2,k_3) = \frac{6}{5} f_{nl,loc} \left[P_\zeta(k_1)P_\zeta(k_2) + P_\zeta(k_2)P_\zeta(k_3) + P_\zeta(k_3)P_\zeta(k_1) \right], \tag{1.82}$$

and therefore the shape function for local non-Gaussianity is

$$S_{\rm local}(k_1,k_2,k_3) = \frac{6}{5} f_{nl,loc} \left(\frac{k_3^2}{k_1 k_2} + \frac{k_1^2}{k_2 k_3} + \frac{k_2^2}{k_3 k_1} \right). \tag{1.83}$$

In the equilateral limit this gives $S_{\rm local}(k,k,k) = \frac{18}{5} f_{nl,loc}$, and we recover Equation (1.77).

Two more templates commonly used in the literature and experimental searches for non-Gaussianity [80–83] are the equilateral shape:

$$B_{\rm equil}(k_1,k_2,k_3) = 6A_s^2 f_{nl,equil} \Bigg\{ -\frac{1}{k_1^{4-n_s} k_2^{4-n_s}} - \frac{1}{k_2^{4-n_s} k_3^{4-n_s}} - \frac{1}{k_3^{4-n_s} k_1^{4-n_s}} - \frac{2}{(k_1 k_2 k_3)^{2(4-n_s)/3}} + \left[\frac{1}{k_1^{(4-n_s)/3} k_2^{2(4-n_s)/3} k_3^{4-n_s}} + 5\,\text{perms.} \right] \Bigg\}, \tag{1.84}$$

and the orthogonal template:

$$B_{\rm ortho}(k_1,k_2,k_3) = 6A_s^2 f_{nl,ortho} \Bigg\{ -\frac{3}{k_1^{4-n_s} k_2^{4-n_s}} - \frac{3}{k_2^{4-n_s} k_3^{4-n_s}} - \frac{3}{k_3^{4-n_s} k_1^{4-n_s}} - \frac{8}{(k_1 k_2 k_3)^{2(4-n_s)/3}} + \left[\frac{3}{k_1^{(4-n_s)/3} k_2^{2(4-n_s)/3} k_3^{4-n_s}} + 5\,\text{perms.} \right] \Bigg\}, \tag{1.85}$$

where A_s is the amplitude of the primordial power spectrum introduced above.

Insight can often be gleaned by examining the behaviour of the bispectrum in certain configurations. One popular choice is the *squeezed* limit where one wavenumber is much smaller than the other two, e.g. $k_1 \ll k_2 \sim k_3$. This is particularly important for local non-Gaussianity as it peaks in this configuration:

$$\lim_{k_1 \ll k_2 \sim k_3} S_{\rm local}(k_1,k_2,k_3) = \frac{12}{5} f_{nl,loc} \frac{k_2}{k_1}. \tag{1.86}$$

Furthermore, the following consistency relation between the primordial bispectrum and power spectrum in the squeezed limit was established in [84]:

$$\lim_{k_1 \to 0} \langle \zeta_{\rm local}(\mathbf{k}_1) \zeta_{\rm local}(\mathbf{k}_2) \zeta_{\rm local}(\mathbf{k}_3) \rangle = (2\pi)^3 \delta_D(\mathbf{k}_1 + \mathbf{k}_2 + \mathbf{k}_3) P_\zeta(k_1) P_\zeta(k_3)(1 - n_s). \tag{1.87}$$

This powerful result states that single-field inflation produces a bispectrum that is suppressed in the squeezed limit, regardless of the dynamics of the inflaton, the shape of the inflaton potential or whether slow-roll inflation is admitted. Another important result due to Maldacena is that standard single field slow-roll inflation generates only small primordial non-Gaussianities (PNG) that are slow roll suppressed [85]. Here we will only quote the final result:

$$\begin{aligned} &S^{SR}(k_1,k_2,k_3) \\ &= \left[\frac{\eta-\varepsilon}{8}\left(\frac{k_1^2}{k_2k_3}+2\,\text{perms.}\right)+\frac{\varepsilon}{8}\left(\frac{k_1}{k_2}+5\,\text{perms.}\right)+\frac{\varepsilon}{K}\left(\frac{k_1k_2}{k_3}+2\,\text{perms.}\right)\right], \end{aligned} \tag{1.88}$$

where $K = k_1 + k_2 + k_3$, such that

$$f_{nl,SR} = \mathcal{O}(\varepsilon,\eta) \ll 1. \tag{1.89}$$

Although these are very strong restrictions on non-Gaussianities produced by single-field inflation, many inflationary models are not bound by them and can produce large non-Gaussian signals. These include, but are not limited to, multi-field inflationary models, the introduction of non-canonical kinetic terms (such as in DBI inflation), sharp or periodic features in the inflaton potential, a non-Bunch-Davies vacuum state, and deviations from Einstein gravity [86].

Primordial non-Gaussianity has not been detected yet, and the latest constraints from Planck are $f_{nl,loc} = -0.9 \pm 5.1$, $f_{nl,equil} = -26 \pm 47$ and $f_{nl,ortho} = -38 \pm 24$ for the local, equilateral and orthogonal templates respectively [80], which remains consistent with single-field, slow roll inflation. Note that in [80] their definition of $B_{\text{local}}(k_1,k_2,k_3)$ lacks the factor of $3/5$ we have here.

1.4 Late time cosmology

Inflation created the initial conditions for our Universe, which became classical perturbations that grew in its subsequent evolution. The two main late-time datasets in cosmology are the CMB temperature anisotropies $\Theta = \frac{\Delta T}{T}$ and the matter overdensity field $\delta(\mathbf{x}) = \frac{\Delta\rho(\mathbf{x})}{\rho} = \frac{\Delta n(\mathbf{x})}{\bar{n}}$ where ρ is the density of the matter in question and $n(\mathbf{x})$ is the number density in the case of discrete objects. While the exact nature of dark matter is unknown, it is typically modelled as a continuous field δ_m that only interacts gravitationally with other matter. The clustering of dark matter produces virialised, bound dark matter halos, creating a discrete field δ_h of halo centres. By definition we cannot observe dark matter, and instead the discrete galaxy

density field δ_g acts as a tracer to the underlying halo and dark matter fields. To make things more difficult the galaxy distribution is not the same as that of the dark matter field, but CMB lensing experiments will help us understand this biased relation [87].

Extensive work has been done with CMB anisotropies, culminating in the tight constraints on parameters such as f_{nl} as previously discussed. However, the constraining power of the CMB has nearly reached its limits and will ultimately be superseded by observations of the large-scale structure of the Universe; this is simply because the three-dimensional galaxy distribution can provide more independent modes than the two-dimensional map of the CMB. This goal is facilitated by upcoming large data sets offered by galaxy surveys such as the Dark Energy Survey (DES) [41, 42], the Large Synoptic Survey Telescope (LSST) [43], the ESA Euclid Satellite [44] and the Dark Energy Spectroscopic Instrument (DESI) [45]. One of the most active areas of cosmological research today is therefore to understand the collapse of matter and evolution of large scale structure in the Universe. Extra value can be obtained from the addition of LSS observational data as it can be cross-correlated and combined with secondary CMB data, e.g. through weak lensing [88], for a wealth of new information.

Due to the linearity of CMB physics and the approximately Gaussian initial conditions most CMB information is encoded in the power spectrum C_l. This is not the case for LSS as non-linear gravitational interaction sources higher correlators, all of which must be measured to extract all the information LSS has to offer. For example, at mildly non-linear scales the bispectrum is the primary diagnostic as it exceeds the power spectrum in terms of cosmological information. A recent comprehensive forecasting of constraints from the galaxy power spectrum and bispectrum [89] has shown that the galaxy bispectrum leads to five times better bounds than the power spectrum alone, giving much tighter constraints for local-type PNG than current limits from Planck. This work is more complete and realistic than previous forecasts, e.g. [90–93], as they combined in their analysis different factors that were previously considered independently. The bispectrum also has a stronger dependence on cosmological parameters so can provide tighter constraints than the power spectrum for the same signal to noise and can help break degeneracies in parameter space through Baryon Acoustic Oscillations (BAOs) and galaxy bias, notably those between σ_8 and bias [94]. Many inflationary scenarios, such as those inspired by fundamental theories like superstring theory, or alternatives to inflation typically yield small, but measurable, PNGs that would be tell-tale signatures of new physics. In addition to constraining and testing early universe theories, the bispectrum can be used to test alternative scenarios such as those that modify standard Einstein gravity. This work builds on earlier efforts to estimate the full three-dimensional bispectrum from simulations (see, for example, [95–98, 11]) and direct

measurements of the galaxy bispectrum using existing galaxy survey data from the Baryon Oscillation Spectroscopic Survey (BOSS) [99–103].

There are many complications when extracting information from LSS compared to the CMB. At the time when recombination took place and CMB photons were released (i.e. redshift $z = 1100$), inhomogeneities in the universe were small, therefore CMB physics is linear and can be well modelled by perturbation theories. By contrast, we still do not have a solid theoretical understanding of the non-linear gravitational evolution of matter and galaxy formation, resulting in the need of large numerical simulations to obtain exact solutions. A combination of perturbation theory, e.g. an effective field theory (EFT) approach [104, 105], and nonlinear halo models has been shown to characterise the dark matter power spectrum and bispectrum very well at small and large scales, but the bispectrum at mildly non-linear regimes remain poorly understood [11]. Here we shall discuss the theoretical modelling of late time clustering of dark matter.

1.4.1 Statistics

As with our discussion on inflation the most commonly used statistic is the power spectrum:

$$\left\langle \delta(\mathbf{k})\delta(\mathbf{k}')\right\rangle = (2\pi)^3\delta_D(\mathbf{k}+\mathbf{k}')P_\delta(k). \tag{1.90}$$

The post-processing of primordial perturbations is non-trivial, especially since the evolution of a mode will depend on when it re-entered the horizon. It is convenient to capture these effects, calculated to linear order, into the *transfer function* $T(k,z)$, such that $\delta_{\rm lin}(\mathbf{k},z) = T(k,z)\delta_i(\mathbf{k})$, where $\delta_i(\mathbf{k})$ is the initial density field at high redshift. The dark matter linear power spectrum is therefore:

$$P_{\rm lin}(k,z) = T^2(k,z)P_i(k), \tag{1.91}$$

where $P_i(k) \propto k^{n_s}$ for standard slow-roll inflation. The transfer function has to be calculated numerically by tracing the interactions between matter and radiation throughout the radiation-dominated era and the subsequent evolution of $\delta_{\rm lin}$ after matter-radiation decoupling. There are many packages available such as `CAMB` [9], `CMBfast` [106] and `CLASS` [107].

At late times gravitational collapse leads to small-scale growth and hence deviation from the linear matter power spectrum. The full non-linear matter power spectrum cannot be calculated analytically, so to make comparisons with measurements from observations (Figure 1.9) we have to rely on numerical simulations. Additionally, non-linear gravitational interactions induce non-Gaussianities, so even in the absence of any primordial non-Gaussianities δ will

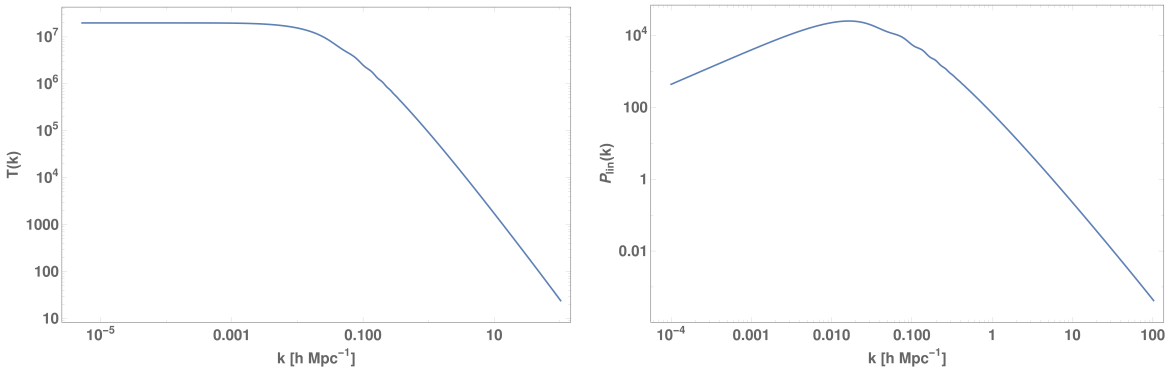

(a) Transfer function $T(k, z = 0)$ (b) Linear matter power spectrum $P_{\rm lin}(k, z = 0)$

Fig. 1.8 Transfer function and linear matter power spectrum at redshift $z = 0$ calculated using `CAMB` [9] with the Planck 2015 cosmological parameters (TT,TE,EE+lowP+lensing+ext, see Table 3.1.

still have a non-zero bispectrum $B_\delta(k_1, k_2, k_3)$:

$$\langle \delta(\mathbf{k}_1)\delta(\mathbf{k}_2)\delta(\mathbf{k}_3)\rangle = (2\pi)^3 \delta_D(\mathbf{k}_1 + \mathbf{k}_2 + \mathbf{k}_3) B_\delta(k_1, k_2, k_3). \tag{1.92}$$

At linear to weakly non-linear scales the framework to calculate the late-time non-linear statistics is cosmological perturbation theory. There are many flavours of perturbation theory, the more sophisticated of which, like the EFT approach mentioned above, are successful in pushing the boundaries of the theory further into the non-linear regime. Here we shall follow [108] and introduce Standard, or Eulerian, Perturbation Theory, as well as Lagrangian Perturbation Theory which is popular for the generation of initial conditions for numerical simulations. These theories only hold for Newtonian dynamics in expanding space, which is an appropriate assumption for cold dark matter.

1.4.2 Standard Perturbation Theory (SPT)

We begin by considering the effects of an expanding space on regular Newtonian gravity. The equation of motion for a dark matter particle with mass m at physical position $\mathbf{r}$ is:

$$\ddot{\mathbf{r}} = -\nabla_{\mathbf{r}}\Phi, \tag{1.93}$$

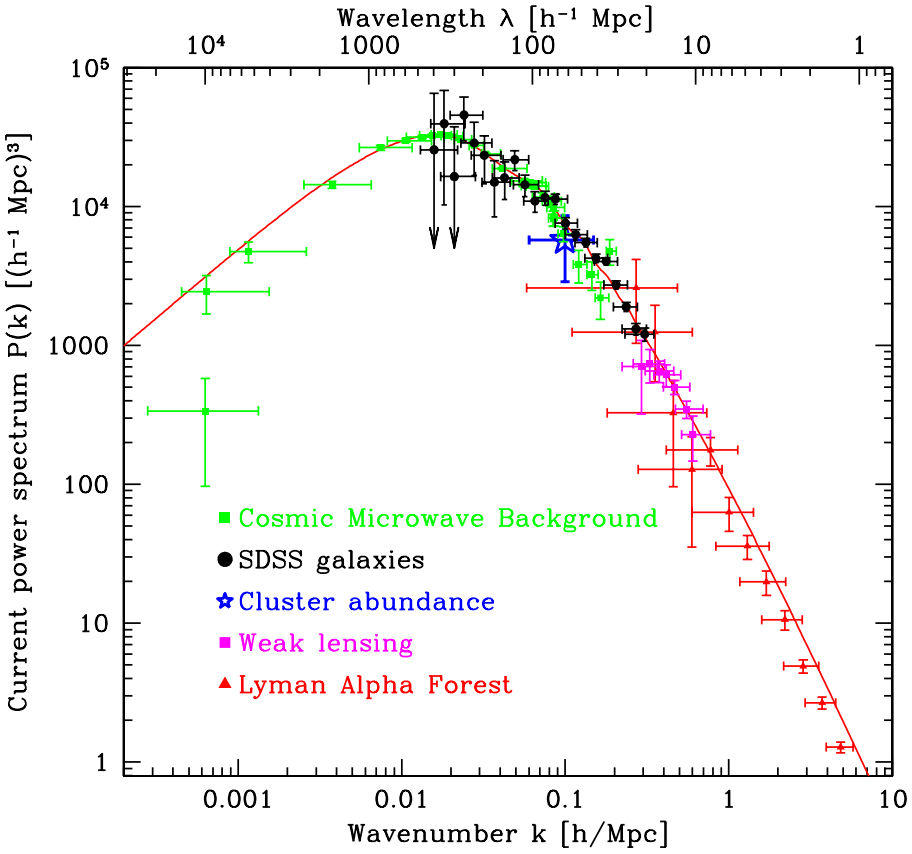

Fig. 1.9 The full non-linear galaxy power spectrum measured by SDSS and other sources [10]. Superimposed is the linear power spectrum predicted by a reference ΛCDM model.

where Φ is the gravitational potential. Switching to comoving coordinates $\mathbf{x} = \mathbf{r}/a$ we have $\mathbf{v} \equiv \dot{\mathbf{r}} = \mathcal{H}\mathbf{x} + \mathbf{x}'$, allowing us to rewrite the above as

$$\ddot{\mathbf{r}} = \frac{1}{a}(\mathcal{H}'\mathbf{x} + \mathcal{H}\mathbf{x}' + \mathbf{x}'') = -\frac{1}{a}\nabla_{\mathbf{x}}\Phi. \tag{1.94}$$

Further identifying the peculiar velocity as $\mathbf{u} \equiv \mathbf{x}'$ and the peculiar potential as

$$\phi \equiv \Phi - \frac{2}{3}\pi G\bar{\rho}a^2x^2, \tag{1.95}$$

we see that in the absence of other matter, such that the Friedmann equation (Equation (1.16)) becomes $\mathcal{H}' = -4\pi Ga\rho/3$, the equation of motion now reads

$$\mathbf{u}' + \mathcal{H}\mathbf{u} = -\nabla\phi, \tag{1.96}$$

where we have dropped the subscript $\mathbf{x}$ for brevity. Since the Universe only recently become Λ-dominated, this approximation is useful as most of structure formation takes place in the matter-dominated era. The peculiar potential is only sourced by density fluctuations δ. To see this we simply rewrite the Poisson equation $\nabla^2_{\mathbf{r}}\Phi = 4\pi G\rho$ in terms of comoving quantities:

$$\nabla^2\phi = 4\pi Ga^2\bar{\rho}\delta = 4\pi Ga^2\bar{\rho}_m\delta_m = \frac{3}{2}\mathcal{H}^2\Omega_m(\tau)\delta_m, \tag{1.97}$$

where we have assumed fluctuations in the energy density is dominated by that of matter, and we have made the time dependence of $\Omega_m(\tau) = 8\pi G\rho_m/3H^2$ explicit. Finally we define the conjugate momentum as $\mathbf{p} \equiv am\mathbf{u}$.

We are now in a position to write down the Vlasov equation, which enforces the conservation of the particle distribution function in phase space $f(\mathbf{x}, \mathbf{p}, \tau)$:

$$\begin{aligned}\frac{df}{d\tau} &= \frac{\partial f}{\partial \tau} + \frac{d\mathbf{x}}{d\tau}\cdot\frac{\partial f}{\partial \mathbf{x}} + \frac{d\mathbf{p}}{d\tau}\cdot\frac{\partial f}{\partial \mathbf{p}} \\ &= \frac{\partial f}{\partial \tau} + \frac{\mathbf{p}}{am}\cdot\frac{\partial f}{\partial \mathbf{x}} - am\nabla\phi\cdot\frac{\partial f}{\partial \mathbf{p}} = 0,\end{aligned} \tag{1.98}$$

where in the last line we used the equation of motion (Equation (1.96)). Momentum moments of the distribution function give rise to functions of the spatial distribution, such as the mass

density, peculiar velocity and anisotropic stress tensor:

$$\rho_m(\mathbf{x},\tau) \equiv \frac{m}{a^3}\int d^3p\, f(\mathbf{x},\mathbf{p},\tau), \tag{1.99}$$

$$u_i(\mathbf{x},\tau) \equiv \frac{m}{\rho_m(\mathbf{x},\tau)a^3}\int d^3p\, \frac{p_i}{am} f(\mathbf{x},\mathbf{p},\tau), \tag{1.100}$$

$$\sigma_{ij}(\mathbf{x},\tau) \equiv \frac{m}{\rho_m(\mathbf{x},\tau)a^3}\int d^3p\, \frac{p_i p_j}{a^2m^2} f(\mathbf{x},\mathbf{p},\tau) - u_i u_j. \tag{1.101}$$

The dark matter equations of motion can then be obtained by taking moments of the Vlasov equation. The zeroth order moment yields the continuity equation, or conversation of mass:

$$\delta' + \nabla\cdot[\mathbf{u}(1+\delta)] = 0. \tag{1.102}$$

Taking the first order moment and using the continuity equation we obtain the Euler equation, or conservation of momentum:

$$u_i' + \mathcal{H}u_i + \mathbf{u}\cdot\nabla u_i = -\partial_i\phi - \frac{1}{\rho}\partial_j(\rho\sigma_{ij}). \tag{1.103}$$

In principle one should repeat this procedure with higher order moments to obtain a hierarchy of equations of motion. For pressureless cold dark matter we make the simple assumption that all moments of f beyond the velocity are vanishing. Although this assumption is valid at early times before the formation of structure, it breaks down at increasingly large scales at late times due to gravitational collapse and virialisation.

Setting $\sigma_{ij} = 0$, and separating the degrees of freedom of $\mathbf{u}$ into its divergence $\theta = \nabla\cdot\mathbf{u}$ and curl (also known as the vorticity) $\mathbf{w} = \nabla\times\mathbf{u}$ finally yields the dark matter equations of motion that we shall solve here:

$$\frac{\partial\delta}{\partial\tau} + \theta = -\delta\theta - u_i\partial_i\delta, \tag{1.104}$$

$$\frac{\partial\theta}{\partial\tau} + \mathcal{H}\theta + \frac{3}{2}\mathcal{H}^2\Omega_m(\tau)\delta = -\partial_i u_j\partial_j u_i - u_j\partial_j\theta, \tag{1.105}$$

$$\frac{\partial\mathbf{w}}{\partial\tau} + \mathcal{H}\mathbf{w} - \nabla\times(\mathbf{u}\times\mathbf{w}) = 0. \tag{1.106}$$

The last equation for the vorticity shows that in the absence of any anisotropic stress and primordial vorticity, the vorticity remains zero at all times and hence can be ignored until

late-time shell-crossing. Using the convolution theorem[3], in Fourier space these equations become:

$$\frac{\partial \delta}{\partial \tau} + \theta = -\int \frac{d^3k_1}{(2\pi)^3}\frac{d^3k_2}{(2\pi)^3}(2\pi)^3\delta_D(\mathbf{k}-\mathbf{k}_1-\mathbf{k}_2)\alpha(\mathbf{k}_1,\mathbf{k}_2)\theta(\mathbf{k}_1)\delta(\mathbf{k}_2), \tag{1.108}$$

$$\frac{\partial \theta}{\partial \tau} + \mathcal{H}\theta + \frac{3}{2}\mathcal{H}^2\Omega_m(\tau)\delta = -\int \frac{d^3k_1}{(2\pi)^3}\frac{d^3k_2}{(2\pi)^3}(2\pi)^3\delta_D(\mathbf{k}-\mathbf{k}_1-\mathbf{k}_2)\beta(\mathbf{k}_1,\mathbf{k}_2)\theta(\mathbf{k}_1)\theta(\mathbf{k}_2). \tag{1.109}$$

The coupling kernels (symmetrised in the case of β) are

$$\alpha(\mathbf{k}_1,\mathbf{k}_2) = \frac{\mathbf{k}_1\cdot(\mathbf{k}_1+\mathbf{k}_2)}{k_1^2}, \tag{1.110}$$

$$\beta(\mathbf{k}_1,\mathbf{k}_2) = \frac{1}{2}(\mathbf{k}_1+\mathbf{k}_2)^2\frac{\mathbf{k}_1\cdot\mathbf{k}_2}{k_1^2k_2^2}. \tag{1.111}$$

We seek solutions in the form of this separable ansatz below:

$$\delta(\mathbf{k},\tau) = \sum_{n=1}^{\infty} D_1^n(\tau)\delta^{(n)}(\mathbf{k}), \tag{1.112}$$

$$\theta(\mathbf{k},\tau) = -\mathcal{H}\sum_{n=1}^{\infty} D_1^n(\tau)\theta^{(n)}(\mathbf{k}), \tag{1.113}$$

where $D_1(\tau)$ is the linear growth factor that satisfies $D_1'' + \mathcal{H}D_1' = \frac{3}{2}\Omega_m(\tau)\mathcal{H}D_1$. We shall first examine solutions in an Einstein-de Sitter (EdS) Universe where $\Omega_m = 1$ and $\Omega_\Lambda = 0$, so that the linear growth factor reduces to the scale factor: $D_1 = a$. Substituting these solutions into the equations of motion give

$$\delta^{(n)}(\mathbf{k}) = \prod_{i=1}^{n}\left\{\int \frac{d^3k_i}{(2\pi)^3}\delta^{(1)}(\mathbf{k}_i)\right\}F_n(\mathbf{k}_1,\ldots,\mathbf{k}_n)(2\pi)^3\delta_D(\mathbf{k}-\mathbf{k}|_1^n), \tag{1.114}$$

$$\theta^{(n)}(\mathbf{k}) = \prod_{i=1}^{n}\left\{\int \frac{d^3k_i}{(2\pi)^3}\delta^{(1)}(\mathbf{k}_i)\right\}G_n(\mathbf{k}_1,\ldots,\mathbf{k}_n)(2\pi)^3\delta_D(\mathbf{k}-\mathbf{k}|_1^n), \tag{1.115}$$

[3]The Fourier Transform of the product of two functions $h(\mathbf{x}) = f(\mathbf{x})g(\mathbf{x})$ is

$$h(\mathbf{k}) = \int \frac{d^3k_1}{(2\pi)^3}f(\mathbf{k}_1)g(\mathbf{k}-\mathbf{k}_1), \tag{1.107}$$

where $\mathbf{k}|_a^b \equiv \sum_{i=a}^b \mathbf{k}_i$. The convergence of this ansatz is reliant on the higher order terms $\delta^{(n)}(\mathbf{k})$ decaying sufficiently fast with n, which in turn is dependent on the magnitude of the linear density field $\delta^{(1)}(\mathbf{k}) = \delta_{\rm lin}(\mathbf{k})$. Perturbation theory therefore breaks down at small scales when the linear fluctuations become large so that the sum diverges. The convolution kernels can be found with the following recurrence relations, with the initial conditions $F_1 = G_1 = 1$:

$$F_n(\mathbf{k}_1,\ldots,\mathbf{k}_n) = \sum_{i=1}^{n-1} \frac{G_i(\mathbf{k}_1,\ldots,\mathbf{k}_i)}{(2n+3)(n-1)} \Big[(2n+1)\alpha(\mathbf{k}|_1^i,\mathbf{k}|_{i+1}^n)F_{n-i}(\mathbf{k}_{i+1},\ldots,\mathbf{k}_n) + 2\beta(\mathbf{k}|_1^i,\mathbf{k}|_{i+1}^n)G_{n-i}(\mathbf{k}_{i+1},\ldots,\mathbf{k}_n)\Big], \tag{1.116}$$

$$G_n(\mathbf{k}_1,\ldots,\mathbf{k}_n) = \sum_{i=1}^{n-1} \frac{G_i(\mathbf{k}_1,\ldots,\mathbf{k}_i)}{(2n+3)(n-1)} \Big[3\alpha(\mathbf{k}|_1^i,\mathbf{k}|_{i+1}^n)F_{n-i}(\mathbf{k}_{i+1},\ldots,\mathbf{k}_n) + 2n\beta(\mathbf{k}|_1^i,\mathbf{k}|_{i+1}^n)G_{n-i}(\mathbf{k}_{i+1},\ldots,\mathbf{k}_n)\Big]. \tag{1.117}$$

The F_2 kernel, $F_2(\mathbf{k}_1,\mathbf{k}_2) = \frac{5}{7}\alpha(\mathbf{k}_1,\mathbf{k}_2) + \frac{2}{7}\beta(\mathbf{k}_1,\mathbf{k}_2)$, and in particularly its symmetrised version:

$$\begin{aligned} F_2^{(s)}(\mathbf{k}_1,\mathbf{k}_2) &\equiv \frac{1}{2!}\sum_{\rm perms.} F_2(\mathbf{k}_1,\mathbf{k}_2) \\ &= \frac{5}{7} + \frac{1}{2}\frac{\mathbf{k}_1\cdot\mathbf{k}_2}{k_1 k_2}\left(\frac{k_1}{k_2}+\frac{k_2}{k_1}\right) + \frac{2}{7}\frac{(\mathbf{k}_1\cdot\mathbf{k}_2)^2}{k_1^2 k_2^2}, \end{aligned} \tag{1.118}$$

will be particularly important for our discussion below.

In a general cosmology this separable ansatz no longer applies [108, 109]. However the difference between the solution above and the exact solution for a ΛCDM Universe are small and generally sub-percent [110]. All the cosmological dependence on Ω_m and Ω_Λ can be absorbed into the linear growth factor D_1, and the recursion relations quoted above still apply.

Now that we have the full solution for δ we can write down its n-spectra in terms of its perturbative expansion. For the two-point correlator we have

$$\langle\delta(\mathbf{k}_1)\delta(\mathbf{k}_2)\rangle = \left\langle\delta^{(1)}(\mathbf{k}_1)\delta^{(1)}(\mathbf{k}_2)\right\rangle + 2\left\langle\delta^{(1)}(\mathbf{k}_1)\delta^{(3)}(\mathbf{k}_2)\right\rangle + \left\langle\delta^{(2)}(\mathbf{k}_1)\delta^{(2)}(\mathbf{k}_2)\right\rangle + \cdots, \tag{1.119}$$

as $\delta^{(1)}$ is a Gaussian random field, and hence its odd correlators vanish. The power spectrum of $\delta^{(1)}$ is the linear power spectrum $P_{\rm lin}$ introduced above, giving the non-linear power

spectrum to 1-loop order as

$$P_{\rm NL}(k) = P_{\rm lin}(k) + 2P_{13}(k) + P_{22}(k) + \cdots, \tag{1.120}$$

where

$$P_{13}(k) = \int \frac{d^3q}{(2\pi)^3} 3P_{\rm lin}(k)P_{\rm lin}(q)F_3^{(s)}(\mathbf{k},\mathbf{q},-\mathbf{q}), \tag{1.121}$$

$$P_{22}(k) = \int \frac{d^3q}{(2\pi)^3} 2P_{\rm lin}(q)P_{\rm lin}(|\mathbf{k}-\mathbf{q}|)\left[F_2^{(s)}(\mathbf{q},\mathbf{k}-\mathbf{q})\right]^2. \tag{1.122}$$

Tree-level bispectrum

For the bispectrum the lowest order of the perturbative expansion, i.e. at tree-level, is the tree-level bispectrum $B^{\rm tree} = B_{112}$:

$$B^{\rm tree}(k_1,k_2,k_3) = 2P_{\rm lin}(k_1)P_{\rm lin}(k_2)F_2^{(s)}(\mathbf{k}_1,\mathbf{k}_2) + 2\,\text{perms.}. \tag{1.123}$$

Following [111], and correcting for a mistake in [108], we modify $F_2^{(s)}$ from its EdS form to take into account the presence of Λ:

$$F_2^{(s),\Lambda}(\mathbf{k}_1,\mathbf{k}_2) = \frac{1}{2}(1+\varepsilon) + \frac{1}{2}\frac{\mathbf{k}_1\cdot\mathbf{k}_2}{k_1k_2}\left(\frac{k_1}{k_2}+\frac{k_2}{k_1}\right) + \frac{1}{2}(1-\varepsilon)\frac{(\mathbf{k}_1\cdot\mathbf{k}_2)^2}{k_1^2k_2^2}, \tag{1.124}$$

where $\varepsilon \approx -(3/7)\Omega_m^{-1/143}$. The tree-level bispectrum is a very useful shape for characterising the matter bispectrum at large scales where density perturbations are small. It fails at smaller scales when perturbation theory breaks down so we need additional shapes for a good fit to the bispectrum in those regimes. The authors of [11, 17] have extended the effectiveness of the tree-level shape by replacing $P_{\rm lin}$ with the non-linear power spectrum $P_{\rm NL}$ and we shall follow their example in our analysis of the dark matter bispectrum in this thesis.

1.4.3 Lagrangian Perturbation Theory (LPT)

Another popular variant of perturbation theory is Lagrangian perturbation theory (LPT), the basics of which is introduced here following [108, 111, 112 (Appendix E)]. Since the explicit calculation of the 2LPT bispectrum is not presented in any of them it is pedagogical to do so here. Our derivation will focus first on the EdS universe, as in [113] so that exact analytical solutions can be obtained, then generalise to ΛCDM. The presentation here will therefore be slightly different from those sources, although the final deduction is the same.

In LPT the object of focus is the displacement field $\boldsymbol{\psi}(\mathbf{q},\tau)$, where $\mathbf{q}$ is the initial position of the particle and τ is conformal time. It is therefore related to Eulerian or Standard perturbation theory (SPT) as follows:

$$\mathbf{x}(\tau) = \mathbf{q} + \boldsymbol{\psi}(\mathbf{q},\tau). \tag{1.125}$$

Conservation of mass, $\bar{\rho}(1+\delta(\mathbf{x},\tau))d^3x = \bar{\rho}d^3q$, then further allows us to write:

$$1+\delta(\mathbf{x},\tau) = \left|\frac{\partial \mathbf{q}}{\partial \mathbf{x}}\right| \equiv \frac{1}{J(\mathbf{q},\tau)}, \tag{1.126}$$

where $J(\mathbf{q},\tau) = \det\left(\delta_{ij} + \psi_{i,j}(\mathbf{q},\tau)\right)$ is the Jacobian of the transformation from Eulerian to Lagrangian coordinates. From now on we denote partial derivatives with respect to q_j as $\frac{\partial \psi_i}{\partial q_j} \equiv \psi_{i,j}$.

In an expanding universe the equation of motion that governs particle motion is (Equation (1.96)):

$$\frac{d^2\mathbf{x}}{d\tau^2} + \mathcal{H}(\tau)\frac{d\mathbf{x}}{d\tau} = -\nabla\Phi, \tag{1.127}$$

By taking the divergence of this equation we arrive at:

$$\nabla\cdot\left[\frac{d^2\mathbf{x}}{d\tau^2} + \mathcal{H}\frac{d\mathbf{x}}{d\tau}\right] = \frac{3}{2}\mathcal{H}^2\Omega_m\frac{J-1}{J} \tag{1.128}$$

by using Poisson's equation (Equation (1.97)) and Equation (1.126). Further substituting for $\mathbf{q}$ gives finally

$$\left(\delta_{ij}+\psi_{i,j}\right)^{-1}\left[\frac{d^2\psi_{i,j}}{d\tau^2} + \mathcal{H}\frac{d\psi_{i,j}}{d\tau}\right] = \frac{3}{2}\mathcal{H}^2\Omega_m\frac{J-1}{J}. \tag{1.129}$$

$\left(\delta_{ij}+\psi_{i,j}\right)^{-1}$ is the transformation matrix from the conversion $\nabla_{\mathbf{x}} \to \nabla_{\mathbf{q}}$ using the chain rule. Equation (1.129) will be the starting point for our perturbative expansion in LPT, and in EdS we invoke the ansatz [114–116]:

$$\begin{aligned}\boldsymbol{\psi} &= \sum_{n=1}^{\infty} D_1^n(\tau)\boldsymbol{\psi}^{(n)}(\mathbf{q}).\\ &= \sum_{n=1}^{\infty} a^n(\tau)\boldsymbol{\psi}^{(n)}(\mathbf{q}),\end{aligned} \tag{1.130}$$

where the scale factor $a \propto \tau^2$.

Zeldovich Approximation (ZA)

The linear approximation in LPT is commonly referred to as the Zeldovich approximation [117]. The transformation matrix becomes:

$$\left(\delta_{ij} + \psi_{i,j}\right)^{-1} \approx \delta_{ij} - a\psi^{(1)}_{i,j}, \tag{1.131}$$

and therefore the Jacobian[4] $J = 1 + a\psi^{(1)}_{i,i}$. Equation (1.129) can then be written as

$$\frac{d^2(a\psi^{(1)}_{i,i})}{d\tau^2} + \mathcal{H}\frac{d(a\psi^{(1)}_{i,i})}{d\tau} = \frac{3}{2}\mathcal{H}^2 a\psi^{(1)}_{i,i}, \tag{1.133}$$

which is trivially satisfied. Furthermore, using the conservation equation (Equation (1.126)) we deduce

$$\delta^{(1)}(\mathbf{q}) = -\nabla_{\mathbf{q}} \cdot \boldsymbol{\psi}^{(1)}(\mathbf{q}) \Rightarrow \boldsymbol{\psi}^{(1)}(\mathbf{k}) = i\frac{\mathbf{k}}{k^2}\delta^{(1)}(\mathbf{k}), \tag{1.134}$$

where $\delta^{(1)}(\mathbf{q},\tau) = a(\tau)\delta^{(1)}(\mathbf{q})$.

Second order Lagrangian perturbation theory (2LPT)

In order to expand Equation (1.129) to 2nd order we require the 2nd order expansion of Jacobian J:

$$J = 1 + a\psi^{(1)}_{i,i} + a^2\psi^{(2)}_{i,i} + \frac{a^2}{2}\left(\psi^{(1)}_{i,i}\psi^{(1)}_{j,j} - \psi^{(1)}_{i,j}\psi^{(1)}_{j,i}\right), \tag{1.135}$$

[4] This expression, as well as Equation (1.135), can be derived simply by noting the well-known matrix identity $\det(\exp(A)) = \exp(\mathrm{tr}(A))$, such that

$$\begin{aligned}\det(I+A) &= \exp(\mathrm{tr}(\log(I+A))) \\ &= \exp\left(\mathrm{tr}\left(-\sum_{n=1}^{\infty}\frac{(-A)^n}{n}\right)\right) \\ &= 1 + \mathrm{tr}(A) + \frac{1}{2}[(\mathrm{tr}(A))^2 - \mathrm{tr}\left(A^2\right)] + O(A^3).\end{aligned} \tag{1.132}$$

but only the 1st order expansion of the transformation matrix $\left(\delta_{ij}+\psi_{i,j}\right)^{-1}$ since the terms in the square brackets on the left hand side are at least first order. We then have

$$\begin{aligned}&\left(\delta_{ij}-a\psi^{(1)}_{i,j}\right)\left[\frac{d^2}{d\tau^2}\left(a\psi^{(1)}_{i,j}+a^2\psi^{(2)}_{i,j}\right)+\mathcal{H}\frac{d}{d\tau}\left(a\psi^{(1)}_{i,j}+a^2\psi^{(2)}_{i,j}\right)\right]\\&=\frac{3}{2}\mathcal{H}^2\left[a\psi^{(1)}_{i,i}+a^2\psi^{(2)}_{i,i}+\frac{a^2}{2}\left(\psi^{(1)}_{i,i}\psi^{(1)}_{j,j}-\psi^{(1)}_{i,j}\psi^{(1)}_{j,i}\right)\right]\left(1-a\psi^{(1)}_{k,k}\right),\end{aligned}\tag{1.136}$$

which leads to

$$\begin{aligned}&\left[\frac{d^2(a^2\psi^{(2)}_{i,i})}{d\tau^2}+\mathcal{H}\frac{d(a^2\psi^{(2)}_{i,i})}{d\tau}\right]-a\psi^{(1)}_{i,j}\left[\frac{d^2(a\psi^{(1)}_{i,j})}{d\tau^2}+\mathcal{H}\frac{d(a\psi^{(1)}_{i,j})}{d\tau}\right]\\&=\frac{3}{2}\mathcal{H}^2a^2[\psi^{(2)}_{i,i}-\psi^{(1)}_{i,i}\psi^{(1)}_{j,j}+\frac{1}{2}(\psi^{(1)}_{i,i}\psi^{(1)}_{j,j}-\psi^{(1)}_{i,j}\psi^{(1)}_{j,i})].\end{aligned}\tag{1.137}$$

Separating the $\psi^{(1)}$ and $\psi^{(2)}$ terms gives

$$\frac{d^2(a^2\psi^{(2)}_{i,i})}{d\tau^2}+\mathcal{H}\frac{d(a^2\psi^{(2)}_{i,i})}{d\tau}-\frac{3}{2}\mathcal{H}^2a^2\psi^{(2)}_{i,i}=-\frac{3}{4}\mathcal{H}^2a^2(\psi^{(1)}_{i,i}\psi^{(1)}_{j,j}-\psi^{(1)}_{i,j}\psi^{(1)}_{j,i}),\tag{1.138}$$

where we used the irrotationality[5] of $\psi^{(1)}_{i,j}$ to write it in terms of a scalar potential $\psi^{(1)}_i=-\phi^{(1)}_{,i}$, so that $\psi^{(1)}_{i,j}=\psi^{(1)}_{j,i}=-\phi^{(1)}_{,ij}$. This finally leads to

$$\begin{aligned}\psi^{(2)}_{i,i}&=-\frac{2}{7}\times\frac{3}{4}\sum_{i\neq j}(\psi^{(1)}_{i,i}\psi^{(1)}_{j,j}-\psi^{(1)}_{i,j}\psi^{(1)}_{j,i})\\&=-\frac{3}{7}\sum_{i>j}(\psi^{(1)}_{i,i}\psi^{(1)}_{j,j}-\psi^{(1)}_{i,j}\psi^{(1)}_{j,i}).\end{aligned}\tag{1.139}$$

The sum is to make explicit the fact that terms where $i=j$ cancel. By using the fact that the Fourier Transform of $\psi^{(1)}_{i,j}(\mathbf{q})$ is $\psi^{(1)}_{i,j}(\mathbf{k})=ik_j\psi^{(1)}_i(\mathbf{k})=-\frac{k_ik_j}{k^2}\delta^{(1)}(\mathbf{k})$, we can take the

[5] See [108] and references therein. For further discussions of irrotationality in higher order LPT please refer to [118, 119].

Fourier Transform of Equation (1.139) to find

$$
\begin{aligned}
& i\mathbf{k}\cdot\boldsymbol{\psi}^{(2)}(\mathbf{k}) \\
&= -\frac{3}{14}\int d^3q[(\delta^{(1)})^2(\mathbf{q}) - (\psi^{(1)}_{i,j})^2(\mathbf{q})]e^{-i\mathbf{k}\cdot\mathbf{q}} \\
&= -\frac{3}{14}\int \frac{d^3k_1}{(2\pi)^3}[\delta^{(1)}(\mathbf{k}_1)\delta^{(1)}(\mathbf{k}-\mathbf{k}_1) - \psi^{(1)}_{i,j}(\mathbf{k}_1)\psi^{(1)}_{i,j}(\mathbf{k}-\mathbf{k}_1)] \\
&= -\frac{3}{14}\int \frac{d^3k_1}{(2\pi)^3}\frac{d^3k_2}{(2\pi)^3}[\delta^{(1)}(\mathbf{k}_1)\delta^{(1)}(\mathbf{k}_2) - \psi^{(1)}_{i,j}(\mathbf{k}_1)\psi^{(1)}_{i,j}(\mathbf{k}_2)]\delta_D(\mathbf{k}-\mathbf{k}_1-\mathbf{k}_2) \\
&= -\frac{3}{14}\int \frac{d^3k_1}{(2\pi)^3}\frac{d^3k_2}{(2\pi)^3}[\delta^{(1)}(\mathbf{k}_1)\delta^{(1)}(\mathbf{k}_2) - \frac{(\mathbf{k}_1\cdot\mathbf{k}_2)^2}{k_1^2k_2^2}\delta^{(1)}(\mathbf{k}_1)\delta^{(1)}(\mathbf{k}_2)]\delta_D(\mathbf{k}-\mathbf{k}_1-\mathbf{k}_2) \\
&= -\frac{3}{14}\int \frac{d^3k_1}{(2\pi)^3}\frac{d^3k_2}{(2\pi)^3}\delta^{(1)}(\mathbf{k}_1)\delta^{(1)}(\mathbf{k}_2)\times\left[1-\frac{(\mathbf{k}_1\cdot\mathbf{k}_2)^2}{k_1^2k_2^2}\right]\delta_D(\mathbf{k}-\mathbf{k}_1-\mathbf{k}_2). \qquad (1.140)
\end{aligned}
$$

The 2LPT bispectrum

Multiplying both sides of Equation (1.126) by $\delta_D(\mathbf{x}-\mathbf{x}')$ and integrating over all $\mathbf{x}$ gives

$$
\begin{aligned}
1+\delta(\mathbf{x}',\tau) &= \int d^3x\left|\frac{\partial\mathbf{q}}{\partial\mathbf{x}}\right|\delta_D(\mathbf{x}-\mathbf{x}') \\
&= \int d^3q\,\delta_D(\mathbf{q}+\boldsymbol{\psi}(\mathbf{q},\tau)-\mathbf{x}'), \qquad (1.141)
\end{aligned}
$$

where we have applied the transformation $\mathbf{x}\to\mathbf{q}+\boldsymbol{\psi}(\mathbf{q},\tau)$. After relabelling variables we arrive at the expression:

$$
1+\delta(\mathbf{x},\tau) = \int d^3q\,\delta_D(\mathbf{x}-\mathbf{q}-\boldsymbol{\psi}(\mathbf{q},\tau)), \qquad (1.142)
$$

or in Fourier space:

$$
\delta(\mathbf{k},\tau) = \int \frac{d^3q}{(2\pi)^3}e^{-i\mathbf{k}\cdot\mathbf{q}}\left(e^{-i\mathbf{k}\cdot\boldsymbol{\psi}(\mathbf{q},\tau)}-1\right). \qquad (1.143)
$$

Substituting in our EdS ansatz (Equation (1.130)), we obtain this expansion up to 2nd order:

$$
\begin{aligned}
&\delta(\mathbf{k},\tau) \\
&= \int \frac{d^3q}{(2\pi)^3} e^{-i\mathbf{k}\cdot\mathbf{q}} \left(e^{-i\mathbf{k}\cdot\boldsymbol{\psi}(\mathbf{q},\tau)} - 1 \right) \\
&= \int \frac{d^3q}{(2\pi)^3} e^{-i\mathbf{k}\cdot\mathbf{q}} \left(-i\mathbf{k}\cdot(a\boldsymbol{\psi}^{(1)}(\mathbf{q}) + a^2\boldsymbol{\psi}^{(2)}(\mathbf{q})) - \frac{1}{2}(a\mathbf{k}\cdot\boldsymbol{\psi}^{(1)}(\mathbf{q}))^2 \right) \\
&= -ia\mathbf{k}\cdot\boldsymbol{\psi}^{(1)}(\mathbf{k}) - ia^2\mathbf{k}\cdot\boldsymbol{\psi}^{(2)}(\mathbf{k}) - \frac{1}{2}a^2 \int \frac{d^3k_1}{(2\pi)^3} (\mathbf{k}\cdot\boldsymbol{\psi}^{(1)}(\mathbf{k}_1))(\mathbf{k}\cdot\boldsymbol{\psi}^{(1)}(\mathbf{k}-\mathbf{k}_1)) \\
&= a\delta^{(1)}(\mathbf{k}) + \frac{3}{14}a^2 \int \frac{d^3k_1}{(2\pi)^3}\frac{d^3k_2}{(2\pi)^3} \delta^{(1)}(\mathbf{k}_1)\delta^{(1)}(\mathbf{k}_2) \left[1 - \frac{(\mathbf{k}_1\cdot\mathbf{k}_2)^2}{k_1^2 k_2^2} \right] \delta_D(\mathbf{k}-\mathbf{k}_1-\mathbf{k}_2) \\
&\qquad - \frac{1}{2}a^2 \int \frac{d^3k_1}{(2\pi)^3}\frac{d^3k_2}{(2\pi)^3} (\mathbf{k}\cdot\boldsymbol{\psi}^{(1)}(\mathbf{k}_1))(\mathbf{k}\cdot\boldsymbol{\psi}^{(1)}(\mathbf{k}_2)) \delta_D(\mathbf{k}-\mathbf{k}_1-\mathbf{k}_2) \\
&= a\delta^{(1)}(\mathbf{k}) + \frac{3}{14}a^2 \int \frac{d^3k_1}{(2\pi)^3}\frac{d^3k_2}{(2\pi)^3} \delta^{(1)}(\mathbf{k}_1)\delta^{(1)}(\mathbf{k}_2) \left[1 - \frac{(\mathbf{k}_1\cdot\mathbf{k}_2)^2}{k_1^2 k_2^2} \right] \delta_D(\mathbf{k}-\mathbf{k}_1-\mathbf{k}_2) \\
&\qquad + \frac{1}{2}a^2 \int \frac{d^3k_1}{(2\pi)^3}\frac{d^3k_2}{(2\pi)^3} \delta^{(1)}(\mathbf{k}_1)\delta^{(1)}(\mathbf{k}_2) \frac{\mathbf{k}\cdot\mathbf{k}_1}{k_1^2}\frac{\mathbf{k}\cdot\mathbf{k}_2}{k_2^2} \delta_D(\mathbf{k}-\mathbf{k}_1-\mathbf{k}_2) \\
&= a\delta^{(1)}(\mathbf{k}) + a^2 \int \frac{d^3k_1}{(2\pi)^3}\frac{d^3k_2}{(2\pi)^3} \delta^{(1)}(\mathbf{k}_1)\delta^{(1)}(\mathbf{k}_2) \\
&\qquad \times \left[\frac{3}{14} - \frac{3}{14}\frac{(\mathbf{k}_1\cdot\mathbf{k}_2)^2}{k_1^2 k_2^2} + \frac{1}{2}\frac{(\mathbf{k}_1+\mathbf{k}_2)\cdot\mathbf{k}_1}{k_1^2}\frac{(\mathbf{k}_1+\mathbf{k}_2)\cdot\mathbf{k}_2}{k_2^2} \right] \delta_D(\mathbf{k}-\mathbf{k}_1-\mathbf{k}_2) \\
&= a\delta^{(1)}(\mathbf{k}) + a^2 \int \frac{d^3k_1}{(2\pi)^3}\frac{d^3k_2}{(2\pi)^3} \delta^{(1)}(\mathbf{k}_1)\delta^{(1)}(\mathbf{k}_2) \\
&\qquad \times \left[\frac{5}{7} + \frac{1}{2}\frac{\mathbf{k}_1\cdot\mathbf{k}_2}{k_1 k_2}\left(\frac{k_1}{k_2} + \frac{k_2}{k_1}\right) + \frac{2}{7}\frac{(\mathbf{k}_1\cdot\mathbf{k}_2)^2}{k_1^2 k_2^2} \right] \delta_D(\mathbf{k}-\mathbf{k}_1-\mathbf{k}_2) \\
&\equiv a\delta^{(1)}(\mathbf{k}) + a^2 \int \frac{d^3k_1}{(2\pi)^3}\frac{d^3k_2}{(2\pi)^3} \delta^{(1)}(\mathbf{k}_1)\delta^{(1)}(\mathbf{k}_2) F_2^{(s)}(\mathbf{k}_1,\mathbf{k}_2) \delta_D(\mathbf{k}-\mathbf{k}_1-\mathbf{k}_2). \qquad (1.144)
\end{aligned}
$$

We therefore recover the same $F_2^{(s)}$ kernel in SPT (Equation (1.118)), thus proving that the SPT and 2LPT tree-level bispectrum are identical. Although this result only holds in EdS, we can similarly modify $F_2^{(s)}$ to $F_2^{(s),\Lambda}$ (Equation (1.124)) to account for cosmologies with $\Omega_\Lambda > 0$.

1.4.4 Bispectrum shapes

The linearity of CMB physics lends itself to testing inflationary theories, as it is easy to project any primordial bispectrum to the time of Recombination. For LSS however this is not

straightforward as gravitational evolution sources additional contributions to any primordial non-Gaussianities in the matter bispectrum. We are therefore more interested in a few phenomenological shapes that will help capture the behaviour of the matter bispectrum at late times, e.g. the tree level bispectrum introduced above, which will eventually enable us to investigate any primordial non-Gaussianities through observational data by subtracting off the dominant contributions from gravitational collapse. Here we present a few of these templates popular in the literature.

Nine-parameter model

The tree-level bispectrum fails to describe the matter bispectrum accurately even at mildly non-linear regimes. A way of extending perturbation theories without resorting to loop corrections is with phenomenological corrections to the kernel $F_2^{(s)}$ by fitting to simulations. One such example was introduced in [97] which proposed

$$\begin{aligned} F_2^{\rm eff}(\mathbf{k}_1,\mathbf{k}_2) = \frac{5}{7}a(n_1,k_1)a(n_2,k_2) \\ + \frac{1}{2}\frac{\mathbf{k}_1\cdot\mathbf{k}_2}{k_1k_2}\left(\frac{k_1}{k_2}+\frac{k_2}{k_1}\right)b(n_1,k_1)b(n_2,k_2) \\ + \frac{2}{7}\frac{(\mathbf{k}_1\cdot\mathbf{k}_2)^2}{k_1^2k_2^2}c(n_1,k_1)c(n_2,k_2), \end{aligned} \tag{1.145}$$

where

$$a(n,k) = \frac{1+\sigma_8^{a_6}(z)[0.7Q_3(n)]^{1/2}(qa_1)^{n(k)+a_2}}{1+(qa_1)^{n(k)+a_2}} \tag{1.146}$$

$$b(n,k) = \frac{1+0.2a_3(n(k)+3)(qa_7)^{n(k)+3+a_8}}{1+(qa_7)^{n(k)+3.5+a_8}} \tag{1.147}$$

$$c(n,k) = \frac{1+4.5a_4/[1.5+(n(k)+3)^4](qa_5)^{n(k)+3+a_9}}{1+(qa_5)^{n(k)+3.5+a_9}}. \tag{1.148}$$

Here $q = k/k_{\rm NL}$, where $k_{\rm NL}$ which is the scale at which perturbation theory breaks down and is found by solving the equation $k_{\rm NL}^3 P_{\rm lin}(k_{\rm NL},z) = 2\pi^2$. The functions $n(k)$ and $Q_3(n)$ are defined as:

$$n(k) = \frac{d\log P_{\rm lin}(k)}{d\log k} \tag{1.149}$$

$$Q_3(n) = \frac{4-2^n}{1+2^{n+1}}. \tag{1.150}$$

$$\tag{1.151}$$

The 9 parameters a_i were fitted to simulations with an error threshold of 10% in the k-range of $0.03\,h\,\mathrm{Mpc}^{-1} \leq k \leq 0.4\,h\,\mathrm{Mpc}^{-1}$ and redshift range of $0 \leq z \leq 1.5$, and take the values of

$$\begin{aligned} a_1 &= 0.484 & a_2 &= 3.740 & a_3 &= -0.849 \\ a_4 &= 0.392 & a_5 &= 1.013 & a_6 &= -0.575 \\ a_7 &= 0.128 & a_8 &= -0.722 & a_9 &= -0.926. \end{aligned} \tag{1.152}$$

Local shape

The local, or squeezed, bispectrum shape is another popular example. Its name derives from the local type non-Gaussianity introduced above. There are two ways of promoting the primordial local bispectrum into late times. The easy, but incorrect, way is to replace P_ϕ with the linear power spectrum:

$$B^{\mathrm{squeez}}(k_1,k_2,k_3) = \frac{1}{3}[P_{\mathrm{lin}}(k_1)P_{\mathrm{lin}}(k_2) + P_{\mathrm{lin}}(k_2)P_{\mathrm{lin}}(k_3) + P_{\mathrm{lin}}(k_3)P_{\mathrm{lin}}(k_1)]. \tag{1.153}$$

Since the linear power spectrum $P_{\mathrm{lin}}(k) \propto k^{n_s-4}$ for large k, B^{squeez} peaks for squeezed triangle configurations where one of the k's is much smaller than the other two, e.g. $k_1 \ll k_2, k_3$. This shape is, however, not the correct extension since at large scales $B \propto D_1^3$, whereas P_{lin} grows as D_1^2. Using $\delta(\mathbf{k},z) = M(k,z)\zeta_{\mathrm{local}}(\mathbf{k})$ and $M(k,z) = \frac{2D_1(z)T(k)k^2}{3\Omega_M H_0^2}$ we obtain

$$\begin{aligned} B^{\mathrm{local,late}}(k_1,k_2,k_3) &= M(k_1)M(k_2)M(k_3)B^{\mathrm{local}}(k_1,k_2,k_3) \\ &\propto \sqrt{\frac{P_{\mathrm{lin}}(k_1)P_{\mathrm{lin}}(k_2)P_{\mathrm{lin}}(k_3)}{(k_1k_2k_3)^{n_s}}} \\ &\quad \times (k_1^{n_s-2}k_2^{n_s-2}k_3^2 + k_1^2k_2^{n_s-2}k_3^{n_s-2} + k_1^{n_s-2}k_2^2k_3^{n_s-2}). \end{aligned} \tag{1.154}$$

Constant shape

Another useful shape is the constant shape produced by equilateral triangles $k_1 = k_2 = k_3$:

$$B^{\mathrm{const}}(k_1,k_2,k_3) = B, \tag{1.155}$$

where B is, expectedly, a constant. This is the bispectrum shape obtained by a set of Poisson-distributed point sources, for instance the late time matter distribution at small scales which consists of point-like dark matter halo particles. The constant shape is therefore ideal for describing the late time matter bispectrum at small scales.

The three-shape model

The authors of [11, 120] have proposed a benchmark model that utilises 3 basic bispectrum shapes to build a phenomenological model for the matter bispectrum calibrated to simulations, very much akin to the HALOFIT model [121] which was introduced to capture the behaviour of the matter power spectrum. For greater flexibility of the model they allowed the shapes to have scale-dependent amplitudes $f_i(K)$ with $K = k_1 + k_2 + k_3$ for a better fit to the data. The three-shape bispectrum is the following linear combination of the 'constant' one-halo model on small length scales, the tree-level gravitational bispectrum on the largest, and a local or 'squeezed' shape interpolating on intermediate scales. The combined three-shape model takes the following form:

$$\begin{aligned} B_{\text{3-shape}}(k_1,k_2,k_3) &= \sum_{i=1}^{3} f_i(K) B^i(k_1,k_2,k_3) \\ &= f_{1h}(K) B^{\text{const}}(k_1,k_2,k_3) + f_{2h}(K) B^{\text{squeez}}(k_1,k_2,k_3) \\ &\quad + f_{3h}(K) B^{\text{treeNL}}(k_1,k_2,k_3), \end{aligned} \tag{1.156}$$

where B^{const} and B^{squeez} are given by Equations (1.153) and (1.155). The tree-level shape is based on Equation (1.123) except we have replaced the linear power spectrum with the non-linear power spectrum obtained from simulations:

$$B^{\text{treeNL}}(k_1,k_2,k_3) = 2P_{\text{NL}}(k_1)P_{\text{NL}}(k_2)F_2^{(s),\Lambda}(\mathbf{k}_1,\mathbf{k}_2) + 2\,\text{perms.}, \tag{1.157}$$

The amplitudes $f_i(K)$ are found by fitting each of these shapes to the three halo model components. For a comprehensive review on the halo model bispectrum please see [11]. The one-halo bispectrum has been shown to correlate very well with the constant shape with the following choice of Lorentzian fitting function:

$$f_{1h}(K) = \frac{A}{(1+BK^2)^2}, \tag{1.158}$$

where A and b are redshift-dependent functions through the linear growth factor $D_1(z)$:

$$A = \frac{2.45 \times 10^6 D_1(z)^8}{0.8 + 0.2 D_1(z)^{-3}}, \tag{1.159}$$

$$B = 0.054\, D_1(z)^{2.2}. \tag{1.160}$$

The two-halo bispectrum has a strong correlation with the squeezed shape but has several notable shortcomings [122–124]. To resolve these deficiencies Valageas and Nishimichi

developed a halo-PT model [125, 126] that combines the halo model with perturbation theory. The authors of [11] have found that the fitting function

$$f_{2h}(K) = \frac{C}{(1+DK^{-1})^3}. \tag{1.161}$$

with this choice of coefficients C and D

$$C = 140 D_1(z)^{-5/4}, \tag{1.162}$$
$$D = 1.9 D_1(z)^{-3/2}, \tag{1.163}$$

gives a good fit to simulations. Finally, the three-halo bispectrum is simply the non-linear tree-level shape predicted for large scales so an exponential fitting function is introduced to suppress it at small scales:

$$f_{3h}(K) = \exp(-K/E). \tag{1.164}$$

An approximate fit for E to simulations is

$$E = 7.5 k_{\rm NL}(z). \tag{1.165}$$

1.4.5 Halos

Our discussion so far has been confined to dark matter particles, but the pertinent quantity for observational data are virialised dark matter halos which are the gravitational bedrock upon which baryons can collapse and form galaxies. These dense objects are in the highly non-linear regime where $\delta \gg 1$, and thus reject the semi-analytical perturbative treatment discussed earlier. As a result the evolution of these structures are typically modelled with large N-body dark matter simulations, followed by 'halo finders' which map the dark matter particles into discrete halos. Nevertheless simple analytical models can be constructed to give an insight into the process of gravitational collapse. Here we follow [127, 128, 122] and discuss the various analytical techniques for populating the Universe with dark matter halos.

Spherical Collapse

We first start with identifying the regions in space where dark matter halos can form. The initial matter density field created by inflation consists of peaks and troughs, which evolves into the complex cosmic web structure full of densely packed regions as well as cosmic voids. However, not all initial overdensities will collapse to form dark matter halos. To study the evolution of these overdensities in an isotropic and homogeneous background we impose

several simplifying assumptions so that analytical solutions can be obtained. First, we shall work with a flat EdS Universe. Second, we assume that the overdensity δ_0 is spherical, which allows us to invoke the well-known shell theorem of Newton, so that the Universe and the overdensity continue to evolve independently of each other. The overdense region therefore behaves like a closed Universe with matter density $\Omega_m = 1 + \delta_0$. This is known as the *spherical collapse* model.

It can be shown that the parametric solution for the evolution of a spherical overdense region with radius R is

$$\frac{R(t)}{R_0} = (1 - \cos\theta)\frac{\Omega_m}{2(\Omega_m - 1)}, \tag{1.166}$$

$$t = (\theta - \sin\theta)\frac{\Omega_m}{2H_0(\Omega_m - 1)^{3/2}}, \tag{1.167}$$

where R_0 is the initial radius, and the parameter θ ranges from 0 to 2π. We can rewrite these expressions in terms of their values at the time of maximum expansion when $\theta = \pi$:

$$\frac{R(t)}{R_{max}} = \frac{1}{2}(1 - \cos\theta), \tag{1.168}$$

$$\frac{t}{t_{max}} = \frac{1}{\pi}(\theta - \sin\theta), \tag{1.169}$$

It is instructive to Taylor expand these quantities to examine their linear behaviour:

$$\frac{R_{lin}(t)}{R_{max}} \approx \frac{1}{2}\left(\frac{\theta^2}{2} - \frac{\theta^4}{24}\right), \tag{1.170}$$

$$\frac{t}{t_{max}} \approx \frac{1}{\pi}\left(\frac{\theta^3}{6} - \frac{\theta^5}{120}\right). \tag{1.171}$$

Substituting $\theta \approx \left(6\pi\frac{t}{t_{max}}\right)^{1/3}$ into Equation (1.168) gives the linear time evolution of the radius:

$$\frac{R_{lin}(t)}{R_{max}} = \frac{1}{4}\left(6\pi\frac{t}{t_{max}}\right)^{2/3}\left[1 - \frac{1}{20}\left(6\pi\frac{t}{t_{max}}\right)^{2/3}\right]. \tag{1.172}$$

The first term, $R_{back}(t)/R_{max} \equiv (6\pi t/t_{max})^{2/3}/4$, gives the expansion of the background Universe, and the second term gives the correction to this background expansion predicted by linear theory. Using conservation of mass, $\rho(t)R(t)^3 = \rho_0 R_0^3$, we deduce the density perturbation $\delta = \rho(t)/\rho_0 - 1$ and radial perturbation $\delta_R = R(t)/R_0 - 1$ are related by $\delta \approx$

$-3\delta_R$ for linear perturbations, and hence

$$\delta_{lin} = \frac{3}{20}\left(6\pi\frac{t}{t_{max}}\right)^{2/3}. \tag{1.173}$$

As noted before an interesting event happens at $\theta = \pi$, i.e. the *turnaround* when the expansion reaches its maximum. After this point the overdense region stops growing and begins its collapse. At turnaround the linear overdensity is

$$\delta_{lin}^{turn} = \frac{3}{20}(6\pi)^{2/3} \approx 1.06. \tag{1.174}$$

Another important moment is when the region collapses to a point. The full non-linear solution (Equation (1.168)) shows that this happens at $\theta = 2\pi$, or $t = 2t_{max}$, when the linear density contrast takes the value

$$\delta_{lin}^{coll} = \frac{3}{20}(12\pi)^{2/3} \approx 1.69. \tag{1.175}$$

This indicates that when the linear density contrast reaches about $\delta_c \equiv 1.69$ we would expect a spherical object to have completely collapsed. At late times in the presence of Λ one needs to redo the analysis, but it turns out that δ_{lin}^{coll} is insensitive to the values of Ω_m and Ω_Λ, therefore a value of 1.69 is a good approximation for all realistic cosmologies [127].

There are two notable shortcomings with the spherical collapse model: (i) gravitational collapse rarely produces spherical halos, but elliptical ones instead, and (ii) in the real Universe the overdense region will obviously not collapse to a point. Instead a process known as *virialisation* takes place where the motion of the dark matter particles become randomised, which serves to balance gravitational collapse and transition the system into a stable equilibrium. To calculate the radius of the resulting dark matter halo we make use of the Virial theorem: $V_{vir} + 2T_{vir} = 0$, where V_{vir} and T_{vir} are the total potential and kinetic energies of the system after virialisation. At turnaround the kinetic energy is zero, thus all the energy is potential energy: $E = V_{max}$. After virialisation takes place the energy of the system is $E = V_{vir} + T_{vir} = \frac{1}{2}V_{vir}$, and using conservation of energy and the fact that $V \propto 1/R$ we deduce that $R_{vir} = R_{max}/2$, i.e. the virialisation radius is half that at turnaround. This implies that the density of the halo grows by a factor of 8. Moreover, from turnaround to collapse the background density shrinks by a factor of 4:

$$\frac{\rho_{back}(2t_{max})}{\rho_{back}(t_{max})} = \left[\frac{a_{back}(2t_{max})}{a_{back}(t_{max})}\right]^{-3} = \left(\frac{2t_{max}}{t_{max}}\right)^{-2} = \frac{1}{4}, \tag{1.176}$$

as during matter domination $\rho \propto a^{-3}$ and $a \propto t^{2/3}$. Using Equation (1.168) we can calculate the non-linear density contrast at turnover:

$$1+\delta^{turn} = \left[\frac{R_{back}(t_{max})}{R_{max}}\right]^3 = \frac{(6\pi)^2}{4^3} \approx 5.55, \tag{1.177}$$

and with the information above we arrive at the conclusion that the overdensity at virialisation is

$$1+\delta^{vir} \approx 5.55 \times 8 \times 4 \approx 178. \tag{1.178}$$

The most important outcome of this analysis is that it allows us to bridge the gap between linear and non-linear evolution: when the linear density contrast reaches a value of 1.69 we expect a halo to have formed there with an overdensity of about 200 times the background.

Halo profile

Having found prescriptions for where the halos will form, we would like to find a phenomenological way to describe the inner structure of the halo. This was investigated extensively using N-body simulations, and Navarro, Frenk and White (NFW) realised in the 90s that there exists a universal profile that fits the dark matter distribution with halos across a large mass range [129–131]. This NFW profile can be expressed in terms of two parameters, the scale radius r_s and the density at that radius $\rho_s = \rho(r_s)$, giving the mass density profile as:

$$\rho(r|r_s,\rho_s) = \frac{4\rho_s}{\frac{r}{r_s}\left(1+\frac{r}{r_s}\right)^2}. \tag{1.179}$$

An alternative parameterisation is with the concentration parameter $c = R_{vir}/r_s$, and the virial mass of the halo M_{vir}. If we further impose conservation of mass:

$$M_{vir} = \int_0^{R_{vir}} \rho(r|r_s,\rho_s) 4\pi r^2 \, dr, \tag{1.180}$$

then we can rewrite the density at the scale radius as

$$\rho_s = \frac{M_{vir}}{16\pi R_{vir}^3} \frac{c^3}{\log(1+c) - \frac{c}{1+c}}. \tag{1.181}$$

Finally this allows us to express the radial density profile as

$$\rho(r|M_{vir},c) = \frac{M_{vir}}{4\pi rc(R_{vir}+rc)^2}\frac{c^3}{\log(1+c)-\frac{c}{1+c}}. \tag{1.182}$$

Another popular radially symmetric profile is due to Einasto [132], who proposed

$$\rho(r|r_{-2},\rho_{-2},\alpha) = \rho_{-2}\exp\left(-\frac{2}{\alpha}\left[\left(\frac{r}{r_{-2}}\right)^{\alpha}-1\right]\right), \tag{1.183}$$

where r_{-2} and ρ_{-2} are the radius and density at which $\rho(r)\propto r^{-2}$, and α controls the shape of the profile [133].

Halo mass function

Another useful quantity we would like to predict is the average number density of the halos with a given mass M, also known as the *halo mass function* $n(M)$. One of the pioneering approaches to this problem is due to Press and Schechter in their seminal paper in 1974 [134]. Although the theory in its original presentation has certain theoretical misgivings, it is nonetheless very successful at reproducing results from N-body simulations and has therefore stood the test of time.

From the spherical collapse model we know that a spherical region with linear overdensity exceeding δ_c will produce a halo. To identify these regions one must first smooth the overdensity field with a window function $W(\mathbf{x};R)$ of some characteristic radius R:

$$\delta_R(\mathbf{x}) = \int \delta(\mathbf{x}')W(\left|\mathbf{x}-\mathbf{x}'\right|;R)\,d^3x'. \tag{1.184}$$

This convolution operation becomes a multiplication in Fourier space between $\delta(\mathbf{k})$ and the Fourier-transformed filter function $\tilde{W}(kR) = \int W(\mathbf{x};R)e^{-i\mathbf{k}\cdot\mathbf{x}}d^3x$. Popular filter functions include the top-hat, Gaussian and a k-space top-hat. To make use of the spherical collapse model we shall adopt the top-hat filter in our discussion here:

$$W_{TH}(r;R) = \begin{cases} \frac{3}{4\pi R^3} & r\le R \\ 0 & r>R \end{cases}, \qquad \tilde{W}_{TH}(kR) = \frac{3}{(kR)^3}\left[\sin(kR)-(kR)\cos(kR)\right]. \tag{1.185}$$

As we are working with the linear density field, in the absence of any primordial non-Gaussianities $\delta_{\rm lin}$ is Gaussian and hence fully described by its mean (which is 0) and its power spectrum. The smoothed field therefore has a root-mean-squared (rms) amplitude of

linear fluctuations at radius R, or mass M, of

$$\sigma^2(M) = \frac{1}{2\pi^2}\int P_{\rm lin}(k)\tilde{W}_{TH}^2(kR)k^2 dk, \tag{1.186}$$

where the conversion between M and R is simply $M = \frac{4\pi}{3}R^3\bar{\rho}$. An important cosmological parameter is σ_8, the amplitude of fluctuations at a scale of $R = 8\,h^{-1}$Mpc, which is used to normalise the linear matter power spectrum.

The basic premise of Press-Schechter theory is that after smoothing of the linear density field with radius R and mass M, those points that satisfy $\delta_R > \delta_c$ will live inside halos of mass greater than M. In other words, the fraction of mass contained in collapsed objects of mass greater than M is the same as the probability that $\delta_R > \delta_c$. One inherent problem with this approach is that a Gaussian linear density field implies half the mass of the Universe resides in underdense regions and hence will not participate in structure formation, which is clearly not a realistic proposition. We shall address this later. Additionally there is an ambiguity in the assignment of halo mass: a point may reside in an overdense region of radius R_1, which in turn belongs to a larger overdense region of radius R_2. It is not necessarily obvious to which halo we should assign this point to; this is known as the 'cloud-in-cloud' problem.

The smoothed linear density field has a Gaussian probability density function given by

$$p(\delta_R|M) = \frac{1}{\sqrt{2\pi\sigma^2(M)}}\exp\left[-\frac{1}{2}\frac{\delta_R^2}{\sigma^2(M)}\right], \tag{1.187}$$

therefore the probability for a region to exceed the density threshold δ_c is

$$P(>\delta_c|M) = \int_{\delta_c}^{\infty} p(\delta_R|M)\,d\delta_R = \frac{1}{\sqrt{2\pi}}\int_{\tilde{\nu}}^{\infty}\exp\left[-\frac{x^2}{2}\right]dx = \frac{1}{2}\,{\rm erfc}\left[-\frac{\tilde{\nu}}{\sqrt{2}}\right], \tag{1.188}$$

where $\tilde{\nu} = \delta_c/\sigma(M)$ is known as the peak height, and ${\rm erfc}(x) = \frac{2}{\sqrt{\pi}}\int_x^{\infty}\exp\left(-u^2\right)du$ is the complementary error function. The Press-Schechter ansatz dictates that $P(>\delta_c|M)$ is equal to $f(>M)$, the fraction of energy density contained in collapsed objects with mass greater than M. However as previously mentioned this naive implementation only accounts for half the mass of the Universe. To correct for this Press and Schechter introduced a 'fudge factor' of 2, leading to $f(>M) = 2P(>\delta_c|M)$. This factor of 2 is now understood properly in the language of Markovian random walks [135]. The derivative of $f(>M)$ with respect to mass, $\frac{df(>M)}{dM}$, gives the fraction of regions that form halos of mass M, therefore the Press-Schechter mass function is this quantity multiplied by the maximum number density of objects of mass

M, $n_{max} = (M_{tot}/M)/V = \bar{\rho}/M$:

$$\begin{aligned} n(M) &= \frac{\bar{\rho}}{M}\frac{df(>M)}{dM} = 2\frac{\bar{\rho}}{M}\frac{dP(>\delta_c|M)}{d\sigma}\frac{d\sigma}{dM} \\ &= -\sqrt{\frac{2}{\pi}}\frac{\bar{\rho}}{M}\frac{\delta_c}{\sigma^2}\exp\left[-\frac{\delta_c^2}{2\sigma^2}\right]\frac{d\sigma}{dM} \\ &= \sqrt{\frac{2}{\pi}}\frac{\bar{\rho}}{M^2}\tilde{\nu}\exp\left[-\frac{\tilde{\nu}^2}{2}\right]\frac{d\ln\tilde{\nu}}{d\ln M} \\ &= \sqrt{\frac{\nu}{2\pi}}\frac{\bar{\rho}}{M^2}\exp\left[-\frac{\nu}{2}\right]\frac{d\ln\nu}{d\ln M}, \end{aligned} \tag{1.189}$$

where we have made the substitution $\nu = \tilde{\nu}^2$ in the last line. The Press-Schechter mass function has been further improved by Sheth and Tormen [122, 136], who proposed the following modifications:

$$n_{\rm ST}(M) = A(p)\sqrt{\frac{q\nu}{2\pi}}\left(1+\frac{1}{(q\nu)^p}\right)\frac{\bar{\rho}}{M^2}\exp\left[-\frac{q\nu}{2}\right]\frac{d\ln\nu}{d\ln M}, \tag{1.190}$$

where $p \approx 0.3$, $A(p) = [1+2^{-p}\Gamma(1/2-p)/\sqrt{\pi}]^{-1} \approx 0.322$ and $q \approx 0.707$. With a choice of $p = 0$ and $q = 1$ we recover the Press-Schechter mass function. For completeness sake we note that another mass function widely used in the literature is the Tinker mass function proposed in [137]. It has a similar appearance as the Press-Schechter mass function:

$$n_{\rm Tinker}(M) = f(\nu)\frac{\bar{\rho}}{M^2}\frac{d\ln\nu}{d\ln M}, \tag{1.191}$$

where the multiplicity function $f(\nu)$ is

$$f(\nu) = A\left[(b\nu)^a + 1\right]e^{-c\nu}. \tag{1.192}$$

The parameters A, a, b and c have to calibrated with simulations. For a comparison of these theoretical mass functions and those measured from N-body simulations please refer to [137].

Halo occupation distribution

Finally, we briefly touch on how one would translate the a catalogue of halos into the galaxies that we observe. With the simple assumption that dark matter only interacts gravitationally, we can now model their evolution very efficiently with N-body codes at very high resolution. However, our theoretical understanding of messy baryonic physics and galaxy formation remains incomplete [138]. This is compounded by the fact that feedback loops often span

a large range of spatial scales, which is not conducive to the use of numerics. As such phenomenological techniques which aim to capture the essence of the physics involved are highly prized, which serve as the first steps toward an accurate modelling of this complicated system.

One such method is known as the Halo Occupation Distribution (HOD) algorithm [139–141], which aims to predict the number of galaxies associated with a halo given its properties. In its simplest form it gives the average number of galaxies as a function of the halo mass, $\bar{N}_g(M)$, but can be extended with more sophisticated statistical techniques, or the introduction of new parameters such the concentration c of the halo. A functional form for $\bar{N}_g(M)$ consisting of 5 parameters is commonly used in the literature [142–145]:

$$\bar{N}_{\text{cent}}(M) = \frac{1}{2}\,\text{erfc}\left[-\frac{\ln M/M_0}{\sqrt{2}\sigma}\right], \tag{1.193}$$

$$\bar{N}_{\text{sat}}(M) = \left(\frac{M-\kappa M_0}{M_1}\right)^{\alpha}, \tag{1.194}$$

where $\bar{N}_{\text{cent}}$ is the expected number of central galaxies and $\bar{N}_{\text{sat}}$ the expected number of satellite galaxies such that $\bar{N}_g(M) = \bar{N}_{\text{cent}}(M) + \bar{N}_{\text{sat}}(M)$. Here M_0 denotes the typical minimum mass scale for a halo to have a central galaxy, and σ is the parameter that controls the scatter around that mass. κM_0 sets the cutoff scale for a halo to host a satellite, M_1 is the typical additional mass above κM_0 for a halo to have one satellite galaxy, and α is the exponent that controls the tail of the HOD, and therefore has a strong influence on the number of high-mass halos.

Although it may seem rather crude, this simple HOD algorithm is used very effective in the generation of mock galaxy catalogues for galaxy surveys, e.g. the Baryon Oscillation Spectroscopic Survey (BOSS) [144], where speed, rather than high precision is more important. Additionally, the HOD algorithm does not inform us of the spatial distribution of galaxies within a halo, merely the number of them. There is still considerable debate as to the correct profile to adopt, ranging from the NFW profile [144], an agnostic approach by using the dark matter distribution [143], or something else [146, 147].

1.5 Outline of the Thesis

In this thesis we make several advances in the analysis of the matter bispectrum in LSS. First, in Chapter 2 we discuss the optimal estimator for the magnitude f_{nl} of a theoretical bispectrum shape against a given matter density field δ, and present the completely rewritten `MODAL-LSS` formalism for the efficient and and optimal estimation of the full bispectrum for

any matter density field. The introduction of custom modes tailored to capture the late-time matter bispectrum signal has given us rapid convergence to most theoretical bispectrum shapes of interest, and to unprecedented accuracy. Coupled with new algorithms which permitted the use of $\mathcal{O}(1000)$ modes in our eigenmode expansion, we can recover the bispectrum signal of large Fourier grids up to 2048^3 at only a fraction of the computational power required by N-body simulation pipelines. Additionally we discuss sources of error in bispectral analysis, writing down for the first time the full covariance of the `MODAL-LSS` bispectrum estimator.

Then in Chapter 3 we present results on the dark matter bispectrum. Fast dark matter codes (e.g. particle-mesh or `COLA`) are increasingly effective at capturing the clustering statistics of dark matter at a much lower computational cost than N-body simulations, making them invaluable for the accurate estimation of covariance matrices as thousands of simulation realisations are typically required. In addition to the power spectrum we benchmarked these codes against `GADGET-3` using the bispectrum, showing quantitatively how the mismatch at large k can be improved with a simple boosting technique in the power spectrum. We have also estimated the non-Gaussian contribution to the dark matter bispectrum covariance, which cannot be computed analytically in the non-linear regime. This will be vital for the extraction of cosmological parameters from data in the future. Finally we make quantitative comparisons between theoretical and numerical bispectra, and discuss problematic transient modes and grid effects in the initial conditions which gave rise to difficulties in this endeavour.

Finally in Chapter 4 we discuss fast phenomenological methods for the production of mock galaxy catalogues. We investigated a number of effects in configuration space on the power spectrum and bispectrum of the mock catalogue, including the spatial distribution of galaxies within the halos, the Halo Occupation Distribution (HOD) model, and assembly bias models which jointly model the occupation number and concentration of the parent halos. We have found that a bivariate lognormal-Gaussian model for the number of galaxies and halo concentration, coupled with a radial power law halo profile of $r^{-1.2}$, is very effective for the recovery of the benchmark power spectrum and bispectrum. This method, with an additional boost in the occupation number of all parent halos with mass $M > 2\times10^{14}\,h^{-1}M_{\odot}$ by an extra galaxy, gives a power spectrum and bispectrum that matches the benchmark `ROCKSTAR` catalogue to better than 1% in the range $0.04\,h\,\mathrm{Mpc}^{-1} < k, K/3 < 1.1\,h\,\mathrm{Mpc}^{-1}$, where $K = k_1 + k_2 + k_3$ which is a significant improvement to other methods we investigated.

Chapter 2

Matter Bispectrum Estimation

A given density field δ, whether it comes from simulation or observation, can be described by a probability density function (pdf) which gives the statistical properties of the field. In the limit of weak non-Gaussianity we can assume that only the power spectrum and bispectrum are required to completely specify the properties of δ while neglecting higher order correlation functions. A theory for δ will have a prediction for its power spectrum $P(k)$ and bispectrum $f_{nl}B^{th}$, where the non-linearity parameter f_{nl} can be thought of as the amplitude of this particular bispectrum shape. We would like to find an optimal estimator for f_{nl} for this given δ.

The estimator can be found in two different ways. We could find an estimator that maximises the likelihood function $P(\delta|f_{nl})$ which is the probability of measuring this data δ given that the underlying bispectrum is described by $f_{nl}B^{th}$; this is known as maximum likelihood estimation (MLE). Alternatively we can do maximum a posteriori estimation (MAP) where we maximise the posterior function $P(f_{nl}|\delta)$, which gives the probability that $f_{nl}B^{th}$ is indeed the correct underlying bispectrum given the evidence δ. These two approaches are related by Bayes theorem [148]: $P(f_{nl}|\delta) = \frac{P(\delta|f_{nl})P(f_{nl})}{P(\delta)}$, or $P(f_{nl}|\delta) \propto P(\delta|f_{nl})P(f_{nl})$, where $P(f_{nl})$ is known as the prior. The probability of the evidence $P(\delta)$ is often neglected as it remains the same regardless of the theoretical model being considered. In the case of a flat prior, i.e. if $P(f_{nl})$ has a uniform distribution, MLE and MAP give the same result.

2.1 Optimal f_{nl} estimator

Here we demonstrate the procedure for finding an optimal estimator using MLE. In the weak non-Gaussianity limit we can approximate the likelihood with the following multivariate

Edgeworth expansion (see [149] and references therein):

$$P(\delta|f_{nl}) \propto \int_{\mathbf{k}_1,\mathbf{k}_2,\mathbf{k}_3} \left[1 - \frac{1}{6}\left\langle \delta_{\mathbf{k}_1}\delta_{\mathbf{k}_2}\delta_{\mathbf{k}_3}\right\rangle_{th} \frac{\partial}{\partial\delta_{\mathbf{k}_1}}\frac{\partial}{\partial\delta_{\mathbf{k}_2}}\frac{\partial}{\partial\delta_{\mathbf{k}_3}} + \cdots\right] \times \frac{1}{\sqrt{\det C}}\prod_{ij}\exp\left(-\frac{1}{2}\delta^*_{\mathbf{k}_i}(C^{-1})_{ij}\delta_{\mathbf{k}_j}\right), \tag{2.1}$$

where $\int_{\mathbf{k}_1,\mathbf{k}_2,\mathbf{k}_3} = \int \frac{d^3k_1}{(2\pi)^3}\frac{d^3k_2}{(2\pi)^3}\frac{d^3k_3}{(2\pi)^3}$, $\left\langle \delta_{\mathbf{k}_1}\delta_{\mathbf{k}_2}\delta_{\mathbf{k}_3}\right\rangle_{th}$ is the theoretical prediction for the bispectrum and $C_{ij} \equiv \langle \delta^*_{\mathbf{k}_i}\delta_{\mathbf{k}_j}\rangle$ is the covariance matrix for the field δ. The product over the i,j indices is shorthand notation for integrals over $\mathbf{k}_i$ and $\mathbf{k}_j$ in the exponent:

$$\prod_{ij}\exp\left(-\frac{1}{2}\delta^*_{\mathbf{k}_i}(C^{-1})_{ij}\delta_{\mathbf{k}_j}\right) = \exp\left(-\frac{V^2}{2}\int\frac{d^3k_i}{(2\pi)^3}\frac{d^3k_j}{(2\pi)^3}\delta^*_{\mathbf{k}_i}(C^{-1})_{ij}\delta_{\mathbf{k}_j}\right). \tag{2.2}$$

A volume factor V associated with the simulation/observational data is added to make the exponent dimensionless.

The functional derivatives in Equation (2.2) are then performed as follows. We wish to evaluate

$$\frac{\partial}{\partial\delta_{\mathbf{k}_1}}\frac{\partial}{\partial\delta_{\mathbf{k}_2}}\frac{\partial}{\partial\delta_{\mathbf{k}_3}}\prod_{ij}\exp\left(-\frac{1}{2}\delta^*_{\mathbf{k}_i}(C^{-1})_{ij}\delta_{\mathbf{k}_j}\right) = \frac{\partial}{\partial\delta_{\mathbf{k}_1}}\frac{\partial}{\partial\delta_{\mathbf{k}_2}}\frac{\partial}{\partial\delta_{\mathbf{k}_3}}\exp\left(-\frac{V}{2}\int\frac{d^3k_i}{(2\pi)^3}|\delta_{\mathbf{k}_i}|^2(C^{-1})_{ii}\right), \tag{2.3}$$

after using statistical isotropy and homogeneity so that the covariance matrix is diagonal $C^{-1}_{ij} = C^{-1}_{ii}(2\pi)^3\delta_D(\mathbf{k}_i - \mathbf{k}_j)/V$.

Since we are working in Fourier space we do not use the usual definition of the functional derivative:

$$\frac{\partial}{\partial\delta_{\mathbf{k}_j}}\delta_{\mathbf{k}_i} = (2\pi)^3\delta_D(\mathbf{k}_i - \mathbf{k}_j) \Rightarrow \frac{\partial}{\partial\delta_{\mathbf{k}_j}}\delta^*_{\mathbf{k}_i} = \frac{\partial}{\partial\delta_{\mathbf{k}_j}}\delta_{-\mathbf{k}_i} = (2\pi)^3\delta_D(\mathbf{k}_i + \mathbf{k}_j). \tag{2.4}$$

The first functional derivative gives

$$\begin{aligned}
&\frac{\partial}{\partial\delta_{\mathbf{k}_3}}\exp\left(-\frac{V}{2}\int\frac{d^3k_i}{(2\pi)^3}\left|\delta_{\mathbf{k}_i}\right|^2(C^{-1})_{ii}\right)\\
&=\left(-\frac{V}{2}\int d^3k_i(C^{-1})_{ii}\left[\delta^*_{\mathbf{k}_i}\delta_D(\mathbf{k}_i-\mathbf{k}_3)+\delta_{\mathbf{k}_i}\delta_D(\mathbf{k}_i+\mathbf{k}_3)\right]\right)e^{-\frac{V}{2}\int\frac{d^3k_i}{(2\pi)^3}\left|\delta_{\mathbf{k}_i}\right|^2(C^{-1})_{ii}},\\
&=-\frac{V}{2}(\delta^*_{\mathbf{k}_3}C^{-1}_{33}+\delta_{-\mathbf{k}_3}C^{-1}_{-3,-3})e^{-\frac{V}{2}\int\frac{d^3k_i}{(2\pi)^3}\left|\delta_{\mathbf{k}_i}\right|^2(C^{-1})_{ii}},\\
&=-V\delta^*_{\mathbf{k}_3}C^{-1}_{33}e^{-\frac{V}{2}\int\frac{d^3k_i}{(2\pi)^3}\left|\delta_{\mathbf{k}_i}\right|^2(C^{-1})_{ii}},
\end{aligned}\tag{2.5}$$

where in the last line we used the fact that $C_{-3,-3}=\langle\delta^*_{-\mathbf{k}_3}\delta_{-\mathbf{k}_3}\rangle=\langle\delta_{\mathbf{k}_3}\delta^*_{\mathbf{k}_3}\rangle=\langle\delta^*_{\mathbf{k}_3}\delta_{\mathbf{k}_3}\rangle=C_{33}$. Doing the other two functional derivatives leads to

$$\begin{aligned}
&\frac{\partial}{\partial\delta_{\mathbf{k}_1}}\frac{\partial}{\partial\delta_{\mathbf{k}_2}}\frac{\partial}{\partial\delta_{\mathbf{k}_3}}\exp\left(-\frac{V}{2}\int\frac{d^3k_i}{(2\pi)^3}\left|\delta_{\mathbf{k}_i}\right|^2(C^{-1})_{ii}\right)\\
&=-V^2\left(V\delta^*_{\mathbf{k}_1}\delta^*_{\mathbf{k}_1}\delta^*_{\mathbf{k}_3}C^{-1}_{11}C^{-1}_{22}C^{-1}_{33}-\{\delta_D(\mathbf{k}_1+\mathbf{k}_2)C^{-1}_{22}C^{-1}_{33}\delta^*_{\mathbf{k}_3}+2\,\text{perms.}\}\right)\\
&\qquad\times e^{-\frac{V}{2}\int\frac{d^3k_i}{(2\pi)^3}\left|\delta_{\mathbf{k}_i}\right|^2(C^{-1})_{ii}},
\end{aligned}\tag{2.6}$$

Finally using the definition of the bispectrum (Equation (1.92)) we can rewrite Equation (2.1) as

$$\begin{aligned}
P(\delta|f_{nl})\propto\int_{\mathbf{k}_1,\mathbf{k}_2,\mathbf{k}_3}&\left(1+\frac{(2\pi)^3\delta_D(\mathbf{k}_1+\mathbf{k}_2+\mathbf{k}_3)f_{nl}B^{th}(k_1,k_2,k_3)}{6C_{11}C_{22}C_{33}}\right.\\
&\left.\times V^2\left[V\delta^*_{\mathbf{k}_1}\delta^*_{\mathbf{k}_2}\delta^*_{\mathbf{k}_3}-\left\{\delta_D(\mathbf{k}_1+\mathbf{k}_2)C_{11}\delta^*_{\mathbf{k}_3}+2\,\text{perms.}\right\}\right]+\mathcal{O}(f^2_{nl})\right)\\
&\times\frac{\prod_i e^{-(C^{-1})_{ii}\left|\delta_{\mathbf{k}_i}\right|^2}}{\sqrt{\prod_i C_{ii}}},
\end{aligned}\tag{2.7}$$

where $\int_{\mathbf{k}_1,\mathbf{k}_2,\mathbf{k}_3}$ denotes the integral over $\mathbf{k}_1,\mathbf{k}_2,\mathbf{k}_3$ as before and we have used the fact that δ is a real field so that $\delta^*_{\mathbf{k}_i}=\delta_{-\mathbf{k}_i}$ holds, and that C_{ij} is a statistical quantity and independent of $\delta_{\mathbf{k}_i}$.

Having found the likelihood we need find the appropriate f_{nl} that maximises it. It is in fact simpler to maximise its logarithm $\ln P(\delta|f_{nl})$ instead. Taylor expanding in f_{nl} gives us

(neglecting terms independent of f_{nl}):

$$\ln P(\delta|f_{nl}) \approx \int_{\mathbf{k}_1,\mathbf{k}_2,\mathbf{k}_3} \Bigg(\frac{(2\pi)^3 \delta_D(\mathbf{k}_1+\mathbf{k}_2+\mathbf{k}_3) f_{nl} B^{th}(k_1,k_2,k_3)}{6C_{11}C_{22}C_{33}} \times V^2 \left[V\delta^*_{\mathbf{k}_1}\delta^*_{\mathbf{k}_2}\delta^*_{\mathbf{k}_3} - \left\{ \delta_D(\mathbf{k}_1+\mathbf{k}_2) C_{11}\delta^*_{\mathbf{k}_3} + 2\,\text{perms.} \right\} \right] + \mathcal{O}(f_{nl}^2) \Bigg), \quad (2.8)$$

After differentiating with respect to f_{nl} we obtain

$$\begin{aligned} \frac{\partial \ln P(\delta|f_{nl})}{\partial f_{nl}} &= \int_{\mathbf{k}_1,\mathbf{k}_2,\mathbf{k}_3} \Bigg(\frac{(2\pi)^3 \delta_D(\mathbf{k}_1+\mathbf{k}_2+\mathbf{k}_3) B^{th}(k_1,k_2,k_3)}{6C_{11}C_{22}C_{33}} \\ &\quad \times V^2 \left[V\delta^*_{\mathbf{k}_1}\delta^*_{\mathbf{k}_2}\delta^*_{\mathbf{k}_3} - \left\{ \delta_D(\mathbf{k}_1+\mathbf{k}_2) C_{11}\delta^*_{\mathbf{k}_3} + 2\,\text{perms.} \right\} \right] + \mathcal{O}(f_{nl}) \Bigg) \\ &= \int_{\mathbf{k}_1,\mathbf{k}_2,\mathbf{k}_3} \Bigg(\frac{(2\pi)^3 \delta_D(\mathbf{k}_1+\mathbf{k}_2+\mathbf{k}_3) B^{th}(k_1,k_2,k_3)}{6C_{11}C_{22}C_{33}} \\ &\quad \times V^2 \left[V\delta^*_{\mathbf{k}_1}\delta^*_{\mathbf{k}_2}\delta^*_{\mathbf{k}_3} - \left\{ \delta_D(\mathbf{k}_1+\mathbf{k}_2) C_{11}\delta^*_{\mathbf{k}_3} + 2\,\text{perms.} \right\} \right] - N_{th} f_{nl} \Bigg). \end{aligned} \quad (2.9)$$

In the second line we have replaced the term of order $\mathcal{O}(f_{nl})$ by its Gaussian expectation value which is proportional to f_{nl}, hence the normalisation factor N_{th}. This is because the non-Gaussian part of that term is suppressed by a factor of f_{nl}^2 relative to its Gaussian counterpart and can therefore be ignored to a good approximation [149]. Setting $\frac{\partial \ln P(\delta|f_{nl})}{\partial f_{nl}} = 0$ and solving for f_{nl} in Equation (2.9) gives

$$\begin{aligned} \hat{f}_{nl} = \frac{(2\pi)^3}{N_{th}} \int_{\mathbf{k}_1,\mathbf{k}_2,\mathbf{k}_3} &\frac{\delta_D(\mathbf{k}_1+\mathbf{k}_2+\mathbf{k}_3) B^{th}(k_1,k_2,k_3)}{6C_{11}C_{22}C_{33}} V^2 \\ &\times \left(V\delta^*_{\mathbf{k}_1}\delta^*_{\mathbf{k}_2}\delta^*_{\mathbf{k}_3} - \left\{ \delta_D(\mathbf{k}_1+\mathbf{k}_2) C_{11}\delta^*_{\mathbf{k}_3} + 2\,\text{perms.} \right\} \right) \end{aligned} \quad (2.10)$$

where a circumflex $\hat{}$ has been added to emphasis that fact that this is an estimator for f_{nl}. Substituting $C_{ii} = \langle \delta^*_{\mathbf{k}_i} \delta_{\mathbf{k}_i} \rangle = (2\pi)^3 \delta_D(\mathbf{0}) P(k_i) = V P(k_i)$ (see Equation (2.13) below) and absorbing some of the multiplicative factors into N_{th} we finally obtain

$$\begin{aligned} \hat{f}_{nl} &= \frac{(2\pi)^6}{N_{th}} \int_{\mathbf{k}_1,\mathbf{k}_2,\mathbf{k}_3} \frac{\delta_D(\mathbf{k}_1+\mathbf{k}_2+\mathbf{k}_3) B^{th}(k_1,k_2,k_3)}{P(k_1)P(k_2)P(k_3)} \\ &\quad \times \left(\delta^*_{\mathbf{k}_1}\delta^*_{\mathbf{k}_2}\delta^*_{\mathbf{k}_3} - \left\{ \langle \delta_{\mathbf{k}_1}\delta_{\mathbf{k}_2} \rangle \delta^*_{\mathbf{k}_3} + 2\,\text{perms.} \right\} \right) \\ &= \frac{(2\pi)^6}{N_{th}} \int_{\mathbf{k}_1,\mathbf{k}_2,\mathbf{k}_3} \frac{\delta_D(\mathbf{k}_1+\mathbf{k}_2+\mathbf{k}_3) B^{th}(k_1,k_2,k_3)}{P(k_1)P(k_2)P(k_3)} \\ &\quad \times \left(\delta_{\mathbf{k}_1}\delta_{\mathbf{k}_2}\delta_{\mathbf{k}_3} - 3 \langle \delta_{\mathbf{k}_1}\delta_{\mathbf{k}_2} \rangle \delta_{\mathbf{k}_3} \right). \end{aligned} \quad (2.11)$$

The integral over $\mathbf{k}_1, \mathbf{k}_2, \mathbf{k}_3$ allows us to combine the permutations and in addition we can remove the complex conjugate on the fields by using $\delta^*_{\mathbf{k}_i} = \delta_{-\mathbf{k}_i}$.

Equation (2.11) is the expression for the optimal estimator for the amplitude f_{nl} of a theoretical bispectrum shape B^{th} for a given δ, in the limit of weak non-Gaussianity and under the assumptions of statistical isotropy and homogeneity. By subtracting the linear term used above ($\langle \delta_{\mathbf{k}_1} \delta_{\mathbf{k}_2} \rangle \delta_{\mathbf{k}_3}$), analogous to that used in CMB analysis, we can suppress error contributions from off-diagonal, i.e. non-Gaussian, covariances in the power spectrum. These arise from mode couplings due to anisotropic effects, e.g. incomplete survey coverage. Clearly this is not an issue for the work on simulations in this thesis so we will neglect it, noting that it could be important for observational analysis.

To extract the value of f_{nl} from data we require the statistical average of $\hat{f}_{nl}$ over different realisations of δ. We invoke the fact that for arbitrary $F(k_1, k_2, k_3)$ we can perform the angular integrals to obtain

$$\int \frac{d^3k_1}{(2\pi)^3} \frac{d^3k_2}{(2\pi)^3} \frac{d^3k_3}{(2\pi)^3} (2\pi)^6 \delta_D^2 (\mathbf{k}_1 + \mathbf{k}_2 + \mathbf{k}_3) F = \frac{V}{8\pi^4} \int_{\mathcal{V}_B} dk_1 dk_2 dk_3 \, k_1 k_2 k_3 F, \tag{2.12}$$

$\mathcal{V}_B$ is the bispectrum domain defined by the triangle condition imposed on the wavenumbers k_i such that $\mathbf{k}_1 + \mathbf{k}_2 + \mathbf{k}_3 = 0$, together with a chosen resolution limit $k_1, k_2, k_3 < k_{max}$. As this is not a trivial result it is instructive to outline the essential steps of the derivation. First, V is a volume factor defined by $V = L^3 = (2\pi)^3 \delta_D(\mathbf{0})$ which comes from the second Dirac delta function. This is because the delta function evaluated at $\mathbf{0}$ can be interpreted in the following way: in a finite cubic box with volume $V = L^3$, we can impose periodic boundary conditions such that the momenta in the box are discretised, i.e. $\mathbf{k} = 2\pi\mathbf{n}/L$ where $\mathbf{n} \in \mathbb{Z}^3$. The delta function can therefore be discretised [150] as

$$\delta_D(\mathbf{k} - \mathbf{k}') = \frac{1}{(2\pi)^3} \int_V d^3x e^{-i(\mathbf{k}-\mathbf{k}')\cdot\mathbf{x}} = \frac{V}{(2\pi)^3} \delta_{\mathbf{k},\mathbf{k}'}, \tag{2.13}$$

which gives the expression above. We can then naturally interpret V as the volume of the simulation/observational data and is therefore the same V in previous expressions. We then employ the formulae

$$\delta_D(\mathbf{k}) = \frac{1}{(2\pi)^3} \int d^3x \, e^{i\mathbf{k}\cdot\mathbf{x}}, \tag{2.14}$$

$$e^{i\mathbf{k}\cdot\mathbf{x}} = 4\pi \sum_{lm} i^l j_l(kx) Y_{lm}(\hat{\mathbf{k}}) Y^*_{lm}(\hat{\mathbf{x}}), \tag{2.15}$$

to expand the delta function in terms of spherical Bessel functions j_l and spherical harmonics Y_{lm}. The k-integrals in Equation (2.12) can therefore be factorised, each taking the form:

$$\int \frac{d^3k}{(2\pi)^3} e^{i\mathbf{k}\cdot\mathbf{x}} = \int \frac{d^3k}{(2\pi)^3} 4\pi \sum_{lm} i^l j_l(kx) Y_{lm}(\hat{\mathbf{k}}) Y^*_{lm}(\hat{\mathbf{x}}). \tag{2.16}$$

The angular integration is straightforward to carry out by using the orthogonality property of the spherical harmonics

$$\int_0^{2\pi} \int_0^{\pi} Y_{lm}(\theta,\phi) Y^*_{l'm'}(\theta,\phi) \sin\theta \, d\theta d\phi = \delta_{ll'}\delta_{mm'}, \tag{2.17}$$

and the fact that $Y^*_{00} = 1/\sqrt{4\pi}$ to obtain

$$\begin{aligned}
\int \frac{d^3k}{(2\pi)^3} e^{i\mathbf{k}\cdot\mathbf{x}} &= \int \frac{dk}{(2\pi)^3} k^2 4\pi \sum_{lm} i^l j_l(kx) \delta_{l0}\delta_{m0} Y^*_{lm}(\hat{\mathbf{x}}) \\
&= \int \frac{dk}{(\pi)^{3/2}} k^2 j_0(kx) Y^*_{00}(\hat{\mathbf{x}}). \\
&= \int \frac{dk}{2\pi^2} k^2 j_0(kx).
\end{aligned} \tag{2.18}$$

We can now rewrite our original integral (Equation (2.12)) as

$$\begin{aligned}
&\int \frac{d^3k_1}{(2\pi)^3} \frac{d^3k_2}{(2\pi)^3} \frac{d^3k_3}{(2\pi)^3} (2\pi)^6 \delta_D^2(\mathbf{k}_1 + \mathbf{k}_2 + \mathbf{k}_3) F \\
&= \frac{V}{8\pi^6} \int d^3x \int dk_1 dk_2 dk_3 (k_1k_2k_3)^2 j_0(k_1x) j_0(k_2x) j_0(k_3x) F.
\end{aligned} \tag{2.19}$$

Since the first spherical Bessel function is $j_0(z) = \sin z/z$ the final step is to compute $\int d^3x \, j_0(k_1x) j_0(k_2x) j_0(k_3x)$ with simple trigonometric identities to yield $\pi^2/(k_1k_2k_3)$. This simultaneously imposes the triangle inequality on the wavenumbers k_1, k_2 and k_3 which restricts the integration domain to be $\mathcal{V}_B$, thus giving the required result in Equation (2.12).

Using Equation (2.12) we obtain $\langle \hat{f}_{nl} \rangle$ as

$$\langle \hat{f}_{nl} \rangle = \frac{1}{N_{th}} \frac{V}{\pi} \int_{\mathcal{V}_B} dV_k \, k_1k_2k_3 \frac{B^{th}(k_1,k_2,k_3) B_\delta(k_1,k_2,k_3)}{P(k_1)P(k_2)P(k_3)}, \tag{2.20}$$

where $dV_k \equiv dk_1dk_2dk_3$. The second term in the parentheses in Equation (2.11) vanishes since $\langle \delta(\mathbf{k}) \rangle = 0$. Setting $B^{th} = B_\delta$ and demanding $\langle \hat{f}_{nl} \rangle = 1$ gives the normalisation factor

as

$$N_{th} = \frac{V}{\pi}\int_{\mathcal{V}_B} dV_k\, k_1 k_2 k_3 \frac{[B^{th}(k_1,k_2,k_3)]^2}{P(k_1)P(k_2)P(k_3)}. \tag{2.21}$$

The form of Equation (2.20) suggests we should define inner products between bispectra as

$$\left[B_i, B_j\right] \equiv \frac{V}{\pi}\int_{\mathcal{V}_B} dV_k\, k_1 k_2 k_3 \frac{B_i(k_1,k_2,k_3)B_j(k_1,k_2,k_3)}{P(k_1)P(k_2)P(k_3)}. \tag{2.22}$$

We use square brackets $[\,]$ for inner products to avoid confusion with expectation values, which are labelled with angle brackets $\langle\rangle$. This naturally motivates the definition of the signal-to-noise (SN) weighted bispectrum,

$$B_i^{SN}(k_1,k_2,k_3) \equiv \sqrt{\frac{k_1 k_2 k_3}{P(k_1)P(k_2)P(k_3)}} B_i(k_1,k_2,k_3). \tag{2.23}$$

This SN-weighted bispectrum is relevant for observations of the matter bispectrum and is useful for providing forecasts for future surveys.

The bispectrum domain $\mathcal{V}_B$ takes the form of a tetrapyd in k-space as shown in Figure 2.1. It is the union of a tetrahedral region and a triangular pyramid on top. Plotting the full tetrapyd obscures it inner structure, and we have found it useful to split it in half to make apparent its internal morphology. As illustrated in Figure 2.2, different bispectrum shapes can be distinguished through the regions in the tetrapyd where they give the strongest signal. In Figure 2.3 we show the bispectra shapes introduced in Section 1.4.4. The bispectra plots in this thesis are generated with `ParaView` [151], an open source scientific visualisation tool.

Using Equation (2.20) we can further define 4 correlators between bispectra. The shape correlator, $\mathcal{S}$, is defined by

$$\mathcal{S}(B_i,B_j) \equiv \frac{\left[B_i,B_j\right]}{\sqrt{\left[B_i,B_i\right]\left[B_j,B_j\right]}}, \tag{2.24}$$

and is restricted to $-1 \leq \mathcal{S} \leq 1$. It can be thought of as the cosine between B_i and B_j. To quantify how well the magnitudes of B_i and B_j match each other we define the amplitude correlator $\mathcal{A}$ as

$$\mathcal{A}(B_i,B_j) \equiv \sqrt{\frac{\left[B_i,B_i\right]}{\left[B_j,B_j\right]}}. \tag{2.25}$$

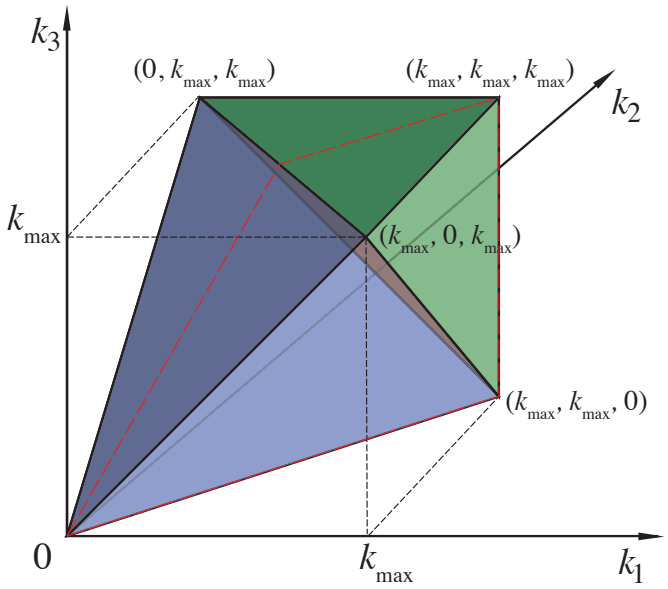

Fig. 2.1 The full tetrapyd bispectrum domain consists of a tetrahedral region (blue) defined by the wavevector triangle condition $\mathbf{k}_1 + \mathbf{k}_2 + \mathbf{k}_3 = 0$, together with a pyramidal region (green) bounded by the resolution limit k_{max}. To show the internal structure of the tetrapyd we split it along the red dashed line to obtain Figure 2.2. [11]

We can combine the information given by the shape and amplitude correlators into a single quantity known as the total correlator $\mathcal{T}$:

$$\begin{aligned}\mathcal{T}(B_i, B_j) &\equiv 1 - \sqrt{\frac{\left[B_j - B_i, B_j - B_i\right]}{\left[B_j, B_j\right]}} \\ &= 1 - \sqrt{1 - 2\mathcal{S}(B_i, B_j)\mathcal{A}(B_i, B_j) + \mathcal{A}^2(B_i, B_j)}. \end{aligned} \tag{2.26}$$

The total correlator is a stringent test of correlation between bispectra, as both misalignment ($\mathcal{S} < 1$) or a difference in amplitude ($\mathcal{A} \neq 1$) lead to a decrease in $\mathcal{T}$. Later on we will use $\mathcal{T}$ to test the ability of `MODAL-LSS` to reconstruct theoretical bispectra (see Section 2.2).

We can interpret $\mathcal{T}$ physically as follows. Let B_T be the true bispectrum and B_A be an approximation to B_T. Now suppose we constrain each of these templates with Equation (2.11) to obtain f_{nl}^T and f_{nl}^A. The variance of each estimate is given by

$$\sigma_i^2 = \left\langle {f_{nl}^i}^2 \right\rangle = N_i^{-1} = \left[B_i, B_i\right]^{-1}, \tag{2.27}$$

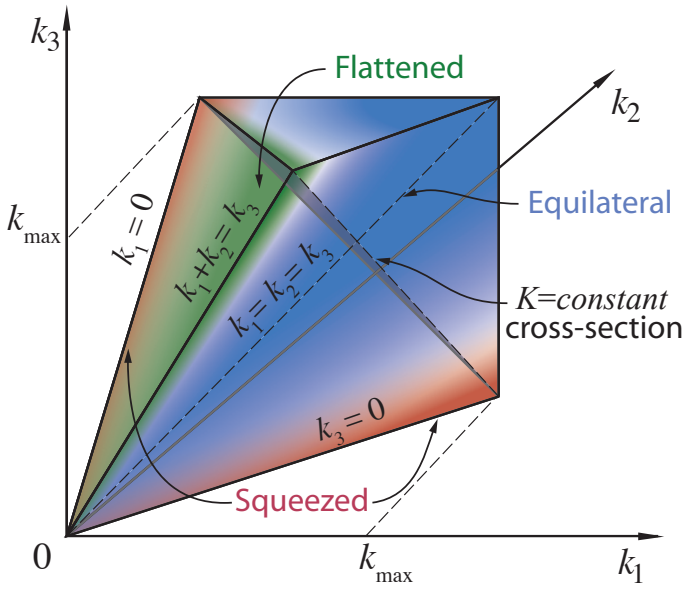

Fig. 2.2 The split 3D tetrapyd region showing only the back half with $k_1 < k_2$. Colour-coded regions show the location of the 'squeezed' (red), 'flattened' (green) and 'equilateral' or 'constant' (blue) shape signals. The scale dependence of the bispectrum is reflected by the $K \equiv k_1 + k_2 + k_3 = \text{const.}$ cross sectional planes. [11]

and the variance of the difference between the two estimates is given by

$$\begin{aligned}\sigma^2_{diff} &= \left\langle \left(f^T_{nl} - f^A_{nl}\right)^2 \right\rangle \\ &= \frac{1}{(N_T N_A)^2}\left[N_A B_T - N_T B_A, N_A B_T - N_T B_A\right] \\ &= \frac{N_A - 2\left[B_A, B_T\right] + N_T}{N_A N_T},\end{aligned} \tag{2.28}$$

If we take the ratio of σ_{diff} and σ_A then we get

$$\begin{aligned}\frac{\sigma^2_{diff}}{\sigma^2_A} &= 1 - 2\frac{1}{N_T}\left[B_A, B_T\right] + \frac{N_A}{N_T} \\ &= \left(1 - \mathcal{T}(B_T, B_A)\right)^2.\end{aligned} \tag{2.29}$$

This allows us to identify $1-\mathcal{T}$ as the coefficient of variation c_v [152]. Therefore if B_A is used as a proxy for B_T, $1-\mathcal{T}$ gives us the standard deviation between our estimate of f_{nl}

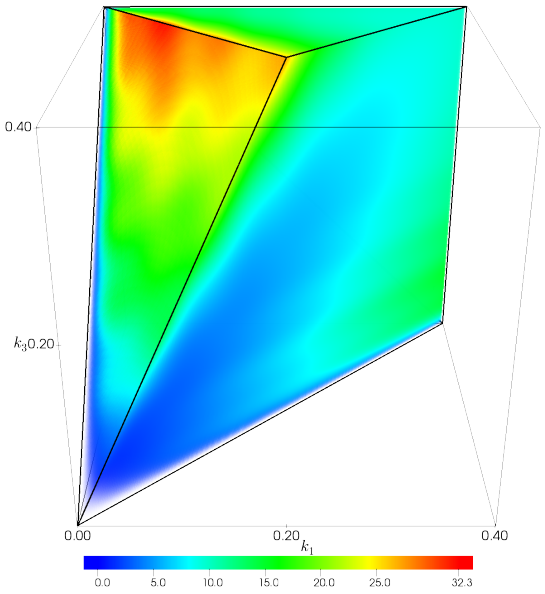

(a) Tree-level shape, $k_{max} = 0.4$

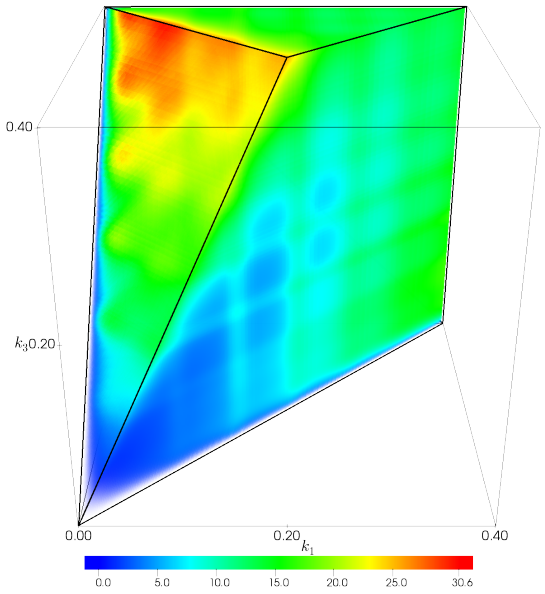

(b) Nine-parameter model, $k_{max} = 0.4$

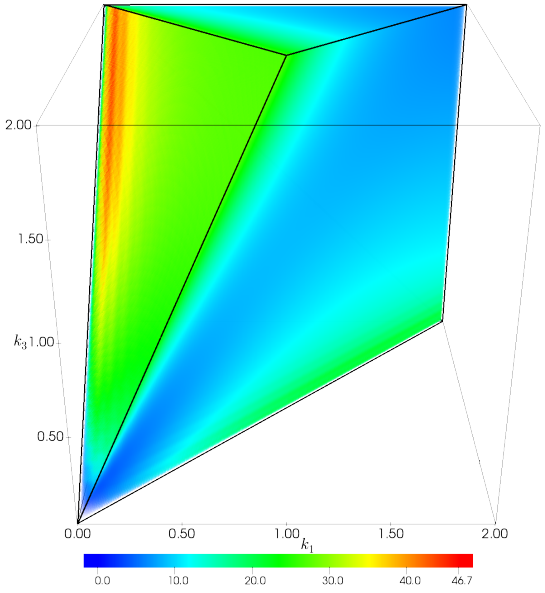

(c) Scaled Tree-level shape, $k_{max} = 2$

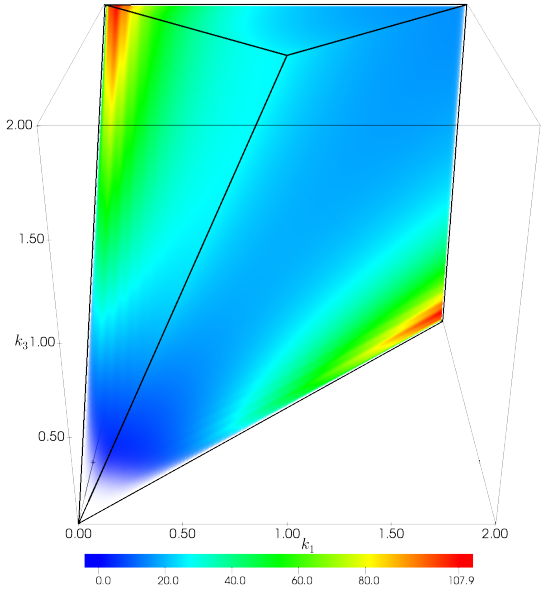

(d) Scaled squeezed shape, $k_{max} = 2$

Fig. 2.3 The bispectrum shapes introduced in Section 1.4.4 plotted at redshift $z = 0.5$ up to various k_{max}. *(cont.)*

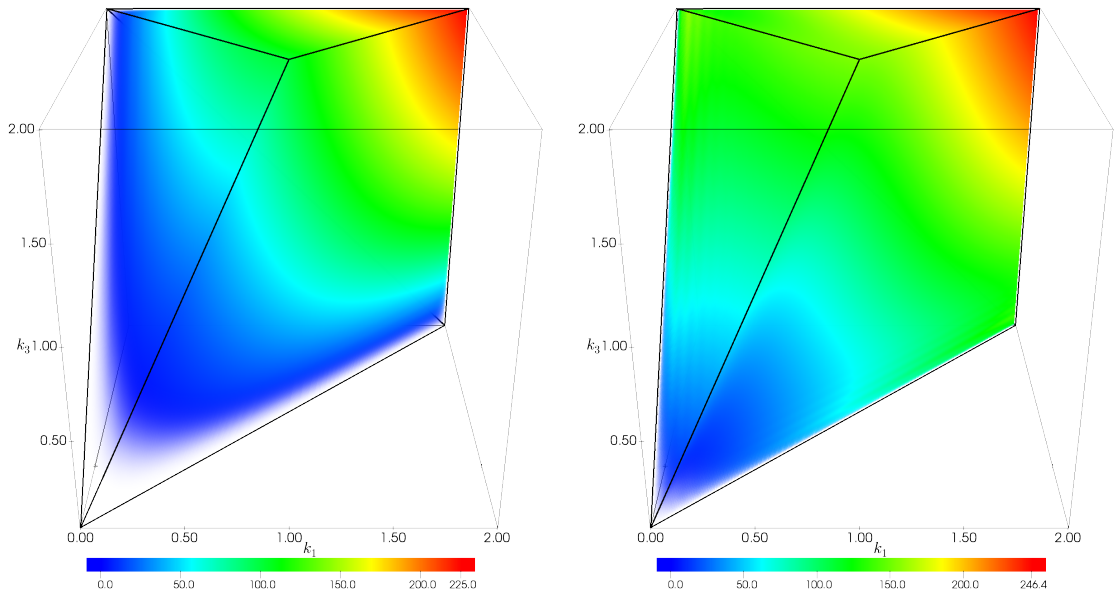

(e) Scaled constant shape, $k_{max} = 2$ (f) 3-shape model, $k_{max} = 2$

Fig. 2.3 The bispectrum shapes introduced in Section 1.4.4 plotted at redshift $z = 0.5$ up to various k_{max}.

and the true value as a fraction of our error bar, i.e.:

$$\sigma_{diff} = (1 - \mathcal{T})\,\sigma_A. \tag{2.30}$$

$\mathcal{T}$ is appropriate for comparing theoretical bispectra, but its performance is easily degraded by cosmic variance and hence another correlator is needed when simulation or observational data is involved. The f_{nl} correlator, named as such due to its similarity to the $\langle \hat{f}_{nl} \rangle$ parameter in Equation (2.20) above, again combines the shape and amplitude correlators:

$$\begin{aligned} f_{nl}(B_i, B_j) &\equiv \frac{[B_i, B_j]}{[B_j, B_j]} \\ &= \mathcal{S}(B_i, B_j)\mathcal{A}(B_i, B_j). \end{aligned} \tag{2.31}$$

This can be interpreted as simply the correlation between our estimate of f_{nl} with the true value, normalised by the true value.

$$\frac{\left\langle f_{nl}^T f_{nl}^A \right\rangle}{\left\langle f_{nl}^{T\,2} \right\rangle} = \frac{1}{N_A}\left[B_T, B_A\right] = f_{nl}(B_T, B_A). \tag{2.32}$$

2.2 MODAL-LSS Methodology

Since the bispectrum $B(k_1,k_2,k_3)$ cannot generally be separated into a product of functions over k_1,k_2,k_3, the 9-dimensional integral in the $\hat{f}_{nl}$ estimator (Equation (2.11)) is computationally intractable. This computation barrier has been solved by a separable method introduced in [153]. This MODAL1 method has been applied to PlanckCMB analysis with great success [154], in which the different methods for foreground subtraction in CMB maps were ranked in terms of their ability to retain information about primordial non-Gaussianity. We hope to extend this framework to analyse the bispectrum of the large scale structure of the universe, which is aptly named MODAL-LSS. This is complimentary to work in real space, i.e. the galaxy three-point correlation function (3PCF) [155, 156], as well as that in redshift space [157]. Here we outline the MODAL-LSS methodology.

2.2.1 MODAL-LSS Basis

We first approximate the SN-weighted theoretical bispectrum in Equation (2.23) by expanding it in a general separable basis (see also Figure 2.4):

$$\sqrt{\frac{k_1k_2k_3}{P(k_1)P(k_2)P(k_3)}}B^{th}(k_1,k_2,k_3) \approx \sum_n^{n_{max}} \alpha_n^Q Q_n^{\texttt{MODAL-LSS}}\left(\frac{k_1}{k_{max}}, \frac{k_2}{k_{max}}, \frac{k_3}{k_{max}}\right). \tag{2.33}$$

The basis functions $Q_n^{\texttt{MODAL-LSS}}$ are symmetrised products over one dimensional functions q_r:

$$Q_n^{\texttt{MODAL-LSS}}(x,y,z) \equiv q_{\{r}(x)q_s(y)q_{t\}}(z), \tag{2.34}$$

with $\{\dots\}$ representing symmetrisation over the indices r,s,t, and each n corresponds to a combination of r,s,t. k_{max} is the resolution of the tetrahedral domain defined above. The choice of q_r is arbitrary and there are many sensible choices including k-bins (which are localised in k-space), wavelets (which are localised in real space), Fourier modes, etc. We adopt polynomials since they offer efficient compression of the data so fewer modes can be

used without information loss. Note that the $\{Q_n^{\texttt{MODAL-LSS}}\}$ forms a complete basis for the expansion of B^{th}, but naturally we truncate the expansion at some n_{max} depending on the accuracy required. In the limit $n_{max} \to \infty$ the approximation is exact and the expansion above is an equality. For convenience in our discussion below we will assume that the truncation causes errors that are tiny and that Equation (2.33) is exact.

It has been shown that the convergence of the sum in Equation (2.33) is independent of the choice of polynomials q_r. This means there is a freedom in the choice of q_r, provided the $Q_n^{\texttt{MODAL-LSS}}$ basis is orthogonal or can be made orthogonal (e.g. through a modified Gram-Schmidt process which ensures numerical stability, see our discussion on the Cholesky decomposition below) on the tetrahedral domain $\mathcal{V}_B$. Different choices of polynomials only change the individual α_n^Q but not the sum. This means we could use Legendre polynomials, Chebyshev polynomials or simply x^r monomials. As we shall see later some of these choices are inappropriate because they lead to numerical instabilities. Currently we find shifted Legendre polynomials $\tilde{P}_l(x) = P_l(2x-1)$, such that $\tilde{P}_l(x)$ is orthogonal over the interval $[0,1]$ instead of the usual $[-1,1]$ for $P_l(x)$, perform well and are adopted for q_r as they demonstrate better orthogonality at low n and encapsulate the behaviour of the bispectrum at non-linear scales very well. Calculation of higher order polynomials also demonstrates good numerical stability when they are calculated recursively.

Another issue is the mapping between n and r,s,t. The ordering of this mapping is arbitrary; here we have adopted 'slice ordering' which orders the triples by the sum $r+s+t$. A sub-ordering is introduced along each column in cases of degeneracy, i.e.

$$\begin{array}{llll} \underline{0 \to 000} & 4 \to 111 & 8 \to 022 & 12 \to 113 \\ \underline{1 \to 001} & 5 \to 012 & 9 \to 013 & 13 \to 023 \\ 2 \to 011 & \underline{6 \to 003} & \underline{10 \to 004} & 14 \to 014 \\ \underline{3 \to 002} & 7 \to 112 & 11 \to 122 & \underline{15 \to 005} \cdots, \end{array} \tag{2.36}$$

where the lines mark the end of each overall polynomial order.

Using the MODAL-LSS expansion in Equation (2.33) we can rewrite $\hat{f}_{nl}$ in Equation (2.11) as:

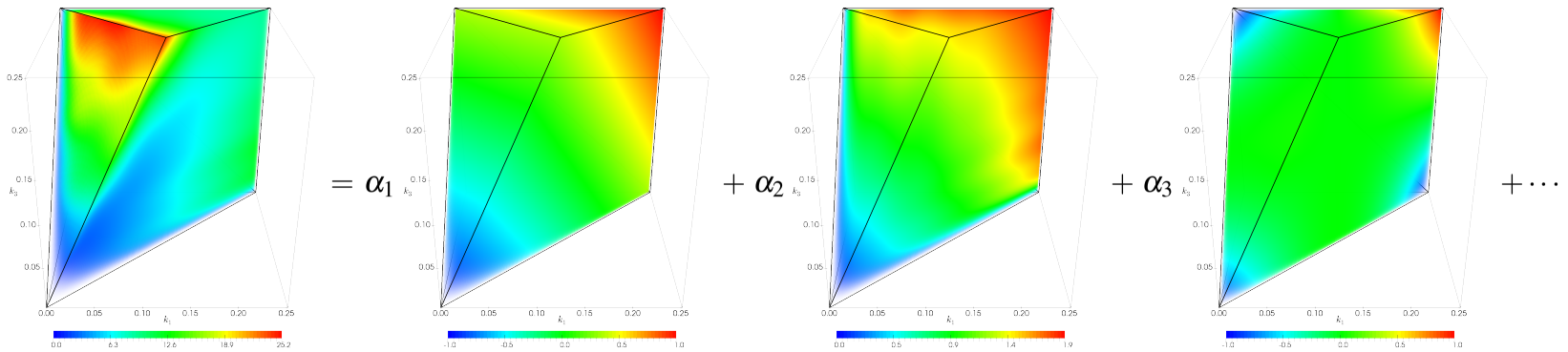

$$= \alpha_1 \; + \alpha_2 \; + \alpha_3 \; + \cdots \tag{2.35}$$

Fig. 2.4 A cartoon demonstrating the `MODAL-LSS` expansion. Here we are expanding the tree level bispectrum (Equation (1.123)) as a linear combination of the $Q_n^{\texttt{MODAL-LSS}}$ basis functions (represented by the tetrapyds), each of which is weighted by an α_n coefficient.

$$\begin{aligned}\hat{f}_{nl} &= \frac{(2\pi)^6}{N_{th}} \int_{\mathbf{k}_1,\mathbf{k}_2,\mathbf{k}_3} \delta_D(\mathbf{k}_1+\mathbf{k}_2+\mathbf{k}_3) \frac{\sum_n \alpha_n^Q q_{\{r}(\frac{k_1}{k_{max}}) q_s(\frac{k_2}{k_{max}}) q_{t\}}(\frac{k_3}{k_{max}})}{\sqrt{k_1 P(k_1) k_2 P(k_2) k_3 P(k_3)}} \\ &\qquad \times (\delta_{\mathbf{k}_1}\delta_{\mathbf{k}_2}\delta_{\mathbf{k}_3} - \langle \delta_{\mathbf{k}_1}\delta_{\mathbf{k}_2}\rangle \delta_{\mathbf{k}_3}) \\ &= \frac{(2\pi)^3}{N_{th}} \sum_n \alpha_n^Q \int d^3x \int \frac{\prod_i d^3k_i}{(2\pi)^9} e^{i(\mathbf{k}_1+\mathbf{k}_2+\mathbf{k}_3)\cdot\mathbf{x}} \frac{q_{\{r}(\frac{k_1}{k_{max}}) q_s(\frac{k_2}{k_{max}}) q_{t\}}(\frac{k_3}{k_{max}})}{\sqrt{k_1 P(k_1) k_2 P(k_2) k_3 P(k_3)}} \\ &\qquad \times (\delta_{\mathbf{k}_1}\delta_{\mathbf{k}_2}\delta_{\mathbf{k}_3} - \langle \delta_{\mathbf{k}_1}\delta_{\mathbf{k}_2}\rangle \delta_{\mathbf{k}_3}) \\ &= \frac{(2\pi)^3}{N_{th}} \sum_n \alpha_n^Q \int d^3x \left[M_r(\mathbf{x}) M_s(\mathbf{x}) M_t(\mathbf{x}) - \langle M_{\{r}(\mathbf{x}) M_s(\mathbf{x})\rangle M_{t\}}(\mathbf{x}) \right], \end{aligned} \tag{2.37}$$

where in the second line we have used the integral from of the delta function with variable $\mathbf{x}$, and we defined

$$M_r(\mathbf{x}) \equiv \int \frac{d^3k}{(2\pi)^3} \frac{\delta_{\mathbf{k}} q_r(k/k_{max})}{\sqrt{kP(k)}} e^{i\mathbf{k}\cdot\mathbf{x}}, \tag{2.38}$$

which is an inverse Fourier transform. Here the choice of the polynomials q_r becomes important. For example, the integral in Equation (2.38) convergences poorly for large r if we choose monomials $q_r = x^r$. Note that there is no symmetrisation over r,s,t in the first term inside the square brackets as the product is already symmetric. As we are only analysing simulation data which are approximately homogeneous and isotropic we can ignore the second term in the square brackets as it evaluates to zero. We then introduce

$$\beta_n^Q = (2\pi)^3 \int d^3x M_r(\mathbf{x}) M_s(\mathbf{x}) M_t(\mathbf{x}) \tag{2.39}$$

which allows us to express $\hat{f}_{nl}$ in a simple and elegant form:

$$\hat{f}_{nl} = \frac{1}{N_{th}} \sum_n \alpha_n^Q \beta_n^Q. \tag{2.40}$$

The beta coefficients β_n^Q are approximately analogous (there is a subtlety we will meet in the next section) to the alpha coefficients α_n^Q but they are used in the expansion of observational/simulation bispectra instead of theoretical ones.

In summary, we have reduced the complicated integral in Equation (2.11) to the calculation of α_n^Q and β_n^Q coefficients. The computation of α_n^Q coefficients is a non-trivial problem but has been made efficient by the authors of [158] whose implementation we use here. The β_n^Q coefficients on the other hand only require a number of (inverse) Fourier transforms

(evident upon inspection of Equation (2.38)) which can be evaluated efficiently with the fast Fourier transform (FFT) algorithm[1], together with an integral over the spatial extent of the data set (Equation (2.39)) which can be highly parallelised with Open Multi-Processing (`OpenMP`).

2.2.2 An orthogonal basis

Unlike the theoretical bispectrum the observational/simulation bispectrum is a statistical quantity, and and it can only be estimated through different realisations of the density field δ. We expand the estimated observational bispectrum $\hat{B}_\delta$ in the following way:

$$\sqrt{\frac{k_1k_2k_3}{P(k_1)P(k_2)P(k_3)}}\hat{B}_\delta(k_1,k_2,k_3) = \sum_n^{n_{max}} \tilde{\beta}_n^Q Q_n(k_1/k_{max}, k_2/k_{max}, k_3/k_{max}), \tag{2.41}$$

the expectation value of which is the true underlying observational bispectrum $B_\delta \equiv \langle \hat{B}_\delta \rangle$:

$$\sqrt{\frac{k_1k_2k_3}{P(k_1)P(k_2)P(k_3)}}B_\delta(k_1,k_2,k_3) = \sum_n^{n_{max}} \langle\tilde{\beta}_n^Q\rangle Q_n(k_1/k_{max}, k_2/k_{max}, k_3/k_{max}). \tag{2.42}$$

We have introduced these new beta coefficients[2] $\tilde{\beta}_n^Q$ as $\{Q_n\}$ is not an orthogonal basis. To relate $\tilde{\beta}_n^Q$ to β_n^Q we substitute Equation (2.42) into Equation (2.20):

$$\begin{aligned}\langle\hat{f}_{nl}\rangle &= \frac{1}{N_{th}}\frac{V}{\pi}\int_{\mathcal{V}_B} dV_k \sum_{nm} \alpha_n^Q \langle\tilde{\beta}_m^Q\rangle Q_n Q_m \\ &= \frac{1}{N_{th}}\sum_{nm} \alpha_n^Q \langle\tilde{\beta}_m^Q\rangle \gamma_{nm},\end{aligned} \tag{2.43}$$

where

$$\gamma_{nm} \equiv \frac{V}{\pi}\int_{\mathcal{V}_B} dV_k Q_n Q_m \tag{2.44}$$

is the inner product between the Q_n functions on the tetrapyd domain. Generally speaking γ_{nm} is not diagonal since the Q_n functions are not orthogonal to each other. Comparing this

[1] We use the `FFTW3` [159] implementation of the algorithm.

[2] We could have instead to reversed the placement of the tilde to make α_n^Q and β_n^Q more analogous, but we have adopted this notation as it more closely represents the computational flow of the method.

with the expectation value of Equation (2.40) we obtain

$$\langle \beta_n^Q \rangle = \sum_m \gamma_{nm} \langle \tilde{\beta}_m^Q \rangle \Rightarrow \beta_n^Q = \sum_m \gamma_{nm} \tilde{\beta}_m^Q. \tag{2.45}$$

While β_n^Q may be straightforward to evaluate numerically through Equation (2.39), it often proves simpler to use an orthonormalised version we create by diagonalising γ_{nm}. We therefore introduce a basis $\{R_n\}$ which is defined relative to $\{Q_n\}$ by

$$R_n \equiv \lambda_{nm} Q_m \Leftrightarrow Q_p \equiv (\lambda^{-1})_{pq} R_q, \tag{2.46}$$

such that it is orthonormal on the tetrapyd domain:

$$\frac{V}{\pi} \int_{\mathcal{V}_B} dV_k R_n R_m = \delta_{nm}. \tag{2.47}$$

From Equations (2.44) and (2.47) we deduce that $\gamma = \lambda^{-1}(\lambda^{-1})^T$. A unique and efficient way to calculate λ^{-1} from γ is through a Cholesky decomposition, which is implemented in a wide range of numerical libraries including the GNU Scientific Library `GSL` [160]. This is essentially a modified version of Gram-Schmidt orthogonalisation but with better numerical stability. The method forces λ^{-1} to be take lower diagonal form and requires γ to be positive definite [161], which is equivalent to linear independence between the Q_n modes. We thus employ shifted Legendre polynomials as they demonstrate good orthogonality, making the Cholesky decomposition more numerically stable. We now apply the expansion in the $\{R_n\}$ basis:

$$\sqrt{\frac{k_1 k_2 k_3}{P(k_1)P(k_2)P(k_3)}} B^{th}(k_1,k_2,k_3) = \sum_n^{n_{max}} \alpha_n^R R_n(k_1/k_{max}, k_2/k_{max}, k_3/k_{max}), \tag{2.48}$$

$$\sqrt{\frac{k_1 k_2 k_3}{P(k_1)P(k_2)P(k_3)}} B_\delta(k_1,k_2,k_3) = \sum_n^{n_{max}} \langle \beta_n^R \rangle R_n(k_1/k_{max}, k_2/k_{max}, k_3/k_{max}). \tag{2.49}$$

Note that due to the orthonormality of the R_n functions we do not need two sets of β coefficients in this basis. Since $\sum_n \alpha_n^Q Q_n = \sum_n \alpha_n^R R_n$, one can derive the following relationships between the coefficients in the $\{Q_n\}$ and $\{R_n\}$ bases:

$$\alpha_n^R \equiv \sum_m (\lambda^{-1})_{nm}^T \alpha_m^Q, \quad \beta_n^R \equiv \sum_m (\lambda^{-1})_{nm}^T \tilde{\beta}_m^Q, \tag{2.50}$$

which allows us to write

$$\langle \hat{f}_{nl} \rangle = \frac{1}{N_{th}} \sum_n \alpha_n^R \langle \beta_n^R \rangle. \tag{2.51}$$

One can very easily show this is consistent with Equation (2.43) above. Using the `MODAL-LSS` ansatz with Equation (2.21) above we find that $N_{th} = \sum_n \alpha_n^R \alpha_n^R$. Therefore if the theoretical and data bispectrum match perfectly, i.e. $B^{th} = B_\delta$ and hence $\langle \hat{f}_{nl} \rangle = 1$, we deduce that $\langle \beta_n^R \rangle = \alpha_n^R$.

2.2.3 Calculation of γ_{nm}

The γ_{nm} integral in Equation (2.44) can be evaluated in two ways. The first is by direct integration on the tetrapydal domain which gives the most accurate answer. In Figure 2.5a we show γ_{nm} calculated in this way for 1000 modes using shifted Legendre polynomials and 42 grid points in each dimension.

Alternatively this can be done with the use of FFTs: by using Equation (2.12) we can write down an expression for γ_{nm} in terms of inverse Fourier Transforms:

$$\begin{aligned}
\gamma_{nm} &= (2\pi)^9 \int_{\mathbf{k}_1,\mathbf{k}_2,\mathbf{k}_3} \delta_D(\mathbf{k}_1+\mathbf{k}_2+\mathbf{k}_3) \frac{Q_n Q_m}{k_1 k_2 k_3} \\
&= (2\pi)^6 \int d^3x \int \frac{\prod_i d^3k_i}{(2\pi)^9} e^{i(\mathbf{k}_1+\mathbf{k}_2+\mathbf{k}_3)\cdot\mathbf{x}} \frac{Q_n Q_m}{k_1 k_2 k_3} \\
&= \frac{(2\pi)^6}{6} \int \left[M_{r_1 r_2}(\mathbf{x}) M_{s_1 s_2}(\mathbf{x}) M_{t_1 t_2}(\mathbf{x}) + 5\,\text{perms.} \right] d^3x,
\end{aligned} \tag{2.52}$$

where we have suppressed the arguments $(\frac{k_1}{k_{max}}, \frac{k_2}{k_{max}}, \frac{k_3}{k_{max}})$ of Q_n and Q_m for brevity, and introduce the integrals

$$M_{r_1 r_2}(\mathbf{x}) = \int \frac{d^3k}{(2\pi)^3} \frac{1}{k} q_{r_1}(k/k_{max}) q_{r_2}(k/k_{max}) e^{i\mathbf{k}\cdot\mathbf{x}} \tag{2.53}$$

resulting from the product $Q_n Q_m$. For $n \equiv \{r_1, s_1, t_1\}$ and $m \equiv \{r_2, s_2, t_2\}$ this product produces 36 terms, but only 6 unique combinations, i.e.

- $(r_1 r_2)(s_1 s_2)(t_1 t_2)$
- $(r_1 s_2)(s_1 t_2)(t_1 r_2)$
- $(r_1 t_2)(s_1 r_2)(t_1 s_2)$
- $(r_1 r_2)(s_1 t_2)(t_1 s_2)$

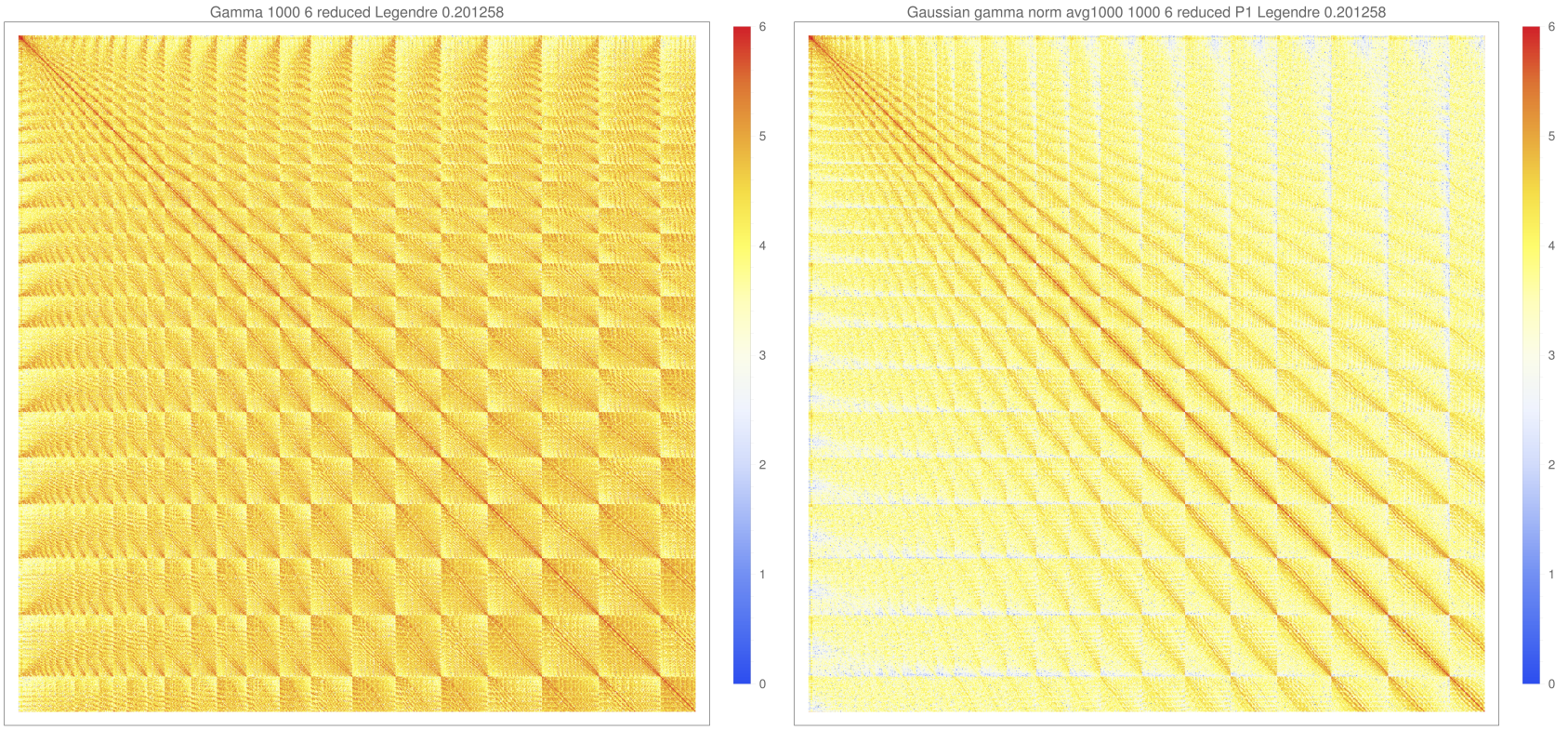

(a) γ_{nm} calculated directly on the tetrapyd for 1000 shifted Legendre polynomials using 42 grid points in each dimension. The abundance of off-diagonal features demonstrate the lack of orthogonality between modes on the tetrapyd, especially for high n.

(b) The same calculation but using FFTs over 128^3 grids in real space, but keeping the same k_{max}. While this qualitatively agrees with the plot to the left, the off-diagonal elements differ wildly quantitatively, demonstrating much stronger orthogonality between the modes.

Fig. 2.5 To better highlight the off-diagonal structure, in both of these figures we plot $\log_{10}\left|\frac{\gamma_{nm}}{\sqrt{\gamma_{nn}\gamma_{mm}}}\times 10^6\right|$, such that the diagonal is always 6, and limit the plot range to $[0,6]$. This is important since we need the inverse of γ_{nm} to rotate the MODAL-LSS coefficients in the Q basis to the R basis, and even small numerical differences in the off-diagonal elements can create large deviations in the final result.

- $(r_1 s_2)(s_1 r_2)(t_1 t_2)$
- $(r_1 t_2)(s_1 s_2)(t_1 r_2)$,

hence the 6 permutations in the final line of Equation (2.52). Figure 2.5b shows the result of such a calculation with 128^3 grids in real space, but keeping the same k_{max}. The discrepancy in number of grid points arises from aliasing considerations when putting particles on a grid, as we will discuss in Section 2.3.3. Although this is not relevant here we only use up to $\frac{2}{3}k_{Ny}$ of FFT grids here for consistency with our analysis of simulation data. Thus, both methods effectively use the same number of grid points as far as the tetrapyd is concerned.

Although Figure 2.5a and Figure 2.5b share qualitative similarities, demonstrating the same grid structure and features along the main diagonal and its close neighbours, the numerical values of the off-diagonal elements are much smaller with the FFT calculation. Curiously this would suggest the modes are more orthogonal to each other when used in conjunction with FFTs. In rotating the `MODAL-LSS` coefficients from the Q to R basis we need to calculate λ_{nm} (Equation (2.46)), given by $\gamma^{-1} = \lambda^T \lambda$. Since the inverse of a matrix is highly susceptible even to small changes in off-diagonal elements, big differences in the final bispectrum estimation can result if one is not careful. To illustrate this effect we made the following tests of the FFT-based `MODAL-LSS` code using randomly generated Gaussian density fields. Gaussianity implies the lack of bispectrum and higher order correlators, which has two consequences on the `MODAL-LSS` coefficients. First, $\left\langle \beta_n^Q \right\rangle = \langle \beta_n^R \rangle = 0$ due to the absence of any bispectrum. Additionally, as shown in the `MODAL-LSS` covariance calculation (Equation (2.85)), for a Gaussian density field the β^Q coefficients satisfy $\left\langle \beta_m^Q \beta_n^Q \right\rangle = \gamma_{mn}$. To ensure the internal consistency of the method we rotate this expression into the R basis with the γ_{nm} calculated with the two methods above and check if we recover $\left\langle \beta_m^R \beta_n^R \right\rangle = \delta_{mn}$. The conversion is achieved in the same manner as discussed in Section 2.2.2 by first taking the Cholesky decomposition of γ to obtain λ^{-1}, then a further matrix inversion gives λ. These are good sanity checks that our numerical code is behaving as expected and that the algorithm does indeed work.

The results of the $\langle \beta_n^R \rangle = 0$ test is shown in Figure 2.6 and the $\left\langle \beta_n^R \beta_n^R \right\rangle = 1$ test in Figure 2.7. Here we used 128^3 FFT grids and 42 tetrapyd points as above. The $\langle \beta_n^R \rangle = 0$ test is inconclusive as $\langle \beta_n^R \rangle$ calculated both ways are consistent with 0, but when the γ_{nm} calculated with the tetrapyd is used a strong divergence from the mean is observed at high n, which might be an indication that something is amiss. On the other hand Figure 2.7 clearly demonstrates the problem with using the tetrapyd-based γ_{nm}, as even stronger deviations are seen due to the inconsistent off-diagonal terms. We conclude that if the incorrect γ_{nm} is used one would not bias the mean (i.e. the bispectrum estimation itself), but would lead to hugely inflated covariances in the estimated bispectrum.

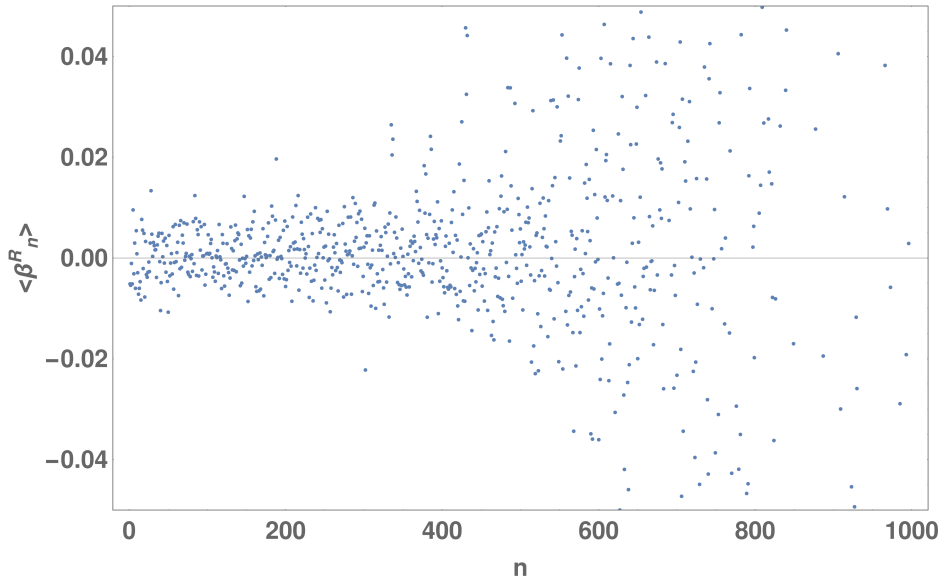

(a) γ_{nm} calculated on the tetrapyd, giving $\langle\beta_n^R\rangle = 0.016 \pm 0.202$. Although this is consistent with 0, it is clear the higher modes are strongly divergent from the mean which is an indication something is wrong.

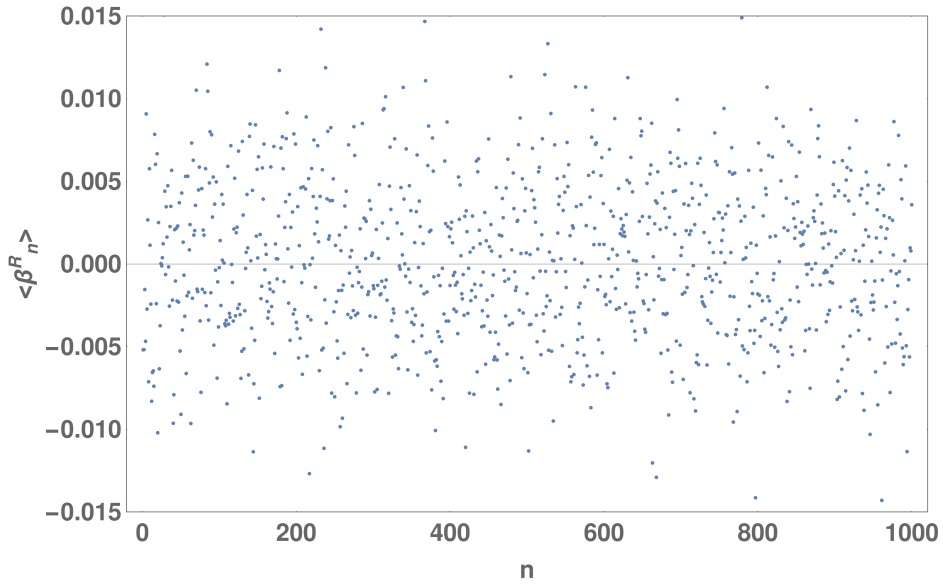

(b) γ_{nm} calculated with FFTs, giving $\langle\beta_n^R\rangle = 0.0001 \pm 0.0048$. The β_n^R thus obtained is much better behaved across the entire range of n, without any of the divergences seen to the left.

Fig. 2.6 Testing the γ_{mn} matrices by rotating β_n^Q into β_n^R and checking $\langle\beta_n^R\rangle = 0$.

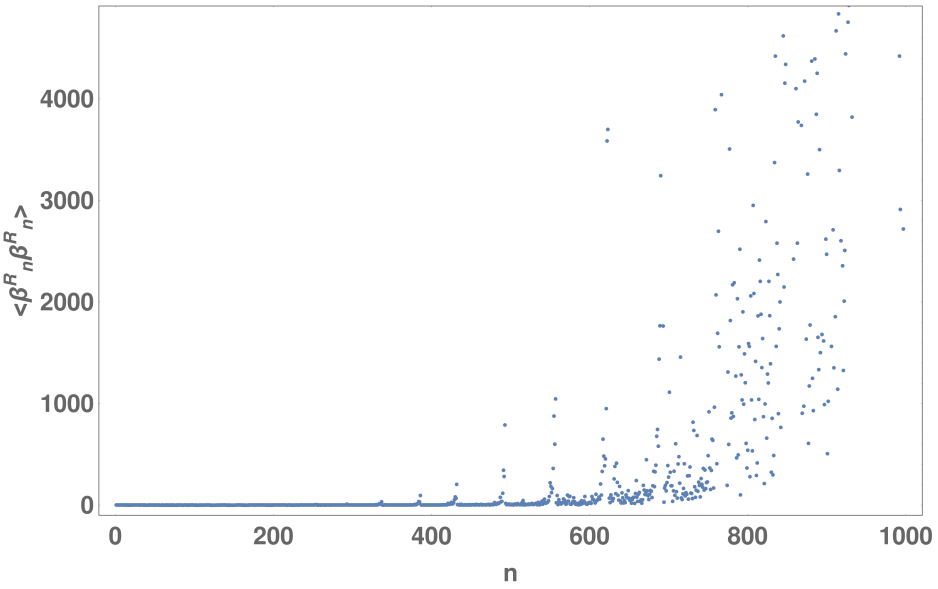

Gaussian betaR^2 avg1000 1000 6 reduced P1 Legendre tetrapyd

(a) γ_{nm} calculated on the tetrapyd, giving $\langle \beta_n^R \beta_n^R \rangle = 4000 \pm 22000$. There is no doubt that using this γ_{nm} will lead to inconsistent bispectrum estimates.

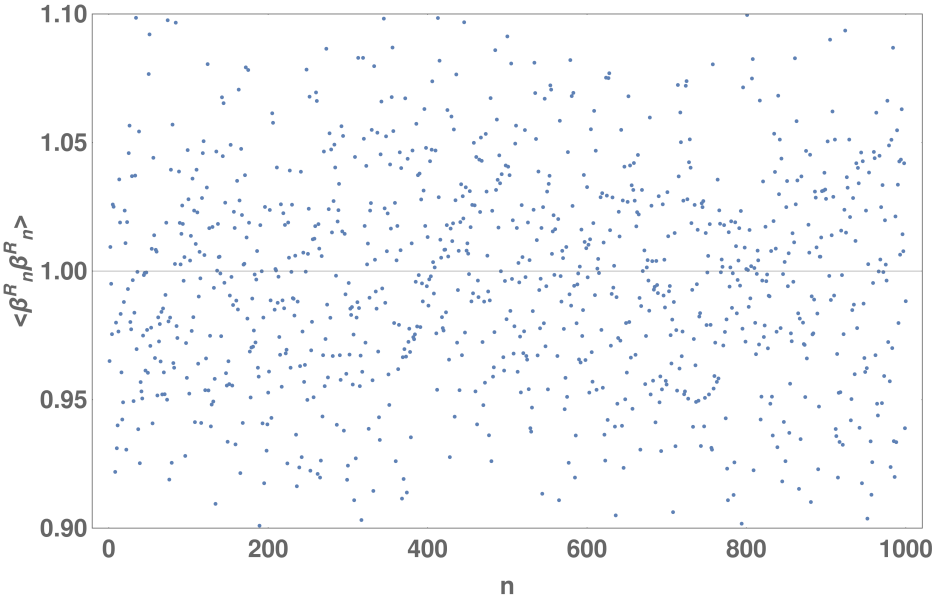

Gaussian betaR^2 avg1000 1000 6 reduced P1 Legendre fft

(b) γ_{nm} calculated with FFTs, giving $\langle \beta_n^R \beta_n^R \rangle = 0.997 \pm 0.045$. This gives the correct mean and the correct order of magnitude in error since $\frac{1}{\sqrt{1000}} \sim 3.3\%$.

Fig. 2.7 Testing the γ_{mn} matrices by checking $\langle \beta_n^R \beta_n^R \rangle = 1$.

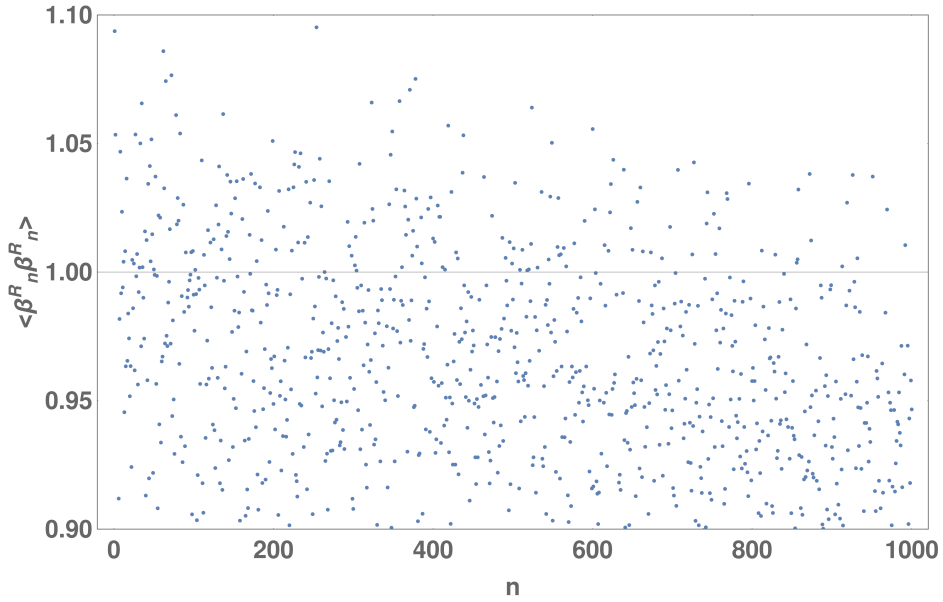

(a) 341 grid points, giving $\langle \beta_n^R \beta_n^R \rangle = 0.960 \pm 0.047$

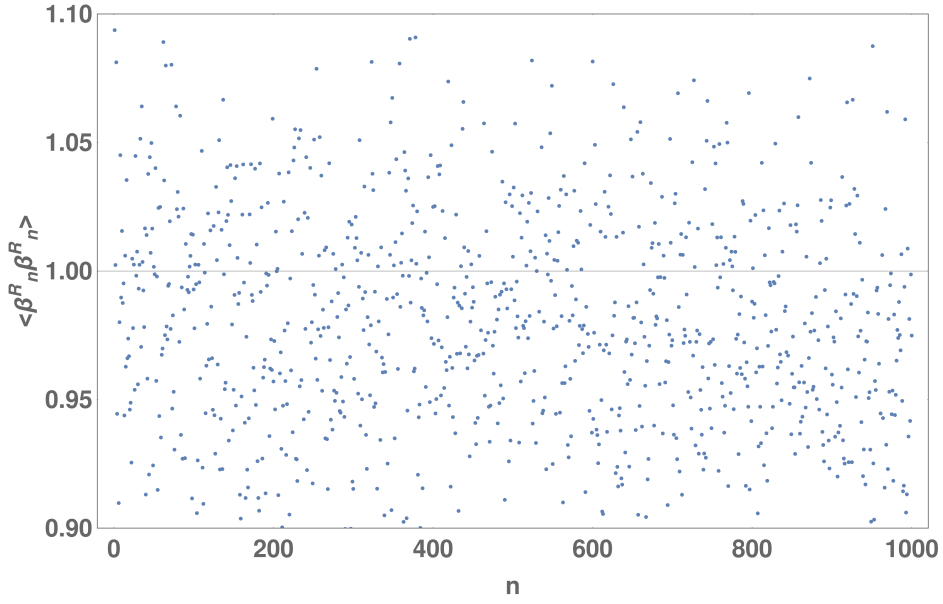

(b) 682 grid points, giving $\langle \beta_n^R \beta_n^R \rangle = 0.977 \pm 0.045$

Fig. 2.8 Checking $\langle \beta_n^R \beta_n^R \rangle = 1$ with γ_{mn} calculated on the tetrapyd with a range of grid points. *(cont.)*

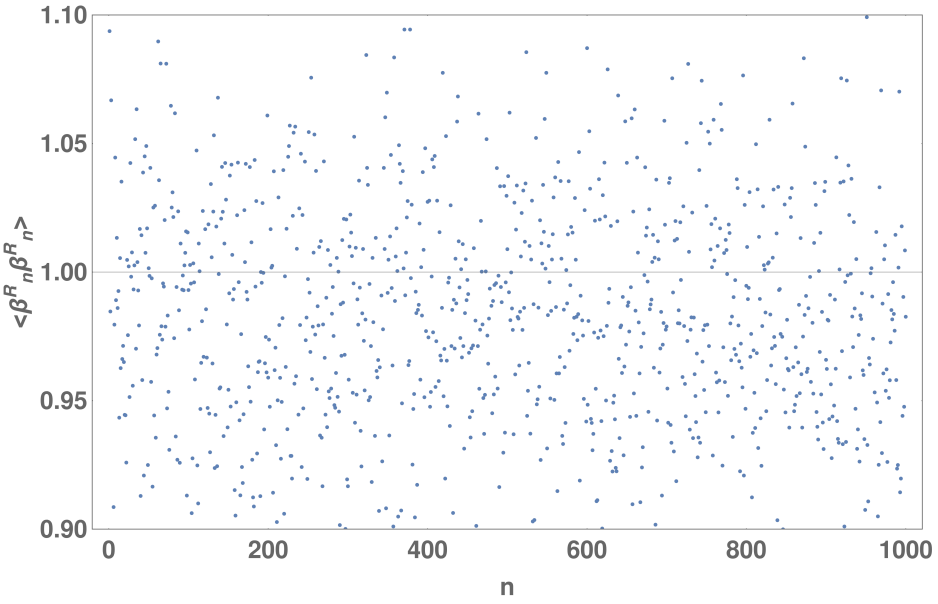

(c) 1024 grid points, giving $\langle \beta_n^R \beta_n^R \rangle = 0.981 \pm 0.045$

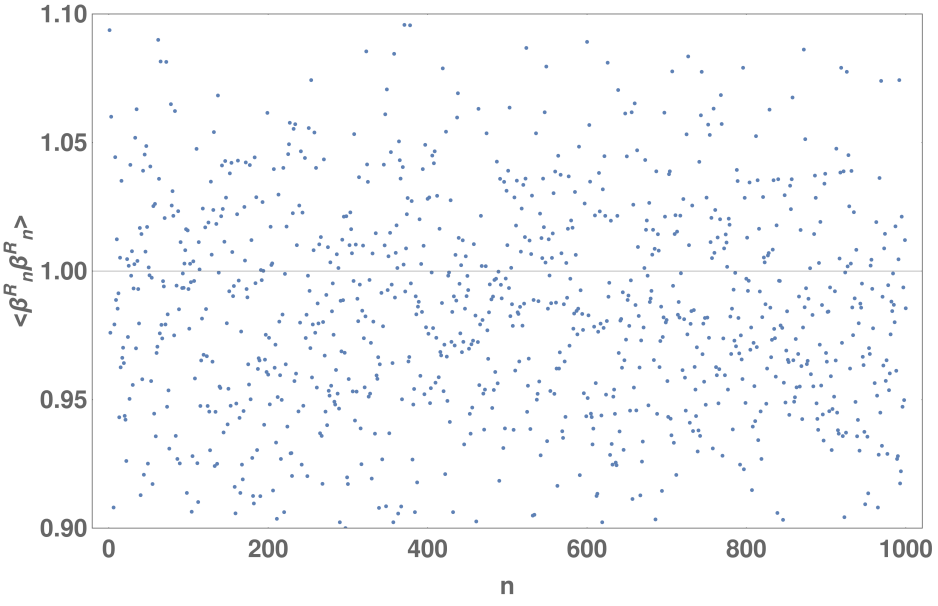

(d) 1365 grid points, giving $\langle \beta_n^R \beta_n^R \rangle = 0.983 \pm 0.045$

Fig. 2.8 Checking $\langle \beta_n^R \beta_n^R \rangle = 1$ with γ_{mn} calculated on the tetrapyd with a range of grid points.

For grid sizes up to 512^3 we can use the FFT method to calculate γ_{mn}, but for 1024^3 grids and above the computational cost becomes impractically big. For this reason we have found a way to use the tetrapyd-based γ_{nm} to deliver consistent results. This is illustrated in Figure 2.8 where we check $\langle \beta_n^R \beta_n^R \rangle = 1$ with 1024^3 FFT grids and γ_{nm} computed on the tetrapyd using different number of grid points. There is a clear improvement over the previous results based on only 41 tetrapyd grid points, but although all 4 plots are consistent with $\langle \beta_n^R \beta_n^R \rangle = 1$ a downward trend at high n can be seen in the 341 and 682 case. However when 1024 or more tetrapyd points are used this trend virtually disappears, with only a marginal improvement in using 1365 points instead of 1024. Therefore for large FFT grids we shall use the same number of tetrapyd points as the FFT grid so as not to bias the bispectrum covariance.

Finally in this section we assess the effectiveness of this procedure on a real signal, i.e. the $1280\,\mathrm{Mpc}$ GADGET-3 simulation at redshift $z = 0$ as presented in Chapter 3. With the β^R coefficients calculated up to a certain k_{max} we can reconstruct the bispectrum tetrapyd of the simulation to a lower one, and thus compare the fidelity of bispectrum estimation when different FFT grids and means of calculating γ_{mn} are used. As shown in Figure 2.9 the set of β^R coefficients from a 2048^3 grid is consistent with the others to 2% level down to $41k_F$, a very impressive result considering this accounts for $\left(\frac{41}{681}\right)^3 \sim 0.02\%$ of the total tetrapyd. It is therefore unnecessary to recalculate β^R coefficients with fewer FFT grid points, as long as we disregard the very tip of the tetrapyd where the MODAL-LSS method breaks down. We also restrict ourselves to using 256^3 grids or larger since it is clear that reliable information cannot be obtained below $41k_F$. One therefore has to carefully choose the box size of the simulation so that the physically interesting k scales are above this limit.

We conclude that discrete sampling has a different effect on direct integration compared to when FFTs are used, and to ensure internal consistency of the α and β coefficients we evaluate γ_{nm} separately by integration on the tetrapyd for α_n^Q and via FFTs for β_n^Q to rotate them into the $\{R_n\}$ basis. For large grids $N_g > \mathcal{O}(1024)$ the memory requirements of computing γ_{nm} with FFTs are too great, but we have verified that for such grids the two methods give consistent results and hence direct integration is used instead.

2.2.4 Numerical implementation

An implementation of the MODAL-LSS method has already produced some good results [162]. It has also been shown in [163] that MODAL-LSS is superior to other bispectrum estimators in terms of data compression. The code has since been completely overhauled and parallelised with OpenMP and multi-threaded FFTW for a dramatic reduction in run time, allowing us to estimate the bispectra of much larger simulations and also using more modes. We are now able to estimate the bispectrum of 2048^3 density grids with $n_{max} = \mathcal{O}(1000)$ modes in ~ 35

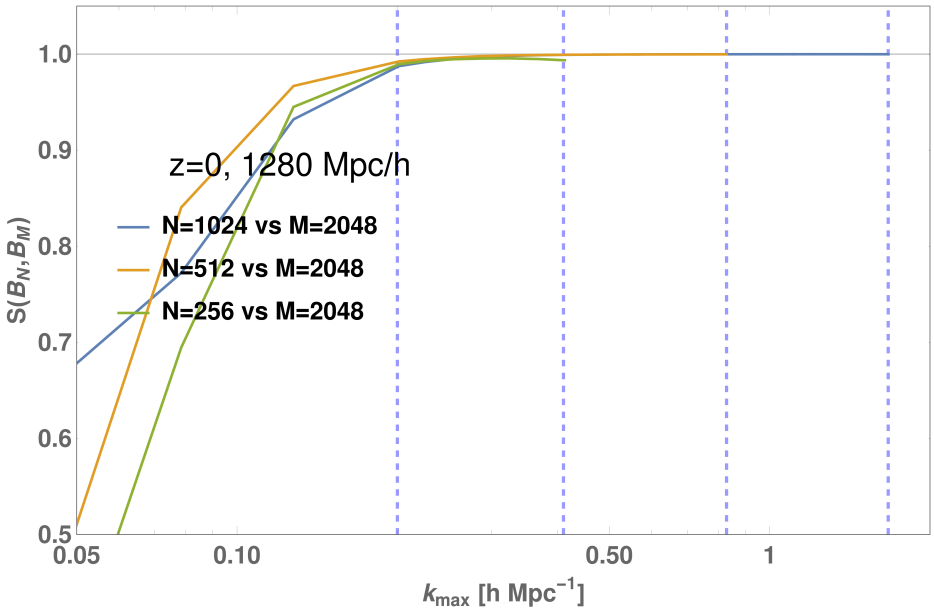

(a) Shape correlator

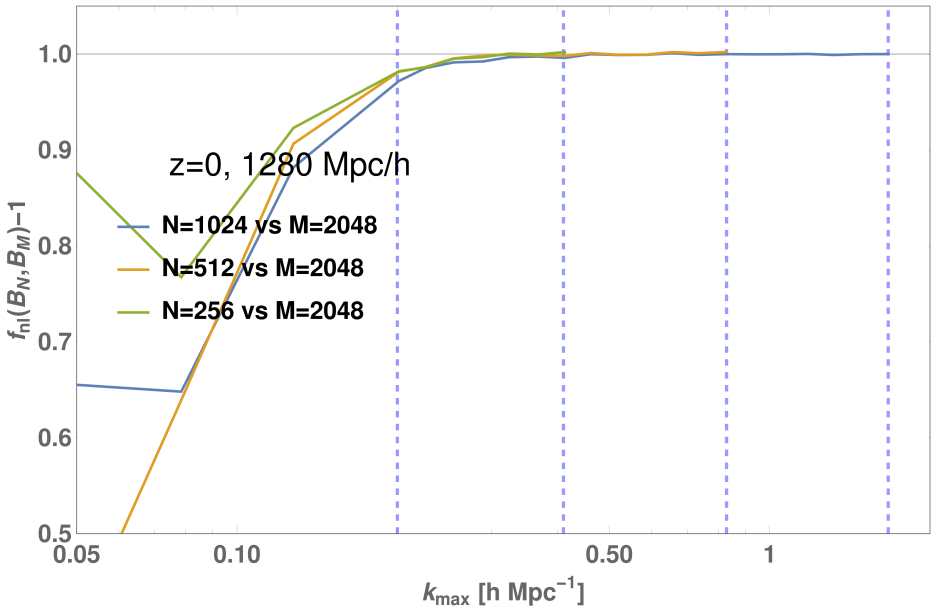

(b) f_{nl} correlator

Fig. 2.9 Correlation coefficients between β^R coefficients calculated with different k_{max}. This is achieved by reconstructing the estimated bispectrum to a lower k_{max} within the range of validity of the β^R coefficients, and calculating the correlation coefficients directly using the resulting tetrapyds. The dashed blue lines represent the cutoff frequency corresponding to 128^3, 256^3, 512^3 and 1024^3 FFT grids, i.e. $41k_F$, $84k_F$, $169k_F$ and $340k_F$ respectively.

minutes using 512 CPU-cores, a significant improvement in run time and resolution over the analysis of 512^3 grids with $n_{max} = \mathcal{O}(50)$ in [162]. We would like to emphasise that the computational costs for bispectrum estimation with MODAL-LSS scale well with the size of the density grid and is a tiny fraction of the costs of N-body runs, and thus can be included in existing pipelines with little additional cost.

Another innovation to improve the performance of MODAL-LSS is the introduction of custom modes based on the separable bispectrum shapes given in Section 1.4.4. Explicitly we split the SN-weighted versions of tree-level bispectrum (Equation (1.123)) and late-time local bispectrum (Equation (1.154)) as follows (note that $P(k)$ represents the non-linear power spectrum of choice):

- The tree-level bispectrum requires 6 custom polynomials:
  - $q_0^{\text{tree}}(k) = \sqrt{\frac{k}{P(k)}}\frac{5}{14}$
  - $q_1^{\text{tree}}(k) = \sqrt{\frac{k}{P(k)}}P(k)$
  - $q_2^{\text{tree}}(k) = -\sqrt{\frac{k}{P(k)}}P(k)k^2$
  - $q_3^{\text{tree}}(k) = \sqrt{\frac{k}{P(k)}}\frac{P(k)}{k^2}$
  - $q_4^{\text{tree}}(k) = \sqrt{\frac{k}{P(k)}}\frac{3}{14}k^2$
  - $q_5^{\text{tree}}(k) = \sqrt{\frac{k}{P(k)}}\frac{1}{14}k^4$

  which are combined into these 4 modes:

  - $Q_0^{\text{tree}} = q_{\{1}(x)q_1(y)q_{0\}}(z)$
  - $Q_1^{\text{tree}} = q_{\{2}(x)q_3(y)q_{0\}}(z)$
  - $Q_2^{\text{tree}} = q_{\{1}(x)q_3(y)q_{4\}}(z)$
  - $Q_3^{\text{tree}} = q_{\{3}(x)q_3(y)q_{5\}}(z)$
- The late-time local bispectrum requires 2 custom polynomials:
  - $q_0^{\text{local,late}}(k) = \sqrt{\frac{k}{P(k)}}\sqrt{P_{\text{lin}}(k)}k^{n_s/2-2}$
  - $q_1^{\text{local,late}}(k) = \sqrt{\frac{k}{P(k)}}\sqrt{P_{\text{lin}}(k)}k^{2-n_s/2}$

  resulting in a single mode:

  - $Q_0^{\text{local,late}} = q_{\{0}(x)q_0(y)q_{1\}}(z)$

The inclusion of the constant shape (Equation (1.155)) is automatic due to the presence of Q_0 in the canonical polynomial basis. These custom modes help pick up general features in the matter bispectra, which combined with the Q_n functions ensures an effective reconstruction of any dark matter bispectrum signal.

We conclude this section by assessing the accuracy of the `MODAL-LSS` expansion. This is only possible with theoretical bispectra where we know the true answer since statistical noise will always be present in simulations. We have however made comprehensive tests of the `MODAL-LSS` algorithm for estimating bispectrum of density fields, detailed above in Section 2.2.3. A qualitative comparison is illustrated in Figures 2.10 and 2.11 where we plot the theoretical and reconstructed bispectra as well as the residuals between them different k_{max}. Quantitatively we evaluate both the shape and total correlator between a theoretical bispectrum B^{th} and its `MODAL-LSS` counterpart $\sum_n \alpha_n^R B_n^R$, where

$$B_n^R(k_1,k_2,k_3) = \sqrt{\frac{P(k_1)P(k_2)P(k_3)}{k_1k_2k_3}} R_n(k_1/k_{max}, k_2/k_{max}, k_3/k_{max}). \tag{2.54}$$

Using Equations (2.24) and (2.26) we find that

$$\begin{aligned} \mathcal{S}_{\alpha,th} &\equiv \mathcal{S}(\sum_n \alpha_n^R B_n^R, B^{th}) = \sqrt{\frac{\sum_n (\alpha_n^R)^2}{\left[B^{th}, B^{th}\right]}}, \\ \mathcal{T}_{\alpha,th} &\equiv \mathcal{T}(\sum_n \alpha_n^R B_n^R, B^{th}) = 1 - \sqrt{1 - \frac{\sum_n (\alpha_n^R)^2}{\left[B^{th}, B^{th}\right]}}, \end{aligned} \tag{2.55}$$

where we have used the orthonormality of the R_n basis functions to obtain[3] $\left[\sum_n \alpha_n^R B_n^R, B^{th}\right] = \sum_n (\alpha_n^R)^2$.

We tested `MODAL-LSS` with a range of bispectrum shapes, including the tree-level bispectrum (Equation (1.157)), nine-parameter model (Equation (1.145)) and the 3-shape model (Equation (1.156)), at different k_{max} and number of modes up to $n_{max} = 1000$ (Table 2.1). `MODAL-LSS` is able to reconstruct all bispectrum shapes with $\mathcal{T}_{\alpha,th} > 99\%$ at different k-ranges, and improvements can certainly be made by using more modes. This result justifies our decision to take the approximation in Equation (2.33) to be exact. This also gives us confidence that `MODAL-LSS` can very accurately estimate simulation and observational bispectra. The computational cost of `MODAL-LSS` is estimated by the CPU-minutes used when reconstructing the various bispectrum. The code for reconstructing theoretical bispectra is parallelised with hybrid `MPI-OpenMP` but the tests here were ran with pure `OpenMP` and 1

[3] Note that in principle $B^{th} = \sum_n^\infty \alpha_n^R B_n^R$.

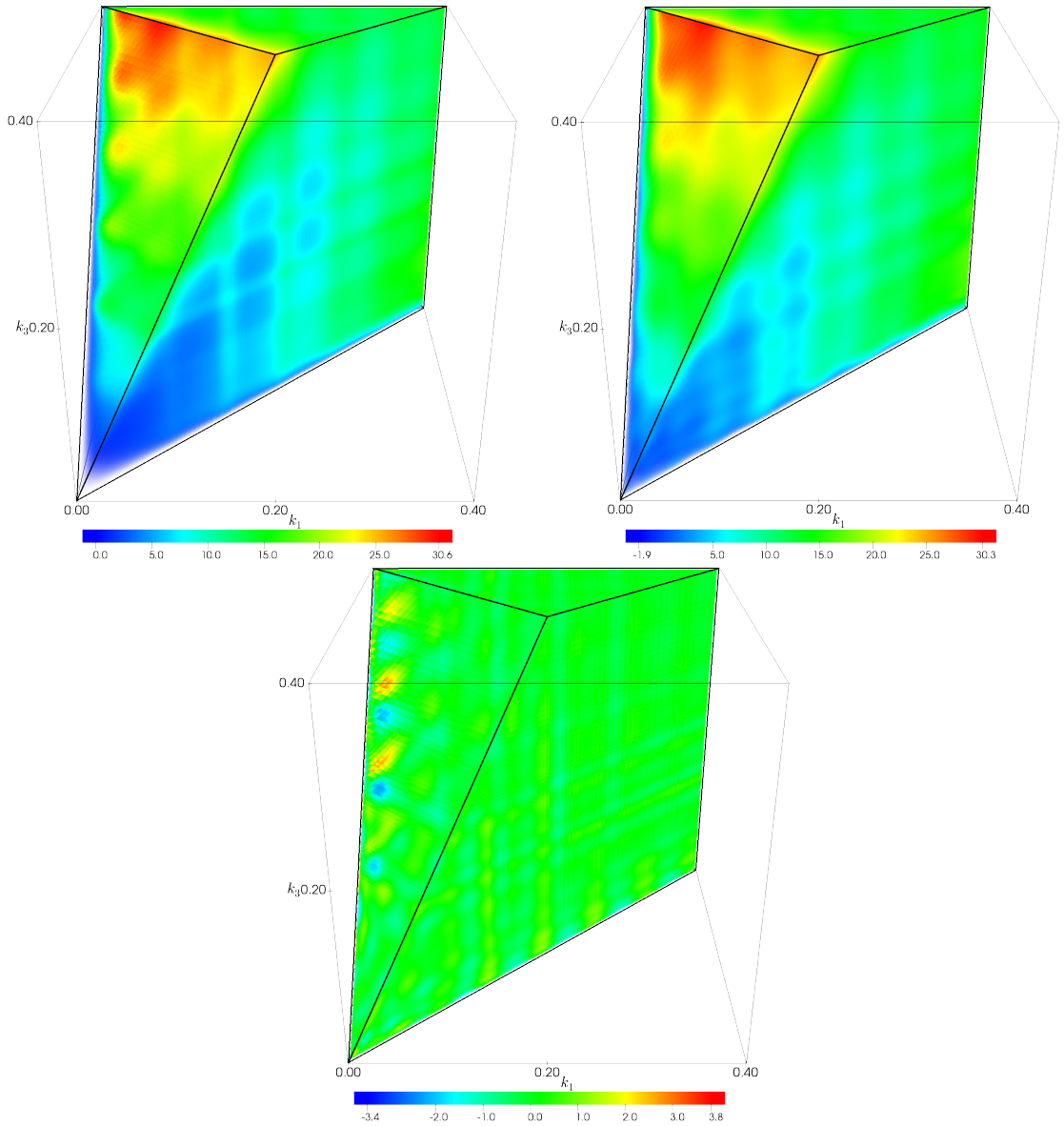

Fig. 2.10 The nine-parameter up to $k_{max} = 0.4\,h\,\mathrm{Mpc}^{-1}$ by direct calculation (top left), its reconstruction by MODAL-LSS with 1000 modes (top right) and the residuals between them (bottom). Note the change of scale in the colour bars.

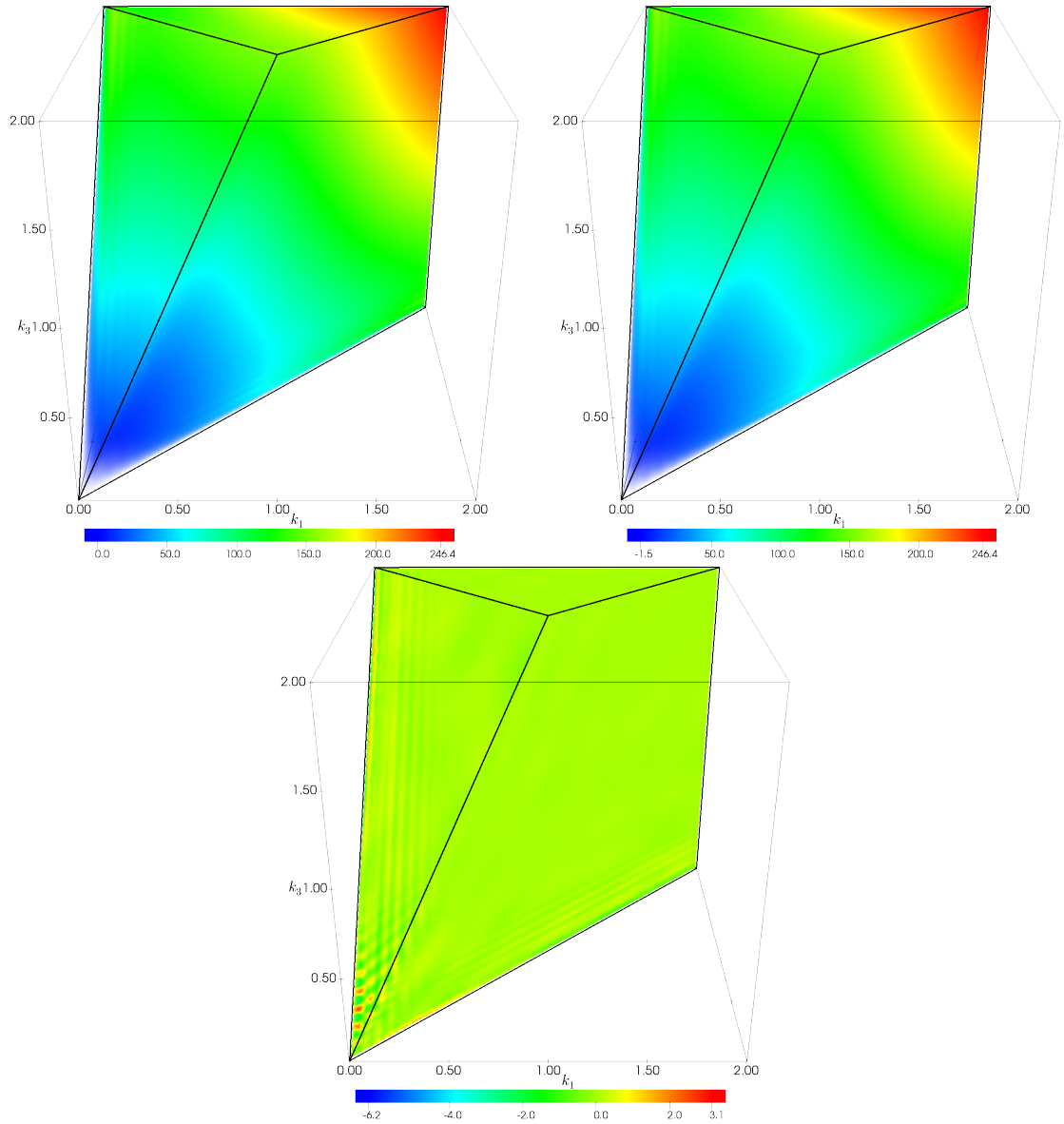

Fig. 2.11 The 3-shape model up to $k_{max} = 2.0h\text{Mpc}^{-1}$ by direct calculation (top left), its reconstruction by `MODAL-LSS` with 1000 modes (top right) and the residuals between them (bottom). Note the change of scale in the colour bars.

Bispectrum shape	n_{max}	$k_{max} = 0.4\,h\mathrm{Mpc}^{-1}$		$k_{max} = 2.0\,h\mathrm{Mpc}^{-1}$		Computational cost
		$1-\mathcal{S}_{\alpha,th}$	$1-\mathcal{T}_{\alpha,th}$	$1-\mathcal{S}_{\alpha,th}$	$1-\mathcal{T}_{\alpha,th}$	(CPU-minutes)
Tree-level bispectrum	50*	6.7×10^{-4}	3.6×10^{-2}	1.3×10^{-3}	5.1×10^{-2}	160
	10	0	0	0	0	90
	50	0	0	0	0	160
	200	0	0	0	0	370
	1000	0	0	0	0	1600
Nine-parameter model	50*	6.6×10^{-4}	3.6×10^{-2}	-	-	450
	10	3.3×10^{-4}	2.6×10^{-2}	-	-	390
	50	2.2×10^{-4}	2.1×10^{-2}	-	-	450
	200	7.9×10^{-5}	1.3×10^{-2}	-	-	660
	1000	2.2×10^{-5}	6.7×10^{-3}	-	-	1870
3-shape model	50*	3.5×10^{-4}	2.6×10^{-2}	5.6×10^{-5}	1.1×10^{-2}	190
	10	5.8×10^{-4}	3.4×10^{-2}	3.8×10^{-4}	2.8×10^{-2}	120
	50	1.1×10^{-4}	1.5×10^{-2}	6.0×10^{-5}	1.1×10^{-2}	190
	200	1.6×10^{-5}	5.7×10^{-3}	1.2×10^{-5}	4.9×10^{-3}	400
	1000	0	0	0	0	1610

Table 2.1 The performance of MODAL-LSS at reconstructing different theoretical bispectrum shapes at different k_{max} while varying the number of modes used in the reconstruction. *(caption cont. next page)*

Table 2.1 50* indicates only shifted Legendre polynomials and no custom modes were used, highlighting the strength of the custom modes in capturing desired bispectrum signals. We use the shape $\mathcal{S}_{\alpha,th}$ and total correlator $\mathcal{T}_{\alpha,th}$ introduced in Equation (2.55) to assess the accuracy of the reconstructed bispectra. It is clear that the total correlator is a much more stringent test than the shape correlator. With 1000 modes we obtain $\mathcal{T}_{\alpha,th} > 0.99$ in all cases, giving us high confidence in the validity of the `MODAL-LSS` expansion. Note that we omit the nine-parameter model at $k_{max} = 2.0\,h\,\mathrm{Mpc}^{-1}$ since it is ill-defined at such non-linear scales. We give the computational cost of the method by the CPU-minutes required to reconstruct the theoretical bispectra on a 2048^3 grid in pure `OpenMP` mode. It demonstrates better than linear scaling with n_{max} which shows the highly optimised nature of the code. The performance also scales with N_{grid}^3, where N_{grid} is the number of grid points, and will therefore run much faster for analyses that do not require such high resolution.

thread per CPU core. Note that this may not be the optimal number of threads and further reductions in run time may be possible.

2.3 Sources of error in bispectrum estimation

In order to make meaningful comparisons between simulation/observational data with theoretical predictions one must have a thorough understanding of the errors that occur in our measurements. Since the main focus of this thesis is on simulations we will not discuss observational effects such as survey geometry and redshift-space distortions (RSD). The main contributions we consider here are Poisson shot noise, covariance of the `MODAL-LSS` estimator, and aliasing due to the use of FFTs, all of which are relevant for the analysis of observational data in the future.

2.3.1 Shot noise

Since dark matter halos and galaxies are discrete tracers of their respective density fields, measurements of their statistics are biased relative to the true values that are of interest to us. This is known as *Poisson shot noise* as the distribution of the objects is modelled as a Poisson sampling process. This effect is well known for the power spectrum and bispectrum, and we quote here the relationships between the statistics of the discrete sample and the underlying continuous field:

$$P_n(k) = P(k) + \frac{1}{\bar{n}} \tag{2.56}$$

$$B_n(k_1,k_2,k_3) = B(k_1,k_2,k_3) + \frac{1}{\bar{n}}[P(k_1)+P(k_2)+P(k_3)] + \frac{1}{\bar{n}^2}, \tag{2.57}$$

where the subscript n denotes the discrete number density and $\bar{n}$ is the mean number density of the sample. The derivation of these expressions is as follows.

Following [164 (Sections 36,41,43), 112 (Chapter 7), 165] we divide our simulation box or survey area into infinitesimal volume elements δV_i, each of which is centred at $\mathbf{r}_i$ and contains n_i objects. We take δV_i to be sufficiently small such that the probability that a cell contains an object is $P(n_i = 1) = \bar{n}[1 + \delta(\mathbf{r}_i)]\delta V_i$ where $\bar{n}$ is the mean occupation and $\delta(\mathbf{r}_i)$ is the density contrast at $\mathbf{r}_i$, whereas the probability that it contains multiple objects is infinitesimally small. The probability of no object being enclosed is therefore $P_0 = 1 - \bar{n}[1 + \delta(\mathbf{r}_i)]\delta V_i$. This is a Bernoulli distribution, and it can be shown that in the limit $\delta V_i \to 0$ the probability distribution of n_i takes the form of the Poisson distribution [166]. The moments of n_i are given by $\langle n_i \rangle = \langle n_i^2 \rangle = \langle n_i^3 \rangle = \cdots = \bar{n}\delta V_i$ to first order in δV_i.

We calculate the two-point correlation between different cells as outlined in [164 (Section 31)]. The joint probability that two volume elements δV_i and δV_j both contain an object is given by $\bar{n}^2 \delta V_i \delta V_j [1 + \langle \delta(\mathbf{r}_i)\delta(\mathbf{r}_j) \rangle]$ and therefore

$$\langle n_i n_j \rangle_{i \neq j} = \bar{n}^2 \delta V_i \delta V_j \left[1 + \langle \delta(\mathbf{r}_i)\delta(\mathbf{r}_j) \rangle\right]. \tag{2.58}$$

Let us now take the limit of infinitesimal small volume elements $\delta V_i \to 0$ such that $n_i / \delta V_i \to n(\mathbf{r}_i) = \sum_j \delta^D(\mathbf{r}_i - \mathbf{r}_j)$. Consider then the expression

$$\begin{aligned}
\sum_{i,j} \langle n_i n_j \rangle &= \sum_{i \neq j} \langle n_i n_j \rangle + \sum_i \langle n_i^2 \rangle \\
&= \sum_{i \neq j} \bar{n}^2 \delta V_i \delta V_j \left[1 + \langle \delta(\mathbf{r}_i)\delta(\mathbf{r}_j) \rangle\right] + \sum_i \bar{n}\delta V_i \\
&\to \int d^3 r \int d^3 r' \, \bar{n}^2 \left[1 + \langle \delta(\mathbf{r})\delta(\mathbf{r}') \rangle\right] + \int d^3 r \, \bar{n} \\
&= \int d^3 r \int d^3 r' \left\{ \bar{n}^2 \left[1 + \langle \delta(\mathbf{r})\delta(\mathbf{r}') \rangle\right] + \bar{n}\, \delta^D(\mathbf{r} - \mathbf{r}') \right\}.
\end{aligned} \tag{2.59}$$

Since $\sum_{i,j} \langle n_i n_j \rangle \to \int d^3 r \int d^3 r' \, \langle n(\mathbf{r}) n(\mathbf{r}') \rangle$ also we deduce the following relationship between the two-point correlators of the discrete number density and the underlying density contrast:

$$\langle n(\mathbf{r}) n(\mathbf{r}') \rangle = \bar{n}^2 \left[1 + \langle \delta(\mathbf{r})\delta(\mathbf{r}') \rangle\right] + \bar{n}\, \delta^D(\mathbf{r} - \mathbf{r}'). \tag{2.60}$$

The second term on the right hand side arises due to the self-correlations of the particles, and is the origin of the Poisson shot noise that is made manifest through the discrete sampling of the true density field. Finally to compute the shot noise contribution to the power spectrum of the discrete sample we first substitute the discrete density contrast $\delta_n(\mathbf{r}) = (n(\mathbf{r}) - \bar{n})/\bar{n}$

into Equation (2.60):

$$\left\langle \delta_n(\mathbf{r})\delta_n(\mathbf{r}')\right\rangle = \left\langle \delta(\mathbf{r})\delta(\mathbf{r}')\right\rangle + \frac{\delta^D(\mathbf{r}-\mathbf{r}')}{\bar{n}}, \tag{2.61}$$

and then take the Fourier transform to yield

$$\left\langle \delta_n(\mathbf{k})\delta_n(\mathbf{k}')\right\rangle = \left\langle \delta(\mathbf{k})\delta(\mathbf{k}')\right\rangle + \frac{(2\pi)^3}{\bar{n}}\delta^D(\mathbf{k}+\mathbf{k}'). \tag{2.62}$$

By using the definition of the power spectrum (Equation (1.90)) we conclude that

$$P_n(k) = P(k) + \frac{1}{\bar{n}}, \tag{2.63}$$

i.e. the power spectrum of a discrete sample $P_n(k)$ is a sum of the true power spectrum $P(k)$ and shot noise. An increase in the number density of the sample leads to a higher density of discrete tracers of the density field, which expectedly lowers the shot noise contribution.

The extension to the three-point correlation function is straightforward. Analogous to the result above, the three-point correlator of n_i has the same expression as the probability that three disjoint volume elements δV_i, δV_j and δV_k all contain an object, and hence takes the form

$$\begin{aligned}&\left\langle n_i n_j n_k\right\rangle_{i\neq j\neq k}\\ &= \bar{n}^3\delta V_i\delta V_j\delta V_k\big[1+\left\langle \delta(\mathbf{r}_i)\delta(\mathbf{r}_j)\right\rangle + \left\langle \delta(\mathbf{r}_j)\delta(\mathbf{r}_k)\right\rangle + \left\langle \delta(\mathbf{r}_k)\delta(\mathbf{r}_i)\right\rangle\\ &\qquad + \left\langle \delta(\mathbf{r}_i)\delta(\mathbf{r}_j)\delta(\mathbf{r}_k)\right\rangle\big].\end{aligned} \tag{2.64}$$

Taking the limit $\delta V_i \to 0$ we derive a similar expression relating the three-point correlators of $n(\mathbf{r})$ and $\delta(\mathbf{r})$:

$$
\begin{aligned}
&\sum_{i,j,k} \langle n_i n_j n_k \rangle \\
&= \sum_{i\neq j\neq k} \langle n_i n_j n_k \rangle + \left(\sum_{i\neq k} \langle n_i^2 n_k \rangle + 2\,\text{perms.} \right) + \sum_i \langle n_i^3 \rangle \\
&= \sum_{i\neq j\neq k} \bar{n}^3 \delta V_i \delta V_j \delta V_k \big[1 + \big\langle \delta(\mathbf{r}_i)\delta(\mathbf{r}_j) \big\rangle + \big\langle \delta(\mathbf{r}_j)\delta(\mathbf{r}_k) \big\rangle + \langle \delta(\mathbf{r}_k)\delta(\mathbf{r}_i) \rangle \\
&\qquad\qquad + \big\langle \delta(\mathbf{r}_i)\delta(\mathbf{r}_j)\delta(\mathbf{r}_k) \big\rangle \big] \\
&\quad + \left(\sum_{i\neq k} \bar{n}^2 \delta V_i \delta V_k \left[1 + \langle \delta(\mathbf{r}_i)\delta(\mathbf{r}_k) \rangle \right] + 2\,\text{perms.} \right) + \sum_i \bar{n} \delta V_i \\
&\to \int d^3 r_1 \int d^3 r_2 \int d^3 r_3\, \bar{n}^3 \big[1 + \langle \delta(\mathbf{r}_1)\delta(\mathbf{r}_2) \rangle + \langle \delta(\mathbf{r}_2)\delta(\mathbf{r}_3) \rangle + \langle \delta(\mathbf{r}_3)\delta(\mathbf{r}_1) \rangle \\
&\qquad\qquad + \langle \delta(\mathbf{r}_1)\delta(\mathbf{r}_2)\delta(\mathbf{r}_3) \rangle \big] \\
&\quad + \left(\int d^3 r_1 \int d^3 r_2\, \bar{n}^2 \left[1 + \langle \delta(\mathbf{r}_1)\delta(\mathbf{r}_2) \rangle \right] + 2\,\text{perms.} \right) + \int d^3 r\, \bar{n} \\
&= \int d^3 r_1 \int d^3 r_2 \int d^3 r_3 \Big\{ \bar{n}^3 \big[1 + \langle \delta(\mathbf{r}_1)\delta(\mathbf{r}_2) \rangle + \langle \delta(\mathbf{r}_2)\delta(\mathbf{r}_3) \rangle + \langle \delta(\mathbf{r}_3)\delta(\mathbf{r}_1) \rangle \\
&\qquad\qquad + \langle \delta(\mathbf{r}_1)\delta(\mathbf{r}_2)\delta(\mathbf{r}_3) \rangle \big] \\
&\quad + \Big(\bar{n}^2 \left[1 + \langle \delta(\mathbf{r}_1)\delta(\mathbf{r}_2) \rangle \right] \delta^D(\mathbf{r}_1 - \mathbf{r}_3) + 2\,\text{perms.} \Big) + \bar{n}\, \delta^D(\mathbf{r}_1 - \mathbf{r}_2) \delta^D(\mathbf{r}_1 - \mathbf{r}_3) \Big\},
\end{aligned}
\tag{2.65}
$$

where from the second line to the third we used the fact that $n_i n_k$ and $n_i^2 n_k$ have the same probability distribution, giving

$$
\begin{aligned}
\langle n(\mathbf{r}_1) n(\mathbf{r}_2) n(\mathbf{r}_3) \rangle = \bar{n}^3 \big[& 1 + \langle \delta(\mathbf{r}_1)\delta(\mathbf{r}_2) \rangle + \langle \delta(\mathbf{r}_2)\delta(\mathbf{r}_3) \rangle + \langle \delta(\mathbf{r}_3)\delta(\mathbf{r}_1) \rangle \\
& + \langle \delta(\mathbf{r}_1)\delta(\mathbf{r}_2)\delta(\mathbf{r}_3) \rangle \big] \\
& + \Big(\bar{n}^2 \left[1 + \langle \delta(\mathbf{r}_1)\delta(\mathbf{r}_2) \rangle \right] \delta^D(\mathbf{r}_1 - \mathbf{r}_3) + 2\,\text{perms.} \Big) \\
& + \bar{n}\, \delta^D(\mathbf{r}_1 - \mathbf{r}_2) \delta^D(\mathbf{r}_1 - \mathbf{r}_3).
\end{aligned}
\tag{2.66}
$$

Substituting $\delta_n(\mathbf{r})$ into Equation (2.66), with the aid of Equation (2.61) to make appropriate cancellations, yields

$$\langle\delta_n(\mathbf{r}_1)\delta_n(\mathbf{r}_2)\delta_n(\mathbf{r}_3)\rangle = \langle\delta(\mathbf{r}_1)\delta(\mathbf{r}_2)\delta(\mathbf{r}_3)\rangle + \left(\frac{1}{\bar{n}}\delta^D(\mathbf{r}_1-\mathbf{r}_3)\langle\delta(\mathbf{r}_1)\delta(\mathbf{r}_2)\rangle + 2\,\text{perms.}\right) + \frac{1}{\bar{n}^2}\delta^D(\mathbf{r}_1-\mathbf{r}_2)\delta^D(\mathbf{r}_1-\mathbf{r}_3). \tag{2.67}$$

Converting this to Fourier space we obtain

$$\langle\delta_n(\mathbf{k}_1)\delta_n(\mathbf{k}_2)\delta_n(\mathbf{k}_3)\rangle = \langle\delta(\mathbf{k}_1)\delta(\mathbf{k}_2)\delta(\mathbf{k}_3)\rangle + \left(\frac{1}{\bar{n}}\langle\delta(\mathbf{k}_1+\mathbf{k}_3)\delta(\mathbf{k}_2)\rangle + 2\,\text{perms.}\right) + \frac{1}{\bar{n}^2}\delta^D(\mathbf{k}_1+\mathbf{k}_2+\mathbf{k}_3). \tag{2.68}$$

Finally when combined with both the definition of the power spectrum Equation (1.90) and the bispectrum Equation (1.92) we obtain the bispectrum of a discrete set of objects:

$$B_n(k_1,k_2,k_3) = B(k_1,k_2,k_3) + \frac{1}{\bar{n}}\Big\{P(k_1)+P(k_2)+P(k_3)\Big\} + \frac{1}{\bar{n}^2}. \tag{2.69}$$

2.3.2 Covariance of estimators

The analysis of statistical properties of cosmological fields involve the use of estimators $\hat{X}(\theta)$, where θ denotes parameters such as the wavenumber k in the case of the matter power spectrum and bispectrum. We require these estimators to be unbiased such that its ensemble average returns the population mean: $\langle\hat{X}(\theta)\rangle = \bar{X}(\theta)$. The estimator is a physical measurement and cannot be error free. In an experiment we would make multiple measurements to estimate and reduce the random error associated with our measurement process; and in cosmological contexts it is necessary for us to estimate the error of our estimators through the use of many different simulation realisations. The variance of an estimator is given by its covariance matrix C_X which can be written schematically as:

$$C_X \equiv \text{cov}(\hat{X}(\theta),\hat{X}(\theta')) = \left\langle\hat{X}(\theta)\hat{X}(\theta')\right\rangle - \left\langle\hat{X}(\theta)\right\rangle\left\langle\hat{X}(\theta')\right\rangle. \tag{2.70}$$

In addition to calculating covariance matrices numerically through simulations we also need a framework to calculate them (semi-)analytically as a consistency check.

Power spectrum covariance We first give a brief introduction to matter power spectrum estimation and the calculation of its covariance as this has been widely discussed in the literature [112 (Appendix F), 167, 168]. This will prepare us for the discussion on the bispectrum covariance later. Consider for example estimating the power spectrum by binning it in k-space and averaging over all modes within each bin [167, 169]:

$$\hat{P}(k) = \frac{k_F^3}{(2\pi)^3} \int_{\Delta k} \frac{d^3p}{V_s(k)} |\delta(\mathbf{p})|^2 , \tag{2.71}$$

where $k_F = 2\pi/L = (1/\delta^D(\mathbf{0}))^{1/3}$ (see Equation (2.13)) is the fundamental frequency of the simulation box of length L, and the integral is performed over all modes that lie in the spherical shell $|\mathbf{p}-k| \leq \Delta k/2$ which has width Δk. The normalisation factor V_s is the volume of the shell: $V_s = \int_{\Delta k} d^3p = 4\pi k^2 \Delta k + \pi(\Delta k)^3/3$. This estimator is unbiased because

$$\begin{aligned}
\left\langle \hat{P}(k) \right\rangle &= \frac{k_F^3}{(2\pi)^3} \int_{\Delta k} \frac{d^3p}{V_s(k)} \left\langle |\delta(\mathbf{p})|^2 \right\rangle \\
&= \frac{k_F^3}{(2\pi)^3} \left\langle |\delta(k)|^2 \right\rangle \\
&= \frac{k_F^3}{(2\pi)^3} (2\pi)^3 \delta(\mathbf{0}) P(k) \\
&= P(k).
\end{aligned} \tag{2.72}$$

The covariance matrix for this estimator is

$$\begin{aligned}
C_P(k,k') &= \frac{k_F^6}{(2\pi)^6} \int_{\Delta k} \frac{d^3p}{V_s(k)} \int_{\Delta k'} \frac{d^3q}{V_s(k')} \left\langle \delta_p^* \delta_p \delta_q^* \delta_q \right\rangle - P(k)P(k') \\
&= \frac{2k_F^3}{V_s(k)} P^2(k) \delta_{k,k'} + \frac{k_F^6}{(2\pi)^6} \int_{\Delta k} \frac{d^3p}{V_s(k)} \int_{\Delta k'} \frac{d^3q}{V_s(k')} \left\langle \delta_p^* \delta_p \delta_q^* \delta_q \right\rangle_c , \\
&= \frac{2k_F^3}{V_s(k)} P^2(k) \delta_{k,k'} + \frac{k_F^3}{(2\pi)^3} \int_{\Delta k} \frac{d^3p}{V_s(k)} \int_{\Delta k'} \frac{d^3q}{V_s(k')} T(\mathbf{p}, -\mathbf{p}, \mathbf{q}, -\mathbf{q}),
\end{aligned} \tag{2.73}$$

where we have expanded the four-point correlator in terms of its connected pieces[4]:

$$\left\langle \delta_p^* \delta_p \delta_q^* \delta_q \right\rangle = \left\langle \delta_p^* \delta_p \right\rangle \left\langle \delta_q^* \delta_q \right\rangle + \left\langle \delta_p^* \delta_q^* \right\rangle \left\langle \delta_p \delta_q \right\rangle + \left\langle \delta_p^* \delta_q \right\rangle \left\langle \delta_q^* \delta_p \right\rangle + \left\langle \delta_p^* \delta_p \delta_q^* \delta_q \right\rangle_c , \tag{2.74}$$

and the trispectrum T is defined by $\langle \delta(\mathbf{k}_1)\delta(\mathbf{k}_2)\delta(\mathbf{k}_3)\delta(\mathbf{k}_4) \rangle_c = (2\pi)^3 \delta_D(\mathbf{k}_1 + \mathbf{k}_2 + \mathbf{k}_3 + \mathbf{k}_4) T(\mathbf{k}_1, \mathbf{k}_2, \mathbf{k}_3, \mathbf{k}_4)$. The subscript c denotes a *connected* correlator which cannot be further expanded with Wick's theorem. Connected n-point correlators with $n > 2$ vanish if δ is

[4] Other contributions vanish since $\langle \delta \rangle = 0$ by definition.

a Gaussian field, but e.g. gravitational evolution induces mode coupling and hence non-Gaussianity in the form of higher order correlators.

The first term in Equation (2.73) is the *Gaussian* contribution to the power spectrum covariance and can be estimated with $\hat{P}$; the Kronecker delta $\delta_{k,k'}$ enforces the diagonality of the Gaussian covariance. The trispectrum term is the non-Gaussian covariance which is non-trivial to estimate directly from simulations or calculate theoretically. Crucially the non-Gaussian covariance does not scale inversely with the number of modes in each bin unlike the Gaussian covariance [167, 168]; this also applies to the bispectrum. However they both scale inversely with the simulation box size through k_F^3, and clearly can both be suppressed by averaging over different simulation realisations.

Covariance of the `MODAL-LSS` estimator Now we turn our attention to the covariance of the `MODAL-LSS` bispectrum estimator (Equation (2.41)), which is unbiased because

$$\begin{aligned}
&\sqrt{\frac{k_1k_2k_3}{P(k_1)P(k_2)P(k_3)}}\left\langle \hat{B}_\delta(k_1,k_2,k_3)\right\rangle \\
&= \sum_n^{n_{max}} \left\langle \tilde{\beta}_n^Q \right\rangle Q_n(k_1/k_{max}, k_2/k_{max}, k_3/k_{max}) \\
&= \sum_n^{n_{max}} \alpha_n^Q Q_n(k_1/k_{max}, k_2/k_{max}, k_3/k_{max}), \\
&= \sqrt{\frac{k_1k_2k_3}{P(k_1)P(k_2)P(k_3)}} B_\delta(k_1,k_2,k_3).
\end{aligned} \tag{2.75}$$

The covariance of $\hat{B}_\delta$, C_B, is given by:

$$\begin{aligned}
&C_B(k_1,k_2,k_3,k_1',k_2',k_3') \\
&= \sqrt{\frac{P_1P_2P_3P_1'P_2'P_3'}{k_1k_2k_3k_1'k_2'k_3'}} \sum_{mn}^{n_{max}} \left\langle \tilde{\beta}_m^Q \tilde{\beta}_n^Q \right\rangle Q_m Q_n' \\
&\quad - B(k_1,k_2,k_3)B(k_1',k_2',k_3') \\
&= \sqrt{\frac{P_1P_2P_3P_1'P_2'P_3'}{k_1k_2k_3k_1'k_2'k_3'}} \sum_{mnop}^{n_{max}} (\gamma^{-1})_{om}(\gamma^{-1})_{pn} \left\langle \beta_m^Q \beta_n^Q \right\rangle Q_o Q_p' \\
&\quad - B(k_1,k_2,k_3)B(k_1',k_2',k_3'),
\end{aligned} \tag{2.76}$$

where $P_1 = P(k_1)$ etc., and the arguments of the Q_n basis functions have been suppressed for brevity. We have also used Equation (2.45) to convert from $\tilde{\beta}_n^Q$ to β_n^Q. In order to evaluate

$\left\langle \beta_m^Q \beta_n^Q \right\rangle$ we write β_n^Q as follows using Equation (2.37):

$$\begin{aligned}\beta_n^Q &= (2\pi)^6 \int_{\mathbf{k}_1,\mathbf{k}_2,\mathbf{k}_3} \frac{\delta_{\mathbf{k}_1}\delta_{\mathbf{k}_2}\delta_{\mathbf{k}_3} Q_n}{\sqrt{k_1 k_2 k_3 P_1 P_2 P_3}} \delta_D(\mathbf{k}_1+\mathbf{k}_2+\mathbf{k}_3) \\ &= (2\pi)^3 \int d^3x \int_{\mathbf{k}_1,\mathbf{k}_2,\mathbf{k}_3} \frac{\delta_{\mathbf{k}_1}\delta_{\mathbf{k}_2}\delta_{\mathbf{k}_3} Q_n}{\sqrt{k_1 k_2 k_3 P_1 P_2 P_3}} e^{i(\mathbf{k}_1+\mathbf{k}_2+\mathbf{k}_3)\cdot\mathbf{x}},\end{aligned} \tag{2.77}$$

which leads to this rather messy expression:

$$\begin{aligned}\left\langle \beta_m^Q \beta_n^Q \right\rangle = (2\pi)^{12} \int_{1,2,3,1',2',3'} & \frac{Q_m}{\sqrt{k_1 k_2 k_3 P_1 P_2 P_3}} \frac{Q'_n}{\sqrt{k'_1 k'_2 k'_3 P'_1 P'_2 P'_3}} \\ & \times \delta_D(\mathbf{k}_1+\mathbf{k}_2+\mathbf{k}_3)\delta_D(\mathbf{k}'_1+\mathbf{k}'_2+\mathbf{k}'_3) \\ & \times \left\langle \delta_{\mathbf{k}_1}\delta_{\mathbf{k}_2}\delta_{\mathbf{k}_3}\delta_{\mathbf{k}'_1}\delta_{\mathbf{k}'_2}\delta_{\mathbf{k}'_3} \right\rangle,\end{aligned} \tag{2.78}$$

where we further abbreviate the integral over the 6 wavevectors to

$$\int_{1,2,3,1',2',3'} \equiv \int \frac{\prod_{i=1}^3 d^3k_i}{(2\pi)^9} \frac{\prod_{i=1}^3 d^3k'_i}{(2\pi)^9}. \tag{2.79}$$

The 6-point correlator here can be expanded into products of connected correlators (again, denoted by the subscript c) in the same way we dealt with the power spectrum covariance [170]:

$$\begin{aligned}\left\langle \delta_{\mathbf{k}_1}\delta_{\mathbf{k}_2}\delta_{\mathbf{k}_3}\delta_{\mathbf{k}'_1}\delta_{\mathbf{k}'_2}\delta_{\mathbf{k}'_3} \right\rangle = & \left\langle \delta_{\mathbf{k}_1}\delta_{\mathbf{k}_2} \right\rangle \left\langle \delta_{\mathbf{k}_3}\delta_{\mathbf{k}'_1} \right\rangle \left\langle \delta_{\mathbf{k}'_2}\delta_{\mathbf{k}'_3} \right\rangle + 14\,\text{perms.} \\ & + \left\langle \delta_{\mathbf{k}_1}\delta_{\mathbf{k}_2}\delta_{\mathbf{k}_3} \right\rangle \left\langle \delta_{\mathbf{k}'_1}\delta_{\mathbf{k}'_2}\delta_{\mathbf{k}'_3} \right\rangle + 9\,\text{perms.} \\ & + \left\langle \delta_{\mathbf{k}_1}\delta_{\mathbf{k}_2}\delta_{\mathbf{k}_3}\delta_{\mathbf{k}'_1} \right\rangle_c \left\langle \delta_{\mathbf{k}'_2}\delta_{\mathbf{k}'_3} \right\rangle + 14\,\text{perms.} \\ & + \left\langle \delta_{\mathbf{k}_1}\delta_{\mathbf{k}_2}\delta_{\mathbf{k}_3}\delta_{\mathbf{k}'_1}\delta_{\mathbf{k}'_2}\delta_{\mathbf{k}'_3} \right\rangle_c.\end{aligned} \tag{2.80}$$

We identify the first set of terms $\langle\delta\delta\rangle\langle\delta\delta\rangle\langle\delta\delta\rangle \sim PPP$ as the Gaussian covariance of the bispectrum which is always present. All other terms vanish in the Gaussian limit of δ and appear due to non-linear evolution.

Let us first calculate the Gaussian contribution to the covariance. Some of the permutations simply vanish due the delta functions in Equation (2.78), e.g.

$$\begin{aligned}
&\delta_D(\mathbf{k}_1+\mathbf{k}_2+\mathbf{k}_3)\delta_D(\mathbf{k}'_1+\mathbf{k}'_2+\mathbf{k}'_3)\left\langle\delta_{\mathbf{k}_1}\delta_{\mathbf{k}_2}\right\rangle\left\langle\delta_{\mathbf{k}_3}\delta_{\mathbf{k}'_1}\right\rangle\left\langle\delta_{\mathbf{k}'_2}\delta_{\mathbf{k}'_3}\right\rangle \\
&= \delta_D(\mathbf{k}_1+\mathbf{k}_2+\mathbf{k}_3)\delta_D(\mathbf{k}'_1+\mathbf{k}'_2+\mathbf{k}'_3) \\
&\quad\times(2\pi)^9\delta_D(\mathbf{k}_1+\mathbf{k}_2)\delta_D(\mathbf{k}_3+\mathbf{k}'_1)\delta_D(\mathbf{k}'_2+\mathbf{k}'_3)P(k_1)P(k_3)P(k'_2) \\
&= \delta_D(\mathbf{k}_3)\delta_D(\mathbf{k}'_1) \\
&\quad\times(2\pi)^9\delta_D(\mathbf{k}_1+\mathbf{k}_2)\delta_D(\mathbf{k}_3+\mathbf{k}'_1)\delta_D(\mathbf{k}'_2+\mathbf{k}'_3)P(k_1)P(0)P(k'_2) \\
&= 0. \qquad (2.81)
\end{aligned}$$

One could easily show this applies to all permutations that do not pair up each of the unprimed wavevectors with a primed one in the correlators. This reduces the number of permutations from 15 to 6. A similar argument holds for the terms with the trispectrum and power spectrum, reducing the number of permutations from 15 to 9. The evaluation of the remaining terms is straightforward:

$$\begin{aligned}
&(2\pi)^{12}\int_{1,2,3,1',2',3'}\frac{Q_m}{\sqrt{k_1k_2k_3P_1P_2P_3}}\frac{Q'_n}{\sqrt{k'_1k'_2k'_3P'_1P'_2P'_3}}\delta_D(\mathbf{k}_1+\mathbf{k}_2+\mathbf{k}_3)\delta_D(\mathbf{k}'_1+\mathbf{k}'_2+\mathbf{k}'_3) \\
&\qquad\times\left(\left\langle\delta_{\mathbf{k}_1}\delta_{\mathbf{k}'_1}\right\rangle\left\langle\delta_{\mathbf{k}_2}\delta_{\mathbf{k}'_2}\right\rangle\left\langle\delta_{\mathbf{k}_3}\delta_{\mathbf{k}'_3}\right\rangle+5\,\text{perms.}\right) \\
&=(2\pi)^{21}\int_{1,2,3,1',2',3'}\frac{Q_m}{\sqrt{k_1k_2k_3P_1P_2P_3}}\frac{Q'_n}{\sqrt{k'_1k'_2k'_3P'_1P'_2P'_3}}\delta_D(\mathbf{k}_1+\mathbf{k}_2+\mathbf{k}_3)\delta_D(\mathbf{k}'_1+\mathbf{k}'_2+\mathbf{k}'_3) \\
&\qquad\times\left(\delta_D(\mathbf{k}_1+\mathbf{k}'_1)\delta_D(\mathbf{k}_2+\mathbf{k}'_2)\delta_D(\mathbf{k}_3+\mathbf{k}'_3)P(k_1)P(k_2)P(k_3)+5\,\text{perms.}\right) \\
&=6(2\pi)^{12}\int_{1,2,3}\frac{Q_mQ_n}{k_1k_2k_3P_1P_2P_3}\delta_D^2(\mathbf{k}_1+\mathbf{k}_2+\mathbf{k}_3)P(k_1)P(k_2)P(k_3) \\
&=6(2\pi)^6\frac{V}{8\pi^4}\int_{\mathcal{V}_B}dk_1dk_2dk_3\,k_1k_2k_3\frac{Q_mQ_n}{k_1k_2k_3} \\
&=6(2\pi)^3\frac{V}{\pi}\int_{\mathcal{V}_B}dV_kQ_mQ_n=6(2\pi)^3\gamma_{mn}, \qquad (2.82)
\end{aligned}$$

where we have used Equation (2.12) and the definition of γ_{mn} (Equation (2.44)).

Normally the non-Gaussian covariances can only be calculated in perturbation theory, but perhaps we can estimate the leading order contributions, i.e. the $\langle\delta\delta\delta\rangle\langle\delta\delta\delta\rangle\sim BB$ terms, with our estimated bispectrum from `MODAL-LSS`. We have to split the terms into two groups,

the first of which is

$$
\begin{aligned}
&(2\pi)^{12}\int_{1,2,3,1',2',3'}\frac{Q_m}{\sqrt{k_1k_2k_3P_1P_2P_3}}\frac{Q'_n}{\sqrt{k'_1k'_2k'_3P'_1P'_2P'_3}}\delta_D(\mathbf{k}_1+\mathbf{k}_2+\mathbf{k}_3)\delta_D(\mathbf{k}'_1+\mathbf{k}'_2+\mathbf{k}'_3)\\
&\qquad\times\left\langle\delta_{\mathbf{k}_1}\delta_{\mathbf{k}_2}\delta_{\mathbf{k}_3}\right\rangle\left\langle\delta_{\mathbf{k}'_1}\delta_{\mathbf{k}'_2}\delta_{\mathbf{k}'_3}\right\rangle\\
&=(2\pi)^{18}\int_{1,2,3,1',2',3'}\frac{Q_m}{\sqrt{k_1k_2k_3P_1P_2P_3}}\frac{Q'_n}{\sqrt{k'_1k'_2k'_3P'_1P'_2P'_3}}\delta_D^2(\mathbf{k}_1+\mathbf{k}_2+\mathbf{k}_3)\delta_D^2(\mathbf{k}'_1+\mathbf{k}'_2+\mathbf{k}'_3)\\
&\qquad\times B(k_1,k_2,k_3)B(k'_1,k'_2,k'_3)\\
&=\left((2\pi)^9\int_{1,2,3}\frac{\delta_D^2(\mathbf{k}_1+\mathbf{k}_2+\mathbf{k}_3)B(k_1,k_2,k_3)}{\sqrt{k_1k_2k_3P_1P_2P_3}}Q_m\right)\\
&\qquad\times\left((2\pi)^9\int_{1,2,3}\frac{\delta_D^2(\mathbf{k}_1+\mathbf{k}_2+\mathbf{k}_3)B(k_1,k_2,k_3)}{\sqrt{k_1k_2k_3P_1P_2P_3}}Q_n\right)\\
&=\left\langle\beta_m^Q\right\rangle\left\langle\beta_n^Q\right\rangle=\alpha_m^Q\alpha_n^Q
\end{aligned}
\tag{2.83}
$$

and eventually cancels with $B(k_1,k_2,k_3)B(k'_1,k'_2,k'_3)$ in the bispectrum covariance (Equation (2.76)). The remaining terms are

$$
\begin{aligned}
&(2\pi)^{12}\int_{1,2,3,1',2',3'}\frac{Q_m}{\sqrt{k_1k_2k_3P_1P_2P_3}}\frac{Q'_n}{\sqrt{k'_1k'_2k'_3P'_1P'_2P'_3}}\delta_D(\mathbf{k}_1+\mathbf{k}_2+\mathbf{k}_3)\delta_D(\mathbf{k}'_1+\mathbf{k}'_2+\mathbf{k}'_3)\\
&\qquad\times\left(\left\langle\delta_{\mathbf{k}_1}\delta_{\mathbf{k}_2}\delta_{\mathbf{k}'_3}\right\rangle\left\langle\delta_{\mathbf{k}'_1}\delta_{\mathbf{k}'_2}\delta_{\mathbf{k}_3}\right\rangle+8\,\text{perms.}\right)\\
&=(2\pi)^{18}\int_{1,2,3,1',2',3'}\frac{Q_m}{\sqrt{k_1k_2k_3P_1P_2P_3}}\frac{Q'_n}{\sqrt{k'_1k'_2k'_3P'_1P'_2P'_3}}\delta_D(\mathbf{k}_1+\mathbf{k}_2+\mathbf{k}_3)\delta_D(\mathbf{k}'_1+\mathbf{k}'_2+\mathbf{k}'_3)\\
&\qquad\times\left(\delta_D(\mathbf{k}_1+\mathbf{k}_2+\mathbf{k}'_3)\delta_D(\mathbf{k}'_1+\mathbf{k}'_2+\mathbf{k}_3)B(k_1,k_2,k'_3)B(k'_1,k'_2,k_3)+8\,\text{perms.}\right)\\
&=(2\pi)^{18}\int_{1,2,3,1',2',3'}\frac{Q_m}{\sqrt{k_1k_2k_3P_1P_2P_3}}\frac{Q'_n}{\sqrt{k'_1k'_2k'_3P'_1P'_2P'_3}}\delta_D(\mathbf{k}_1+\mathbf{k}_2+\mathbf{k}_3)\delta_D(\mathbf{k}'_1+\mathbf{k}'_2+\mathbf{k}'_3)\\
&\qquad\times\left(\delta_D^2(\mathbf{k}_3-\mathbf{k}'_3)B(k_1,k_2,k'_3)B(k'_1,k'_2,k_3)+8\,\text{perms.}\right).
\end{aligned}
\tag{2.84}
$$

Unfortunately the integrals are no longer separable even if we apply the `MODAL-LSS` method. We therefore do not attempt to compute this, and putting everything together we obtain:

$$
\begin{aligned}
&\left\langle \beta_m^Q \beta_n^Q \right\rangle \\
&= (2\pi)^{12} \int_{1,2,3,1',2',3'} \frac{Q_m}{\sqrt{k_1 k_2 k_3 P_1 P_2 P_3}} \frac{Q'_n}{\sqrt{k'_1 k'_2 k'_3 P'_1 P'_2 P'_3}} \\
&\qquad \times \delta_D(\mathbf{k}_1 + \mathbf{k}_2 + \mathbf{k}_3) \delta_D(\mathbf{k}'_1 + \mathbf{k}'_2 + \mathbf{k}'_3) \left\langle \delta_{\mathbf{k}_1} \delta_{\mathbf{k}_2} \delta_{\mathbf{k}_3} \delta_{\mathbf{k}'_1} \delta_{\mathbf{k}'_2} \delta_{\mathbf{k}'_3} \right\rangle \\
&= 6(2\pi)^3 \gamma_{mn} + \alpha_m^Q \alpha_n^Q \\
&\qquad + (2\pi)^{12} \int_{1,2,3,1',2',3'} \frac{Q_m}{\sqrt{k_1 k_2 k_3 P_1 P_2 P_3}} \frac{Q'_n}{\sqrt{k'_1 k'_2 k'_3 P'_1 P'_2 P'_3}} \\
&\qquad\quad \times \delta_D(\mathbf{k}_1 + \mathbf{k}_2 + \mathbf{k}_3) \delta_D(\mathbf{k}'_1 + \mathbf{k}'_2 + \mathbf{k}'_3) \\
&\qquad\quad \times \Bigg((2\pi)^6 \delta_D^2(\mathbf{k}_3 - \mathbf{k}'_3) B(k_1, k_2, k'_3) B(k'_1, k'_2, k_3) + 8\,\text{perms.} \\
&\qquad\qquad + (2\pi)^6 \delta_D(\mathbf{k}_2 + \mathbf{k}_3 + \mathbf{k}'_2 + \mathbf{k}'_3) \delta_D(\mathbf{k}_1 + \mathbf{k}'_1) T(\mathbf{k}_2, \mathbf{k}_3, \mathbf{k}'_2, \mathbf{k}'_3) P(k_1) + 8\,\text{perms.} \\
&\qquad\qquad + (2\pi)^3 \delta_D(\mathbf{k}_1 + \mathbf{k}_2 + \mathbf{k}_3 + \mathbf{k}'_1 + \mathbf{k}'_2 + \mathbf{k}'_3) P_6(\mathbf{k}_1, \mathbf{k}_2, \mathbf{k}_3, \mathbf{k}'_1, \mathbf{k}'_2, \mathbf{k}'_3) \Bigg). \\
&= 6(2\pi)^3 \gamma_{mn} + \alpha_m^Q \alpha_n^Q \\
&\qquad + V(2\pi)^{12} \int_{1,2,3,1',2',3'} \frac{Q_m}{\sqrt{k_1 k_2 k_3 P_1 P_2 P_3}} \frac{Q'_n}{\sqrt{k'_1 k'_2 k'_3 P'_1 P'_2 P'_3}} \\
&\qquad\quad \times \delta_D(\mathbf{k}_1 + \mathbf{k}_2 + \mathbf{k}_3) \delta_D(\mathbf{k}'_1 + \mathbf{k}'_2 + \mathbf{k}'_3) \\
&\qquad\quad \times \Bigg((2\pi)^3 \delta_D(\mathbf{k}_3 - \mathbf{k}'_3) B(k_1, k_2, k'_3) B(k'_1, k'_2, k_3) + 8\,\text{perms.} \\
&\qquad\qquad + (2\pi)^3 \delta_D(\mathbf{k}_1 + \mathbf{k}'_1) T(\mathbf{k}_2, \mathbf{k}_3, \mathbf{k}'_2, \mathbf{k}'_3) P(k_1) + 8\,\text{perms.} \\
&\qquad\qquad + P_6(\mathbf{k}_1, \mathbf{k}_2, \mathbf{k}_3, \mathbf{k}'_1, \mathbf{k}'_2, \mathbf{k}'_3) \Bigg),
\end{aligned}
\tag{2.85}
$$

where the pentaspectrum P_6 is defined by

$$
\begin{aligned}
\langle \delta(\mathbf{k}_1) \delta(\mathbf{k}_2) \delta(\mathbf{k}_3) \delta(\mathbf{k}_4) \delta(\mathbf{k}_5) \delta(\mathbf{k}_6) \rangle_c &= (2\pi)^3 \delta_D(\mathbf{k}_1 + \mathbf{k}_2 + \mathbf{k}_3 + \mathbf{k}_4 + \mathbf{k}_5 + \mathbf{k}_6) \\
&\quad \times P_6(\mathbf{k}_1, \mathbf{k}_2, \mathbf{k}_3, \mathbf{k}_4, \mathbf{k}_5, \mathbf{k}_6).
\end{aligned}
\tag{2.86}
$$

While there is no easy way to evaluate the last two set of terms involving the trispectrum and pentaspectrum, in the Gaussian limit we have

$$\left\langle \beta_m^R \beta_n^R \right\rangle \approx 6(2\pi)^3 \sum_{op}^{n_{max}} \lambda_{mo} \gamma_{op} \lambda_{pn}^T = 6(2\pi)^3 \delta_{mn}, \tag{2.87}$$

where we have used that fact that $\gamma = \lambda^{-1}(\lambda^{-1})^T$ and $\beta_n^R = \sum_m \lambda_{nm} \beta_m^Q$, therefore the Gaussian covariance of the β_n^R is given trivially as

$$C_{mn}^{\beta} \equiv \left\langle \beta_m^R \beta_n^R \right\rangle - \left\langle \beta_m^R \right\rangle \left\langle \beta_n^R \right\rangle \approx 6(2\pi)^3 \delta_{mn}, \tag{2.88}$$

which is diagonal. Unfortunately C_B cannot be evaluated analytically, even in the Gaussian limit, since Equation (2.76) yields

$$\begin{aligned}
&\sqrt{\frac{k_1 k_2 k_3 k_1' k_2' k_3'}{P_1 P_2 P_3 P_1' P_2' P_3'}} C_B(k_1, k_2, k_3, k_1', k_2', k_3') \\
&\approx 6(2\pi)^3 \sum_{mn}^{n_{max}} Q_m'(k_1', k_2', k_3') (\gamma^{-1})_{mn} Q_n(k_1, k_2, k_3) \\
&= 6(2\pi)^3 \sum_{mn}^{n_{max}} R_o'(k_1', k_2', k_3') (\lambda^{-1})_{om}^T (\gamma^{-1})_{mn} (\lambda^{-1})_{np} R_p(k_1, k_2, k_3) \\
&= 6(2\pi)^3 \sum_{n}^{n_{max}} R_n'(k_1', k_2', k_3') R_n(k_1, k_2, k_3)
\end{aligned} \tag{2.89}$$

where we have used Equation (2.46) and the fact that $\gamma^{-1} = \lambda^T \lambda$ to convert from the $\{Q_n\}$ basis to $\{R_n\}$. The last line cannot be further simplified because in practice we can never use enough modes to ensure $\{R_n\}$ forms a complete basis. Nevertheless we can calculate the Gaussian covariance of $\hat{f}_{nl} = \sum_n \alpha_n^R \beta_n^R / \sum_n \alpha_n^R \alpha_n^R$ here which we will explore numerically in

Section 3.5:

$$
\begin{aligned}
C_{f_{nl}} &\equiv \left\langle \hat{f}_{nl}^2 \right\rangle - \left\langle \hat{f}_{nl} \right\rangle^2 \\
&= \frac{\sum_{mn} \alpha_m^R \alpha_n^R \left\langle \beta_m^R \beta_n^R \right\rangle - (\sum_n \alpha_n^R \left\langle \beta_n^R \right\rangle)^2}{(\sum_n \alpha_n^R \alpha_n^R)^2} \\
&\approx \frac{1}{(\sum_n \alpha_n^R \alpha_n^R)^2} \left(\sum_{mn} \alpha_m^R \alpha_n^R \left(6(2\pi)^3 \delta_{mn} + \alpha_m^R \alpha_n^R \right) \right. \\
&\qquad \left. - (\sum_n \alpha_n^R \alpha_n^R)^2 \right) \\
&= \frac{6(2\pi)^3}{\sum_n \alpha_n^R \alpha_n^R}.
\end{aligned}
\tag{2.90}
$$

Suppression of large-scale variances Large variances are particularly prominent at large scales due to the finite volume of the simulation box or observational area leading to a lack of Fourier modes for statistical calculations. These are typically known as *finite box* or *cosmic variance* effects, although in the former case there is the added complication of mode coupling induced by non-linear gravitational evolution [171].

While cosmic variance, which is defined by the observational volume of a given survey, is difficult to curtail, we have much more control over theoretical errors, including errors in simulations. These errors have important ramifications on the level of accuracy at which we can extract cosmological parameters from galaxy surveys, and there is evidence to suggest detection of new physics may require $\mathcal{O}(0.1\%)$ accuracy in simulations [46]. While cosmic variance, which is defined by the observational volume of a given survey, is unavoidable, we could reduce *finite box* errors in simulations by simply expanding the box or averaging multiple simulations. Unfortunately both of these approaches are costly in terms of time and computational resources. For a more efficient way of obtaining ensemble averaged quantities such as the power spectrum and bispectrum the authors of [172, 171] have proposed a method of pairing up simulations which have opposite phases in their initial conditions. The phase inversion has no affect on the statistical properties of the simulation thus the pairing up process does not bias power spectra and bispectra estimation. However, leading order contributions to the Gaussian covariances, which are the dominant contribution to cosmic variance, will cancel in the pairing-up process as they are out-of-phase with each other.

We will quickly review the method. As introduced in Section 1.4.2, the non-linear power spectrum $P_{NL}(k)$ can be expanded in terms of the linear power spectrum $P_{\rm lin}$ and integrals

involving $P_{\rm lin}(k)$ convolved with the F_n kernels:

$$P_{\rm NL} = P_{\rm lin} + P_{12} + P_{21} + P_{13} + P_{22} + P_{31} + \cdots . \tag{2.91}$$

Assuming Gaussian initial conditions so that δ_1 is also Gaussian, we can use Wick's theorem to eliminate terms containing odd multiples of $\delta^{(1)}$, thus giving:

$$P_{\rm NL}^{\text{Gaussian IC}} = P_{\rm lin} + P_{13} + P_{22} + P_{31} + \cdots . \tag{2.92}$$

The effect of phase inversion is to reverse the sign of $\delta^{(1)}$, and the pairing up procedure serves to annihilate the same odd-parity terms that are expected to vanish in the ensemble average, while leaving the signal terms, which have even parity, intact. On the other hand since the non-Gaussian covariances also have even parity they remain unaffected.

The same applies for the bispectrum. The expansion in SPT is now (neglecting permutations)

$$B = B_{111} + B_{112} + B_{113} + B_{122} + B_{114} + B_{123} + B_{222} + \cdots , \tag{2.93}$$

so that for Gaussian initial conditions we have

$$B^{\text{Gaussian IC}} = B_{112} + B_{122} + B_{114} + B_{123} + B_{222} + \cdots . \tag{2.94}$$

Again we see that terms containing an odd number of $\delta^{(1)}$ vanish which coincides with the effect of pairing up phase inverted simulations. While the suppression of variance in power spectra estimation was explored in great detail in [171] no equivalent test have been performed with the bispectrum, which we leave to future work.

2.3.3 Systematic offsets due to aliasing contributions

While the discrete sampling of the underlying field by a finite number of particles merely distorts the statistics of the field by simple Poisson shot noise, the discrete sampling of the field with a regular grid can lead to large systematic errors in the power spectrum and bispectrum estimates if one is not careful. As pointed out in [165] the estimation of correlation functions in simulations by direct calculation is computationally intractable. As such virtually all power spectra and bispectra analyses are now done with FFTs due to its efficiency in calculating Fourier transforms, and `MODAL-LSS` is no exception. Here we discuss problems that arise by using this discrete method of obtaining the Fourier transform. These sampling effects in the power spectrum are discussed in detail in e.g. [165, 173, 12, 174],

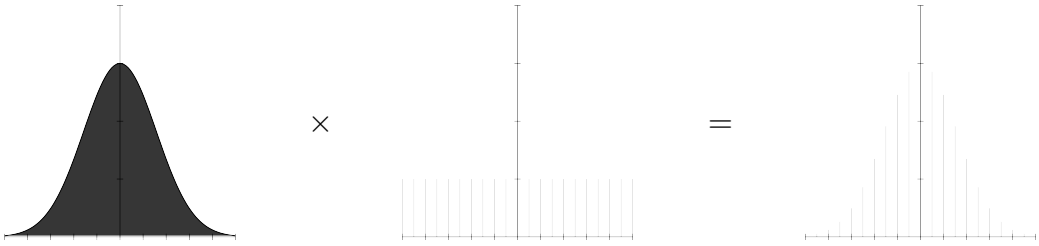

(a) Sampling in real space is a multiplication of the signal with a Dirac comb.

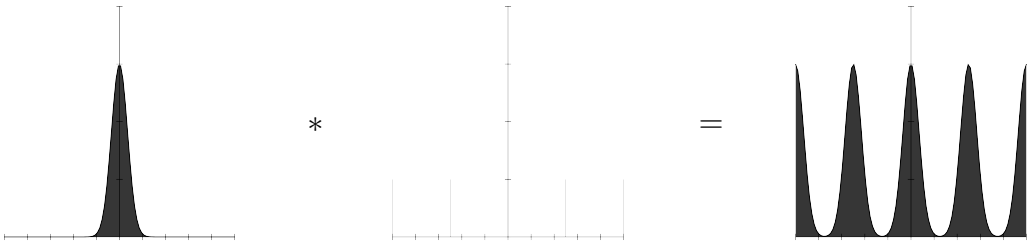

(b) In Fourier space this becomes a convolution between the signal and a Dirac comb, resulting in multiple, aliased copies of the signal.

Fig. 2.12 Sampling in real and Fourier space (Figure 1 from [12]).

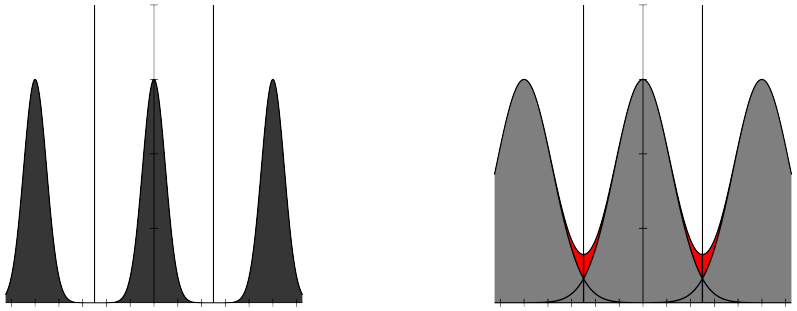

(a) If the sampling frequency is more than twice the highest frequency in the signal, then the aliased images that appear after convolving the signal with the Dirac comb do not overlap. In this case the signal is undistorted and can be uniquely restored.

(b) On the other hand if the Nyquist criterion is not met, the images will overlap with each other due to contributions from the higher frequencies, leading to significant distortions near the Nyquist frequency. There is no easy way to recover the original signal.

Fig. 2.13 If the sampling frequency is too low, aliasing occurs (Figure 2 from [12]).

but remains poorly understood for the bispectrum. This is likely due to the lack of efficient bispectrum estimators that are publicly available.

The first step in using FFTs is to put the particles on a regular grid. This involves a mass assignment scheme which dictates the weighting with which each particle is distributed across its surrounding grid points. Many of these schemes are well known in the literature, e.g. Nearest Grid Point (NGP), Cloud in cell (CIC) and Triangular Shaped Clouds (TSC) [165], as well as higher order interpolation schemes such as Piecewise Cubic Spline (PCS) [174] and Daubechies wavelet transformations [173]. The effect of this assignment manifests as a convolution with the density field which becomes a product with the corresponding window function $W(\mathbf{k})$ in Fourier space. In principle this can be corrected for easily by dividing out the window function in Fourier space but as we shall see shortly complications arise due to the discrete nature of the Fourier grid.

However even in this case the use of discrete FFTs inevitably leads to information loss [12]. By the Shannon sampling theorem [175] all the information in a signal can be recovered if the sampling frequency is twice that of the highest frequency in the signal, i.e. with a sufficiently high sampling frequency a *band-limited* signal can be reproduced without information loss. This is known as the *Nyquist criterion*. For cosmological purposes these conditions are clearly violated, and the sampling frequency controlled by the grid size dictates the extent to which we can calculate correlation functions by FFTs. The sampling theorem states that this limit is the Nyquist frequency $k_{Ny} = k_{max}/2 = \pi/H$, where k_{max} is the sampling frequency of the grid and H is the grid spacing. For the purpose of estimating correlation functions with FFTs it is known that the cutoff frequency for the power spectrum is the Nyquist frequency k_{Ny} [165, 173, 12, 174]. For the bispectrum [112] and [174] propose the limit should be $2k_{Ny}/3$. The former takes into consideration the number of triangular configurations used in the estimation and the latter is based on the invariance of the exponential factor in Equation (2.77) under the transformation $\mathbf{k}_i \rightarrow \mathbf{k}_i\left(1+\frac{2\pi}{3H}\right)$, since $\mathbf{x}$ is confined to be multiples of the grid spacing H. The loss of information above the cutoff is typically outweighed by the computational efficiency brought on by using FFT techniques, and the lack of viable alternative methods.

There is a second serious problem associated with discrete grids which is the introduction of sampling artefacts near the Nyquist frequency. As explained in further detail in [12], discrete sampling in real space is effectively a multiplication of the signal with a Dirac comb (Figure 2.12a). In Fourier space this multiplication becomes a convolution operation, resulting in multiple images of the signal evenly spaced at the sampling frequency of the grid (Figure 2.12b). In the case that the sampling frequency is more than twice the maximum frequency of the signal, as in Figure 2.13a, then the images of the signal do not overlap

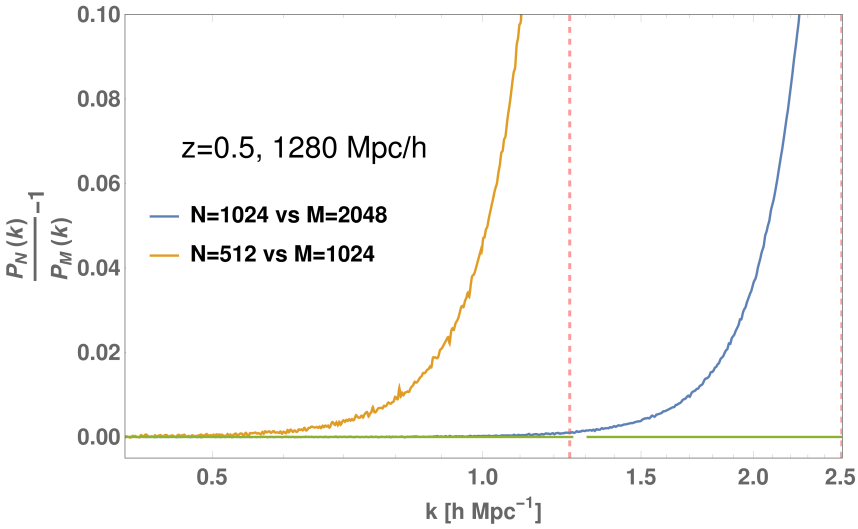

(a) Ratio between GADGET-3 power spectra estimated with FFT grids of different sizes. The baseline is the larger of the two CIC grids, and the pink, dashed lines indicate the Nyquist frequencies k_{Ny} for the 512^3 and 1024^3 CIC grids. It is clear how aliasing contributions lead to overestimation of the power spectra near $k = k_{Ny}$, but the functional form of this overshoot cannot be calculated analytically.

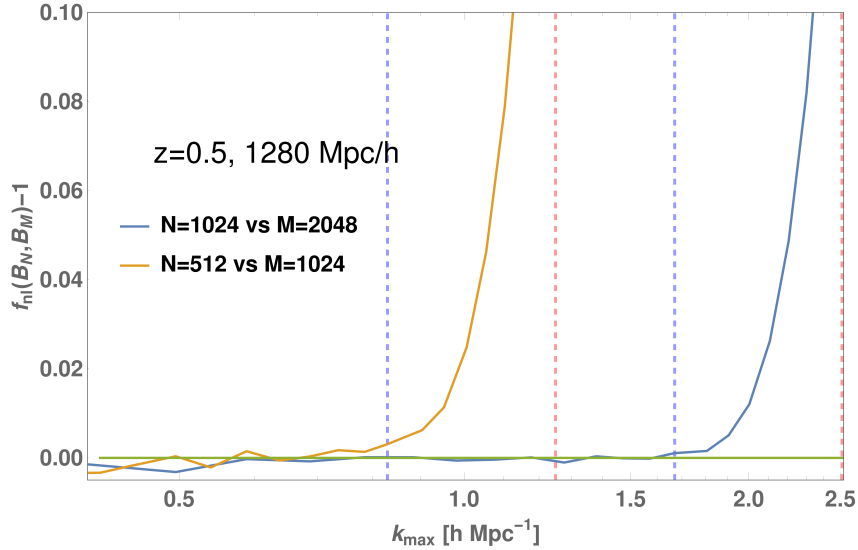

(b) f_{nl} correlators between GADGET-3 bispectra estimated with the same FFT grids in Figure 2.14a. Again the pink, dashed lines indicate k_{Ny} for the various grids, but here we additionally label $k = \frac{2}{3}k_{Ny}$ with blue, dashed lines to find the correct cutoff frequency. Contrary to [112, 174] there is little to suggest that bispectrum estimation breaks down at $\frac{2}{3}k_{Ny}$, but rather at k_{Ny} as for the power spectrum.

Fig. 2.14 A demonstration of aliasing in the power spectrum and bispectrum for a GADGET-3 simulation.

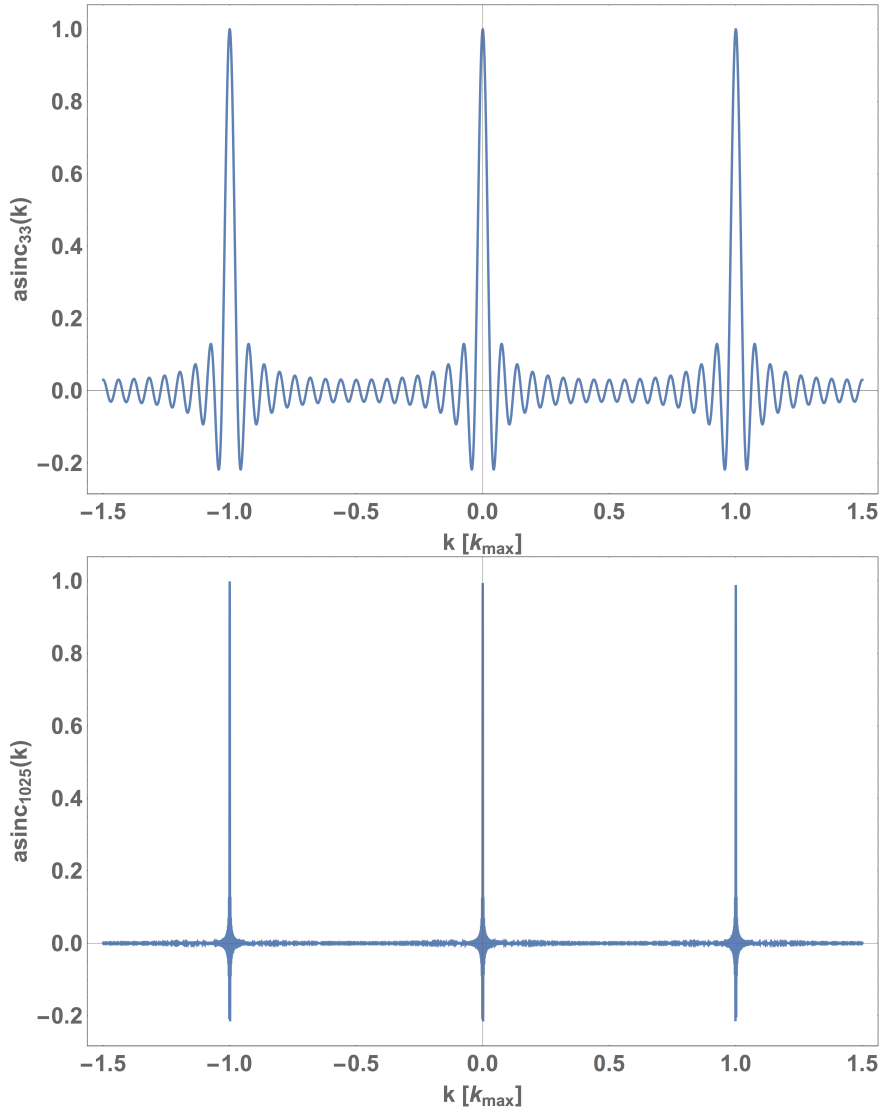

Fig. 2.15 The aliased sinc function with $\text{asinc}_M(k)$ with $M = 33$ and 1025 plotted in units of the sampling frequency of the grid k_{max}. Unlike the Dirac comb $\text{asinc}_M(k)$ is non-local and oscillatory between the peaks, leading to distortions and aliasing effects even for band-limited signals. As is evident in the $M = 1025$ case, both of these effects can be mitigated by using finer sampling grids since the width of the primary peaks at its base is $2/M$, and the value of the function at $k = k_{Ny} = k_{max}/2$ is $1/M$.

each other and no artefacts are induced. Otherwise if higher frequencies are indeed present (Figure 2.13b), which certainly holds true in cosmological contexts, then the copies of the replicated signal will overlap and distort the sampled signal near the Nyquist frequency. We demonstrate this effect with `GADGET-3` power spectra and bispectra in Figure 2.14 (for details of the simulations see Section 3.2 below). Here we find that the cutoff frequency for the bispectrum is the same as the power spectrum, k_{Ny} in disagreement with the predictions of [112, 174].

We follow [165] in deriving the aliasing contributions to the power spectrum and further extend it for the bispectrum. We begin by denoting the FFT density grid in real space as

$$\delta_n^f(\mathbf{r}) = \text{Ш}_r\left(\frac{\mathbf{r}}{H}\right)(\delta_n * W)(\mathbf{r}) \tag{2.95}$$

where the superscript f labels an FFT quantity and the subscript n indicates sampling with discrete objects as before. This is equivalent to the statement that the $\delta_n^f(\mathbf{r})$ is a multiplication of the sampling grid, i.e. the Dirac comb $\text{Ш}_r(\mathbf{r}) = \sum_{\mathbf{r}_g}\delta_D(\mathbf{r}-\mathbf{r}_g) = \sum_{\mathbf{n}}\delta_D(\mathbf{r}-H\mathbf{n})$ where $\mathbf{r}_g$ are the grid points and $\mathbf{n}\in\mathbb{Z}^3$ is a vector composed of integers, with the convolution between the density field sampled by discrete objects $\delta_n(\mathbf{r})$ and the window function $W(\mathbf{r})$ due to mass assignment. The Fourier Transform of this grid is

$$\delta_n^f(\mathbf{k}) = \mathcal{F}\left[\delta_n^f(\mathbf{r})\right] = \mathcal{F}\left[\text{Ш}_r\left(\frac{\mathbf{r}}{H}\right)(\delta_n * W)(\mathbf{r})\right], \tag{2.96}$$

but one should bear in mind that to obtain the FFT output one needs to further multiply this by the Dirac comb in $\mathbf{k}$-space, $\text{Ш}_k(\mathbf{k}) = \sum_{\mathbf{n}}\delta_D(\mathbf{k}-k_F\mathbf{n})$. Before we can evaluate Equation (2.96) with the convolution theorem, i.e. that convolution in real space becomes multiplication in Fourier space, we also need the Fourier Transform of the Dirac comb:

$$\begin{aligned}\mathcal{F}\left[\text{Ш}_r\left(\frac{\mathbf{r}}{H}\right)\right] &= \sum_{\mathbf{n}}\int\delta_D\left(\frac{1}{H}(\mathbf{r}-H\mathbf{n})\right)e^{-i\mathbf{k}\cdot\mathbf{r}}d^3r \\ &= H^3\sum_{\mathbf{n}}e^{-iH\mathbf{k}\cdot\mathbf{n}} \\ &= (2\pi)^3\sum_{\mathbf{n}}\delta_D(\mathbf{k}-k_{max}\mathbf{n}).\end{aligned} \tag{2.97}$$

To get to the last line we note that the Fourier series for $\text{Ш}_r(\mathbf{r})$ is

$$\text{Ш}_r(\mathbf{r}) = \sum_{\mathbf{n}}\delta_D(\mathbf{r}-H\mathbf{n}) = \sum_{\mathbf{n}}\frac{1}{H^3}e^{-i2\pi\mathbf{r}\cdot\mathbf{n}/H}, \tag{2.98}$$

as the Fourier coefficients $c_{\mathbf{n}}$ for $\text{Ш}_r(\mathbf{r}) = \sum_{\mathbf{n}} c_{\mathbf{n}} e^{-i2\pi\mathbf{r}\cdot\mathbf{n}/H}$ can be obtained by

$$c_{\mathbf{n}} = \frac{1}{H^3}\int_{-H/2}^{H/2}\int_{-H/2}^{H/2}\int_{-H/2}^{H/2}\delta_D(\mathbf{r})e^{i2\pi\mathbf{r}\cdot\mathbf{n}/H}d^3r = \frac{1}{H^3}. \tag{2.99}$$

Therefore with a change of variables $2\pi\mathbf{r}/H \to H\mathbf{k}$ and using the properties of the Dirac delta function it is straightforward to find

$$\sum_{\mathbf{n}} e^{-iH\mathbf{k}\cdot\mathbf{n}} = \frac{(2\pi)^3}{H^3}\sum_{\mathbf{n}}\delta_D(\mathbf{k}-k_{max}\mathbf{n}). \tag{2.100}$$

With all of this in mind we can finally evaluate Equation (2.96):

$$\begin{aligned}\delta_n^f(\mathbf{k}) &= \frac{1}{(2\pi)^3}\int \mathcal{F}\left[\text{Ш}_r\left(\frac{\mathbf{r}}{H}\right)\right]\delta_n(\mathbf{k}-\mathbf{k}')W(\mathbf{k}-\mathbf{k}')d^3k' \\ &= \sum_{\mathbf{n}}\int \delta_D(\mathbf{k}'-k_{max}\mathbf{n})\delta_n(\mathbf{k}-\mathbf{k}')W(\mathbf{k}-\mathbf{k}')d^3k' \\ &= \sum_{\mathbf{n}}\delta_n(\mathbf{k}-k_{max}\mathbf{n})W(\mathbf{k}-k_{max}\mathbf{n}),\end{aligned} \tag{2.101}$$

which makes the aliasing effects previously discussed immediately apparent. This is merely a restatement of Figure 2.12b: sampling with a Dirac comb leads to aliased images spaced at intervals of k_{max} in Fourier space. If the Nyquist criterion is satisfied, i.e. all frequencies in the signal satisfy $k < k_{max}/2 = k_{Ny}$, then the images will not overlap and the signal remains undistorted (Figure 2.13a). Otherwise aliasing artefacts will occur (Figure 2.13b).

We now turn our attention to the power spectrum of $\delta_n^f(\mathbf{k})$. First we need

$$\begin{aligned}&\left\langle \delta_n^f(\mathbf{k}_1)\delta_n^f(\mathbf{k}_2)\right\rangle \\ &= \sum_{\mathbf{nm}}\left\langle \delta_n(\mathbf{k}_1-k_{max}\mathbf{n})\delta_n(\mathbf{k}_2-k_{max}\mathbf{m})\right\rangle W(\mathbf{k}_1-k_{max}\mathbf{n})W(\mathbf{k}_2-k_{max}\mathbf{m}) \\ &= (2\pi)^3\sum_{\mathbf{nm}}P_n\left(|\mathbf{k}_1-k_{max}\mathbf{n}|\right)\delta_D(\mathbf{k}_1-k_{max}\mathbf{n}+\mathbf{k}_2-k_{max}\mathbf{m}) \\ &\qquad\qquad \times\left|W(\mathbf{k}_1-k_{max}\mathbf{n})\right|^2.\end{aligned} \tag{2.102}$$

Taking the expectation values on the left hand side and setting $\mathbf{k}_1 = -\mathbf{k}_2 = \mathbf{k}$ gives

$$\begin{aligned}(2\pi)^3P_n^f(k)\delta_D(\mathbf{0}) &= (2\pi)^3\sum_{\mathbf{nm}}P_n\left(|\mathbf{k}-k_{max}\mathbf{n}|\right)\delta_D(k_{max}\mathbf{n}+k_{max}\mathbf{m}) \\ &\qquad \times\left|W(\mathbf{k}-k_{max}\mathbf{n})\right|^2 \\ &= (2\pi)^3\delta_D(\mathbf{0})\sum_{\mathbf{n}}P_n\left(|\mathbf{k}-k_{max}\mathbf{n}|\right)\left|W(\mathbf{k}-k_{max}\mathbf{n})\right|^2.\end{aligned} \tag{2.103}$$

The factor of $\delta_D(\mathbf{0})$ in the last line comes from the fact that for every value of $\mathbf{n}$ in the summation we can find a value of $\mathbf{m}$ such that $\mathbf{n}+\mathbf{m}=\mathbf{0}$. We can therefore do the summation over $\mathbf{m}$ which brings gives $\delta_D(\mathbf{0})$. Finally this simplifies to produce the relationship between the FFT power spectrum $P_n^f(k)$ and the true underlying power spectrum $P(k)$:

$$\begin{aligned} P_n^f(k) &= \sum_{\mathbf{n}} P_n\left(|\mathbf{k}-k_{max}\mathbf{n}|\right)|W(\mathbf{k}-k_{max}\mathbf{n})|^2 \\ &= \sum_{\mathbf{n}} \left(P\left(|\mathbf{k}-k_{max}\mathbf{n}|\right)+\frac{1}{\bar{n}}\right)|W(\mathbf{k}-k_{max}\mathbf{n})|^2, \end{aligned} \tag{2.104}$$

where we have included the effects of Poisson shot noise. We can see that the aliasing contributions are most prominent near the Nyquist frequency k_{Ny} as was the case for the density field. We note that since Equation (2.104) is continuous in k it cannot be the true FFT output. An additional factor of

$$\begin{aligned} &\text{Ш}_f\left(\frac{\mathbf{k}}{k_F}\right)\text{Ш}_f\left(\frac{-\mathbf{k}}{k_F}\right) \\ &= \sum_{\mathbf{nm}} \delta_D\left(\frac{\mathbf{k}}{k_F}-\mathbf{n}\right)\delta_D\left(-\frac{\mathbf{k}}{k_F}-\mathbf{m}\right) \\ &= k_F^3 \sum_{\mathbf{nm}} \delta_D\left(\frac{\mathbf{k}}{k_F}-\mathbf{n}\right)\delta_D(k_F(\mathbf{n}+\mathbf{m})) \\ &= k_F^3 \sum_{\mathbf{n}} \delta_D\left(\frac{\mathbf{k}}{k_F}-\mathbf{n}\right)\delta_D(\mathbf{0}) \\ &= \sum_{\mathbf{n}} \delta_D\left(\frac{\mathbf{k}}{k_F}-\mathbf{n}\right) \\ &= \text{Ш}_f\left(\frac{\mathbf{k}}{k_F}\right) \end{aligned} \tag{2.105}$$

is required to account for the discrete sampling in Fourier space.

Finally to obtain the corresponding expressions for the bispectrum we begin with

$$\begin{aligned}
&\left\langle \delta_n^f(\mathbf{k}_1)\delta_n^f(\mathbf{k}_2)\delta_n^f(\mathbf{k}_3)\right\rangle \\
&= \sum_{\mathbf{n}_1\mathbf{n}_2\mathbf{n}_3} \langle \delta_n(\mathbf{k}_1 - k_{max}\mathbf{n}_1)\delta_n(\mathbf{k}_2 - k_{max}\mathbf{n}_2)\delta_n(\mathbf{k}_2 - k_{max}\mathbf{n}_3)\rangle \\
&\qquad \times W(\mathbf{k}_1 - k_{max}\mathbf{n}_1)W(\mathbf{k}_2 - k_{max}\mathbf{n}_2)W(\mathbf{k}_2 - k_{max}\mathbf{n}_3) \\
&= (2\pi)^3 \sum_{\mathbf{n}_1\mathbf{n}_2\mathbf{n}_3} B_n(q_1, q_2, |\mathbf{q}_1 + \mathbf{q}_2|)\, \delta_D(\mathbf{k}_1 - k_{max}\mathbf{n}_1 + \mathbf{k}_2 - k_{max}\mathbf{n}_2 + \mathbf{k}_3 - k_{max}\mathbf{n}_3) \\
&\qquad \times W(\mathbf{q}_1)W(\mathbf{q}_2)W(-\mathbf{q}_1 - \mathbf{q}_2) \\
&= (2\pi)^3 \sum_{\mathbf{n}_1\mathbf{n}_2\mathbf{n}_3} B_n(q_1, q_2, |\mathbf{q}_1 + \mathbf{q}_2|)\, \delta_D(\mathbf{k}_1 + \mathbf{k}_2 + \mathbf{k}_3)\delta_D(k_{max}\mathbf{n}_1 + k_{max}\mathbf{n}_2 + k_{max}\mathbf{n}_3) \\
&\qquad \times W(\mathbf{q}_1)W(\mathbf{q}_2)W(-\mathbf{q}_1 - \mathbf{q}_2) \\
&= (2\pi)^3 \delta_n(\mathbf{0}) \sum_{\mathbf{n}_1\mathbf{n}_2} B_n(q_1, q_2, |\mathbf{q}_1 + \mathbf{q}_2|)\, \delta_D(\mathbf{k}_1 + \mathbf{k}_2 + \mathbf{k}_3)W(\mathbf{q}_1)W(\mathbf{q}_2)W(-\mathbf{q}_1 - \mathbf{q}_2),
\end{aligned} \tag{2.106}$$

where we denote $\mathbf{q}_i = \mathbf{k}_i - k_{max}\mathbf{n}_i$. After using the definition of the bispectrum, it immediately follows that

$$\begin{aligned}
&B_n^f(k_1, k_2, k_3) \\
&= \sum_{\mathbf{n}_1\mathbf{n}_2} \left(B(q_1, q_2, |\mathbf{q}_1 + \mathbf{q}_2|) + \frac{1}{\bar{n}}[P(q_1) + P(q_2) + P(|\mathbf{q}_1 + \mathbf{q}_2|)] + \frac{1}{\bar{n}^2} \right) \\
&\qquad \times W(\mathbf{q}_1)W(\mathbf{q}_2)W(-\mathbf{q}_1 - \mathbf{q}_2).
\end{aligned} \tag{2.107}$$

The multiplicative factor due to discrete sampling in Fourier space is

$$\begin{aligned}
&\text{Ш}_f\left(\frac{\mathbf{k}_1}{k_F}\right)\text{Ш}_f\left(\frac{\mathbf{k}_2}{k_F}\right)\text{Ш}_f\left(\frac{-\mathbf{k}_1 - \mathbf{k}_2}{k_F}\right) \\
&= \sum_{\mathbf{n}_1\mathbf{n}_2\mathbf{n}_3} \delta_D\left(\frac{\mathbf{k}_1}{k_F} - \mathbf{n}_1\right)\delta_D\left(\frac{\mathbf{k}_2}{k_F} - \mathbf{n}_2\right)\delta_D\left(\frac{-\mathbf{k}_1 - \mathbf{k}_2}{k_F} - \mathbf{n}_3\right) \\
&= \sum_{\mathbf{n}_1\mathbf{n}_2\mathbf{n}_3} \delta_D\left(\frac{\mathbf{k}_1}{k_F} - \mathbf{n}_1\right)\delta_D\left(\frac{\mathbf{k}_2}{k_F} - \mathbf{n}_2\right)\delta_D(\mathbf{n}_1 + \mathbf{n}_2 + \mathbf{n}_3) \\
&= k_F^3 \sum_{\mathbf{n}_1\mathbf{n}_2} \delta_D\left(\frac{\mathbf{k}_1}{k_F} - \mathbf{n}_1\right)\delta_D\left(\frac{\mathbf{k}_2}{k_F} - \mathbf{n}_2\right)\delta_D(\mathbf{0}) \\
&= \sum_{\mathbf{n}_1\mathbf{n}_2} \delta_D\left(\frac{\mathbf{k}_1}{k_F} - \mathbf{n}_1\right)\delta_D\left(\frac{\mathbf{k}_2}{k_F} - \mathbf{n}_2\right) = \text{Ш}_f\left(\frac{\mathbf{k}_1}{k_F}\right)\text{Ш}_f\left(\frac{\mathbf{k}_2}{k_F}\right).
\end{aligned} \tag{2.108}$$

In principle this aliasing effect can be completely avoided by low-pass filtering the signal to remove the high-frequency contributions. This is equivalent to convolving the real-space signal with a sinc function [12]. However the sinc function is highly non-local and such an operation is computationally expensive since we would have to distribute all particles to every grid point. In addition we have assumed so far that our sampling operation in real space, i.e. $\text{Ш}_r(\mathbf{r})$, has infinite extent, so that its Fourier transform is also an infinite Dirac comb. This cannot be achieved for practical reasons, and the Fourier transform of a truncated one-dimensional Dirac comb is the aliased sinc function $\text{asinc}_M(k)$:

$$\begin{aligned}
\mathcal{F}\left[\frac{1}{M}\sum_{n=-\frac{M-1}{2}}^{\frac{M-1}{2}}\delta_D(r-Hn)\right] &= \frac{1}{M}\sum_{n=-\frac{M-1}{2}}^{\frac{M-1}{2}} e^{ikHn} \\
&= \frac{e^{-ikH(M-1)/2}}{M}\frac{1-e^{-ikHM}}{1-e^{-ikH}} \\
&= \frac{1}{M}\frac{e^{ikHM/2}-e^{-ikHM/2}}{e^{ikH/2}-e^{-ikH/2}} \\
&= \frac{\sin\left(\frac{kHM}{2}\right)}{M\sin\left(\frac{kH}{2}\right)} \\
&= \frac{\sin\left(\frac{\pi kM}{k_{max}}\right)}{M\sin\left(\frac{\pi k}{k_{max}}\right)} \\
&\equiv \text{asinc}_M(k),
\end{aligned} \tag{2.109}$$

where we have introduced the normalisation factor $1/M$. We plot $\text{asinc}_M(k)$ for $M = 33$ and 1025 in Figure 2.15, which correspond to sampling with FFT grids of size 32^3 and 1024^3 respectively. The aliased sinc function differs from the infinite Dirac comb in a very important way, i.e. its non-locality. When convolved with $\delta_n(\mathbf{r})$ the oscillatory features will distort the signal, and aliased images will always overlap even if the signal is band-limited. These aliasing contributions can be alleviated by low-pass filtering the signal, but one can not eradicate them nor uniquely restore the original signal [12]. However it should be noted that with sufficiently large M one can typically neglect these contributions: the base width of the primary peaks is $2/M$ and the value of $\text{asinc}_M(k)$ at the Nyquist frequency is $1/M$. Finally we remark that these finite, discrete sampling effects are exacerbated by the mass assignment procedure as the window function $W(\mathbf{k})$ also enters the aliased sum. This is a mild complication for the shot noise terms in Equations (2.104) and (2.107) as $W(\mathbf{k} - k_{max}\mathbf{n})$ are typically simple analytical expressions [165]. As for the product between the power spectrum and window function [165] proposed a procedure to cure these sampling effects

iteratively by assuming the power spectrum $P(k)$ behaves like a power-law near the Nyquist frequency $k \sim k_{Ny}$. While this approximation seemed to work effectively for the power spectrum, it is not clear how one would similarly construct a simple analytical formula that captures the local behaviour of the bispectrum and higher order correlators effectively.

While no method has been found to fully recover the bispectrum near the Nyquist frequency, various solutions have been put forward to diminish the effects of aliasing. A straightforward approach is using higher order interpolation kernels such as PCS or Daubechies wavelets which are closer approximations to the ideal low-pass filter. In particular the authors of [173] claim that even without deconvolution of the corresponding window function, the power spectrum can be measured with the wavelets to an accuracy level of 2% in for wavenumbers up to $0.7k_{Ny}$. Since particle-mesh simulation codes rely on FFTs for rapid calculations of the gravitational potential, the Daubechies wavelets may prove useful as an inexpensive yet accurate way of representing particles on a grid. An alternative method is to push the aliasing effects to higher k by first 'supersampling' the density field at some higher resolution than the one desired [12]. The super-sampled grid naturally has a higher Nyquist frequency thus we expect the aliasing effects at the target resolution to be much reduced. Finally we down-sample the super-sampled grid by deconvolving the relevant window function and removing all unwanted k-modes to obtain the signal sampled at the frequency of interest. The advantages of 'supersampling' over other methods are its effectiveness at removing undesirable aliasing distortions *at the target frequency*, and since low order mass assignment schemes such as CIC and TSC can be used for supersampling it is also computationally fast. However to super-sample at n times the required resolution demands n^3 the amount of memory which can be a big limiting factor. A third method, propounded by [174], sets out to remove the dominant aliasing contributions from odd images (cf. Figure 2.13b) by interlacing two density grids that are shifted by half the grid spacing with respect to each other. The authors claim that the method, combined with a high order interpolation scheme such as PCS, can reduce systematic biases from aliasing to levels below 0.01% all the way up to the Nyquist frequency for both power spectra and bispectra estimates.

Investigation of these effects in the case of the bispectrum is beyond the current scope of this thesis and we leave it to future work. For the remainder of the thesis we will instead avoid the issues mentioned above by simply limiting ourselves to $k < k_{max}/3 = \frac{2}{3}k_{Ny}$.

2.4 Conclusions

To conclude this chapter we have presented the newly improved `MODAL-LSS` code for efficiently computing the bispectrum of any 3D input density field. This code enables us to do

high precision analysis with the dark matter bispectrum from large N-body simulations or faster alternative codes, and to make detailed quantitative comparisons between theory and simulations (see Chapter 3). By exploiting highly optimised numerical libraries, we were able to incorporate 1000 separable modes in the bispectrum analysis (relative to 50 modes previously [162]), also including specially tailored modes to accurately recover the tree-level bispectrum. This allows convergence to a much broader range of nonlinear gravitational and primordial bispectra and makes generic non-Gaussian searches feasible in huge future galaxy surveys.

Furthermore, we have addressed a few common areas where errors in the `MODAL-LSS` estimator can be significant, i.e. shot noise, the covariance of the estimator, and aliasing effects from using FFTs. Shot noise in the bispectrum is well-known and required little discussion. The full covariance of the `MODAL-LSS` estimator was derived for the first time, but the non-Gaussian contributions to the covariance appear to be analytically intractable, even with the separable `MODAL-LSS` expansion, so we can only estimate the Gaussian covariance, and we must tackle the problem numerically. While others have investigated discrete FFT methods on bispectrum estimation, we find that contrary to other estimators the `MODAL-LSS` estimator breaks down at the same frequency as power spectra estimators, i.e. at the Nyquist frequency k_{Ny}, rather than at $\frac{2}{3}k_{Ny}$. We believe this is not a consequence of the `MODAL-LSS` method but rather a general result in bispectrum estimation since the aliasing effects come from the discrete sampling of the density field and not the use of FFTs itself.

Chapter 3

Dark Matter Bispectrum

3.1 Fast Dark Matter Simulation Codes

As we enter the age of precision cosmology we are ever more reliant on cosmological simulations to understand the dynamics of dark matter and baryons. Numerical simulations act as a buffer between theory and observation: we test cosmological models by matching simulation results to observational data, and hence obtain constraints on cosmological parameters. On the other hand since we only observe one universe we must turn to simulations to understand the statistical significance of our measurements. This is especially important with large galaxy data sets coming from current and near-future surveys such as DES, LSST, Euclid and DESI. While it would be ideal to use full N-body simulations to generate these so-called mock catalogues for statistical analysis, their huge demand for computational resources is prohibitive for generating the large number of simulations required for accurate estimates of covariances [13]. This has led to a proliferation of fast dark matter simulation tools, such as PINOCCHIO [176, 177], Quick Particle Mesh (QPM) [178], Augmented Lagrangian Perturbation Theory (ALPT) [179] and the Comoving Lagrangian Acceleration method (COLA) [180]. While the algorithms employed in all these methods are different, they all share the common aim of speeding up the simulation process at the expense of reduced accuracy at small scales. Alternatively, compression methods have also been developed to reduce the number of mocks required, see e.g. [181–185].

These fast methods are typically bench-marked against N-body codes with the power spectrum and other two-point clustering statistics, as well as some form of three-point

correlation, e.g. the reduced bispectrum

$$Q(k_1,k_2,k_3) = \frac{B(k_1,k_2,k_3)}{P(k_1)P(k_2)+P(k_2)P(k_3)+P(k_3)P(k_1)} \tag{3.1}$$

in some restricted domain. With `MODAL-LSS` we can incorporate full bispectrum estimation into the validation testing for these methods. The importance of these tests cannot be underestimated: as aforementioned the analysis in [46] has shown that theoretical and numerical uncertainties can strongly influence the extent to which observational data can be used to put constraints on cosmological parameters and hence possibilities of detecting new physics.

As a proof of concept we have elected to test the bispectra of three different fast dark matter methods, i.e. COLA, Particle-Mesh (PM) and second-order Lagrangian perturbation theory (2LPT) [186], against the Tree-PM N-body code `GADGET-3` at various redshifts. `L-PICOLA` [13, 187] was used to generate the COLA, PM and 2LPT data due to its versatility and massively parallel performance, and its ability to generate and evolve the same 2LPT initial conditions used in our `GADGET-3` runs. This means that all final outputs share the same initial seed and random phases, thus eliminating the need for cosmic variance considerations when comparing them.

Here we briefly summarise the three algorithms we test in this thesis. For further details we refer the reader to relevant literature for 2LPT [186], PM [188] and COLA [13, 180].

2LPT In Lagrangian perturbation theory (LPT) we track particles by their displacement $\boldsymbol{\psi}(\boldsymbol{q},t)$ from their initial position $\boldsymbol{q}$, i.e. $\boldsymbol{x}(t) = \boldsymbol{q} + \boldsymbol{\psi}(\boldsymbol{q},t)$, where $\boldsymbol{x}$ is the Eulerian position. First order in LPT leads to the well-known Zeldovich Approximation (ZA), which is particularly useful due to its analytical simplicity, and is often used to generate initial conditions for numerical simulations. However as shown in [189] 2LPT is a superior method at limited additional computational cost, and has since replaced ZA as the standard.

PM The PM algorithm speeds up the calculation of gravitational forces though the use of a mesh: instead of summing all interactions between all the particles, we calculate the density field on a grid and use the Poisson equation to derive the gravitational potential in Fourier space. This computation is sped up greatly with FFTs, and it is straightforward to calculate the forces in real space at each grid point with the gradient of the potential and an inverse-FFT. The force on each particle is found by reversing the interpolation scheme used to place the particles on the grid. Here we use `L-PICOLA`'s implementation of the PM algorithm which is based on `PMCODE` [190].

COLA While the 2LPT produces excellent results at large scales, it quickly becomes deficient going into smaller scales as it fails to capture the full non-linearity of the system. The COLA algorithm is an efficient extension of 2LPT, boasting both speed and accuracy by trying to recover the residual Lagrangian displacement $\boldsymbol{\psi}_{res}$ between the 2LPT displacement and the full non-linear counterpart. The extra computations rely on variables already calculated and stored, such as the LPT and 2LPT displacements and the gravitational potential, the last of which is provided by the PM method.

3.2 Simulation Data

In order to probe a range of scales we have chosen two simulation box sizes of $1280\,h^{-1}$ Mpc and $640\,h^{-1}$ Mpc, corresponding to $k_F = 0.005\,h\,\mathrm{Mpc}^{-1}$ and $k_{Ny} = 5.0\,h\,\mathrm{Mpc}^{-1}$, and $k_F = 0.01\,h\,\mathrm{Mpc}^{-1}$ and $k_{Ny} = 10.0\,h\,\mathrm{Mpc}^{-1}$ respectively. We have generated the Gaussian initial conditions from second-order Lagrangian Perturbation Theory (2LPT) displacements using `L-PICOLA` [13, 187] at redshift $z_i = 99$ to ensure the suppression of transients in power spectra and bispectra estimates of our simulations [17]. Our input linear power spectrum at redshift $z = 0$ was produced by `CAMB` [9] using a flat ΛCDM cosmology with extended Planck 2015 cosmological parameters (TT,TE,EE+lowP+lensing+ext, see Table 3.1). For neutrinos we had one massive neutrino species and two massless neutrinos. The lack of radiation and neutrino evolution in `L-PICOLA` and `GADGET-3` has led us to define the matter power spectrum to consist only of cold dark matter and baryons, which leads us to recover the input power spectrum at $z = 0$ to linear order. This causes the raised value of σ_8 instead of the Planck value of 0.8159. A PM grid size of 2048^3 was then used to evolve the 2048^3 particles in each run where applicable. Table 3.2 shows a number of `GADGET-3` parameter values we used to guarantee high numerical precision in our simulation.

The expensive `GADGET-3` runs were completed on the `COSMA` facility at Durham while the other codes and all subsequent analysis was finished with the `COSMOS` supercomputer at Cambridge. The small deviations in output redshifts between `GADGET-3` and `L-PICOLA` were corrected with the appropriate linear growth factor

$$D_1(a) = \frac{E(a)}{D_{1,0}} \int_0^a \frac{da'}{a'^3 E^3(a')}, \tag{3.2}$$

where

$$E(a) = \frac{H(a)}{H_0} = \sqrt{\Omega_m a^{-3} + \Omega_\Lambda} \tag{3.3}$$

Description	Symbol	Value
Hubble constant	H_0	$67.74\ \mathrm{km\,s^{-1}}$
Physical baryon density parameter	$\Omega_b h^2$	0.02230
Matter density parameter	Ω_m	0.3089
Dark energy density parameter	Ω_Λ	0.6911
Fluctuation amplitude at $8h^{-1}$ Mpc	σ_8	0.8196
Scalar spectral index	n_s	0.9667
Primordial amplitude	$10^9 A_s$	2.142
Physical neutrino density parameter	$\Omega_\nu h^2$	0.000642
Number of effective neutrino species	N_{eff}	3.046
Curvature density parameter	Ω_k	0.0000

Table 3.1 Planck 2015 cosmological parameters (Tables 4 and 5 in [16], rightmost columns), which we used to generate the input power spectrum from `CAMB`. The pivot scale for n_s is $0.05\ \mathrm{Mpc}^{-1}$.

for a flat cosmology, and

$$D_{1,0} = \int_0^1 \frac{da'}{a'^3 E^3(a')} \tag{3.4}$$

is introduced to normalise $D_1(z=0)=1$.

In addition to Tables 3.1 and 3.2, the following are key parameters we used to generate the initial power spectrum and evolve the initial conditions:

Name	Description	Value
MaxRMSDisplacementFac	Timestepping criteria	0.1
ErrTolIntAccuracy		0.01
MaxSizeTimestep		0.01
ErrTolTheta	Gravitational force criteria	0.2
ErrTolForceAcc		0.002
Smoothing length		$30h^{-1}$ kpc

Table 3.2 `GADGET-3` parameters chosen in reference to [17, 18] to ensure high numerical accuracy in our simulations.

`CAMB` We use only cold dark matter (CDM) and baryons to define the matter power spectrum and σ_8, i.e. transfer_power_var = 8. For neutrinos we incorporated one massive neutrino species with a small energy density, so that the relevant neutrino parameters are massless_neutrinos = 2.046 and massive_neutrinos = 1.

`L-PICOLA` Three different logarithmic time steppings in a were used to test the accuracy of COLA: $\Delta(\ln a) = 0.01$ (the same time-stepping we use for `GADGET-3`), 0.046 and 0.23. They correspond to 460, 100 and 20 time-steps from $z = 99$ to $z = 0$ respectively.

3.3 Simulation Power Spectra

We estimated the power spectra of our simulations with `GADGET-3`. To minimise errors coming from aliasing effects the power spectra of each simulation was estimated three times: once with a 2048^3 PM grid and two further times by 'folding' [191] that grid onto itself by factors of 2 and 4 respectively. The disadvantage of this folding method is the reduction in the number of modes at large scales leading to greater cosmic variance. We therefore combine these three power spectra together to guarantee precision over the entire k-ranges considered here. We did not observe shot noise in the power spectra of the initial conditions, and due to large number densities used did not find it necessary to correct for shot noise in the simulation outputs (cf. Equation (2.56)).

Figure 3.1 shows the ratio between the power spectra of the fast codes and `GADGET-3` at redshift $z = 0.5$. While 2LPT and $\Delta(\ln a)_{0.23}$ COLA compare poorly to `GADGET-3` as expected, the power of the COLA algorithm to imitate the performance of PM in fewer time-steps is shown by the $\Delta(\ln a)_{0.046}$ case. It should be noted that PM does perform slightly better than COLA when the same number of time-steps are used.

3.4 Simulation Bispectra

The density field of the simulations were first obtained via a CIC mass assignment. A smoothed `GADGET-3` power spectrum at the appropriate redshifts were used in the signal-to-noise weighting of the bispectrum (Equation (2.23)). Smoothing is especially necessary at large scales where the lack of modes creates large variance in the estimated power spectrum, and was achieved by 'dividing' out the variance:

$$\hat{P}_{smooth}(k,z) = \hat{P}_{var}(k,z)\frac{P_L(k,z)}{\hat{P}_{IC}(k,z_i)} \times \frac{D_1^2(z_i)}{D_1^2(z)} \tag{3.5}$$

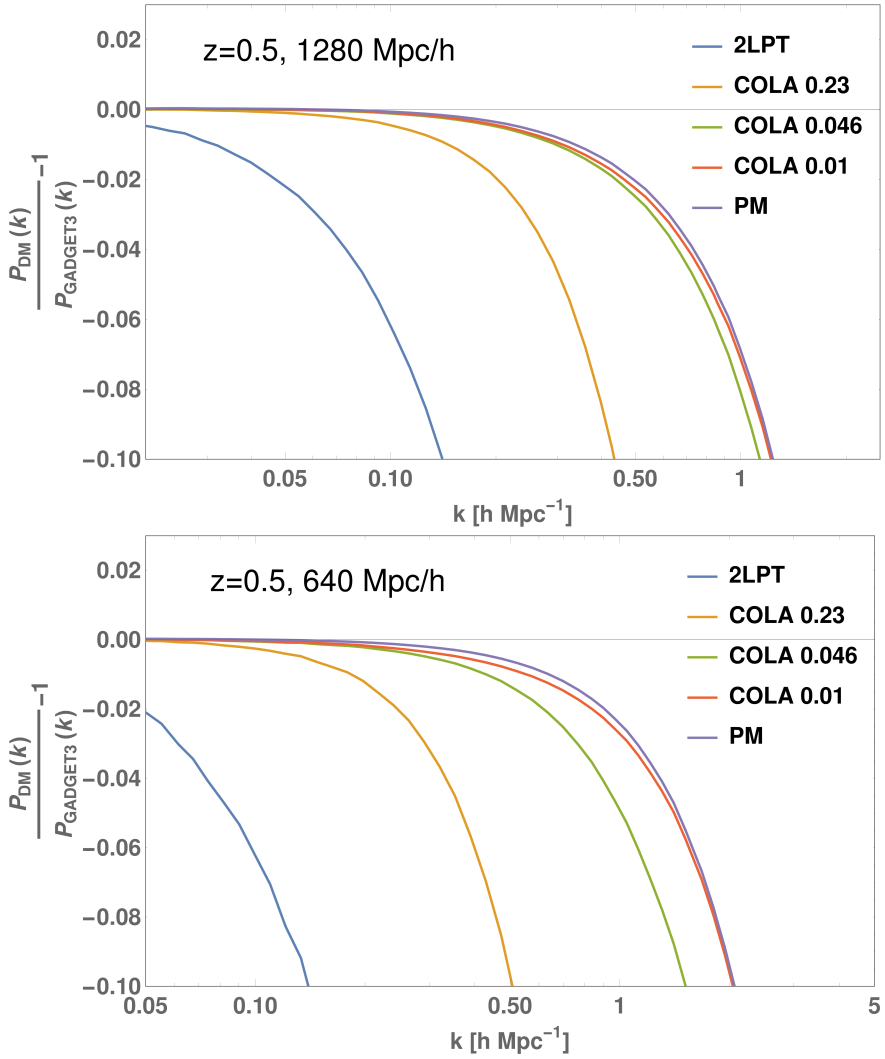

Fig. 3.1 Ratio between the power spectra of the various fast dark matter codes and GADGET-3 for the 2 simulation boxes. All the power spectrum estimates were performed with GADGET-3. The sub-par performance of 2LPT and COLA with a coarse time-stepping of $\Delta(\ln a) = 0.23$ is unsurprising, but the $\Delta(\ln a)_{0.046}$ COLA simulation compares quite favourably with PM and the $\Delta(\ln a)_{0.01}$ COLA with at a fraction of the computational cost. As noted by its authors the ability to reproduce the matter power spectrum at a reasonable accuracy but with reduced computational resources compared to conventional PM methods is the strength of the COLA method [13].

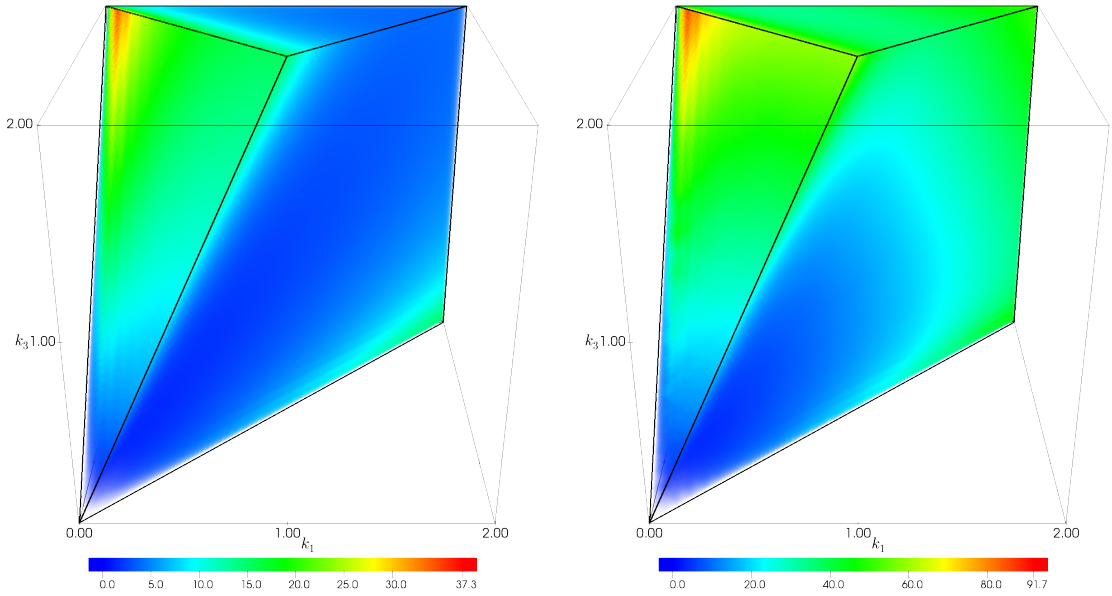

(a) Redshift $z = 9$ (b) Redshift $z = 3$

Fig. 3.2 Redshift evolution of the estimated bispectra from a $1280h^{-1}$ Mpc GADGET-3 simulation, plotted up to $k_{max} = 2.0h\text{Mpc}^{-1}$. This shows clearly how the flattened tree-level signal dominates the early time bispectra, but the constant shape brought about by the aggregation of matter takes over at late times. To emphasise this point we have scaled the maxima of the colour bars for redshifts $z = 3 \to 0$ relative to redshift $z = 9$ by the appropriate linear growth factor, $D_1(z)/D_1(z = 9)$. The SN-weighted tree-level bispectrum grows as $D_1(z)$, and the saturation of the signal for redshifts $z = 1, 0.5, 0$ demonstrate faster growth than that dictated by perturbation theory in the non-linear regime. It is remarkable that the only shape generated by the collapse of dark matter into halos is the constant shape. Therefore after $z \sim 2$ we observe a steady growth in the strength of the signal but very little change in the bispectrum morphology. *(cont.)*

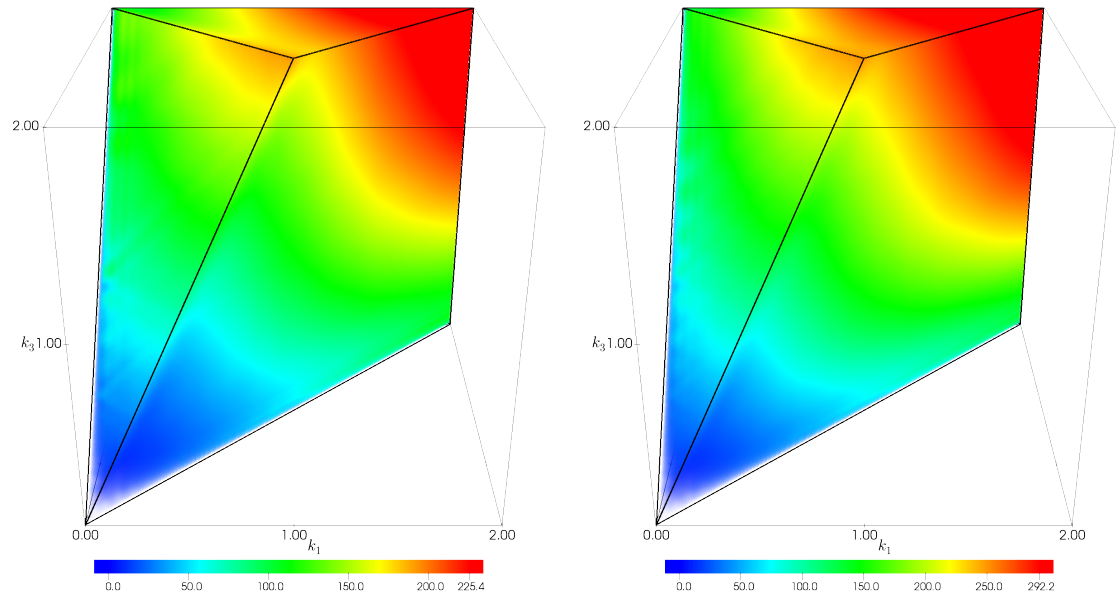

(c) Redshift $z = 0.5$ (d) Redshift $z = 0$

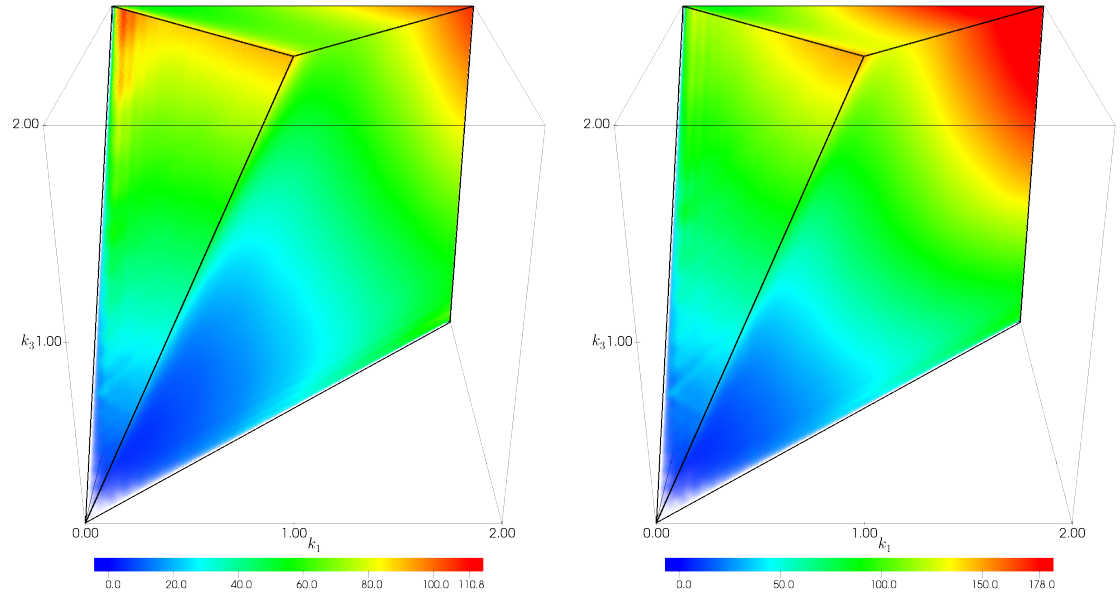

(e) Redshift $z = 2$ (f) Redshift $z = 1$

Fig. 3.2 Redshift evolution of the estimated bispectra from a $1280\,h^{-1}$ Mpc GADGET-3 simulation, plotted up to $k_{max} = 2.0\,h\,\mathrm{Mpc}^{-1}$.

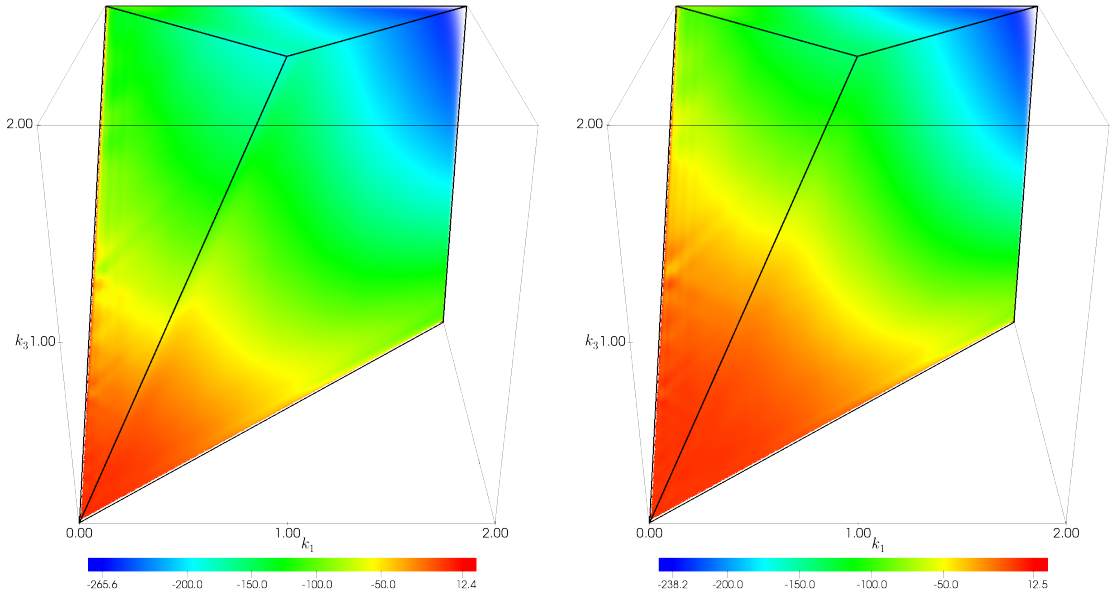

(a) 2LPT

(b) $\Delta(\ln a)_{0.23}$ COLA

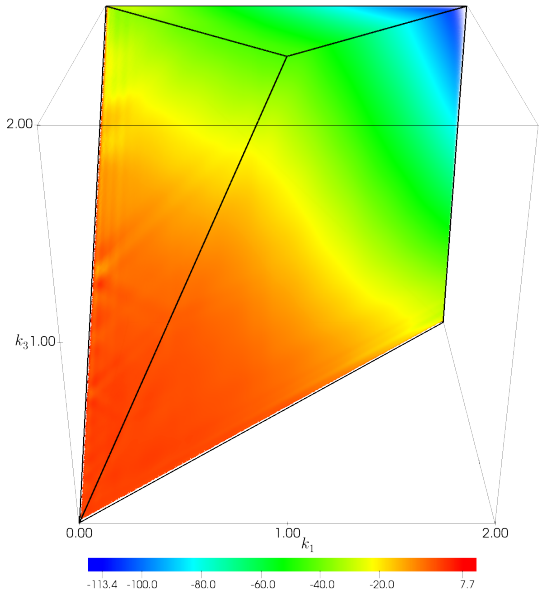

(c) $\Delta(\ln a)_{0.01}$ COLA

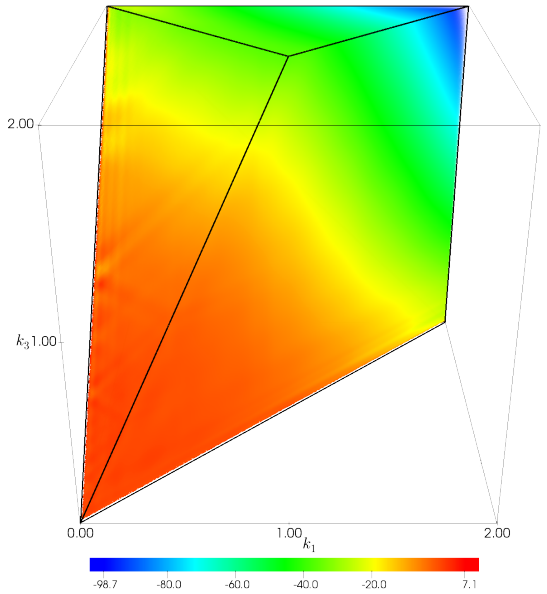

(d) $\Delta(\ln a)_{0.046}$ COLA

Fig. 3.3 Bispectrum residuals at redshift $z = 0.5$ between the $1280\,h^{-1}$ Mpc fast dark matter and `GADGET-3` simulations, plotted up to $k_{max} = 2.0\,h\,\mathrm{Mpc}^{-1}$. The lack of non-linear signal in the fast dark matter simulations is evident, leading to a deficient constant shape in their bispectra. *(cont.)*

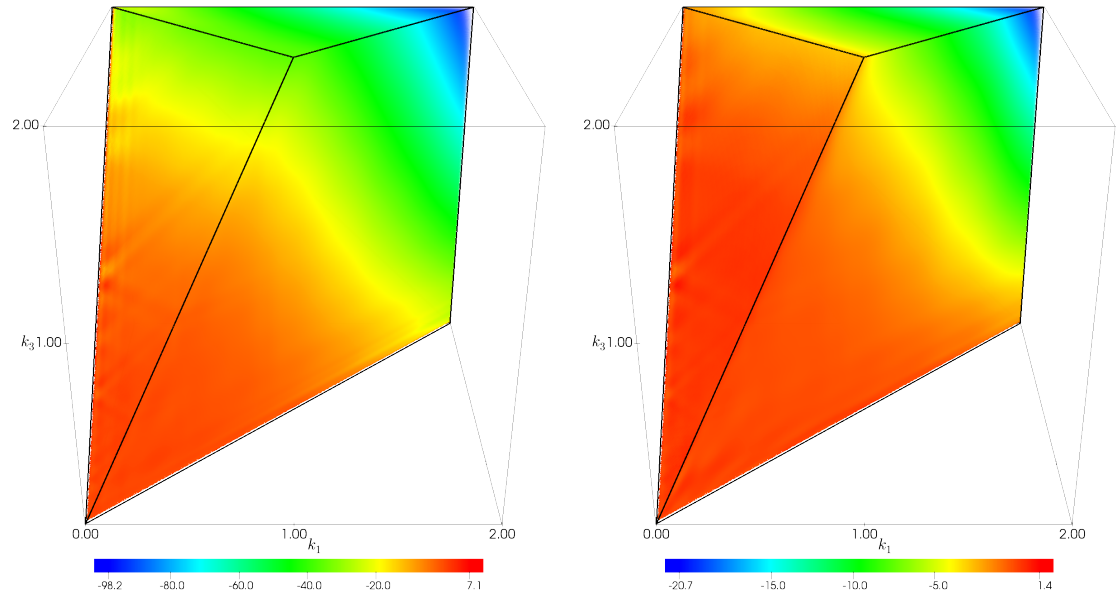

(e) PM (f) Boosted $\Delta(\ln a)_{0.01}$ COLA

Fig. 3.3 Bispectrum residuals at redshift $z = 0.5$ between the $1280\,h^{-1}$ Mpc fast dark matter and GADGET-3 simulations, plotted up to $k_{max} = 2.0\,h\,\mathrm{Mpc}^{-1}$.

where $\hat{P}_{var}(k,z)$ is the original, variance-contaminated, power spectrum estimate, $P_L(k,z)$ is the linear power spectrum computed by CAMB at the same redshift and $\hat{P}_{IC}(k,z_i)$ is the estimated power spectrum of the initial conditions. This step is crucial for producing a smooth theoretical bispectrum since they often take the non-linear power spectrum as input, and a simulation power spectrum is usually chosen for that purpose to ensure fair comparison between simulation and theory (see Section 3.6).

In Figure 3.2 we show the estimated bispectra for the $1280\,h^{-1}$ Mpc GADGET-3 simulations described in Section 3.2 up to $k_{max} = 2.0\,h\,\mathrm{Mpc}^{-1}$. We choose this resolution to best highlight the transition from the tree-level dominant signal seen in early redshifts to the strong constant shape presence induced by non-linear gravitational evolution at late times. In particular we see that this happens most prominently from redshift $z = 3$, where there is still some competition between the flattened and equilateral signals, to redshift $z = 2$, in which the constant shape has taken over. This is one of the many advantages of estimating the full bispectrum, as its morphology typically offers unique information regarding structure formation that cannot be gained from the power spectrum. Another point of note is that the formation of dark matter halos through virialisation generates only one bispectrum shape which is the constant shape, as evidenced by the lack of change in the bispectrum past $z = 2$ bar a growth in signal strength. We also show the bispectrum residuals between the fast dark

matter codes and GADGET-3 in Figure 3.3. The inability of the fast codes to resolve small scale structure is illustrated by the lack of constant shape signal in their bispectra. These pictures agrees qualitatively with the power spectra results in Figure 3.1.

To make quantitative comparisons we invoke the correlators introduced in Section 2.1. The f_{nl} correlators of the fast dark matter codes with GADGET-3:

$$f_{nl}(\hat{B}_{\rm DM}, \hat{B}_{\texttt{GADGET-3}}) = \frac{\sum_n \beta^R_{{\rm DM},n}\beta^R_{\texttt{GADGET-3},n}}{\sum_n (\beta^R_{\texttt{GADGET-3},n})^2} \tag{3.6}$$

are shown in Figure 3.4; we do not plot the shape correlators as they only provide redundant information. The first thing to note is a striking resemblance to the power spectra plots in Figure 3.1, as the power spectrum enters the f_{nl} correlator through the weighted inner products between bispectra (Equation (2.22)). Since we use the GADGET-3 power spectrum for the weighting, bispectra comparisons will inevitably be biased by the lack of power in the fast dark matter power spectra. To address this issue and show the differences due to the bispectrum alone we propose boosting the power spectrum of the fast code in Fourier space:

$$\delta_{\rm DM}(\mathbf{k}) \to \sqrt{\frac{\hat{P}_{\texttt{GADGET-3}}(k)}{\hat{P}_{\rm DM}(k)}}\,\delta_{\rm DM}(\mathbf{k}). \tag{3.7}$$

The residuals between the boosted $1280\,h^{-1}$ Mpc $\Delta(\ln a)_{0.01}$ COLA simulation and GADGET-3 is shown in Figure 3.3, demonstrating more than a 3x reduction in magnitude compared to the unboosted COLA and PM runs. More quantitatively the boosted $\Delta(\ln a)_{0.01}$ COLA bispectra also show much improved f_{nl} correlation with GADGET-3 as seen in Figure 3.4. We therefore conclude this is an effective yet relatively inexpensive method to improve the performance of fast simulation codes, as only one GADGET-3 and one fast code run that share the same initial conditions is required to obtain a smooth boosting factor in Equation (3.7). This only has to be done once as the boosting factor should be reasonably realisation-independent. Nevertheless a dip in correlation at small scales remain after boosting which reflects the fact that particle distributions with the same power spectra need not have the same bispectra, confirming the fact that there is information carried by the bispectrum that is not encoded in the power spectrum.

3.5 Gaussian vs Non-Gaussian covariances

The extent to which we can put constraints on cosmological parameters through the bispectrum is dependent on the covariance of MODAL-LSS estimator. To find the full covariance

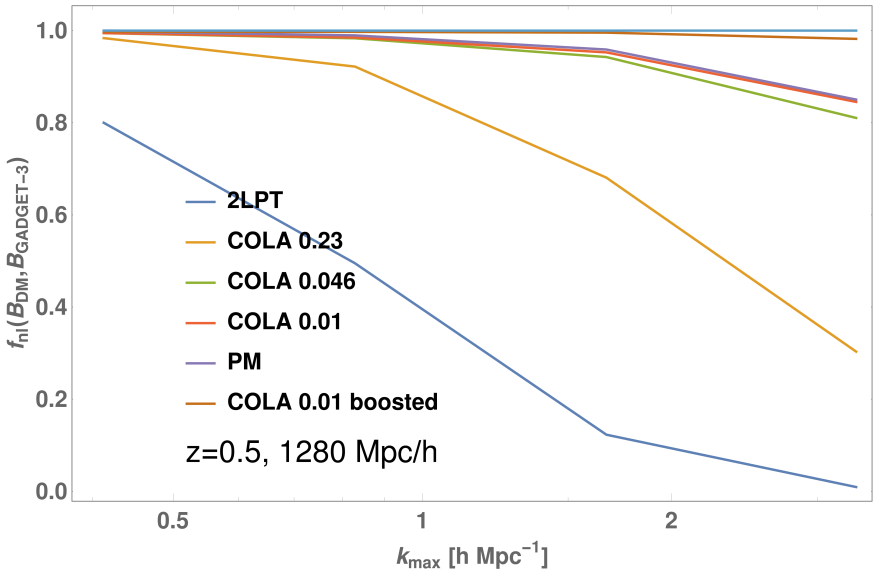

(a)

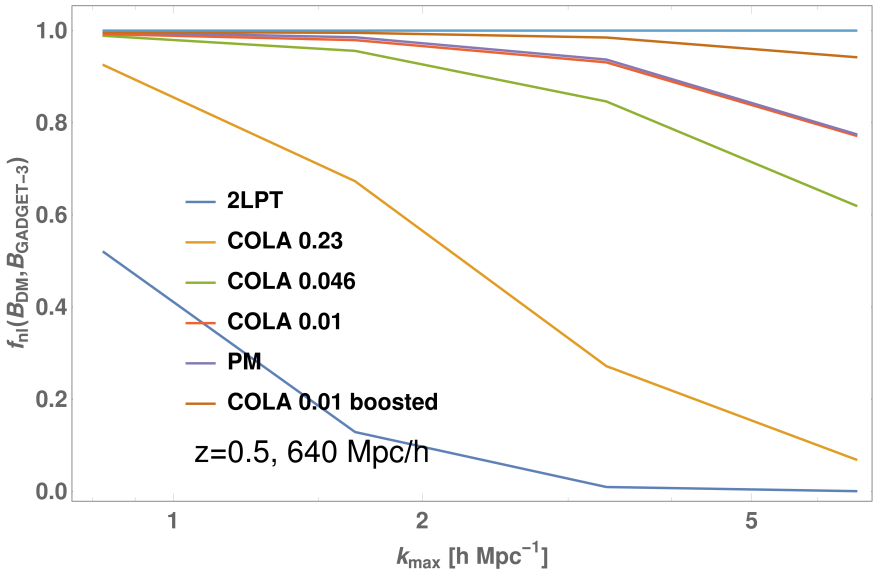

(b)

Fig. 3.4 f_{nl} correlators between the bispectra of fast dark matter codes and `GADGET-3`. The similarities of these plots to those in Figure 3.1 is due to the power spectrum weighting present in inner products between bispectra (Equation (2.22)), thus a mismatch in power spectra naturally leads to discrepancies in bispectrum comparisons. This may suggest that the differences we see here are due to the power spectrum alone, but clearly this is not the case since the 'boosted' COLA simulation has an identical power spectrum to `GADGET-3` yet still suffers from a lack of bispectrum signal at small scales. However, the improved performance of the boosted COLA bispectrum demonstrates the effectiveness of the 'boosting' method.

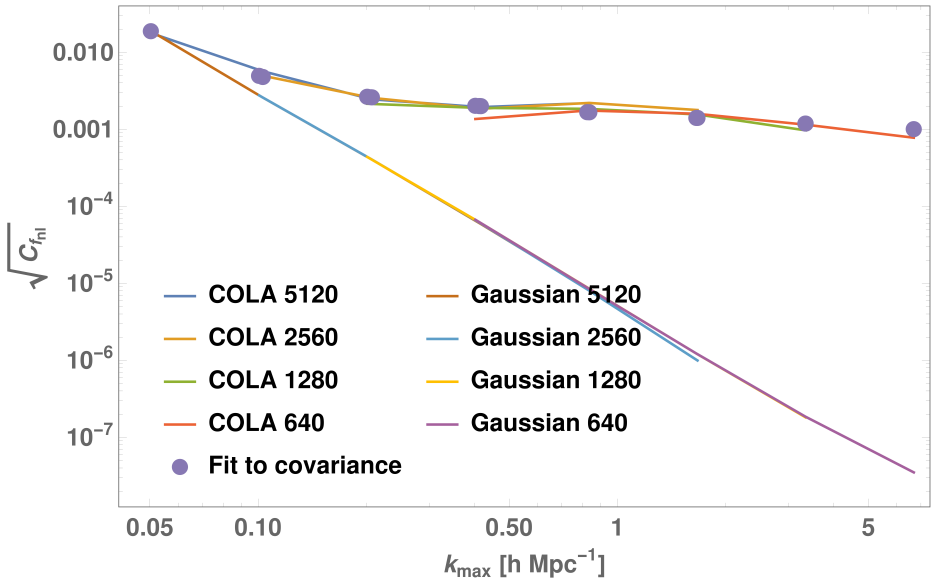

Fig. 3.5 The full covariance of the f_{nl} correlator estimated using 10 COLA runs compared to the Gaussian contribution calculated using Equation (2.90) with the 3-shape model. The two begin to diverge significantly at $k \sim 0.1\,h\mathrm{Mpc}^{-1}$, signalling the dominance of non-Gaussian covariances. Since the covariance scales inversely as the cube of the box size, in order to combine the estimates from the different simulations we have re-scaled them accordingly against the $5120\,h^{-1}$ Mpc runs. The purple points are the best-fit to the full covariance with the function $f = Ak^{-a} + Bk^{-b}$ and the parameters $A = 3.2477 \times 10^{-6}, B = 1.5871 \times 10^{-3}, a = 2.8339, b = 0.2409$.

we first average over 10 boosted COLA realisations for an estimate of the mean bispectrum $\bar{\beta}$, then calculate the variance in $f_{nl}(\beta,\bar{\beta})$ as an estimate for $C_{f_{nl}}$ (Equation (2.90)). The computational cost of COLA runs are sufficiently low that additional to the $1280\,h^{-1}$ Mpc and $640\,h^{-1}$ Mpc boxes we have also completed runs with $5120\,h^{-1}$ Mpc and $2560\,h^{-1}$ Mpc box sizes, so that we can explore the regime where Gaussian covariances dominate. Since we do not have `GADGET-3` simulations for the $5120\,h^{-1}$ Mpc and $2560\,h^{-1}$ Mpc boxes we estimate the dark matter power spectrum by boosting a COLA run as follows. First we repeat the smoothing procedure to obtain a smoothed COLA power spectrum, then estimate the appropriate boosting factor with the $1280\,h^{-1}$ Mpc one. We have made a least-squares fit of the full covariance $\sqrt{C_{f_{nl}}}$ with the `curve_fit` algorithm in `Scipy`, using the default Levenberg-Marquardt method [192]. We model the full covariance as a sum of two power laws: $f = Ak^{-a} + Bk^{-b}$, which represents the Gaussian and non-Gaussian contributions respectively. The best-fit is obtained using the following values for these parameters: $A = 4.6480 \times 10^{-6}, B = 1.0900 \times 10^{-3}, a = 2.5978, b = 0.2315$.

Our estimates are shown in Figure 3.5 where we also plot the Gaussian covariances calculated using Equation (2.90) with the 3-shape model α_n^R coefficients. It is clear that while the Gaussian covariance continues to diminish in the non-linear regime due to more modes being available, the non-Gaussian covariance starts to dominate at $k \sim 0.1\,h\,\mathrm{Mpc}^{-1}$ and then asymptotes towards $\sim 0.1\%$. This has important consequences on e.g. Fisher matrix forecasts, especially if non-Gaussian covariances are not taken in account which could strongly skew theoretical error estimates. While the combination of power spectrum and bispectrum is superior to using the power spectrum alone, the improvement may not be as significant as one might have hoped due to this plateauing in the bispectrum covariance.

3.6 Comparison between Dark Matter Simulations and Theory

The development of the `MODAL-LSS` toolkit is to allow straightforward comparisons between bispectra, either from simulations, observational data, or theory. In that cause we first test our method by estimating the bispectrum of 2LPT initial conditions (IC) generated by `L-PICOLA`, using the fact that it should reproduce the tree-level bispectrum[1]. We used a range of grid sizes to generate the initial conditions, and to combat cosmic variance at large scales we average over multiple realisations. Similar to the test in Section 2.2.4 we use Equations (2.11)

[1] See Section 1.4.3 for the derivation.

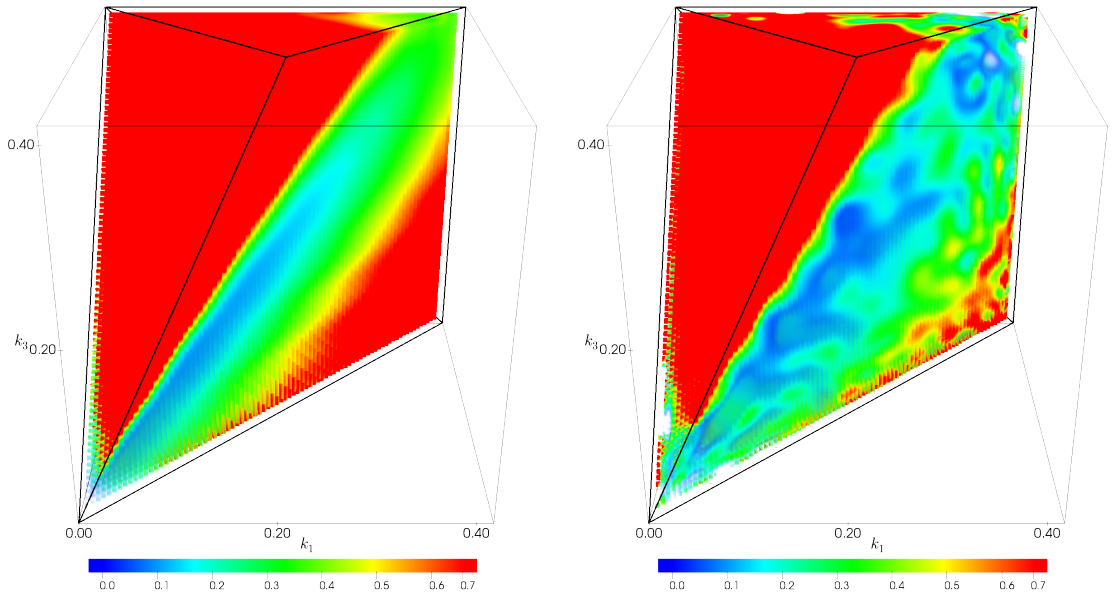

(a) 10000 averaged 256^3 COLA runs

(b) 10 averaged 512^3 COLA runs

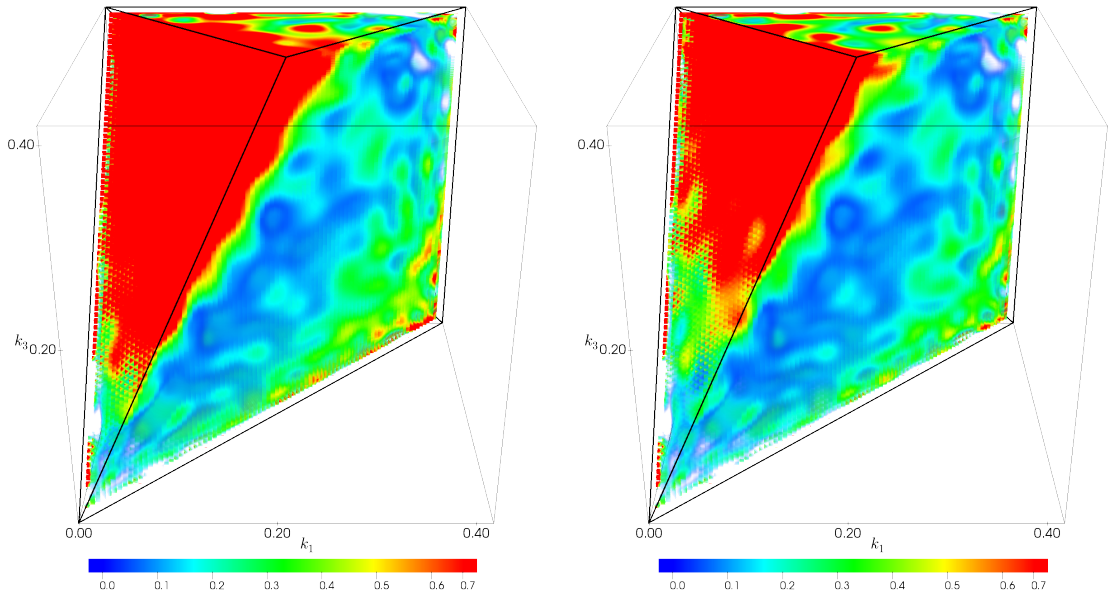

(c) 10 averaged 1024^3 COLA runs

(d) 10 averaged 2048^3 COLA runs

Fig. 3.6 The reconstructed bispectra from averaged 2LPT IC, and the desired signal, i.e. the tree-level bispectrum, plotted up to $k_{max} = 0.41\,h\,\mathrm{Mpc}^{-1}$. The colour scale is chosen to show the full range of the tree-level bispectrum, leading to significant saturation for the simulation bispectra. With increasing FFT grid size the IC bispectrum morphology approaches the theoretical one, but the amplitude remains grossly inflated. *(cont.)*

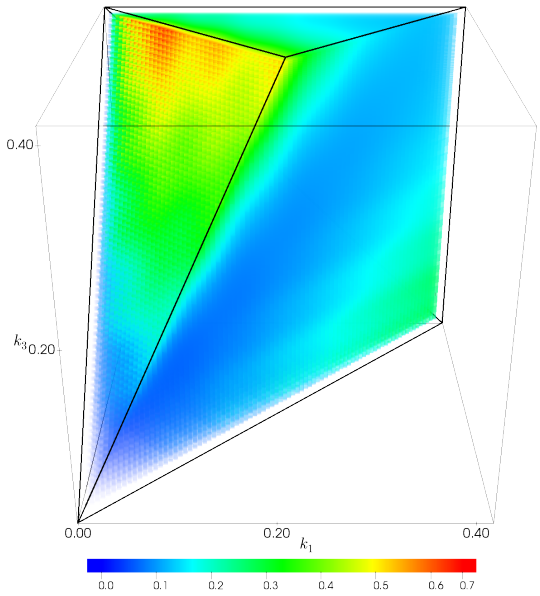

(e) Tree-level bispectrum

Fig. 3.6 The reconstructed bispectra from averaged 2LPT IC, and the desired signal, i.e. the tree-level bispectrum, plotted up to $k_{max} = 0.41\,h\,\mathrm{Mpc}^{-1}$.

and (2.24) to find that

$$\begin{aligned} \mathcal{S}_{\beta,\alpha} &= \frac{\sum_n \beta_n^R \alpha_n^R}{\sqrt{\sum_n (\beta_n^R)^2 \sum_n (\alpha_n^R)^2}}, \\ f_{nl}^{\beta,\alpha} &= \frac{\sum_n \beta_n^R \alpha_n^R}{\sum_n (\alpha_n^R)^2}. \end{aligned} \tag{3.8}$$

The correlators between the averaged runs and the tree-level bispectrum are shown in Table 3.3, and we also plot the reconstructed simulation bispectra in Figure 3.6.

The poor shape correlation ($< 95\%$) for low k is a strong indication that something is wrong with the IC, but cosmic variance cannot be the only source of error since a very large number of runs were used in the 256^3 case. We have also ruled out shot noise since it is not the correct shape. Moreover the large amplitude of the simulation bispectra leads to an inflated f_{nl} in a way that is dependent on the size of the FFT grid used. We propose this failure of the IC code to reproduce the correct bispectrum is due to both (i) transients, as discussed in [17, 193], and (ii) grid effects. Similar problems were observed in [98], and subsequently alleviated by the use of glass initial conditions. With more sophisticated technology at hand now we shall investigate this further in the near future.

$k_{max}\,(h\mathrm{Mpc}^{-1})$	10000 averaged 256^3 runs		10 averaged 512^3 runs		10 averaged 1024^3 runs		10 averaged 2048^3 runs	
	$\mathcal{S}_{\beta,\alpha}$	$f_{nl}^{\beta,\alpha}$	$\mathcal{S}_{\beta,\alpha}$	$f_{nl}^{\beta,\alpha}$	$\mathcal{S}_{\beta,\alpha}$	$f_{nl}^{\beta,\alpha}$	$\mathcal{S}_{\beta,\alpha}$	$f_{nl}^{\beta,\alpha}$
0.4123	0.9300	11.12	0.9339	5.603	0.9469	3.072	0.9583	1.830
0.8296	-	-	0.9501	6.076	0.9613	3.228	0.9794	1.895
1.6690	-	-	-	-	0.9696	3.442	0.9830	1.950
3.3429	-	-	-	-	-	-	0.9870	2.064

Table 3.3 Comparisons between averaged 2LPT IC bispectra and the tree-level bispectrum, where the IC have been generated with different grid sizes. The poor shape correlation at low k cannot be caused by cosmic variance alone due to the high number of runs used, and a clear trend of scale dependence can be seen in the f_{nl} correlator.

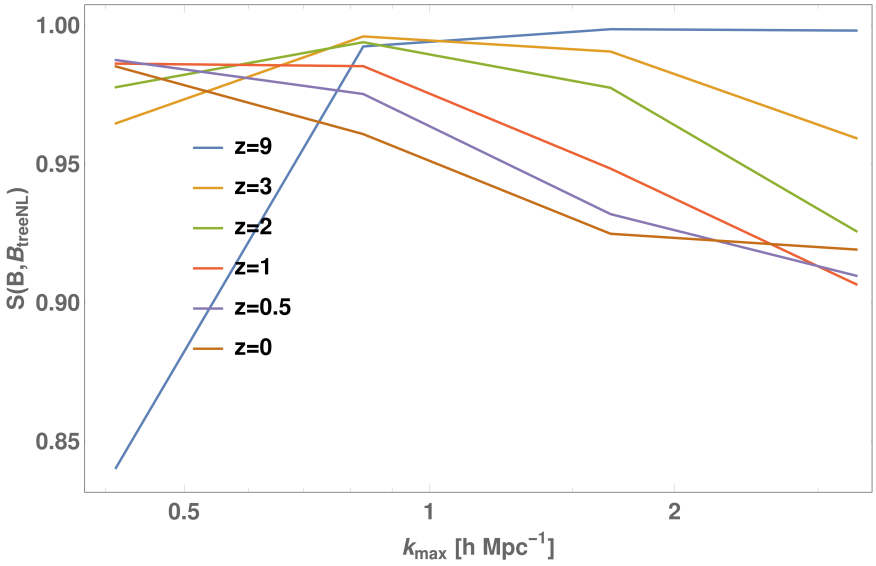

(a) Shape correlator

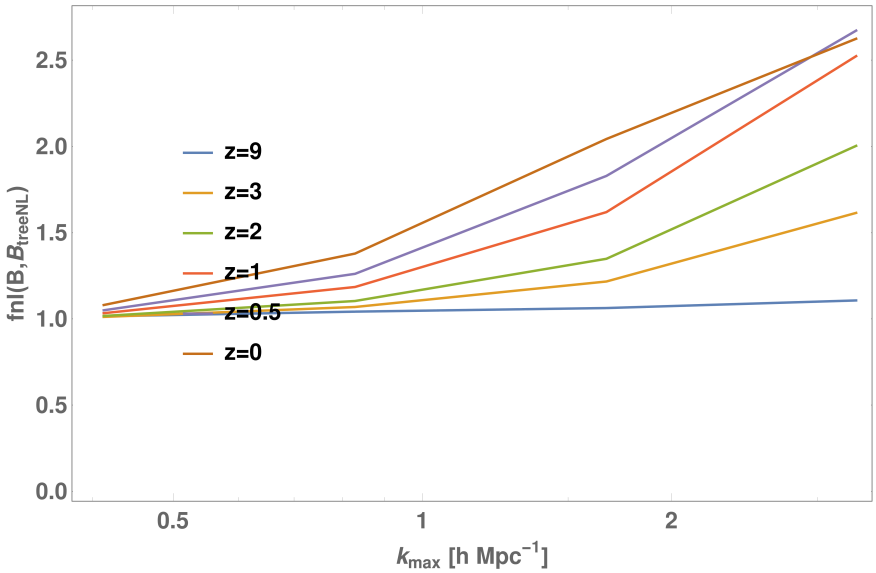

(b) f_{nl} correlator

Fig. 3.7 Correlators between a $1280\,h^{-1}$ Mpc `GADGET-3` simulation and the tree-level bispectrum at various redshifts. Transients is the likely suspect for the especially poor shape correlation at low k at redshift $z = 9$.

Another obvious candidate for our tests is the redshift evolution of a simulation. It is natural to expect a faithful adherence to the tree-level bispectrum at earlier times, even at high k. With the passage of time, and hence gravitational collapse, the non-linear signal will eventually dominate at small scales, leading to significant deviations from perturbation theory. This is shown clearly in Figure 3.7, where we compare the $1280\,h^{-1}$ Mpc GADGET-3 simulation to the tree-level bispectrum. As the smallest FFT grid we use in bispectrum estimation is 256^3 we unfortunately miss out on the observationally relevant scales of $k \sim 0.1\,h\mathrm{Mpc}^{-1}$, but our efforts to recover the tree-level bispectrum in larger simulations (i.e. 2560 and $5120\,h^{-1}$ Mpc) have failed, probably due to the same issues we encountered when we tried to extract the initial conditions bispectra. Transients are the most likely explanation for the poor shape correlation at low k, especially at redshift $z = 9$, as the correlation improves with time when these modes decay away.

3.7 Conclusions

With many large galaxy data-sets on the horizon, there is a pressing need for fast mock catalogue codes. While these fast codes are designed to only replicate the accuracy of N-body codes at large scales without resolving finer structure, we have found a simple and effective way to enhance their performance. A comparison between the 2LPT, PM and COLA algorithms against GADGET-3 shows 2LPT is deficient in both the power spectrum and bispectrum, while the COLA algorithm is successful in giving comparable performance to PM with fewer time-steps. Noting that the drop in bispectrum at large scales might be influenced by the power spectrum, we attempted to rectify this by boosting the power spectrum of the COLA simulation and saw a significant reduction in the power lost.

We have also addressed the theoretical modelling of the dark matter bispectrum by examining the full covariance of the MODAL-LSS estimator, showing that non-Gaussian contributions begin to dominate at $k \sim 0.1\,h\mathrm{Mpc}^{-1}$ and plateaus towards $\sim 0.1\%$. This is a significant adjustment as the non-Gaussian covariance is difficult to calculate even numerically, leading to the use of only the Gaussian covariance in most Fisher matrix forecasts. In principle, this will lead to gross underestimates of the theoretical error and thus the ability to put constraints on cosmological parameters. To show the power of the MODAL-LSS method in testing theoretical models against simulations we have compared (i) 2LPT initial conditions against the tree-level bispectrum, and (ii) a GADGET-3 simulation against the tree-level bispectrum at various redshifts. We have observed problematic transient modes and grid effects that affect the initial conditions, where the tree-level bispectrum should be recovered after averaging over many realisations. These effects propagate and

persist to late times on the largest scales, as shown in a GADGET-3 comparison, and must be addressed in the initial conditions.

Chapter 4

Halo Bispectrum

4.1 Introduction

Although dark matter simulations have given us a wealth of information about the clustering of matter in the universe, ultimately we need to map this information to the visible universe. Gravitational pull induces the formation of bound dark matter halos, and these virialised objects in turn create an environment in which baryons can collapse and form bound objects such as galaxies. The galaxies we observe in galaxy surveys, which live inside these halos, therefore act as biased tracers to the underlying dark matter distribution, as the spatial distribution of galaxies need not exactly mirror that of the dark matter [194]. To take advantage of high resolution galaxy data from future surveys we must therefore have a robust way to extract halo and galaxy distributions from N-body dark matter simulations. Many techniques for this process, known as halo finding, have been developed over the years (e.g. [195, 123, 124, 196–210, 14, 211–215]), but it remains a computationally intensive task, especially with the sheer number of simulations required for covariance matrix estimation. Additionally, to put constraints on cosmological parameters halo properties must be understood to percent level in order for theoretical and statistical uncertainties to be at the same level [14, 216, 217]. In this Thesis we present fast phenomenological prescriptions for producing mock galaxy catalogues that reproduce the power spectrum and bispectrum of a reference catalogue to better than 1% accuracy. In order to do so we examine the effects of the spatial distribution of galaxies within their host halos, the halo occupation number through the Halo Occupation Distribution (HOD) model, as well as a more sophisticated assembly bias model that jointly models the occupation number and halo concentration. Previous work estimating the dark matter bispectrum has shown its power in helping benchmark fast dark

matter codes (Chapter 3), and here we likewise validate these methods with both the power spectrum and bispectrum.

4.2 Halo catalogues

There are many techniques that have been developed to identify collapsed objects in dark matter simulations, but two methods remain a core part of the halo finding process. These are the Friends-of-Friends (FoF) algorithm [218], originally proposed in 1985, and the Spherical Overdensity (SO) algorithm [219], originally proposed in 1974. In its simplest form the FoF algorithm simply links together particles that are separated by a distance less than a given linking length b, resulting in distinct connected regions that are identified as collapsed halos. The SO algorithm on the other hand identifies peaks in the density field as the candidate halo centres, then assuming a spherical profile grows the halo until a density threshold is reached. There are shortcomings associated with naive implementations of both of these methods: the FoF algorithm is susceptible to erroneously connecting two distinct halos to each other via *linking bridges*, which are filaments between linked particles belonging to the 2 distinct halos; whereas the spherical assumption in SO does not reflect the true shape of halos. A particular difficulty of these position-based finders, yet crucial for the mapping of dark matter distribution to the galaxies we observe, is the classification of halos within halos, or *subhalos*, i.e. virialised objects that sit inside and orbit a larger, host halo. Many have introduced refinements to extend the capabilities of FoF and SO, for example by changing the FoF linking length or the SO density threshold as well as better taking advantage of other information given to us by cosmological simulations; please see [220] for a comprehensive review.

A relatively recent and novel approach to this old problem is the incorporation of velocity information of the particles, reducing the ambiguity in determining particle membership between overlapping halos. While this additional information is clearly useful for distinguishing subhalos from its host halos due to their relative motion, working in phase-space necessitates the creation of a metric that suitably weights the relative positions and velocities of the particles. The 6D phase-space halo finder we adopt for this Thesis is `ROCKSTAR` [14], which further utilises *temporal* data across simulation time steps to ensure consistency of halo properties. Furthermore the authors claim it to be the first grid- and orientation-independent adaptive phase-space code, and possesses the unprecedented ability to probe substructure masses down to the very centres of host halos. Here we give a brief overview of the mechanics of the `ROCKSTAR` algorithm (see also Figure 4.1).

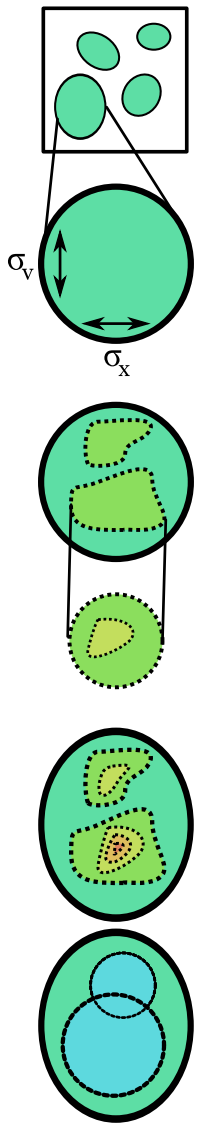

1. The simulation volume is divided into 3D Friends-of-Friends groups for easy parallelization.

2. For each group, particle positions and velocities are divided (normalized) by the group position and velocity dispersions, giving a natural phase-space metric.

3. A phase-space linking length is adaptively chosen such that 70% of the group's particles are linked together in subgroups.

4. The process repeats for each subgroup: renormalization, a new linking-length, and a new level of substructure calculated.

5. Once all levels of substructure are found, seed halos are placed at the lowest substructure levels and particles are assigned hierarchically to the closest seed halo in phase space.

6. Once particles have been assigned to halos, unbound particles are removed and halo properties (positions, velocities, etc.) are calculated.

Fig. 4.1 A visual summary of the ROCKSTAR algorithm [14].

The simulation box is first partitioned with a fast implementation of position-based FoF and a large linking length of $b = 0.28$ (in units of the mean inter-particle distance). Likewise in the 3D case, an adaptive metric must be used if one is to find substructures at all levels. For each of these 3D FoF groups a hierarchy of 6D phase-space FoF subgroups is built up by adapting the phase-space linking length at every level so that only 70% of the particles are linked together in its subgroups, until the number of particles in the deepest level falls under a predefined threshold (here set to 10). The phase-space metric they adopt is weighted by the standard deviations in position, σ_x, and velocity σ_v, of the particles within a (3D or 6D) FoF group, i.e. for two particles p_1 and p_2 the metric is:

$$d(p_1, p_2) = \left(\frac{|\mathbf{x}_1 - \mathbf{x}_2|^2}{\sigma_x^2} + \frac{|\mathbf{v}_1 - \mathbf{v}_2|^2}{\sigma_v^2} \right)^{1/2} . \tag{4.1}$$

Once this phase-space hierarchy is built, the deepest levels in the hierarchy are identified as seed halos, and all particles in the base 3D FoF group are assigned to these seed halos from the bottom-up. If a seed halo is the only child of its parent then all the particles of the parent will be assigned to that seed halo. Otherwise if a parent has multiple subgroups then particle membership is determined by proximity in phase-space. In this instance the metric (Equation (4.1)) is modified to reflect halo and not particle properties; for a halo h and particle p the metric is

$$d(h, p) = \left(\frac{|\mathbf{x}_h - \mathbf{x}_p|^2}{r_{vir}^2} + \frac{|\mathbf{v}_h - \mathbf{v}_p|^2}{\sigma_v^2} \right)^{1/2} , \tag{4.2}$$

where r_{vir} is the current virial radius of the halo and now σ_v is the current velocity dispersion of the halo. This procedure is repeated recursively along the hierarchical ladder until particle assignment is complete. A significant advantage of this assignment scheme is the assurance that particles that belong to the host halo will not be mis-assigned to the subhalo, or vice versa, even if the subhalo sits close to the host halo centre. This is because host halo particles and subhalo particles should have different distributions in phase-space even if they are close in position-space.

Finally, host-subhalo relationships are determined based on phase-space distances before halo masses are calculated to avoid ambiguity when multiple halos are involved. At each level the halos are first ordered by the number of assigned particles. Starting with the lowest one, each halo centre is treated as a particle, and its distance to the other halos are calculated with Equation (4.2). The halo being examined is then assigned as a subhalo of the closest larger halo. These relationships are checked against the previous time-step, if available, for

consistency across time-steps. After all assignments have been made, unbounded particles are removed by a modified Barnes-Hut method from the halos, and halo properties are calculated.

4.2.1 Benchmark galaxy mock catalogue

Our benchmark dark matter simulation is the $1280\,h^{-1}$ Mpc `GADGET-3` simulation previously introduced in Section 3.2. The particle mass of the simulation is $M_p = \rho_{crit}\Omega_m \frac{L^3}{N_p^3} = \frac{3H^2\Omega_m}{8\pi G}\frac{L^3}{N_p^3} = 2.093 \times 10^{10}\,h^{-1}M_\odot$.

To obtain a benchmark galaxy mock catalogue we first ran `ROCKSTAR` on the `GADGET-3` output. Since small halos are unreliable we impose a mass threshold of $M_{200b} > 10^{12}\,h^{-1}M_\odot$ on the parent halos of the `ROCKSTAR` output, where M_{200b} means the mass enclosed by the halo corresponds to a spherical overdensity of 200 times the background density of the Universe. This cuts all parent halos with fewer than 50 particles, which is roughly the same criterion adopted in [143, 144]. The benchmark halo mock catalogue then consists of all parent halos that pass this threshold alongside all subhalos they contain, if any. In this Thesis we use the halos as proxies for galaxies, such that every parent halo hosts a central galaxy at its core, and all the subhalos of the parent hosts a satellite galaxy each. Our benchmark galaxy mock catalogue is therefore identical to the benchmark halo mock catalogue, and we will be using these terms interchangeably.

The purpose of this Chapter is to investigate phenomenological methods to reproduce the statistics of the benchmark galaxy mock catalogue without detailed information given by the simulation. We restrict ourselves to the mass, position, and halo concentration of the parent halos, and build models that inform us of the number and positions of the satellite galaxies in each parent halo. We define the benchmark catalogue as above to examine these effects rather than reproduce a realistic mock galaxy catalogue that matches observational data, e.g. in [143]. We are also interested in first understanding these effects in configuration space, and as such will not include observational effects such as Redshift Space Distortions (RSD). This is because the RSD signal will dominate in the bispectrum at small scales and swamp the contributions that we are interested in here. After we correctly model these effects in configuration space we shall tackle RSD effects in the future. Additionally, both the projected bispectrum [221] or bispectrum monopole [222] are rather insensitive to RSD effects, thus our methods are well suited to the study of these observables. We note here that our previous investigation of the dark matter bispectrum using these simulations have uncovered problematic transient modes that persist to late times (Section 3.6). However this should not interfere with our work here, as these modes only distort the bispectrum signal at large scales, and their effects will cancel when we make comparisons between

different phenomenological methods. When calculating statistics we follow the example of others, e.g. [145, 223], and use the number density field where each object is weighted by 1 instead of their mass in the Cloud in Cell (CIC) assignment scheme, which is on a 1024^3 grid throughout this Chapter.

4.2.2 Halo profile

We tackle the distribution of galaxies within a halo by first examining the relevance of the halo shape. It is well known in the literature, particularly from dark matter simulations, that halos are triaxial objects [224–226], and that their shape are complicated functions of time, halo mass, and choice of halo radius. Halo shapes have been predicted analytically as well within the ellipsoidal-collapse model in [227]. In principle one should take into account these effects when building a halo mock catalogue, but as we shall see in Section 4.4, halo triaxiality only has a small effect compared to the choice of halo profile in the power spectrum and bispectrum, and only at small scales. Consequently, in this Thesis we only consider radially symmetric profiles here and randomise the solid angle distribution of each halo. We leave the inclusion of halo triaxiality for future work.

There are a number of radially symmetric halo profiles in the literature that we can use to populate halos with satellite galaxies. One popular choice is the NFW profile introduced in Section 1.4.5, which was adopted in the generation of BOSS galaxy mock catalogues [145]:

$$\rho(r|M_{vir},c) = \frac{M_{vir}}{4\pi rc(R_{vir}+rc)^2}\frac{c^3}{\log(1+c)-\frac{c}{1+c}}. \tag{4.3}$$

To populate the halos with the NFW profile we assume the radial probability density function (PDF) of the mass distribution in a halo is proportional to $\rho(r|M_{vir},c)$, and then obtain the positions of the galaxies by inverse sampling. This first involves calculating the cumulative distribution function (CDF) from the PDF:

$$\begin{aligned}\mathrm{CDF}_{\mathrm{NFW}}(r|M_{vir},c) &= \frac{\int_0^r \rho(r'|M_{vir},c)4\pi r'^2\,dr'}{\int_0^{R_{vir}} \rho(r'|M_{vir},c)4\pi r'^2\,dr'},\\ &= \frac{\log\left(1+\frac{cr}{R_{vir}}\right)-\frac{cr}{R_{vir}+cr}}{\log(1+c)-\frac{c}{1+c}}.\end{aligned} \tag{4.4}$$

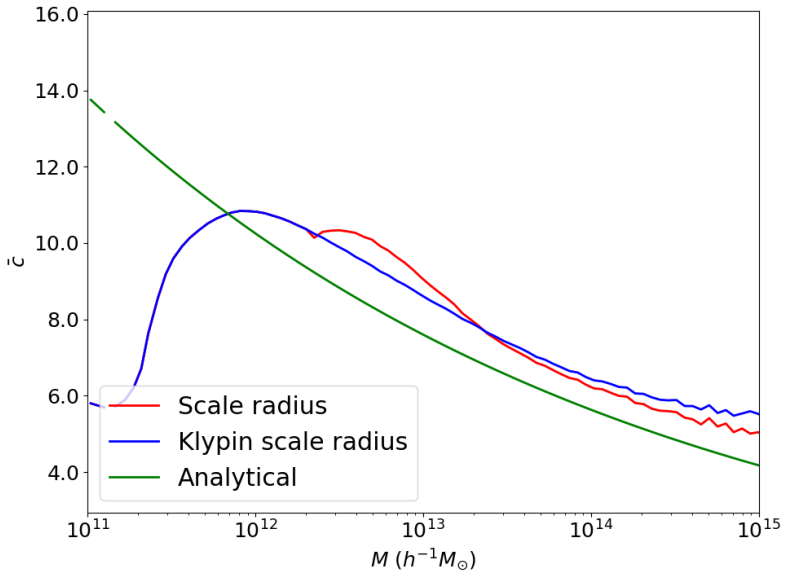

Fig. 4.2 Mean concentration of the benchmark ROCKSTAR halos as a function of their mass, calculated from both the scale radius and Klypin scale radius, as well as the analytical fit in [15] (Equation (4.6)).

We then draw samples from the inverse of the CDF, $\mathrm{CDF}^{-1}_{\mathrm{NFW}}$, with a uniform distribution $u \sim U \in [0,1]$:

$$r = \mathrm{CDF}^{-1}_{\mathrm{NFW}}(u|M_{vir},c). \tag{4.5}$$

Since the inversion of the CDF is numerically expensive we instead calculate the desired r by interpolating the tabulated CDF. This is 20-30 times faster and allows much greater efficiency in the generation of mock catalogues at a small cost in accuracy. Finally, we model the concentration c with this analytical fit as proposed in [15]:

$$\bar{c}(M,z) = \frac{9}{1+z}\left(\frac{M}{M_{NL}}\right)^{-0.13}, \tag{4.6}$$

where $M_{NL} = \frac{4\pi}{3}\bar{\rho}(z)(\frac{2\pi}{k_{NL}})^3$ is the non-linear mass scale, and k_{NL} is defined by the linear power spectrum P_L as $k^3_{NL}P_L(k_{NL},z) = 2\pi^2$.

To judge whether the NFW profile is a good choice for our purposes we first compared the benchmark mean concentration to the analytical fit in Equation (4.6). ROCKSTAR fits an NFW profile by calculating both the scale radius r_s and the Klypin scale radius $r_{s,K}$ [228], which is derived from v_{max}, the maximum circular velocity, and M_{vir}. We have plotted the

mean concentration computed from r_s and $r_{s,K}$ against the analytical fit in Figure 4.2. While the Klypin concentration demonstrates better numerical stability overall, it is not clear that it is more robust for halos with fewer than 100 particles as the authors of ROCKSTAR claim [14]. We shall be using the Klypin concentration in all our methods discussed below. We note that while Equation (4.6) seems to qualitatively capture the correct power law behaviour, the magnitude is too low by about 10-20%.

More importantly, while the NFW profile is used in the literature to populate halos with galaxies, it is ultimately a fit to the dark matter profile and may not reflect the subhalo density profile. Comparisons between the NFW profile and the number density profile for the ROCKSTAR benchmark catalogue at different mass bins is shown in Figure 4.3. Throughout the paper we only populate subhalos to the virial radius R_{vir}. In these plots, the NFW profile is calculated using the average Klypin concentration given by ROCKSTAR for the mean halo mass of the bin. Additionally, distances are scaled by the virial radius R_{vir}, since that is the distance ROCKSTAR uses when fitting the NFW profile.

We found that the NFW profile is clearly more concentrated near the centre of the halo than the density profile of the benchmark subhalos (as observed already in, for example, [229, 146, 147, 230]). Consequently, for a NFW profile based galaxy catalogue we expect a stronger correlation than the benchmark at small scales. We have also modified the NFW profile by keeping its functional form but changing the concentration, but this was not a good fit to the ROCKSTAR profile as shown in Figure 4.3. Following [231], we then adopted a universal power law $\rho \propto r^{-\gamma}$, where $\gamma \sim 1$ is our fiducial halo profile, such that

$$\mathrm{CDF}_{\mathrm{pow}}(r|M_{vir},c) = \left(\frac{r}{R_{vir}}\right)^{3-\gamma}. \tag{4.7}$$

We have found that $\gamma \approx 1$ is a satisfactory fit to the subhalo number distribution, as shown in Figures 4.3 and 4.4.

4.2.3 Halo Occupation Distribution (HOD)

Another important consideration in the population of parent halos is the halo occupation number, i.e. the number of galaxies per halo. This is typically modelled with the 5-parameter HOD algorithm discussed in Section 1.4.5. Here instead of using the error function we employ a Heaviside cut for $\bar{N}_{\mathrm{cent}}$:

$$\bar{N}_{\mathrm{cent}}(M) = \theta(M - M_0), \tag{4.8}$$

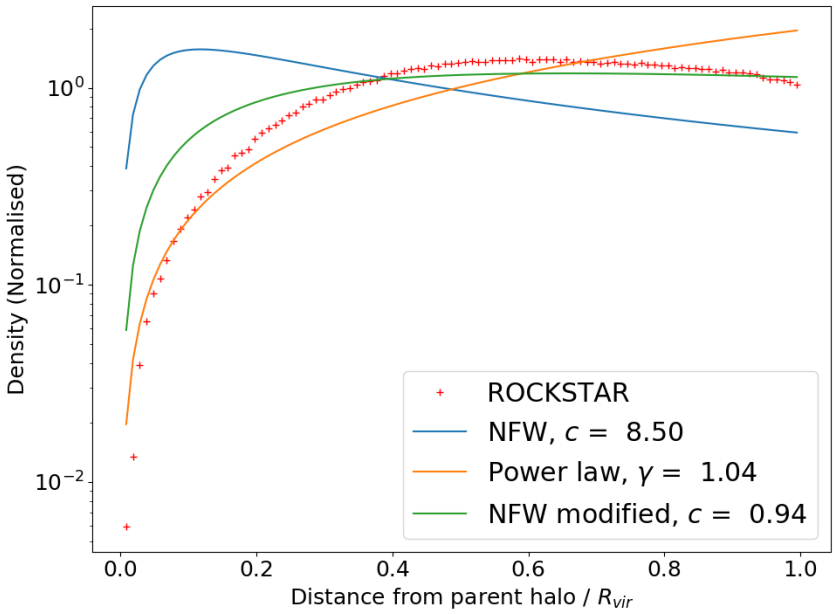

$$M = (0.62 - 2.2) \times 10^{13} h^{-1} M_{\odot}$$

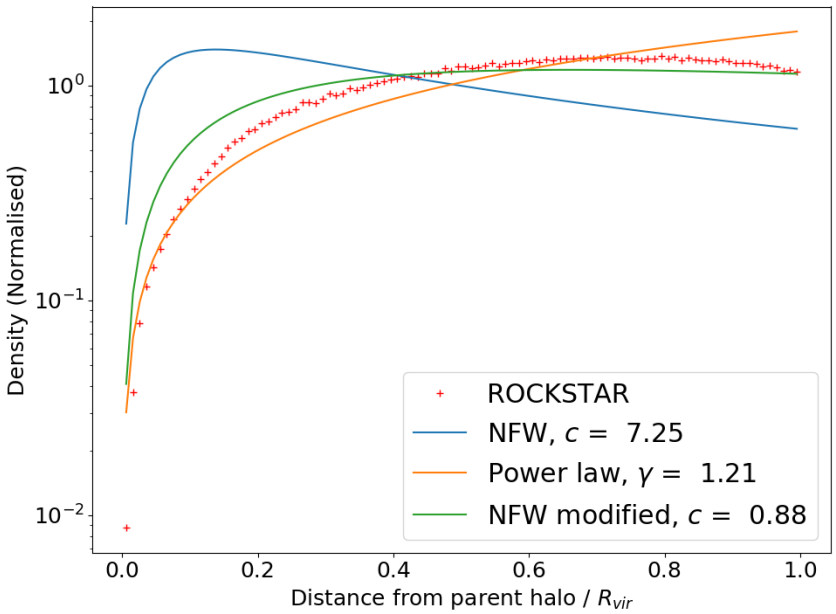

$$M = (2.2 - 7.6) \times 10^{13} h^{-1} M_{\odot}$$

Fig. 4.3 The subhalo number density profile given by ROCKSTAR and NFW for parent halos in various mass bins, as well as a power law and modified NFW fits to the ROCKSTAR data. Distances are scaled by R_{vir} measured by ROCKSTAR. *(cont.)*

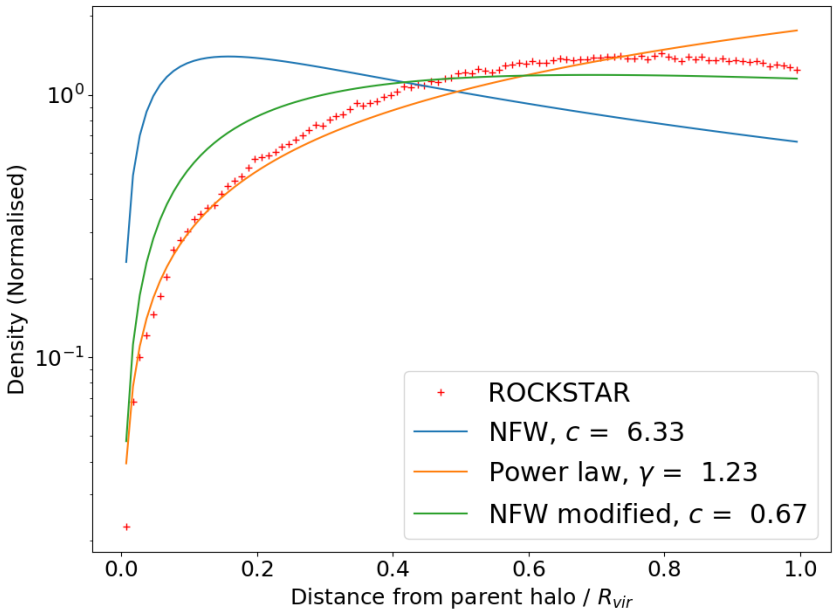

$$M = (0.76 - 2.7) \times 10^{14} h^{-1} M_{\odot}$$

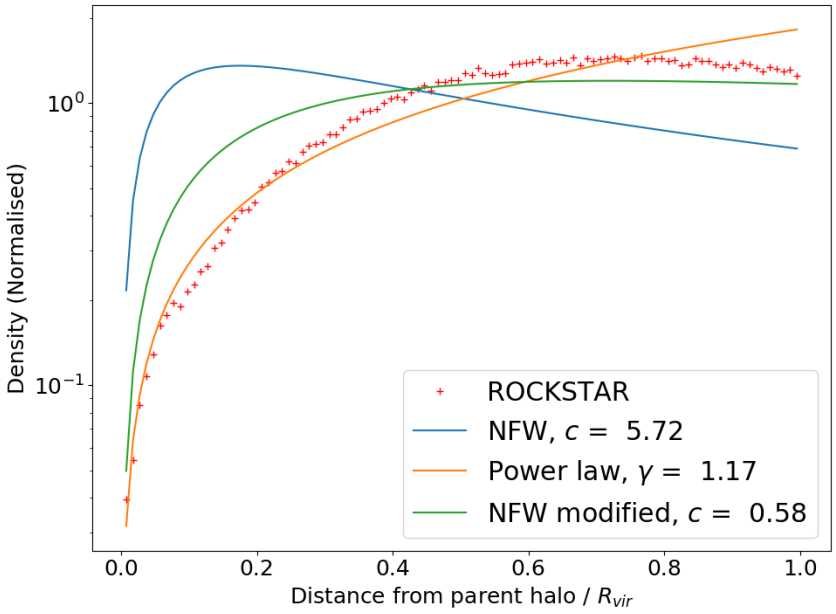

$$M = (2.7 - 9.3) \times 10^{14} h^{-1} M_{\odot}$$

Fig. 4.3 The subhalo number density profile given by ROCKSTAR and NFW for parent halos in various mass bins, as well as a power law and modified NFW fits to the ROCKSTAR data. Distances are scaled by R_{vir} measured by ROCKSTAR.

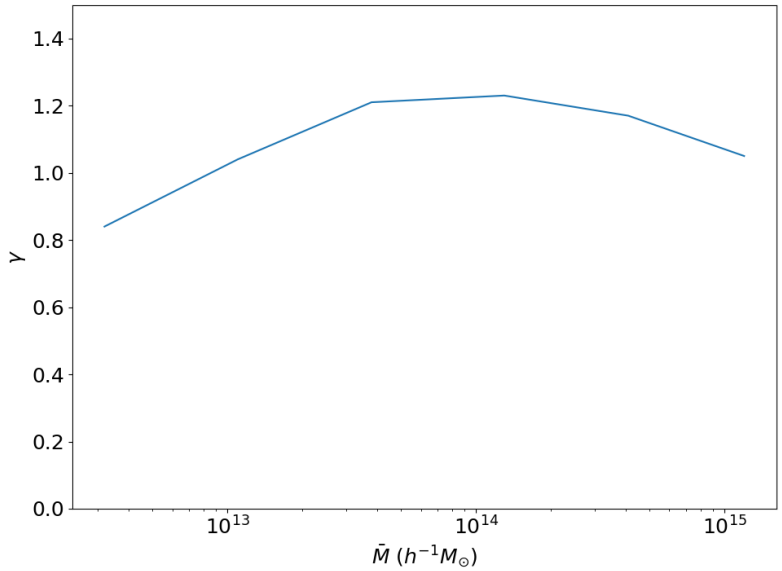

Fig. 4.4 Power law fit to the halo profile at different mass bins.

reducing the number of parameters to 4. This is appropriate as we impose a mass cut on the parent halo when constructing the benchmark galaxy catalogue. These 4 parameters give us freedom to tweak the power spectrum and bispectrum of our galaxy mock catalogues to better reproduce those of the benchmark sample. The total number of galaxies is

$$n_g = \int dM\, n(M)\theta(M - M_0)\left(1 + \left(\frac{M - \kappa M_0}{M_1}\right)^{\alpha}\right), \tag{4.9}$$

where $n(M)$ is the halo mass function that gives the number density of halos for a given mass M. If the variation in the parameters are small we obtain the following perturbation to the

number of galaxies to first order:

$$
\begin{aligned}
&\Delta n_g \\
&= -\int dM\, n(M) \\
&\quad \times \left(\delta(M-M_0)\frac{\Delta M_0}{M_0} M_0 \left(1+\frac{\alpha\kappa}{M_1}\left(\frac{M-\kappa M_0}{M_1}\right)^{\alpha-1}\right)\right. \\
&\qquad + \theta(M-M_0)\frac{\Delta\kappa}{\kappa}\kappa\frac{\alpha M_0}{M_1}\left(\frac{M-\kappa M_0}{M_1}\right)^{\alpha-1} \\
&\qquad + \theta(M-M_0)\frac{\Delta M_1}{M_1} M_1 \frac{\alpha(M-\kappa M_0)}{M_1^2}\left(\frac{M-\kappa M_0}{M_1}\right)^{\alpha-1} \\
&\qquad \left. - \theta(M-M_0)\frac{\Delta\alpha}{\alpha}\alpha\log\left(\frac{M-\kappa M_0}{M_1}\right)\left(\frac{M-\kappa M_0}{M_1}\right)^{\alpha}\right),
\end{aligned}
\tag{4.10}
$$

and we enforce $\Delta n_g = 0$ to conserve particle number when changing the parameters.

In Figure 4.5 we show the HOD $\bar{N}_g(M)$ from our benchmark `ROCKSTAR` catalogue (which will be referred to as the benchmark HOD model below), and the best fit for the 4-parameter HOD using the `least_squares` algorithm with the default Trust Region Reflective method [232] in `Scipy`, while keeping the total number of galaxies constant. As a comparison we also utilise the `curve_fit` algorithm from `Scipy`, using the default Levenberg-Marquardt method [192], to obtain an unconstrained fit to the benchmark HOD. The best fit parameters for the constrained fit are $\log(M_0) = 11.76$, $\kappa = 0.89$, $\log(M_1) = 13.35$ and $\alpha = 1.04$, with only a $4\times10^{-4}\%$ deficiency in the number of galaxies.

4.3 Halo polyspectra

4.3.1 Power spectrum and Bispectrum

The power spectra of our benchmark dark matter and galaxy catalogues at redshifts $z = 0, 0.5, 1$ are plotted in Figure 4.6. Our galaxy catalogue consists of parent halos with mass in the range of 1×10^{12} and $3.2\times10^{15}h^{-1}M_\odot$ and all their subhalos, and has a number density of $0.0056\,h^3\,\mathrm{Mpc}^{-3}$, which is similar to the number density of the LOWZ galaxy sample in BOSS at low redshift [233]. It is well known in the literature that while the dark matter power spectrum grows with time, the growth of the halo power spectrum is slow [234, 235]. At large scales the linear bias relationship $b_1 = \delta_g/\delta$ between dark matter and galaxies tends to a constant [236], and since the dark matter power spectrum grows as $D_1^2(z)$ at these scales,

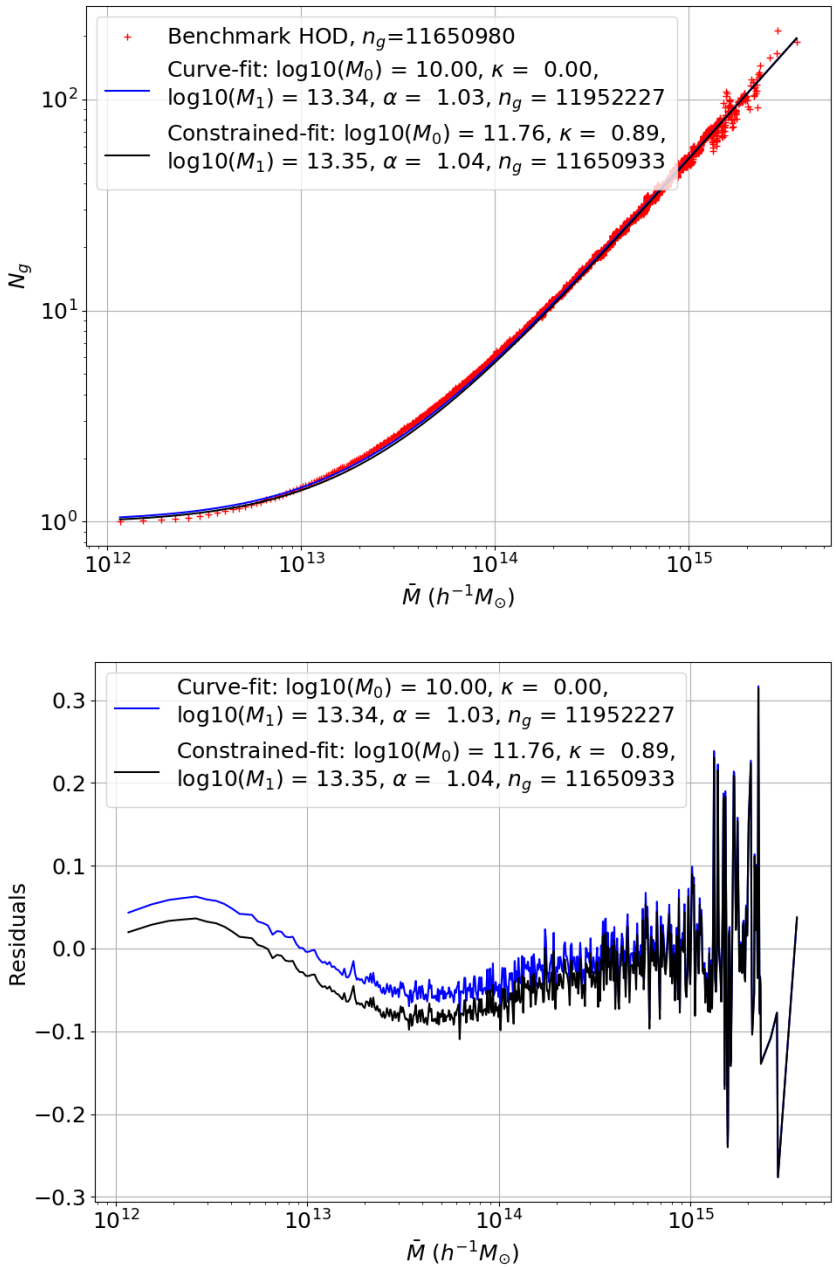

Fig. 4.5 Top panel: Fits to the benchmark HOD with our 4 parameters, both constraining and not constraining the total number of galaxies. Bottom panel: Residuals of these fits.

where $D_1(z)$ is the linear growth factor, we expect $b_1(z) \propto 1/D_1(z)$. This is also shown clearly in Figure 4.6, giving a value of $b_1 \approx 1.1$.

The full bispectra of the benchmark catalogue at various redshifts estimated with `MODAL-LSS` are shown in Figure 4.7, along with the corresponding dark matter bispectra plotted for reference.

4.3.2 `MODAL-LSS` bispectrum methodology

The `MODAL-LSS` methodology for estimating the bispectrum has already been introduced in Section 2.2. Here we further define a 'sliced' correlator between bispectra which integrates over transverse degrees of freedom $K \equiv k_1 + k_2 + k_3 = \text{const.}$ on the tetrahedron:

$$\left[B_i, B_j\right]^S_K \equiv \frac{V}{\pi} \int_{\Delta\mathcal{V}_B} dV_k \, k_1 k_2 k_3 \frac{B_i(k_1,k_2,k_3) B_j(k_1,k_2,k_3)}{P(k_1)P(k_2)P(k_3)}. \tag{4.11}$$

The new restricted integration region, $\Delta\mathcal{V}_B$, encompasses a range of these K slices such that:

$$K < k_1 + k_2 + k_3 < K + \Delta K. \tag{4.12}$$

Similarly we define the sliced f_{nl} correlator as

$$f^S_{nl}(B_i, B_j, K) \equiv \frac{\left[B_i, B_j\right]^S_K}{\left[B_j, B_j\right]^S_K}. \tag{4.13}$$

4.3.3 Halo three-shape model

The three-shape bispectrum model was previously introduced in Section 1.4.4. The parameters $A - F$ at redshift $z = 0$ across the range $0.1\,h\,\text{Mpc}^{-1} < K < 6\,h\,\text{Mpc}^{-1}$ take the values [11]:

$$\begin{aligned} A &= 2.45 \times 10^6, & B &= 0.054, \\ C &= 140, & D &= 1.9, \\ E &= 7.5\,k_{\text{NL}}, & F &\equiv 1.0 \end{aligned} \tag{4.14}$$

with $k_{\text{NL}} = 0.25\,h\,\text{Mpc}^{-1}$. We note that this approximate fit applies across a much wider set of redshifts $z < 10$ (at about 10% precision) and, here, F has been fixed to unity to match the tree-level gravitational bispectrum as $K \to 0$ (i.e. with unit bias). Since the dark matter simulation we currently have is of much higher resolution and precision than previously, we

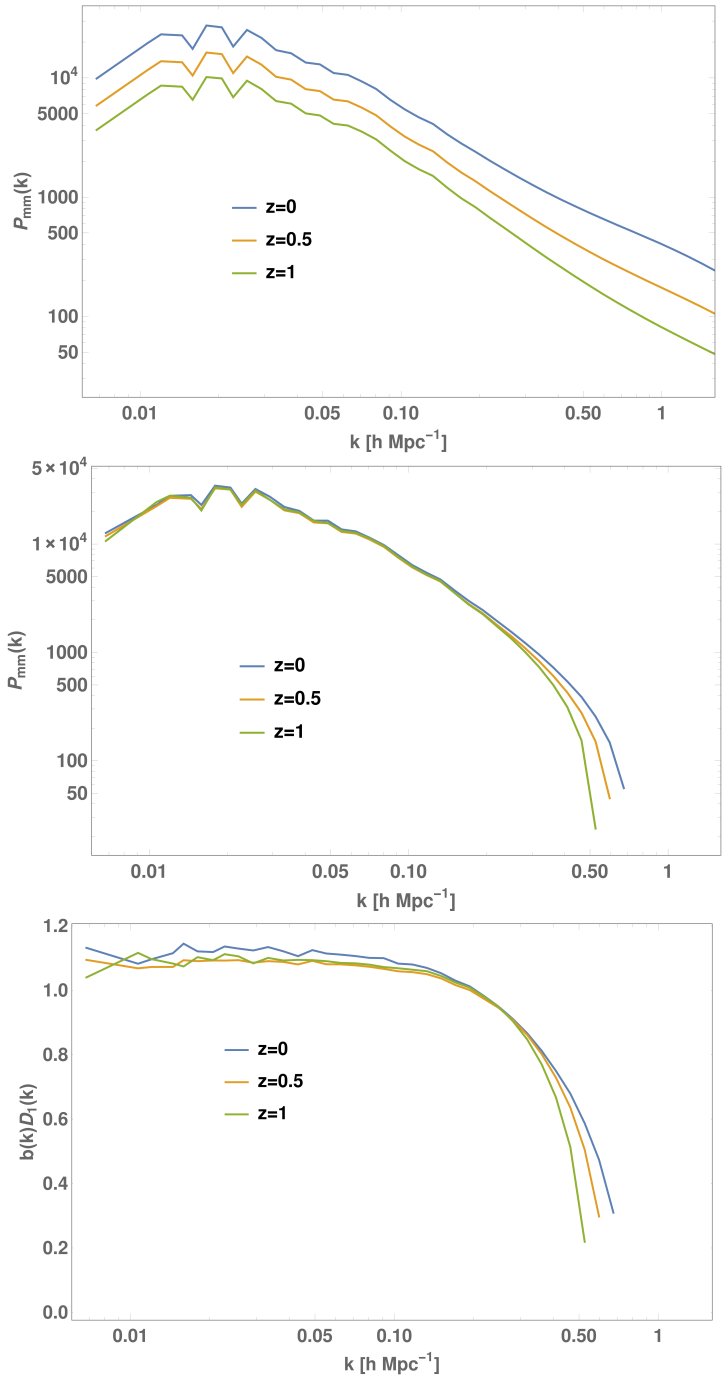

Fig. 4.6 Redshift evolution of the estimated power spectrum of the $1280\,h^{-1}$ Mpc benchmark GADGET-3 dark matter simulation (top), and the benchmark galaxy mock catalogue derived from it using ROCKSTAR (after shot noise subtraction, middle), plotted up to $k_{max} = 1.6\,h\,\mathrm{Mpc}^{-1}$. The bottom panel shows the product between the bias parameter, obtained from $b = \sqrt{P_{hh}/P_{mm}}$, and the linear growth factor D_1, which tends to a constant at large scales irrespective of redshift.

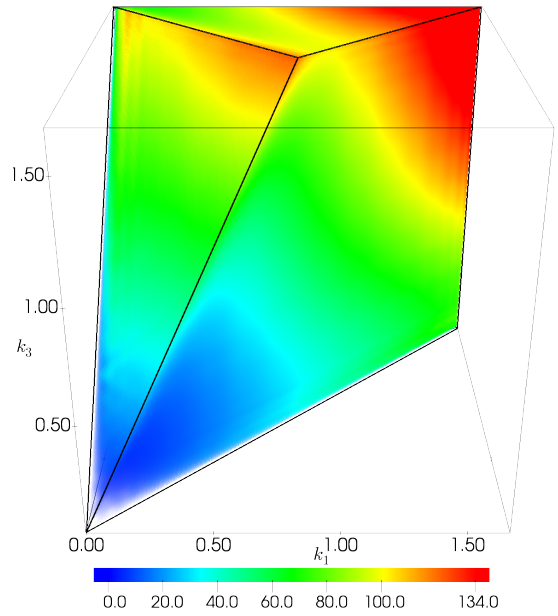

Dark matter, $z = 1$

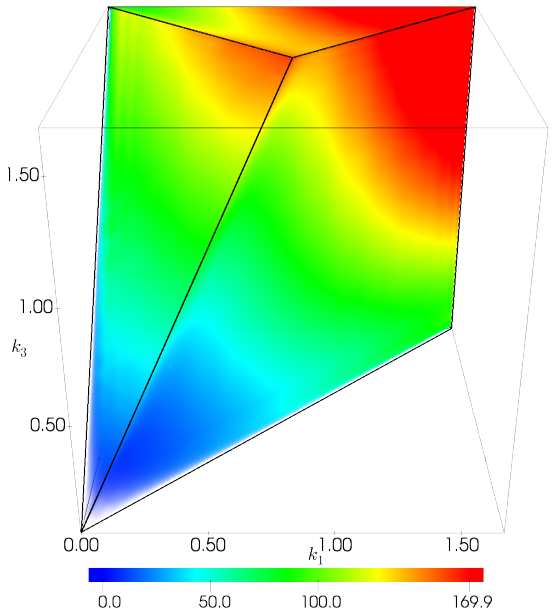

Dark matter, $z = 0.5$

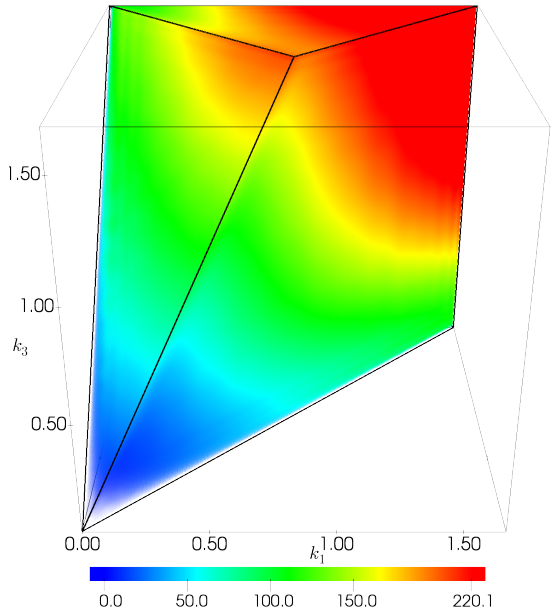

Dark matter, $z = 0$

Fig. 4.7 Redshift evolution of the estimated bispectra of the $1280\,h^{-1}$ Mpc benchmark GADGET-3 dark matter simulation, and the benchmark galaxy mock catalogue derived from it using ROCKSTAR, plotted up to $k_{max} = 1.6\,h\,\mathrm{Mpc}^{-1}$. *(cont.)*

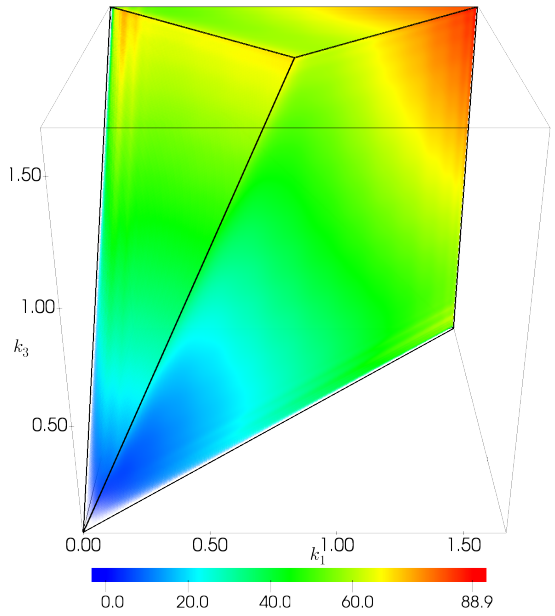

(d) Galaxies, $z = 1$

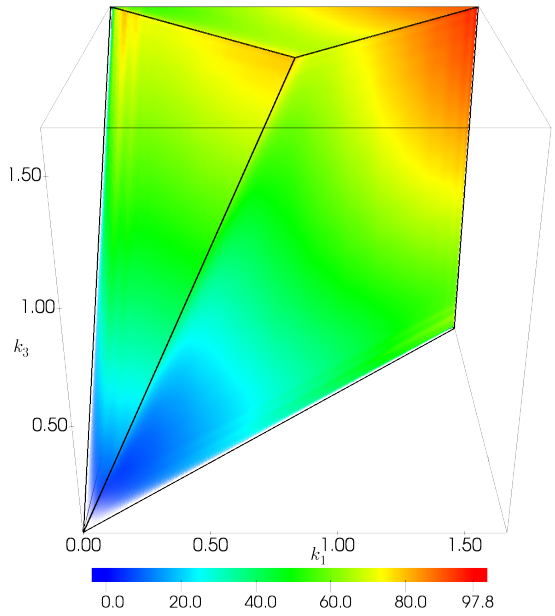

(e) Galaxies, $z = 0.5$

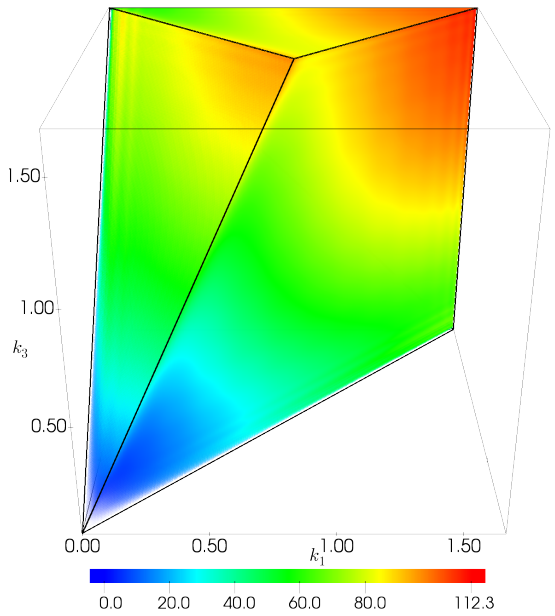

(f) Galaxies, $z = 0$

Fig. 4.7 Redshift evolution of the estimated bispectra of the $1280\,h^{-1}$ Mpc benchmark GADGET-3 dark matter simulation, and the benchmark galaxy mock catalogue derived from it using ROCKSTAR, plotted up to $k_{max} = 1.6\,h\,\mathrm{Mpc}^{-1}$.

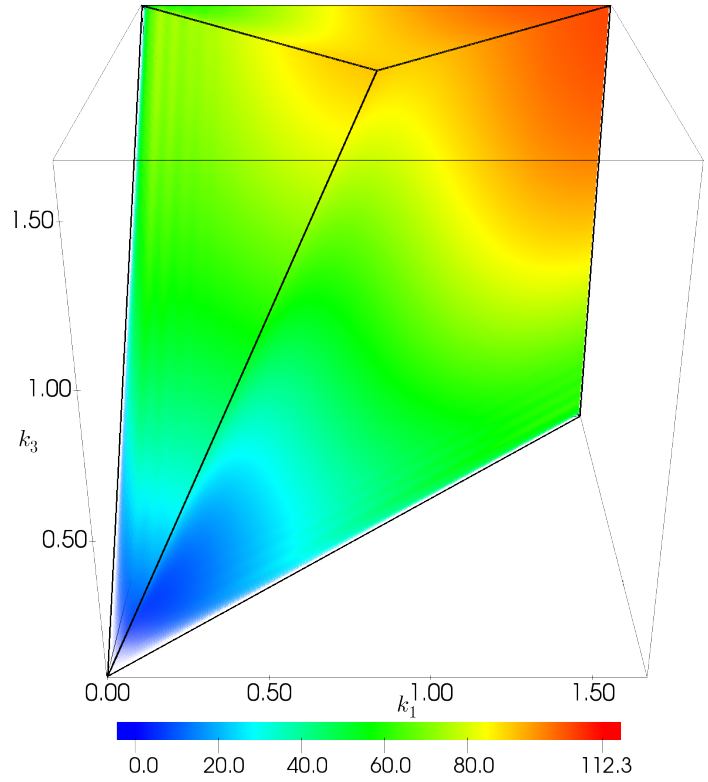

Fig. 4.8 Best fit three-shape model to the bispectrum of the benchmark ROCKSTAR catalogue.

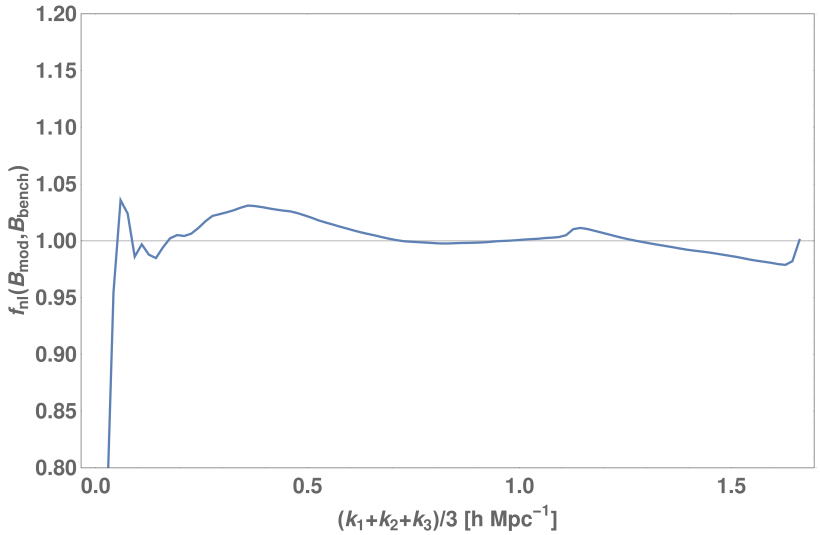

Fig. 4.9 Sliced f_{nl} correlation between the best fit three-shape model to the benchmark, and the benchmark. The feature observed at $K/3 = 1.1\,h\,\mathrm{Mpc}^{-1}$ here is due to the transition from the tetrahedral region in the bottom to the pyramid at the top, causing a kink in the sliced correlator, and is not a real physical effect.

update the best fit parameter values to the following:

$$\begin{aligned} A &= 2.64 \times 10^6, & B &= 0.057, \\ C &= 95, & D &= 2.0, \\ E &= 10.1\, k_{\mathrm{NL}}, & F &\equiv 1.0, \end{aligned} \tag{4.15}$$

This yields a high total correlation at $k_{\mathrm{max}} = 1.7\, h\,\mathrm{Mpc}^{-1}$ of 98.4% with new simulation data, and 97.1% with the original three-shape model (Equation (4.14)). We note that there are some degeneracies between the three shapes, but we leave detailed error estimation of these dark matter parameters for a future publication. We also note that there are transient grid effects that temporarily increase the tree-level gravitational bispectrum for N-body simulations with 2LPT initial conditions (identified in previous papers [98, 11]); even for the high redshift initial conditions used in this Thesis, this persists at late times leaving an offset in the dark matter bispectrum of a few percent for small k. This small systematic effect can be avoided with 'glass' initial conditions for the N-body simulations [98, 11] or through quantitative analysis and subtraction (but this is not the focus of the present work, see the discussion in Section 3.6).

We can consider using the same three shapes to fit to our benchmark halo bispectrum $B_{\mathrm{hhh}}(k_1, k_2, k_3)$, but in principle we might require more than three shapes to achieve an adequate correlation. For example, bias considerations bifurcate the tree-level gravitational bispectrum (Equation (1.123)) into several apparently different shapes at leading order (LO) [237]:

$$\begin{aligned} B^{\mathrm{LO}}_{\mathrm{hhh}}(k_1, k_2, k_3) = {} & b_1^3 B^{\mathrm{treeNL}}(k_1, k_2, k_3) \\ & + b_1^2 \left[b_2 + b_{K^2} \left((\hat{\mathbf{k}}_1 \cdot \hat{\mathbf{k}}_2)^2 + \tfrac{1}{3} \right) \right] \left(P(k_1) P(k_2) + 2\,\mathrm{perms.} \right) \\ & + B^{\mathrm{stoch}}_{\mathcal{E}} + b_1^3 \left(P^{\mathrm{stoch}}_{\mathcal{E}} P(k_1) + 2\,\mathrm{perms.} \right), \end{aligned} \tag{4.16}$$

where b_1, b_2 are the first- and second-order bias parameters, b_{K^2} is the 'tidal' bias parameter, and $P^{\mathrm{stoch}}_{\mathcal{E}}$, $B^{\mathrm{stoch}}_{\mathcal{E}}$ are the stochastic power spectrum and bispectrum respectively. Closer examination, however, reveals that the second-order bias shape can be incorporated with appropriate scalings in the squeezed two-halo shape B^{squeez} and the stochastic bispectrum $B^{\mathrm{stoch}}_{\mathcal{E}}$ in the constant shape B^{const} (if not subtracted as per usual). This leaves only the modulated 'tidal' bias term, but this can be expected to be relatively small and would be straightforward to include as an additionally modulated version of the squeezed shape B^{squeez} (a 'four-shape' model).

For this reason, as a preliminary exercise we endeavour to fit the original three-shape model Equation (1.156) to the measured halo bispectrum, finding the best fit parameters using the `minimise` algorithm with the L-BFGS-B method [238, 239] in `Scipy` as:

$$\begin{aligned} A &= 1.55 \times 10^6, & B &= 0.042, \\ C &= 287, & D &= 3.7, \\ E &= 8.0 k_{\rm NL}, & F &= 0.97. \end{aligned} \tag{4.17}$$

Again we will leave error estimation in these parameters for future work. The three-shape bispectrum calculated with these values is shown in Figure 4.8. It gives an overall total correlation of 97.4% with our benchmark bispectrum, and a 4% f_{nl} correlation fit across the entire range of the data apart from the very tip of the tetrapyd where $K/3 < 0.2h\,\mathrm{Mpc}^{-1}$ (Figure 4.9). Note again there are degeneracies in the model parameters for the limited wavenumber range we have used; there are significant caveats on large length scales (discussed above), as well as small length scales because we do not probe deep enough into the nonlinear regime on small scales to specify the one-halo parameters. In principle, we could use this to specify the averaged bias parameter $b_1 \approx 0.99$ (assuming this to be the dominant contribution) or we could estimate b_1, b_2 jointly with the power spectrum, but we would have to investigate and calibrate transient grid effects at small k much more carefully [98] and we leave this for a future publication. Nevertheless, this analysis gives an initial indication that an accurate phenomenological fit to the halo (or galaxy) bispectrum is likely to be possible with a few well-motivated bispectrum shapes and a limited number of parameters.

4.4 Phenomenological halo catalogues

Having characterised the halo power spectrum and bispectrum from our benchmark `ROCKSTAR` catalogue (as a proxy for a galaxy catalogue), we investigate whether these polyspectra can be accurately reproduced using fast statistical prescriptions for populating halos with subhalos, that is, without using costly N-body simulations for individual mocks. We first consider minimal approaches by modifying the subhalo distribution using different halo profiles or altering the average occupation number as a function of halo mass. Next, we develop this further by exploiting halo concentrations, populating individual halos using typical correlations with the occupation number, that is, incorporating statistical information related to the assembly history of halos.

4.4.1 Halo profile

Modifying the typical halo profile significantly impacts both the power spectrum and bispectrum, especially on small length scales. We can demonstrate (see below) this by keeping the number of subhalos fixed in each halo, while displacing their radial distribution according to a profile of our choosing (such as the popular NFW profile Equation (1.179)). First, however, we briefly study the importance of halo anisotropy. This was motivated by investigations of N-body simulations (such as that in Section 4.2.2), which have revealed that the dark matter profiles of halos are not spherical, reflecting more complex internal substructure [224–226]. The subhalos that live within those halos, therefore, also have a non-spherical distribution, as well as internal structure. We have quantified the importance of these effects by randomising the solid angular distribution of the subhalos within a halo, while keeping the radial distance to the parent halo seed unchanged. This effectively removes halo triaxiality, destroying the original internal structure of the halos. For the new 'random angle' halo catalogue, we have estimated both the power spectrum and the bispectrum (using the sliced f_{nl} correlator (Equation (4.11)) at a given $K = k_1 + k_2 + k_3$); the relative effect is shown by the blue lines in Figure 4.10. There is a small diminution of power even at relatively high wavenumbers $k, K/3 = 1\,h\,\mathrm{Mpc}^{-1}$, with less than a 1% and 4% decrease for the power spectrum and bispectrum respectively. Randomisation of the angles tends to reduce subhalo clustering but this remains a subpercent effect on the bispectrum for $K/3 \leq 0.5\,h\,\mathrm{Mpc}^{-1}$. The small effect of a randomisation process has on the power spectrum has also been confirmed in [240]. This indicates that triaxial effects will predominantly arise from RSDs (see, for instance, [241]).

The radial halo profile can have a larger effect, notably if we populate subhalos using the NFW profile obtained from the halo dark matter distribution, as shown by the orange line in Figure 4.10. In this case, by $k, K/3 = 1\,h\,\mathrm{Mpc}^{-1}$ there are large deviations of 2% and 15% from the halo power spectrum and bispectrum respectively. This is not unexpected as we have previously seen that the dark matter NFW profile does not fit the measured subhalo profile from our benchmark catalogue (given the mass resolution of our N-body simulation). The discrepancies would in fact have been even larger had we used the measured concentration from ROCKSTAR, instead of the analytical fit for $\langle c \rangle$ in Equation (4.6).

We turn now to effects of modelling the halo profile with a power law. As we have seen already in Figure 4.4, a power law of $0.8 < \gamma < 1.2$ will fit most halo profiles for the subhalo distributions found in our benchmark simulation. Modelling the halos with the best fit power law inevitably removes some signal from the power spectrum and bispectrum, as the resulting halos have a uniform solid angular distribution, unlike subhalos in an N-body simulation. The lack of power can be seen in the $\gamma = 1$ profile shown as green line in Figure 4.10. We

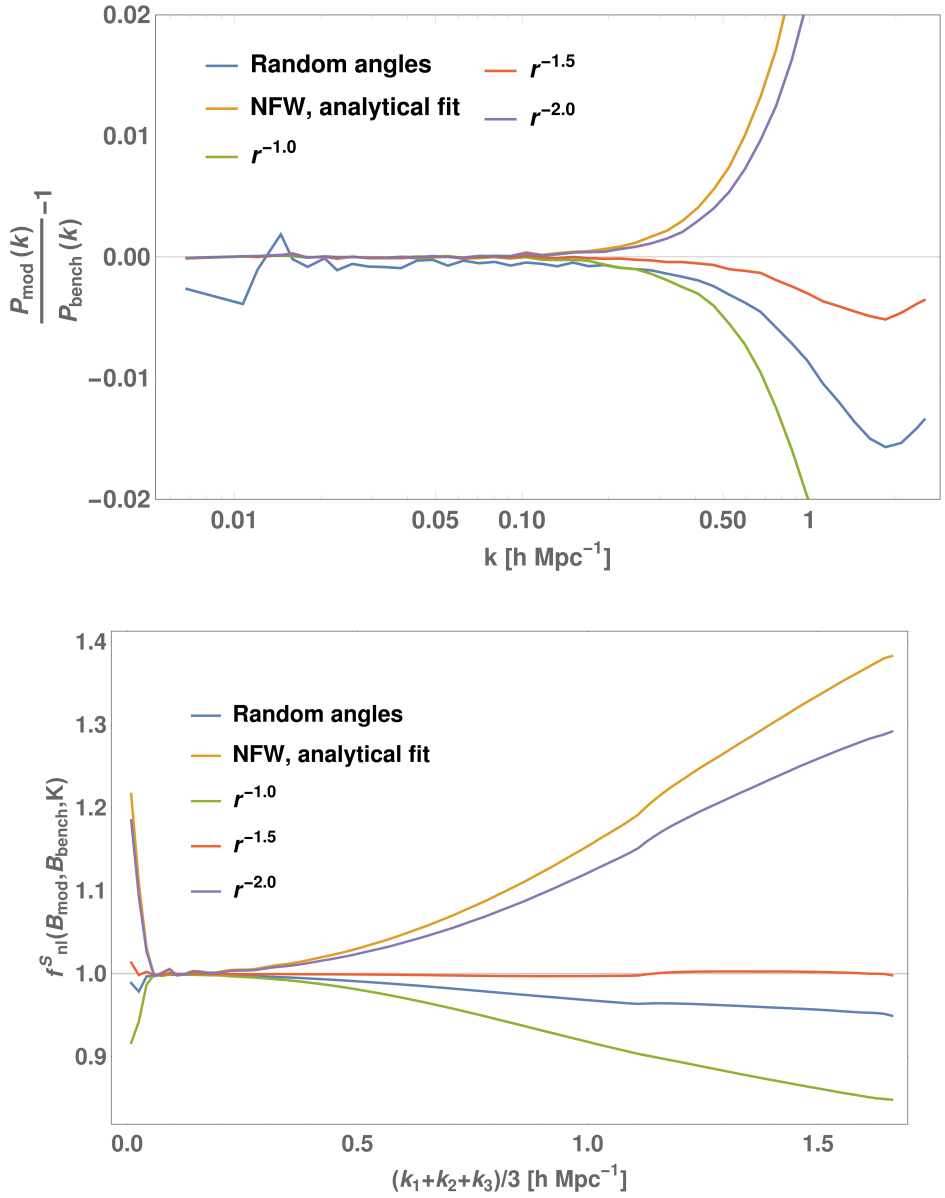

Fig. 4.10 The relative power spectrum (top) and the sliced f_{nl} bispectrum correlator (bottom) for different radial halo profile prescriptions for populating halos with subhalos. The power law profile $r^{-\gamma}$ is a much better fit to the actual subhalo distribution than the dark matter NFW profile, although the index $\gamma \approx 1$ suggested by the best fit to the true profile is power deficient. For $\gamma = 1.5$ we obtain a near-perfect fit to both the power spectrum and bispectrum to high wavenumbers $k, K/3 \leq 1.6\,h\,\mathrm{Mpc}^{-1}$.

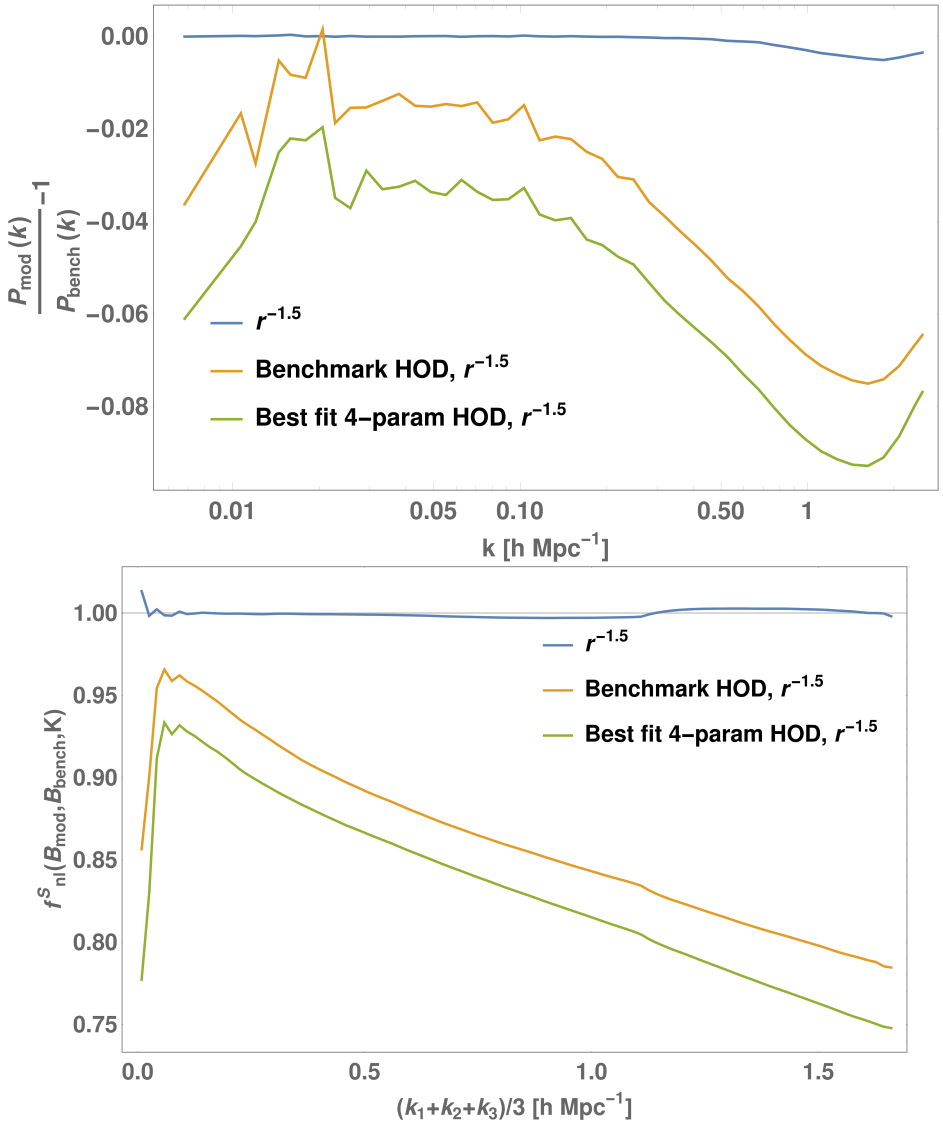

Fig. 4.11 HOD prescriptions for statistically populating halos with subhalos yield a deficient power spectrum (top) and sliced bispectrum correlation (bottom). Neither the benchmark HOD nor the 4-parameter HOD model (using best fit parameters) can recover the benchmark power spectrum to better than 2% and the bispectrum to better than 4% at large scales, with much larger discrepancies on smaller scales.

can phenomenologically compensate for this effect by considering spherically symmetric halo profiles with an increased power law exponent. Coincidentally, for $\gamma = 1.5$ both the power spectrum and the bispectrum are very well fitted at all scales, with a difference of less than 0.5% up to $k, K/3 \leq 1.6\,h\,\mathrm{Mpc}^{-1}$. We can exploit this dual effect when populating the halos with a statistical halo occupation number rather than that measured from the N-body simulation.

4.4.2 Halo occupation number

We have also investigated the effect on the power spectrum and bispectrum of assigning subhalos using the Halo Occupation Distribution (HOD). First, we populated halos using the benchmark HOD model, i.e. we assigned to each halo the measured mean number of galaxies (subhalos) for a halo of that mass. This model is shown in Figure 4.5 along with our 4-parameter fit to it. As shown in Figure 4.11, we have found that neither the benchmark HOD nor the 4-parameter HOD fit recovers the power spectrum or the bispectrum to better than 2% at large scales $k, K/3 < 0.1\,h\,\mathrm{Mpc}^{-1}$. The 4-parameter fit to the benchmark HOD is 4% below the simulation power spectrum, and the difference gets rapidly worse at smaller length scales. The fit to the benchmark HOD is only accurate to 10%, indicating a better functional form should be adopted. The discrepancy in the bispectrum is considerably higher than the power spectrum, and also demonstrates much worse scaling in k.

To better understand the power deficiency observed in Figure 4.11 from using the HOD model we first binned the parent halos by mass, then shuffled around the halo occupation number within the halos in each mass bin. Since the halo profile plays only a marginal role on large length scales, for simplicity we collapsed all objects to the centre of the parent halo, and the power spectrum of the resulting sample is shown in Figure 4.12. The fact that this shuffling method, which preserves the statistical distribution of the halo occupation number in every mass bin, produces the same effect as the benchmark HOD strongly implies that number of subhalos in a halo depends on halo properties other than halo mass. The shuffling procedure is very similar to populating halos by using a subhalo dispersion around the mean HOD; initial experimentation indicated that including such a dispersion had no impact resolving the key bispectrum deficit.

Finally, we explored whether phenomenologically changing the parameters in our 4-parameter HOD could yield a satisfactory fit to both the power spectrum and bispectrum. As discussed in Section 4.2.3 we enforce conservation of galaxy number $\Delta n_g = 0$ (Equation (4.10)) when changing the values of the parameters, which entails compensating by changing at least 2 parameters simultaneously. By exploring all 6 different ways to pair up the parameters, it was found that the index α in (Equation (4.10)), i.e. the exponent of the

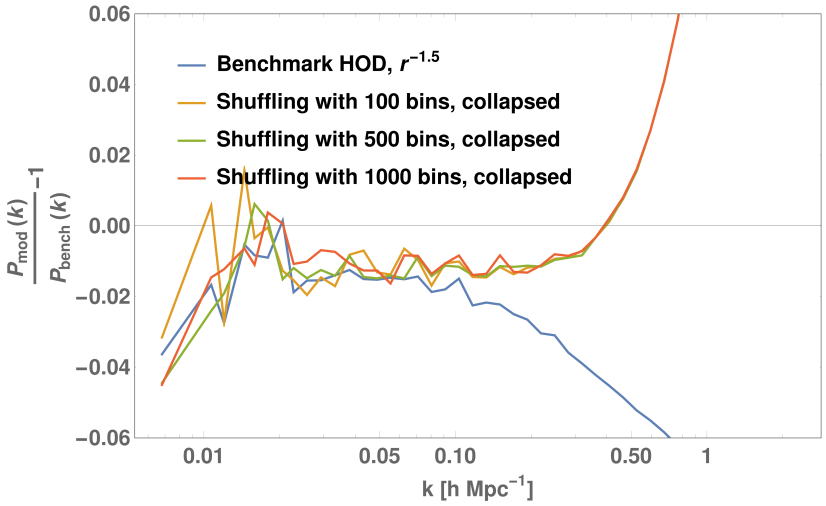

Fig. 4.12 Shuffling the halo occupation number within a mass bin has the same effect as using the benchmark HOD.

power law, appears to make the most dramatic contribution to the power spectrum relative to the other parameters. As can be seen in panels (a)-(c) in Figure 4.15, boosting α by 4.5% helps match the benchmark power spectrum up to $k \leq 0.5\,h\,\mathrm{Mpc}^{-1}$, regardless of the choice of the other compensating parameter. However, panel (d) in the same plot reveals that this boost in α grossly inflates the bispectrum, resulting in more than 5% difference between $0.2\,h\,\mathrm{Mpc}^{-1} < K/3 < 1.3\,h\,\mathrm{Mpc}^{-1}$. We conclude that populating halos using an HOD that depends only on mass will not simultaneously recover both the benchmark power spectrum and bispectrum (with correlation discrepancies in the latter exceeding 4%).

4.4.3 Assembly bias

Since using the benchmark HOD yields a suppression of power in the power spectrum and bispectrum, and tuning the 4-parameter HOD model fares no better in matching both the power spectrum and bispectrum, we considered alternative methods of modelling the halo occupation number that take into account the formation history of the halos, known as assembly bias (see, for example, [242–246]). Amongst halos with the same mass those formed at higher redshifts in N-body simulations are known to typically have higher concentrations c [247–250, 246] (although this relationship should not be over-simplified [251]). For this reason, we investigate whether incorporating halo concentration into our HOD model can simultaneously reduce the measured mock catalogue deficit in both the power spectrum and bispectrum. The probability distribution of the occupation number N_g becomes $P(N_g|c,M)$, which is a function of both mass and concentration.

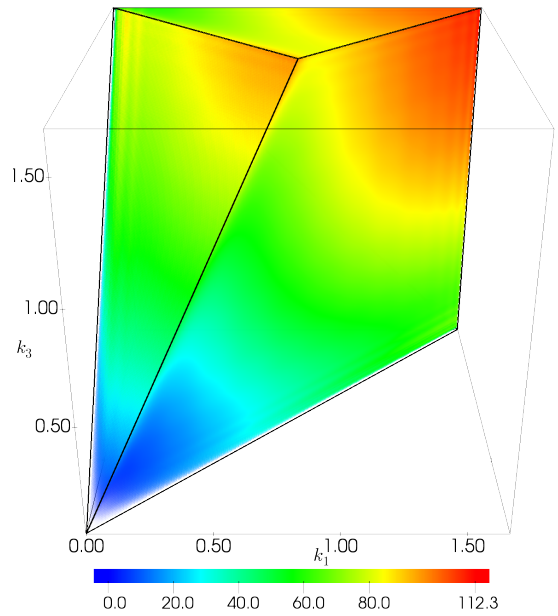

Benchmark `ROCKSTAR` catalogue

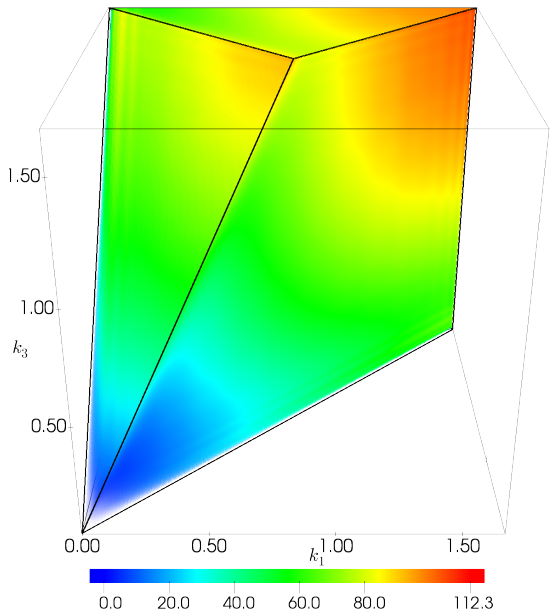

Random solid angle

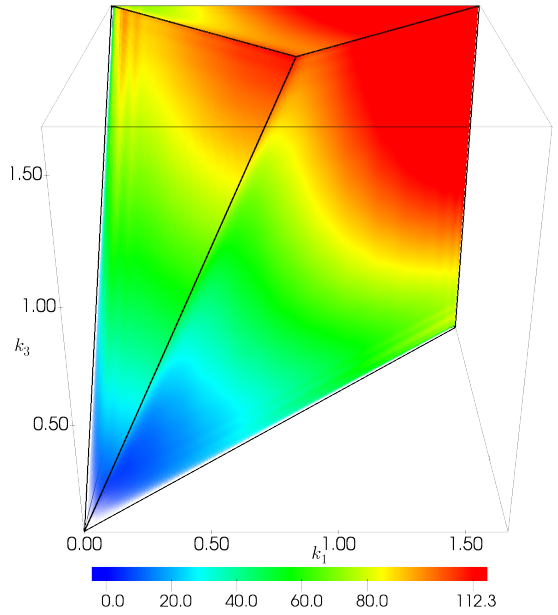

NFW profile

Fig. 4.13 Bispectra of the simple galaxy mock catalogues. *(cont.)*

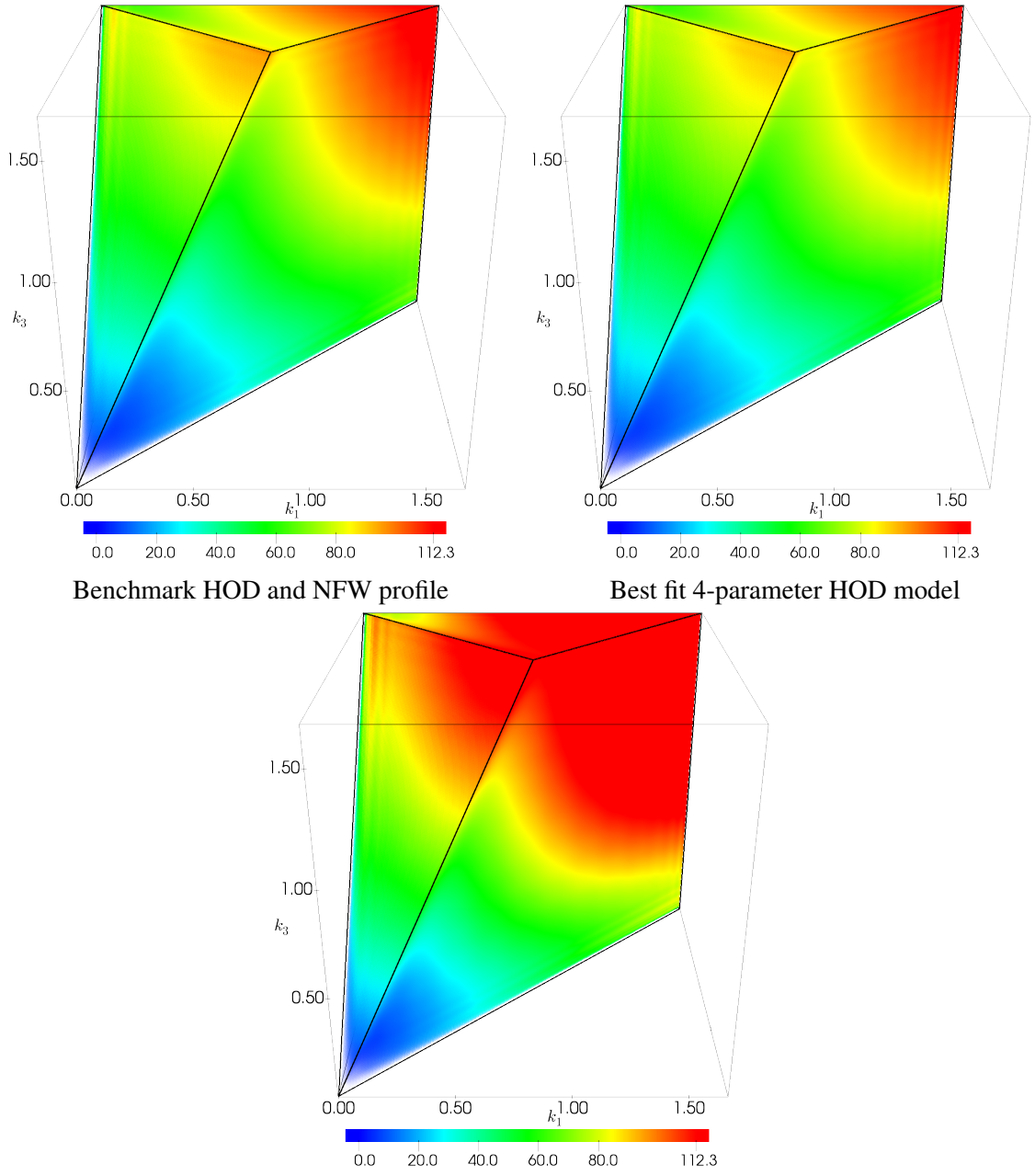

Benchmark HOD and NFW profile

Best fit 4-parameter HOD model

4-parameter HOD model, boost in α and κ

Fig. 4.13 Bispectra of the simple galaxy mock catalogues.

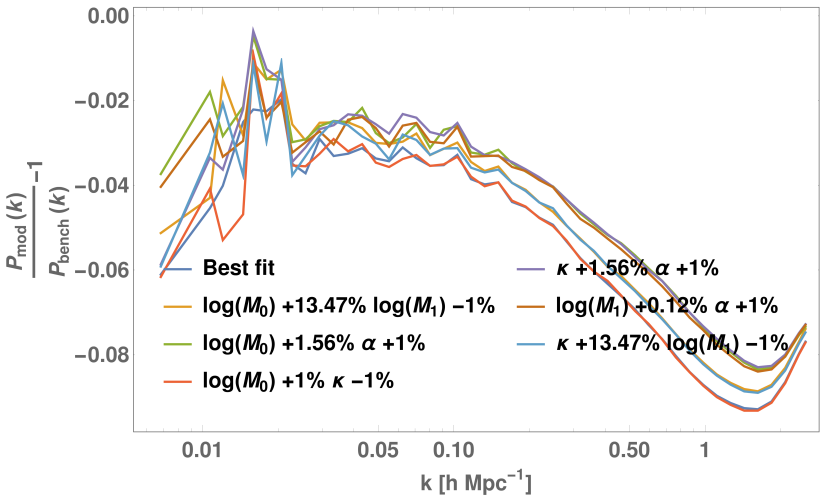

Fig. 4.14 α has a strong influence on the power spectrum, but the other parameters do not have as much of an effect. A radial profile with $\gamma = -1.5$ is used in all these cases.

To gain insight into how the concentration affects halo occupation we took inspiration from [144] with a simple model that, first, bins parent halos by mass and then, secondly, divides these into two bins based on their concentration. The threshold for this split into concentration bins was the median concentration, such that both the higher and the lower concentration samples at a given mass have the same number of subhalos. For each mass bin, we calculated the mean occupation number in the high and low concentration bins (as well as the whole sample). Figure 4.16 shows that halos with lower concentration clearly have more subhalos than the average, amounting to a 20% difference in the mass range between of $10^{13}h^{-1}M_\odot$ and $10^{14}h^{-1}M_\odot$. The significant anticorrelation of the concentration with the number of subhalos may or may not be reflected in actual galaxy distributions because of resolution limitations and absent dynamical effects in our DM-only N-body simulations. If halos with high concentration are indeed typically those that are formed earlier, then the lower number of subhalos will be affected by merging of substructure which is, in turn, influenced by halo resolution (see, for example, [252]).

The positive impact of accounting for concentration with this simple split bin model is illustrated in Figure 4.24 for both the power spectrum and bispectrum. Here, we have populated halos with subhalos drawn from a lognormal distribution to model the total occupation number of the two concentration bins at each mass scale (see below). These results should be compared with the benchmark HOD model in Figure 4.5 where the bispectrum was very discrepant. In particular, this reduces the deficit in the bispectrum from around 6%

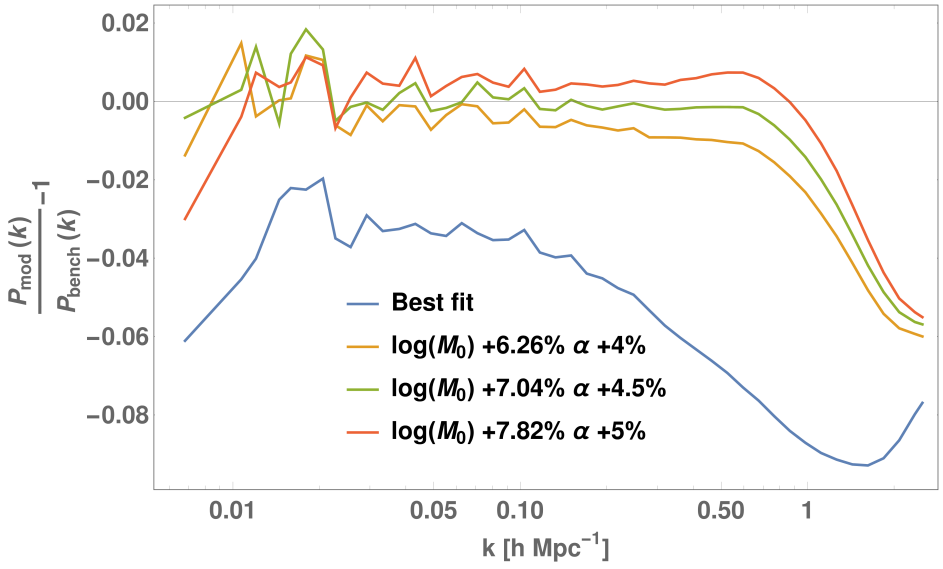

(a)

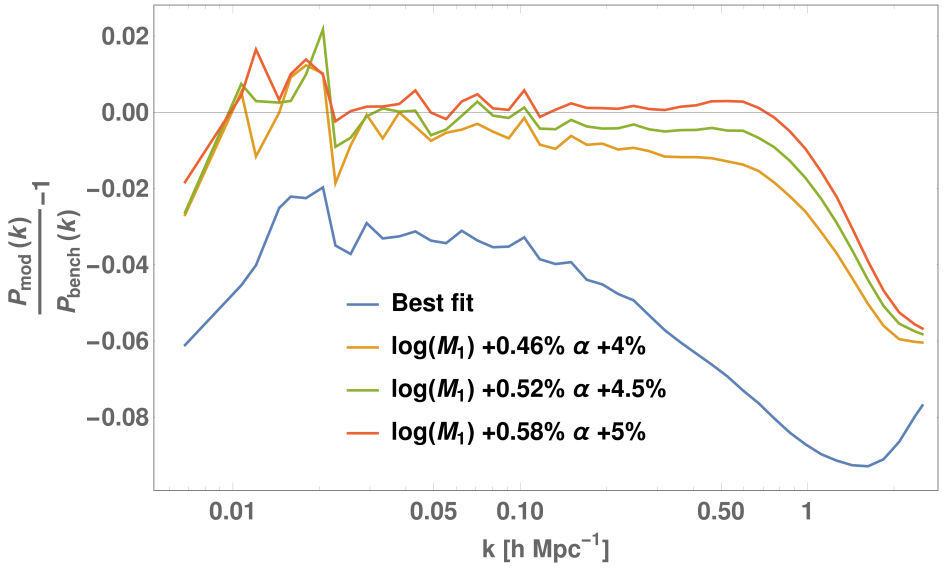

(b)

Fig. 4.15 Panels (a)-(c): increasing α by 4.5% helps match the power spectrum to the benchmark, regardless of choice in the other parameter. Panel (d): the boost in power spectrum over-boosts the bispectrum. *(cont.)*

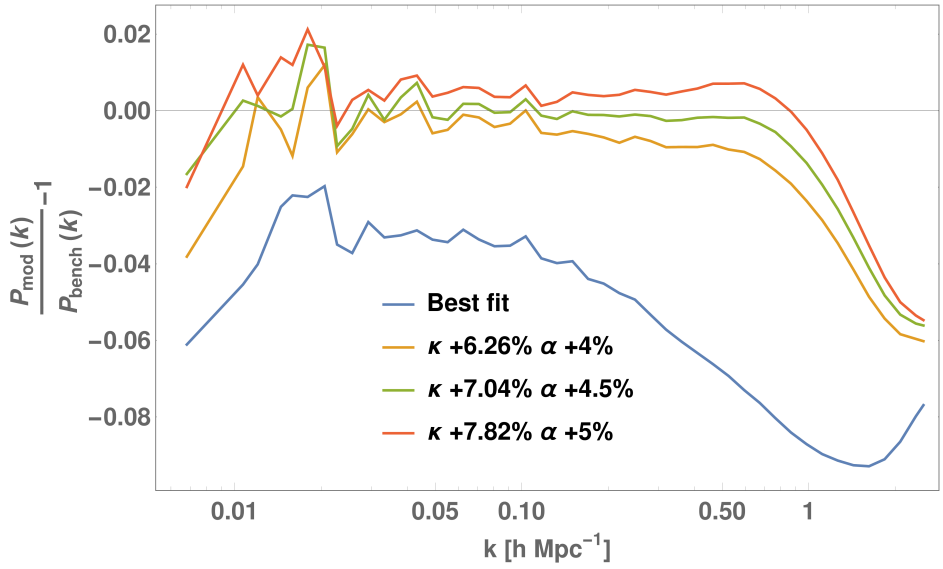

(c)

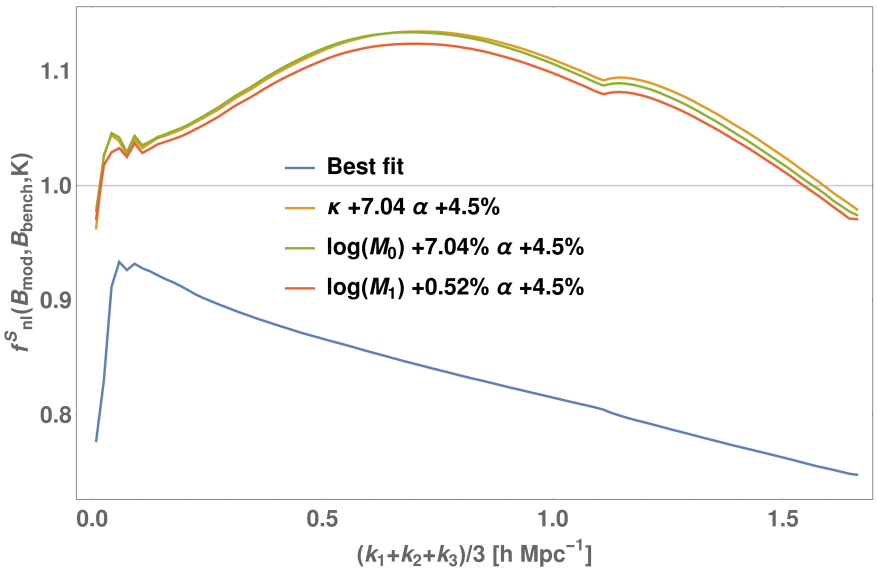

(d)

Fig. 4.15 Panels (a)-(c): increasing α by 4.5% helps match the power spectrum to the benchmark, regardless of choice in the other parameter. Panel (d): the boost in power spectrum over-boosts the bispectrum.

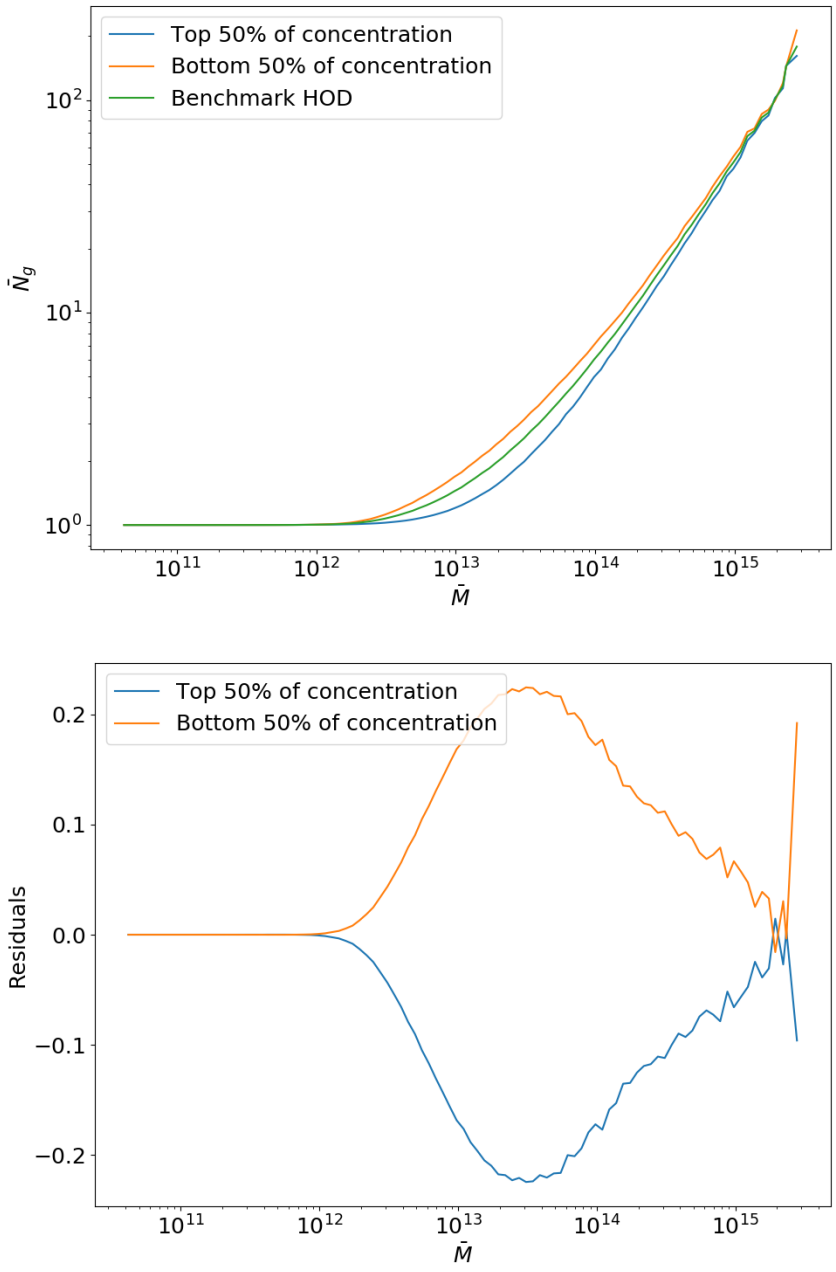

Fig. 4.16 Top panel: We separate halos within a mass bin into 2 samples split by the median concentration, and calculate their average halo occupation. Bottom panel: Residuals of those 2 samples relative to the benchmark HOD.

to 3% at $K/3 = 0.2h\,\mathrm{Mpc}^{-1}$, so assembly bias is clearly an important factor which should be taken into account when creating mock catalogues.

In light of the impact of concentration on subhalo number, our goal is to develop a more sophisticated statistical model that allows us to populate individual halos of a given mass, with or without specifying the concentration from information given by the simulation. To achieve this, we require the joint probability distribution $P(N_g \cap c\,|M)$ as a function of subhalo number N_g and concentration c, so that we can derive $P(N_g|c,M)$ from Bayes theorem [148]:

$$P(N_g|c,M) = \frac{P(N_g \cap c\,|M)}{P(c|M)}. \tag{4.18}$$

To find an appropriate joint distribution we first investigate the marginalised distributions for N_g and c. It was found that the standard lognormal distribution with 2 parameters, Lognormal(μ,σ^2) where e^{μ} is known as the scale parameter and σ the shape parameter, provides a good fit to the marginalised halo occupation number. Figure 4.17 shows the lognormal fits to the total occupation number, and occupation number in the high and low concentration bins, for several mass bins. In Figure 4.18 we show the shape and scale parameters of these fits in 100 mass bins across the whole range of the benchmark catalogue. Note that we have adopted the total occupation number, i.e. including the central galaxy instead of just the satellites, because when the average number of satellites falls below unity the lognormal fit automatically fails.

For the marginalised concentration distribution, we found that it could be more accurately modelled with a Gaussian distribution, particularly at low masses. The lognormal distribution provides a significantly worse fit, a comparison which is shown in Figure 4.20, where we display the normalised counts in several mass bins along with the best fit values for both Gaussian and lognormal fits.

Either the Gaussian or lognormal distributions for c can be easily combined with the lognormal distribution for N_g to give a joint distribution. To do so we simply have to take the natural logarithm of N_g and calculate the mean $\boldsymbol{\mu}$ and covariance $\boldsymbol{\Sigma}$ for this joint Gaussian distribution:

$$\begin{pmatrix} \ln(N_g) \\ X \end{pmatrix} \sim \mathcal{N}(\boldsymbol{\mu},\boldsymbol{\Sigma}), \tag{4.19}$$

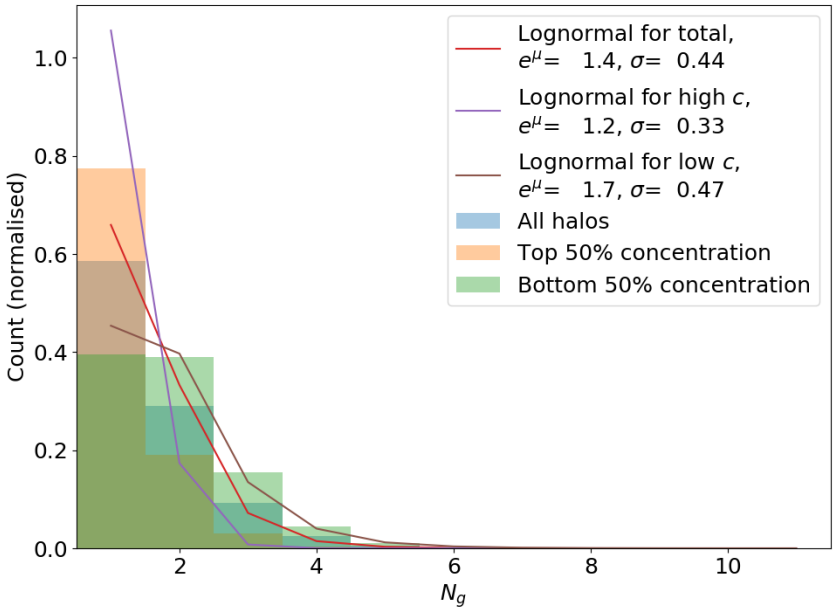

$$M = (0.62 - 2.2) \times 10^{13} h^{-1} M_{\odot}$$

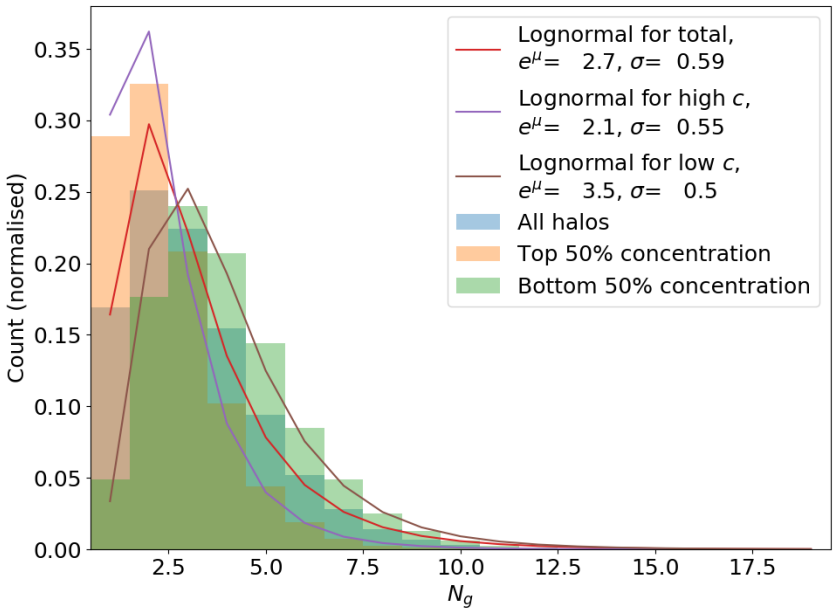

$$M = (2.2 - 7.6) \times 10^{13} h^{-1} M_{\odot}$$

Fig. 4.17 The standard lognormal distribution fitted to the total halo occupation number, as well as the occupation number for the high and low concentration bins. *(cont.)*

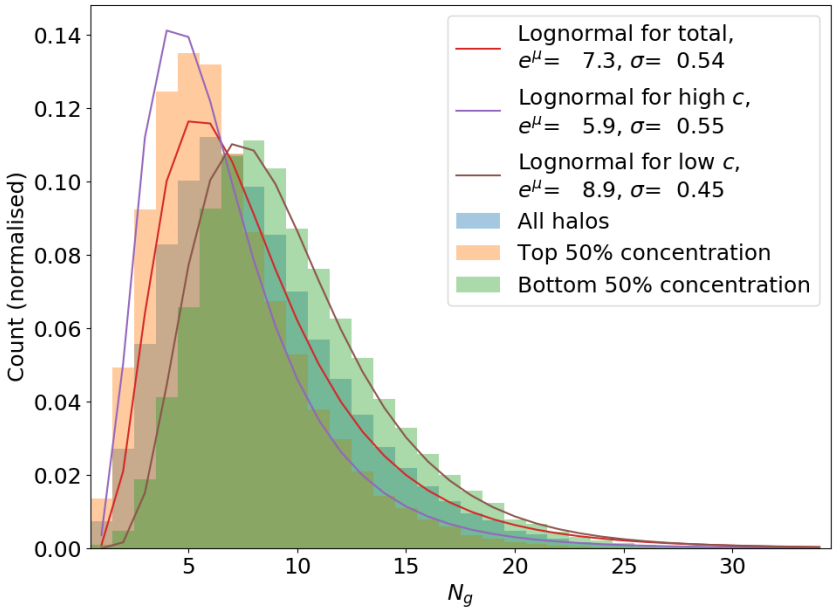

$$M = (0.76 - 2.7) \times 10^{14} h^{-1} M_{\odot}$$

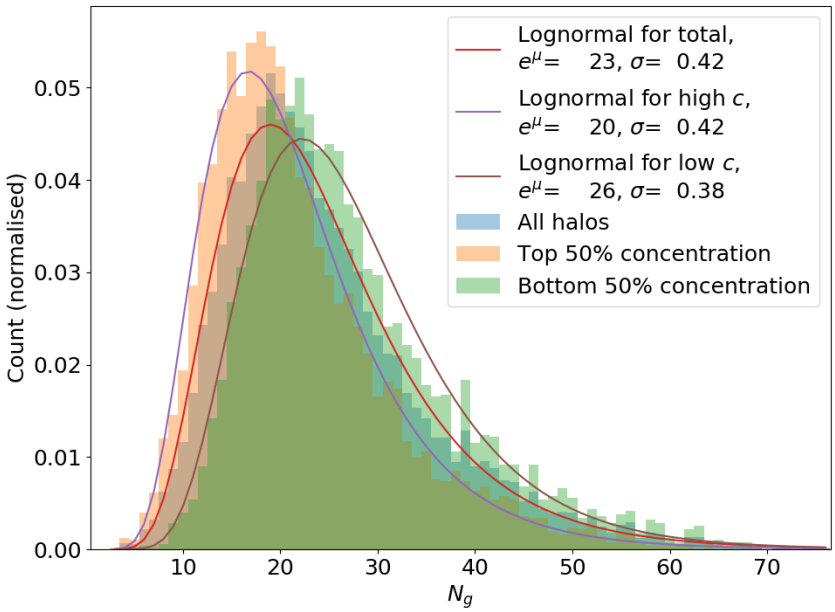

$$M = (2.7 - 9.3) \times 10^{14} h^{-1} M_{\odot}$$

Fig. 4.17 The standard lognormal distribution fitted to the total halo occupation number, as well as the occupation number for the high and low concentration bins.

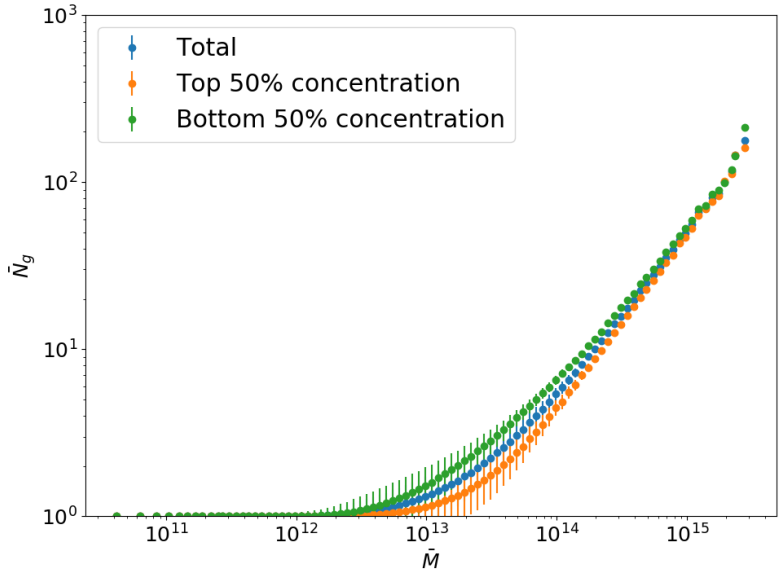

Fig. 4.18 Lognormal fits to the total occupation number and the high and low concentration bins. The vertical error bars indicate the shape parameter σ of the fits.

where $X = c$ or $\ln(c)$ depending on whether a Gaussian or lognormal distribution for c is desired, and

$$\boldsymbol{\mu} = \begin{pmatrix} \langle \ln(N_g) \rangle \\ \langle X \rangle \end{pmatrix}, \qquad \boldsymbol{\Sigma} = \begin{pmatrix} \sigma^2_{\ln(N_g)} & \sigma_{\ln(N_g),X} \\ \sigma_{\ln(N_g),X} & \sigma^2_X \end{pmatrix}. \tag{4.20}$$

$\sigma^2_{\ln(N_g)}$ and σ^2_X are the usual variances for $\ln(N_g)$ and X, and

$$\sigma_{\ln(N_g),X} = \big\langle (\ln(N_g) - \langle \ln(N_g) \rangle)(X - \langle X \rangle) \big\rangle \tag{4.21}$$

is the covariance between them.

To draw from the joint distribution one would then sample from the joint Gaussian distribution and exponentiate the result as required. The joint distribution obtained from the ROCKSTAR halo benchmark is shown for various mass bins in Figure 4.21. For comparison, we show for the same mass bins calculated both from the joint lognormal distribution in Figure 4.23 and from the joint lognormal-Gaussian distribution in Figure 4.22. The joint lognormal-Gaussian distribution appears to reproduce the benchmark distribution more accurately, though small discrepancies remain at high mass.

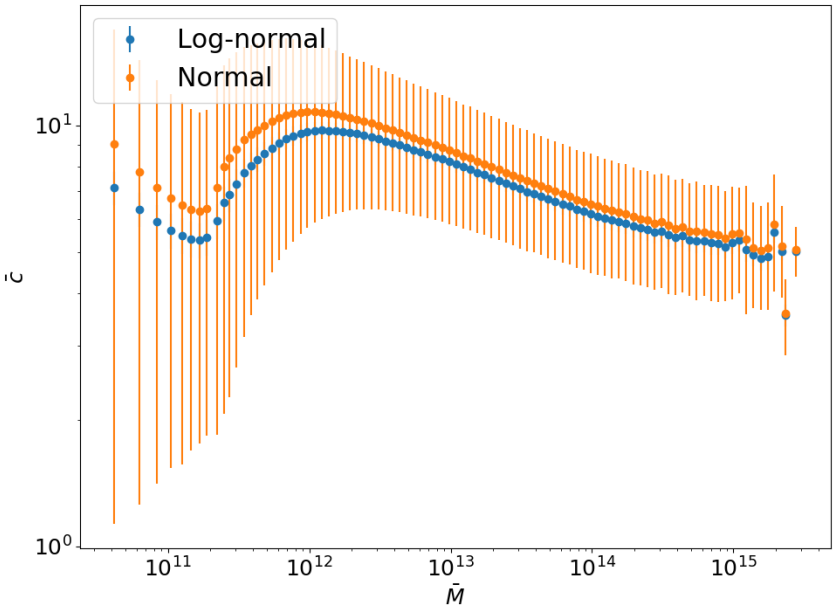

(a)

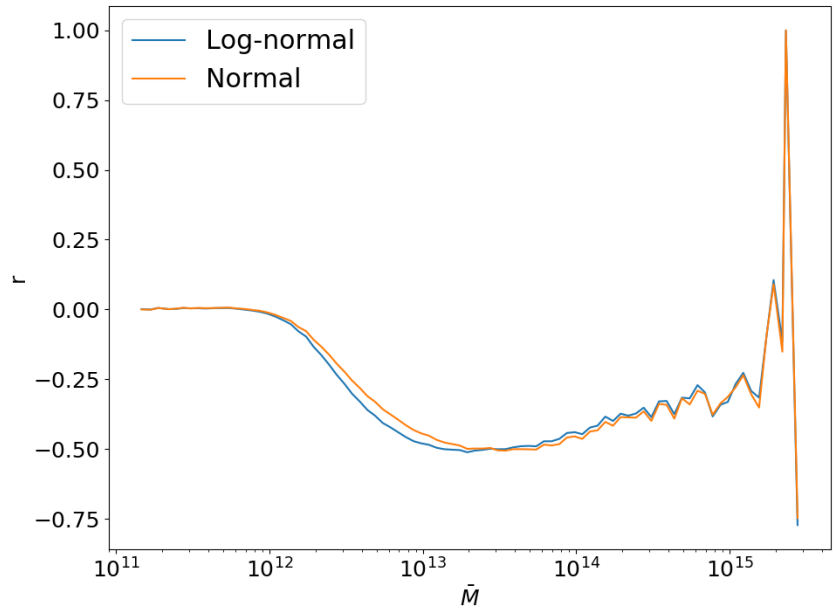

(b)

Fig. 4.19 Top panel: Lognormal and Gaussian fits to mean concentration. The vertical error bars indicate the shape parameter σ of the fits. Bottom panel: Correlation coefficient $r = \frac{\sigma_{\ln(N_g),X}}{\sqrt{\sigma_{\ln(N_g)}\sigma_X}}$ of the bivariate Gaussian distribution between $\ln(N_g)$ and X.

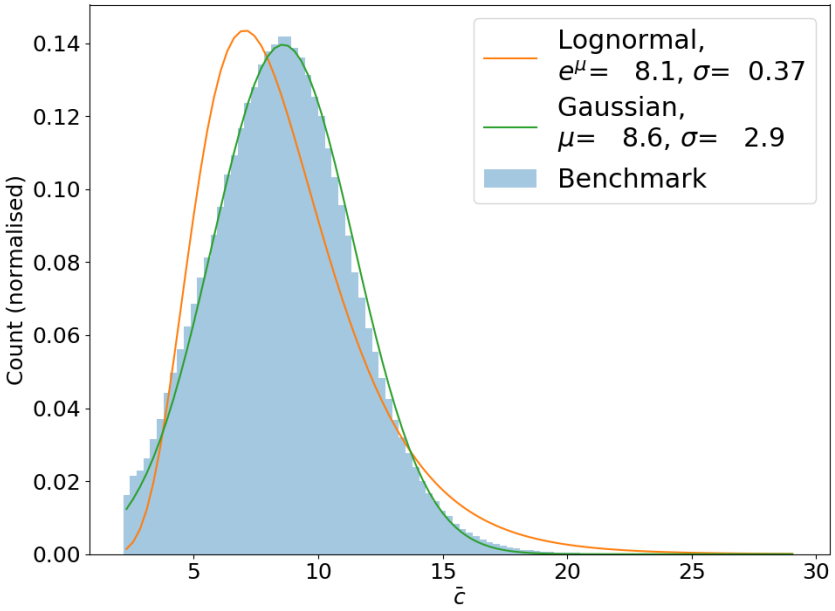

$$M = (0.62 - 2.2) \times 10^{13} h^{-1} M_{\odot}$$

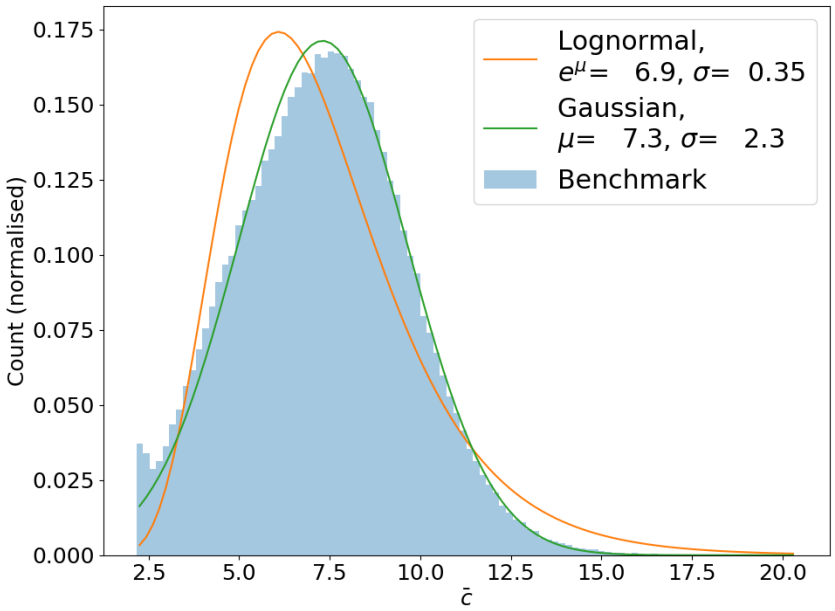

$$M = (2.2 - 7.6) \times 10^{13} h^{-1} M_{\odot}$$

Fig. 4.20 A lognormal distribution is too skewed to model the distribution of halo concentration, but a Gaussian fits very well especially at low mass. *(cont.)*

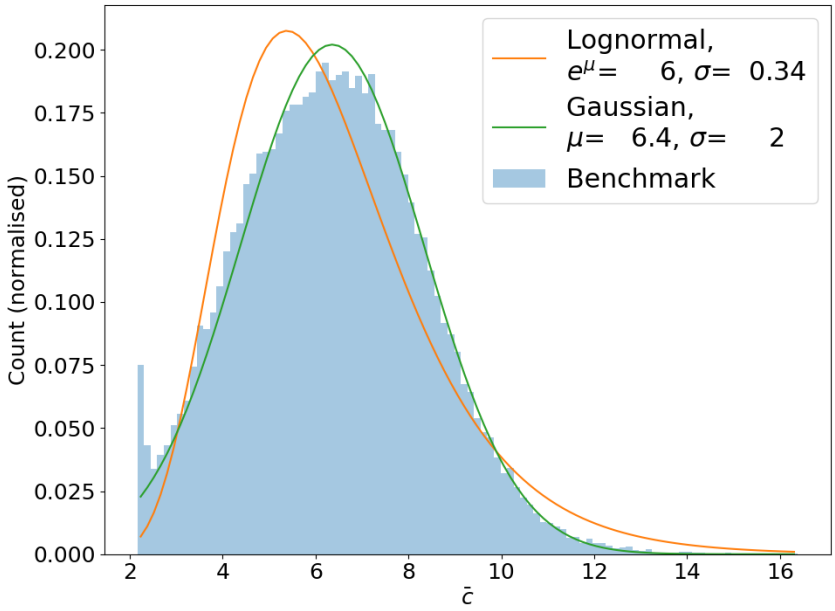

$$M = (0.76 - 2.7) \times 10^{14} h^{-1} M_{\odot}$$

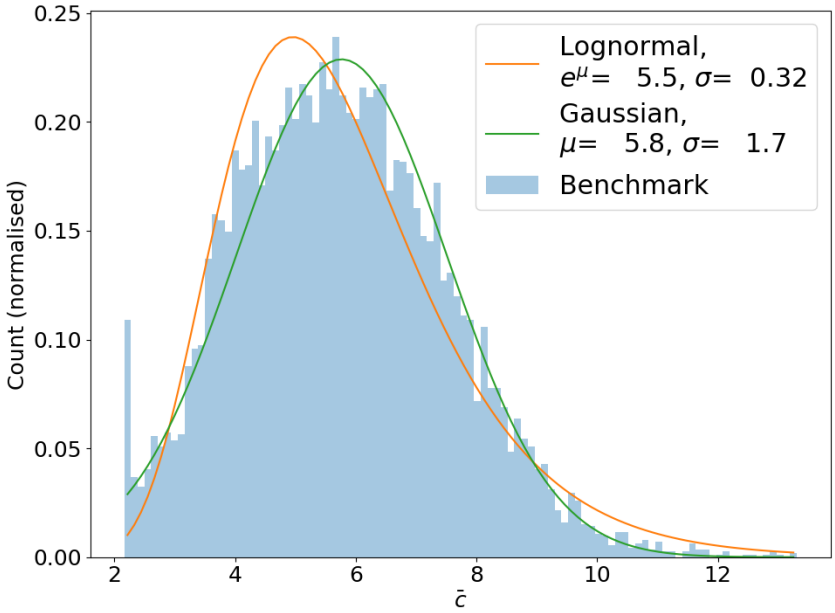

$$M = (2.7 - 9.3) \times 10^{14} h^{-1} M_{\odot}$$

Fig. 4.20 A lognormal distribution is too skewed to model the distribution of halo concentration, but a Gaussian fits very well especially at low mass.

In order to obtain $P(N_g|M,c)$ we first shift the distribution for $\ln(N_g)$ from $\mathcal{N}(\langle\ln(N_g)\rangle, \sigma^2_{\ln(N_g)})$ to $\mathcal{N}(\langle\ln(N_g)\rangle', \sigma'^2_{\ln(N_g)})$, where [253]

$$\langle\ln(N_g)\rangle' = \langle\ln(N_g)\rangle + \frac{\sigma_{\ln(N_g),X}}{\sigma_X^2}(X - \langle X\rangle) \tag{4.22}$$

$$\sigma'^2_{\ln(N_g)} = \sigma^2_{\ln(N_g)} - \frac{\sigma^2_{\ln(N_g),X}}{\sigma_X^2}, \tag{4.23}$$

then exponentiate draws from this shifted Gaussian distribution. This shift can be derived using the bivariate Gaussian distribution in Equation (4.19), the Gaussian distribution for X and Bayes theorem (Equation (4.18)). For the benchmark catalogue in Figure 4.19a we show the parameters of the lognormal and Gaussian fits to c, and the correlation coefficient

$$r = \frac{\sigma_{\ln(N_g),X}}{\sqrt{\sigma_{\ln(N_g)}\sigma_X}} \tag{4.24}$$

obtained for the joint Gaussian distribution in Figure 4.19b. It is worth noting that there are only minor differences in the correlation coefficient between the Gaussian and lognormal cases, with a robust value of around $r \approx -0.5$ found for the mass range $M = 10^{13} - 10^{14} h^{-1} M_\odot$.

In summary, we can now implement our assembly bias model using the joint probability distribution $P(N_g|M,c)$ using one of four possible methods:

1. For an individual halo, use the joint lognormal distribution to draw a suitable value for N_g by shifting the Gaussian distribution for $\ln(N_g)$ using the the concentration c given for that halo by `ROCKSTAR`;

2. Follow the same procedure as in 1 but with the joint lognormal-Gaussian, shifting the Gaussian distribution for $\ln(N_g)$ using the individual halo concentration given by `ROCKSTAR`;

3. Use the joint lognormal distribution for N_g and c, but draw values at random for c from the Gaussian distribution for $\ln(c)$, thus eliminating the need for the simulation to provide this information.

4. Follow the same procedure as in 3 but with the joint lognormal-Gaussian distribution, drawing both c and N_g randomly, so the simulation again does not provide information about concentration. (For methods 3 and 4 we impose a lower bound of 2 for random draws of c, which is lowest value of c calculated by `ROCKSTAR`.)

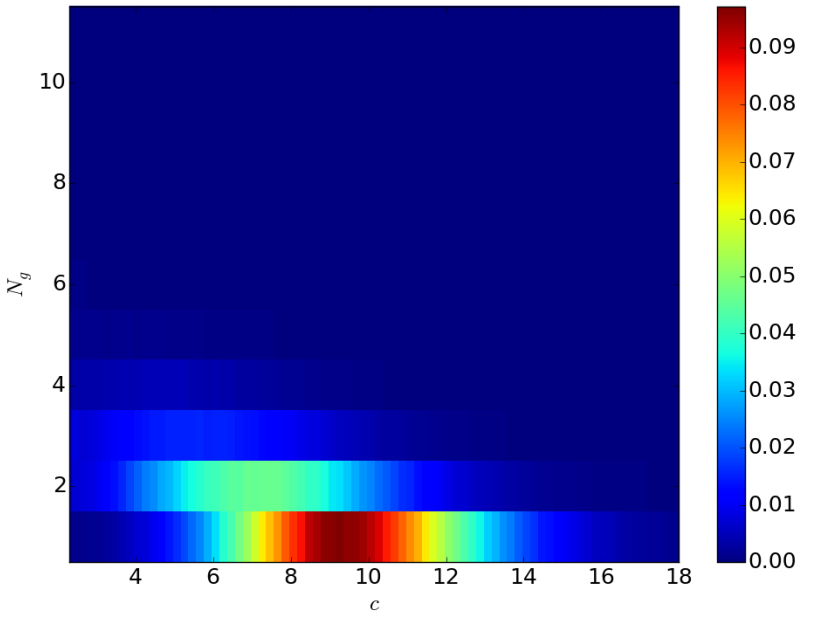

$$M = (0.62 - 2.2) \times 10^{13} h^{-1} M_{\odot}$$

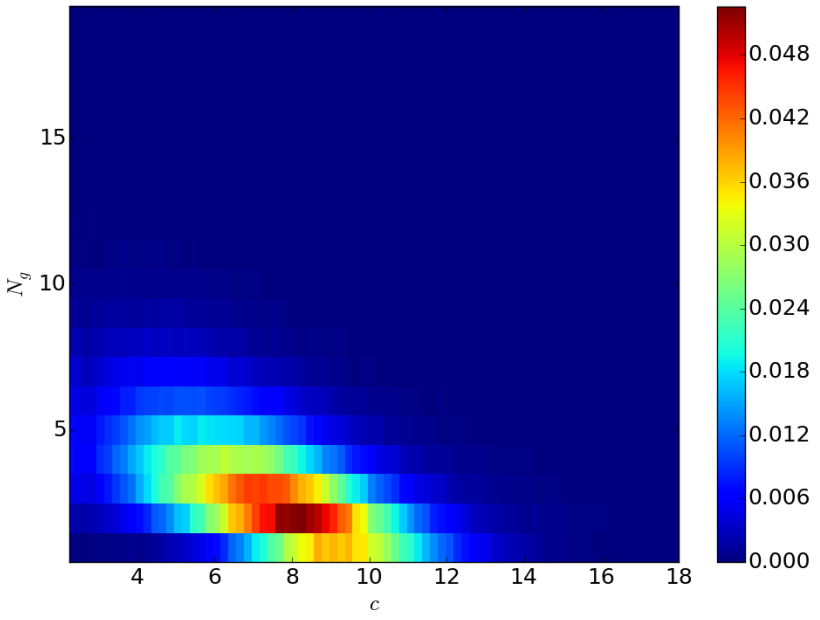

$$M = (2.2 - 7.6) \times 10^{13} h^{-1} M_{\odot}$$

Fig. 4.21 Joint probability distribution for the subhalo number N_g and concentration c for halos in different mass bins of the benchmark ROCKSTAR catalogue. *(cont.)*

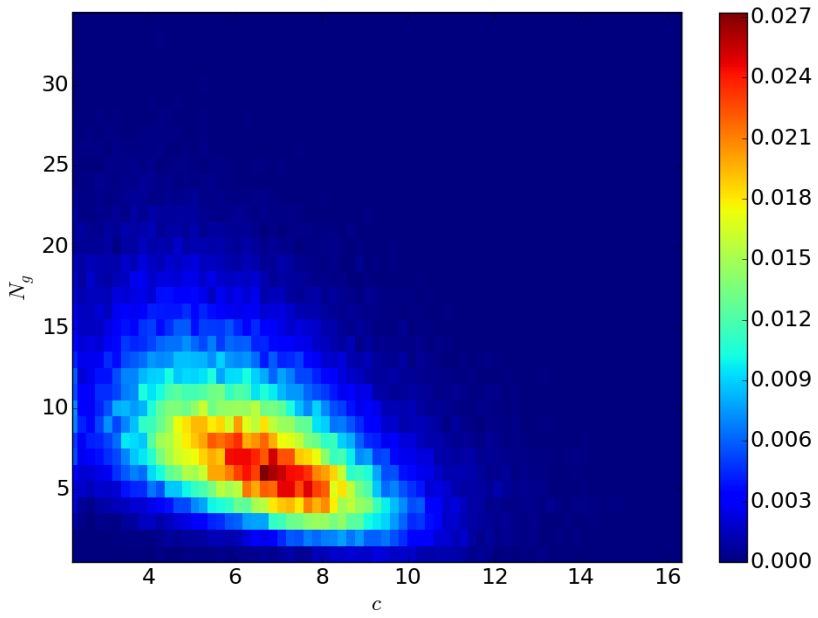

$$M = (0.76 - 2.7) \times 10^{14} h^{-1} M_{\odot}$$

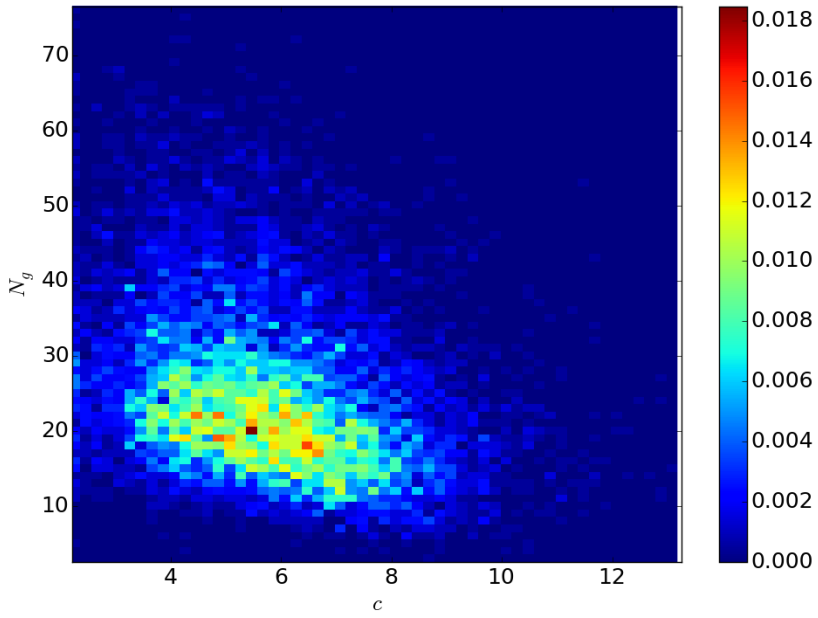

$$M = (2.7 - 9.3) \times 10^{14} h^{-1} M_{\odot}$$

Fig. 4.21 Joint probability distribution for the subhalo number N_g and concentration c for halos in different mass bins of the benchmark ROCKSTAR catalogue.

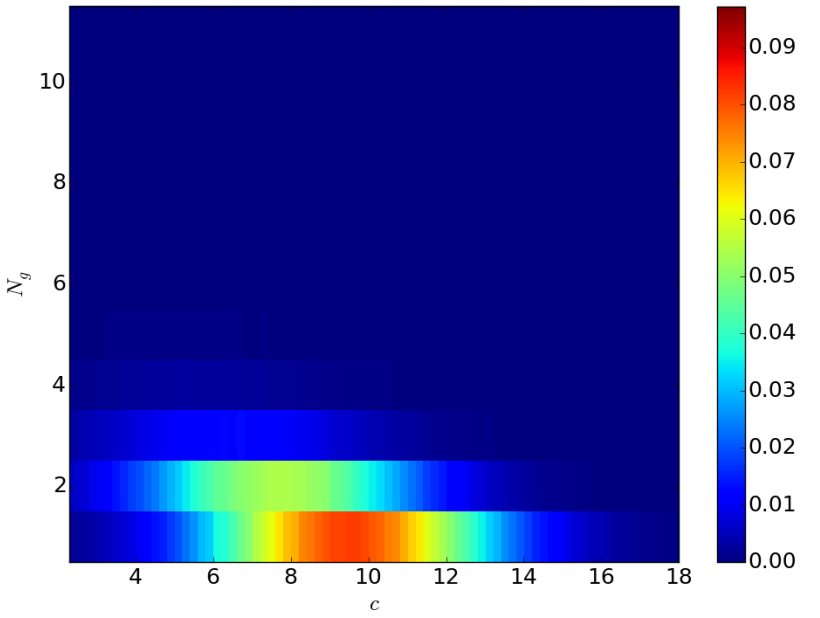

$$M = (0.62 - 2.2) \times 10^{13} h^{-1} M_{\odot}$$

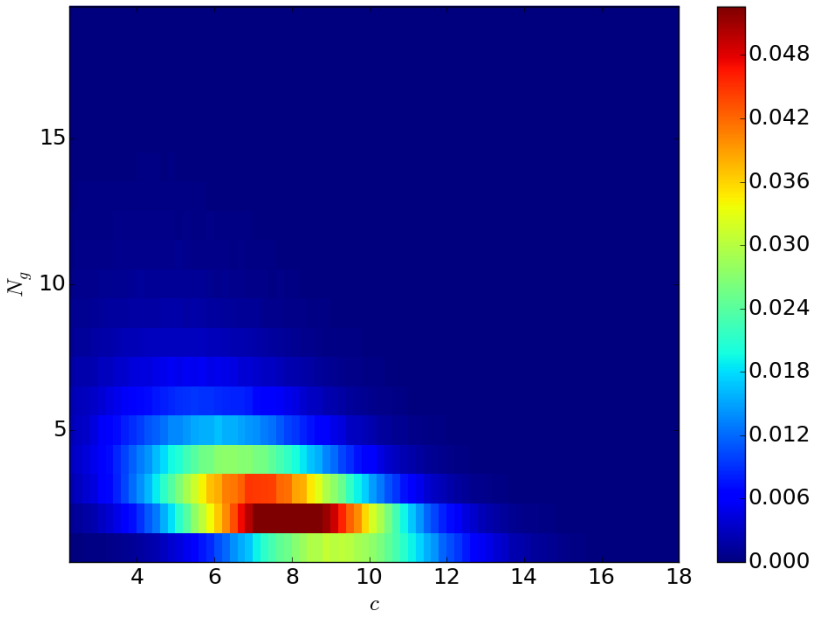

$$M = (2.2 - 7.6) \times 10^{13} h^{-1} M_{\odot}$$

Fig. 4.22 Joint lognormal-Gaussian fit to the joint distribution in Figure 4.21 which should be compared with benchmark distribution shown in Figure 4.21. *(cont.)*

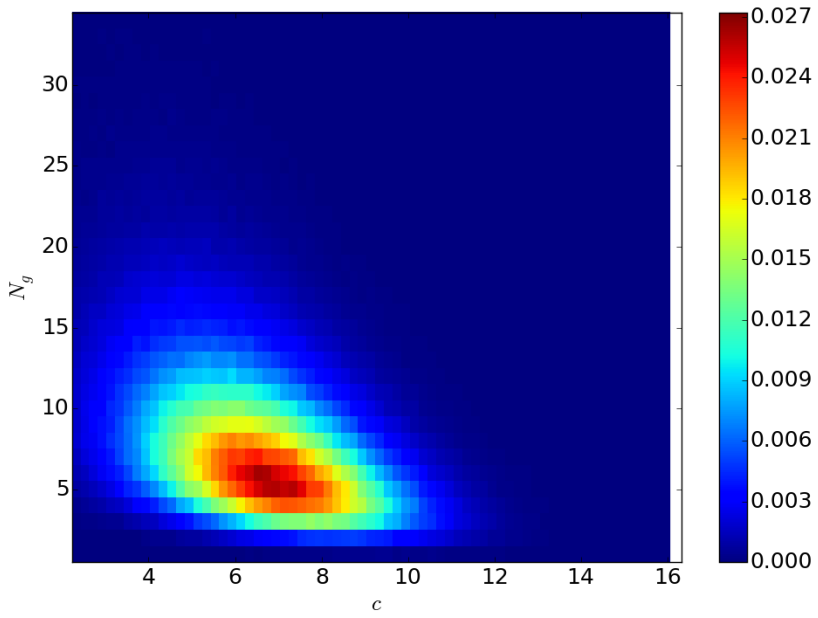

$$M = (0.76 - 2.7) \times 10^{14} h^{-1} M_{\odot}$$

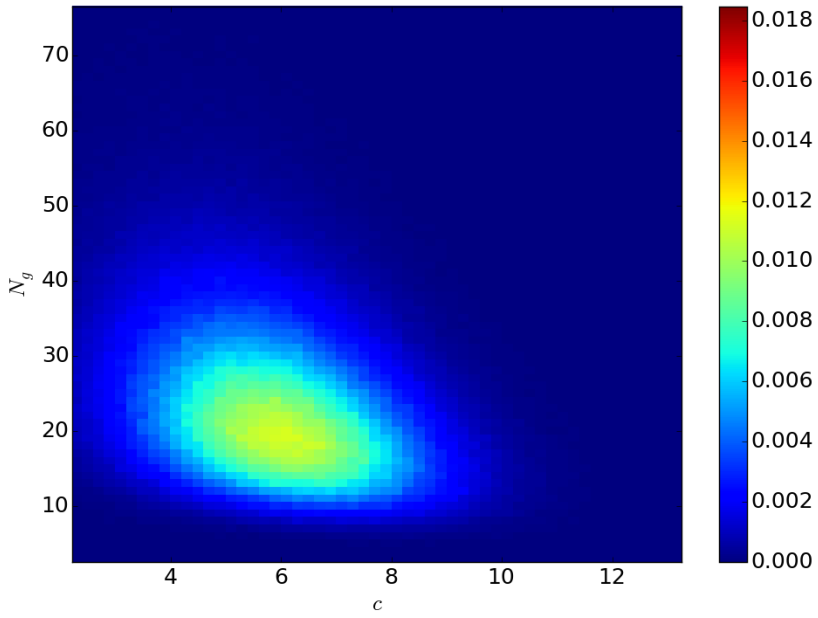

$$M = (2.7 - 9.3) \times 10^{14} h^{-1} M_{\odot}$$

Fig. 4.22 Joint lognormal-Gaussian fit to the joint distribution in Figure 4.21 which should be compared with benchmark distribution shown in Figure 4.21.

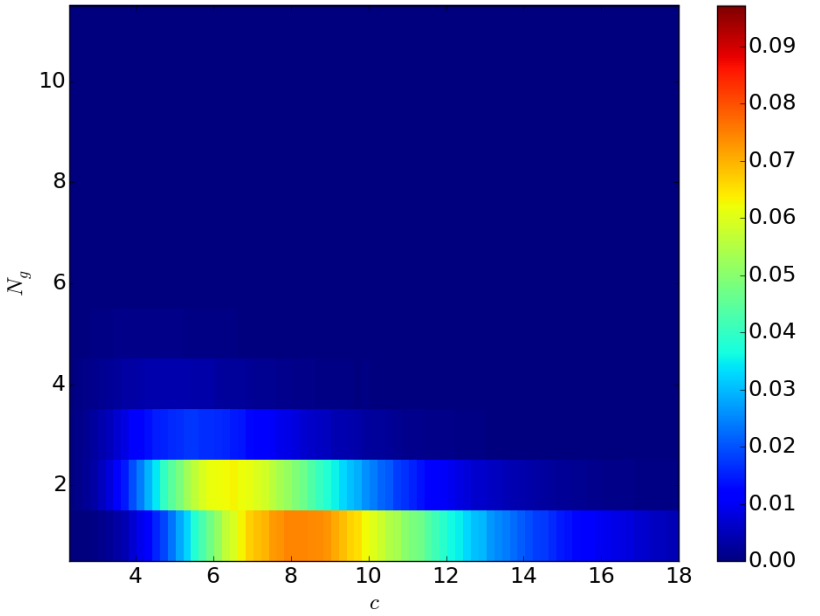

$$M = (0.62 - 2.2) \times 10^{13} h^{-1} M_{\odot}$$

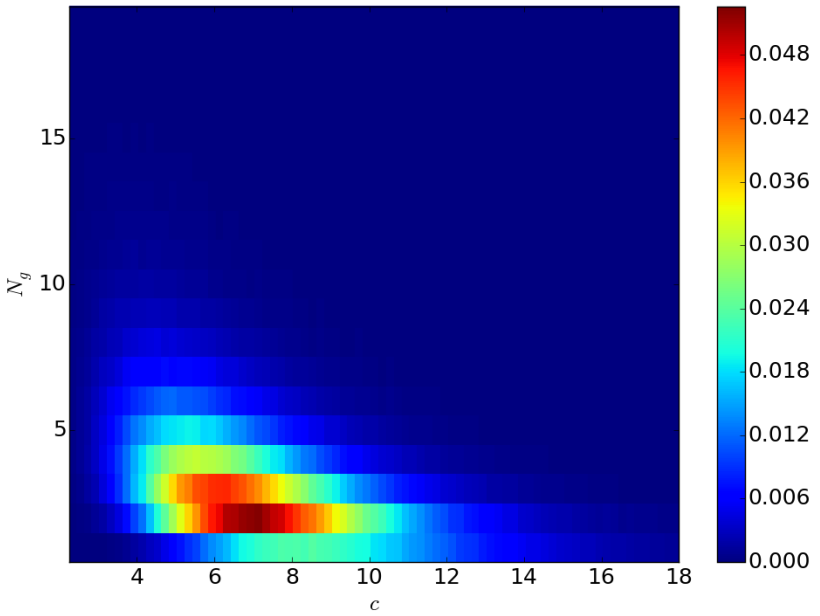

$$M = (2.2 - 7.6) \times 10^{13} h^{-1} M_{\odot}$$

Fig. 4.23 Joint lognormal fit to the joint distribution in Figure 4.21. *(cont.)*

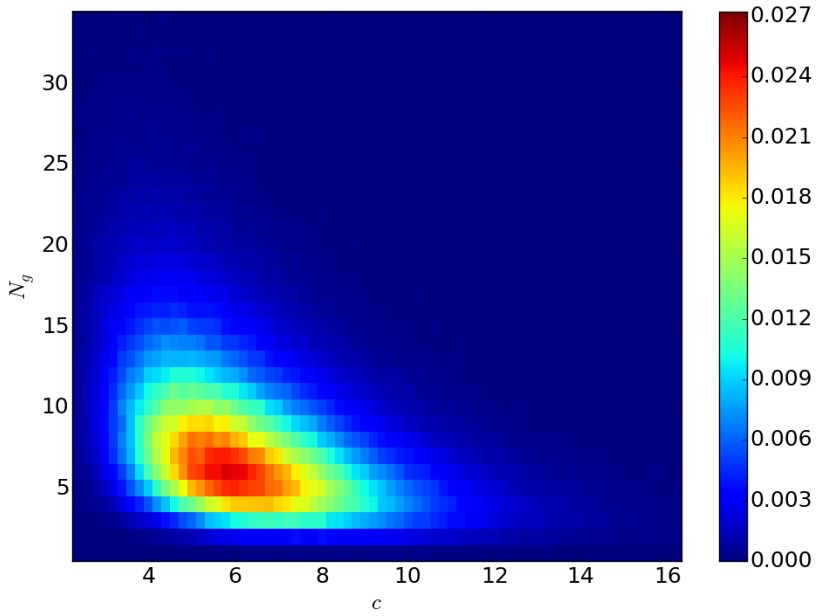

$$M = (0.76 - 2.7) \times 10^{14} h^{-1} M_{\odot}$$

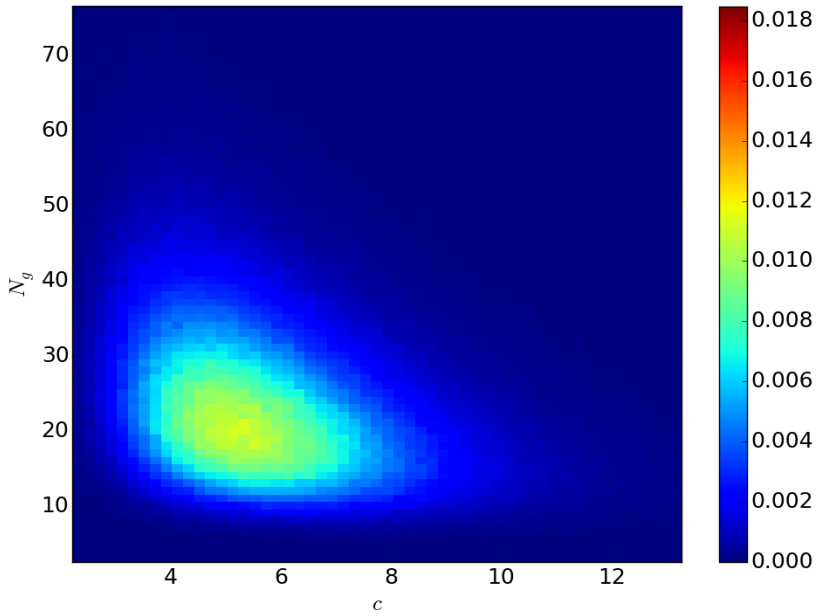

$$M = (2.7 - 9.3) \times 10^{14} h^{-1} M_{\odot}$$

Fig. 4.23 Joint lognormal fit to the joint distribution in Figure 4.21.

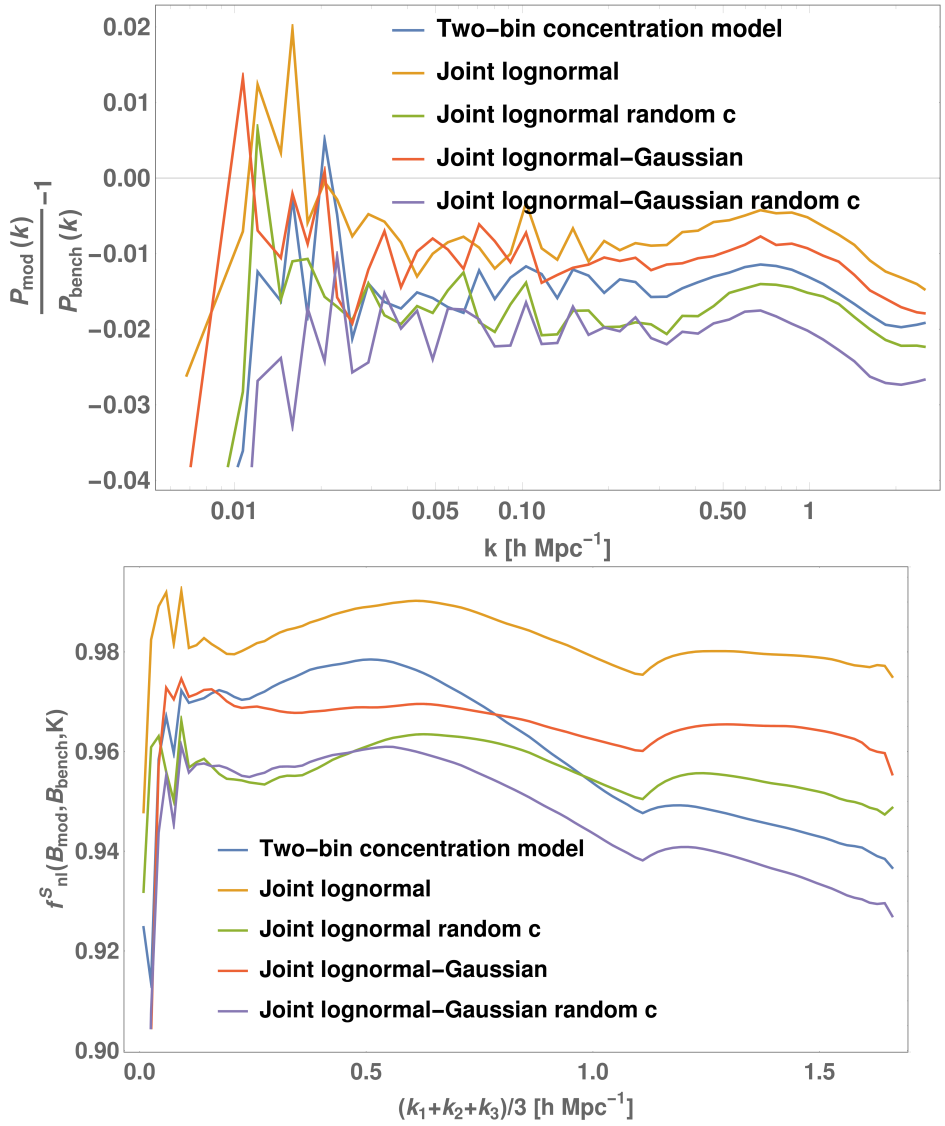

Fig. 4.24 Power spectra (top) and bispectra (bottom) comparisons of the two-bin and joint distribution assembly bias HOD models relative to the measured benchmark polyspectra. Prescriptions using the joint probability distribution and information about the individual halo concentrations improve the fit to better than 2% for $k < 1.0\,h\,\mathrm{Mpc}^{-1}$. The halo profile adopted here is a power law with $\gamma = 1.5$.

The resulting power spectra and bispectra from these prescriptions for creating mock catalogues are shown in Figure 4.24, with a comparison also to the two-bin concentration model described above. As explained in Figure 4.9 the kink at $K/3 = 1.1\,h\,\mathrm{Mpc}^{-1}$ is due to the geometry of the tetrapyd rather than a physical discontinuation. All these methods, endeavouring to incorporate assembly bias in some form, offer a very substantial improvement over the simplest HOD case shown in Figure 4.5. Out of these four possibilities, the superior methods also exploit knowledge of individual halo concentrations given by the ROCKSTAR simulation (which to some extent also includes the simpler two-bin method described earlier). The well-motivated joint lognormal-Gaussian modelling of the occupation number and concentration, with a power law halo profile of $\gamma = 1.2$, yields a better than 1% accuracy in the power spectrum and 4% accuracy in the bispectrum for $k, K/3 < 1.0\,h\,\mathrm{Mpc}^{-1}$, which is significantly better than methods previously investigated in this Chapter. Moreover, both its power spectrum and bispectrum are flatter than the joint lognormal-lognormal case which makes it the more suitable model. It is clear that some information about the assembly history of halos is certainly helpful when creating mock catalogues targeting an accurate halo bispectrum, as it can be used a proxy for concentration. Information about the merger history of halos can be obtained by fast simulation methods without resorting to N-body simulations (see, for example, PINOCCHIO [254]). A number of methods have been developed to correlate halo concentration with halo mass and redshift [255–257], and furthermore the authors of [258] have shown that these models, combined with an empirical model of environmental effects on halo formation times, gives the correct mean concentration and scatter as a function of halo mass.

As can be seen from Figure 4.24, there is still some room for improvement to obtain high precision mock power spectra and bispectra to match the benchmark results. In Figure 4.25 we explore changes to the halo profile for the joint lognormal-Gaussian model to curtail the excess power at small scales. It is clear that a value of $\gamma = 1.2$, which is in the range of best fit values shown in Figure 4.4, gives both a flat relative power spectrum and bispectrum. We also studied methods by which we might be able to generically boost the power spectrum and bispectrum across all scales, notable large length scales. From our investigations of different mass halos, we found that the high mass halos dominate the power at large scales, due to their high occupation number. One way to boost the power is therefore to add an extra galaxy to every parent halo above a certain mass threshold. We tested this tweak using the joint lognormal-Gaussian model, the results of which are shown in Figure 4.27. We found that $M = 2 \times 10^{14}\,h^{-1} M_{\odot}$ seems to be the appropriate mass threshold, which coupled with a radial profile of $r^{-1.2}$ allows us to obtain a fit to both the power spectrum and bispectrum to 1% accuracy between $0.04\,h\,\mathrm{Mpc}^{-1} < k < 1.1\,h\,\mathrm{Mpc}^{-1}$. The average occupation number

at this mass threshold is about 11, therefore this boost is at the 10% level in magnitude. A more natural, continuous transition, such as the erfc function used in the 5-parameter HOD model, can be adopted instead of a step function to obtain smoother behaviour. This may seem a rather contrived way to boost power, but it is presumably compensating some missing physical correlation (such as triaxiality etc.).

Another means by which to achieve a power boost is to raise the the power law exponent index α in the marginalised HOD (Equation (1.194)), as we did with the 4-parameter model. Instead of using the analytical form as we did previously, we change the occupation number drawn from the joint distribution by scaling the number of satellites by this factor:

$$\left(\frac{M-\kappa' M_0}{M_1}\right)^{\alpha'} / \left(\frac{M-\kappa M_0}{M_1}\right)^{\alpha}, \tag{4.25}$$

as we boost both α and κ to conserve particle number. We use the best fit parameters for α, κ, M_0 and M_1, and the results are shown in Figure 4.27. The power spectrum results are comparably to the extra galaxy method above, but this has the additional property of over-boosting the bispectrum, as we have observed in the 4-parameter HOD case. Finally, we show the 3D bispectrum tetrapyd of these improved models in Figure 4.28 which are qualitatively indistinguishable from the bispectrum obtained directly from the benchmark halo distribution.

4.5 Conclusions

In this Chapter we have applied the fast bispectrum estimator `MODAL-LSS` to accurately measure the bispectrum from a large mock galaxy catalogue. This catalogue was generated from a `GADGET-3` N-body simulation using the `ROCKSTAR` halo-finder. We have provided a quantitative three-shape fit to the resulting halo bispectrum, comparing it with the corresponding bispectrum of the underlying dark matter, studied previously [11]. A key goal has been to determine phenomenological methods to create fast mock catalogues that can reproduce the benchmark halo bispectrum from `ROCKSTAR`. In doing so we have restricted ourselves to using only the mass, position and concentration information for parent halos, relying on statistical modelling of the halo profile and occupation number to recover the benchmark power spectrum and bispectrum. We modelled these effects in configuration space to obtain accurate mock power spectra and bispectra, and we aim to incorporate further observational effects such as RSDs in future work.

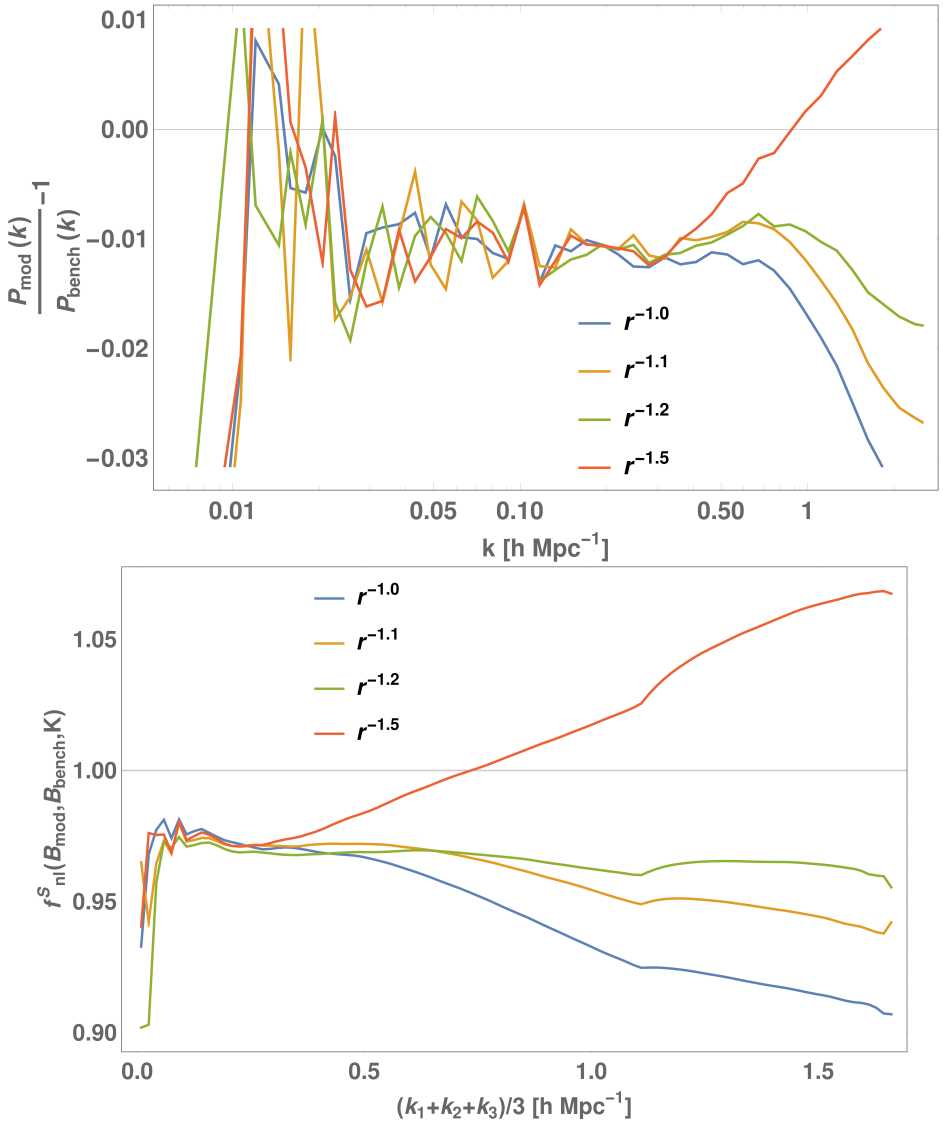

Fig. 4.25 Fine-tuning the halo profile for the joint lognormal-Gaussian model to dampen the high-k tail.

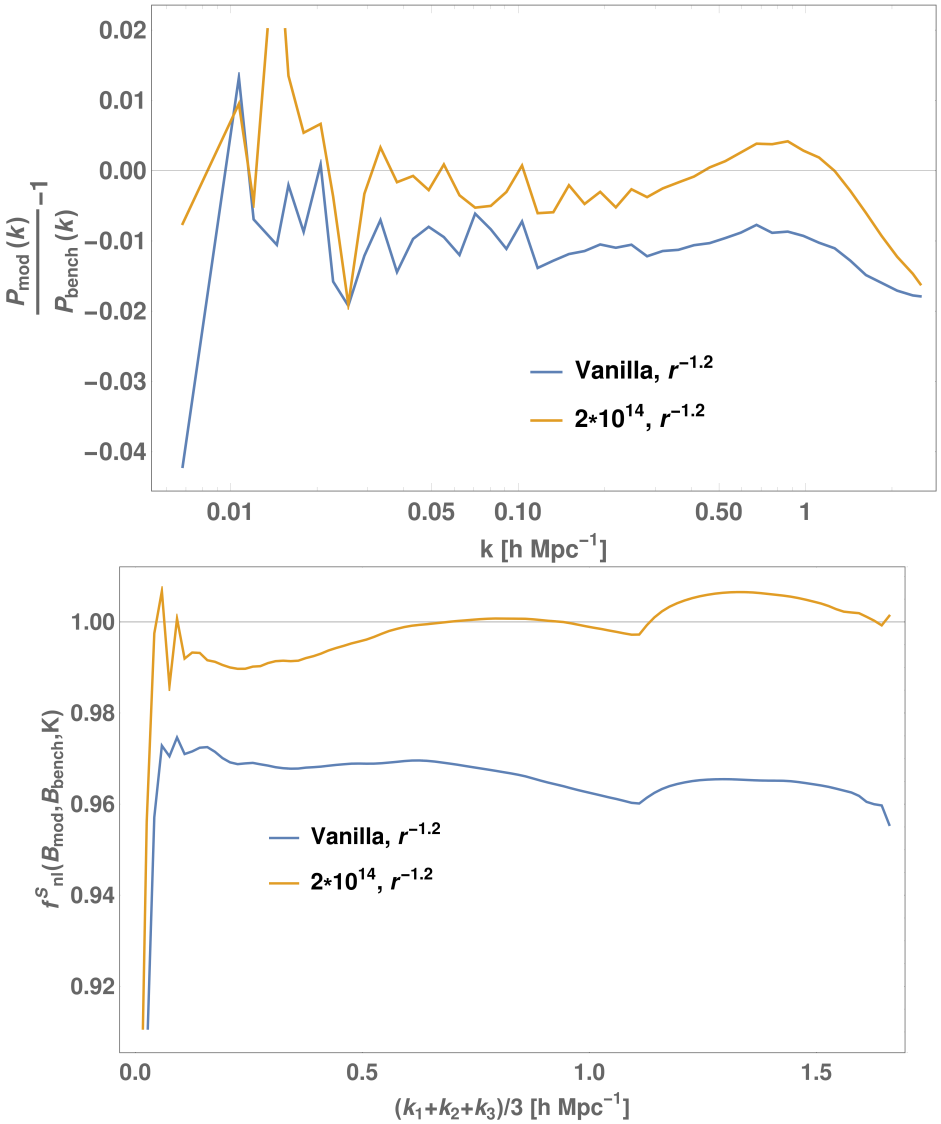

Fig. 4.26 Improvements to joint lognormal-Gaussian assembly bias model by putting an extra galaxy into high mass halos. The number in the labels represent the mass threshold, and 'Vanilla' denotes the original joint lognormal-Gaussian model without alterations.

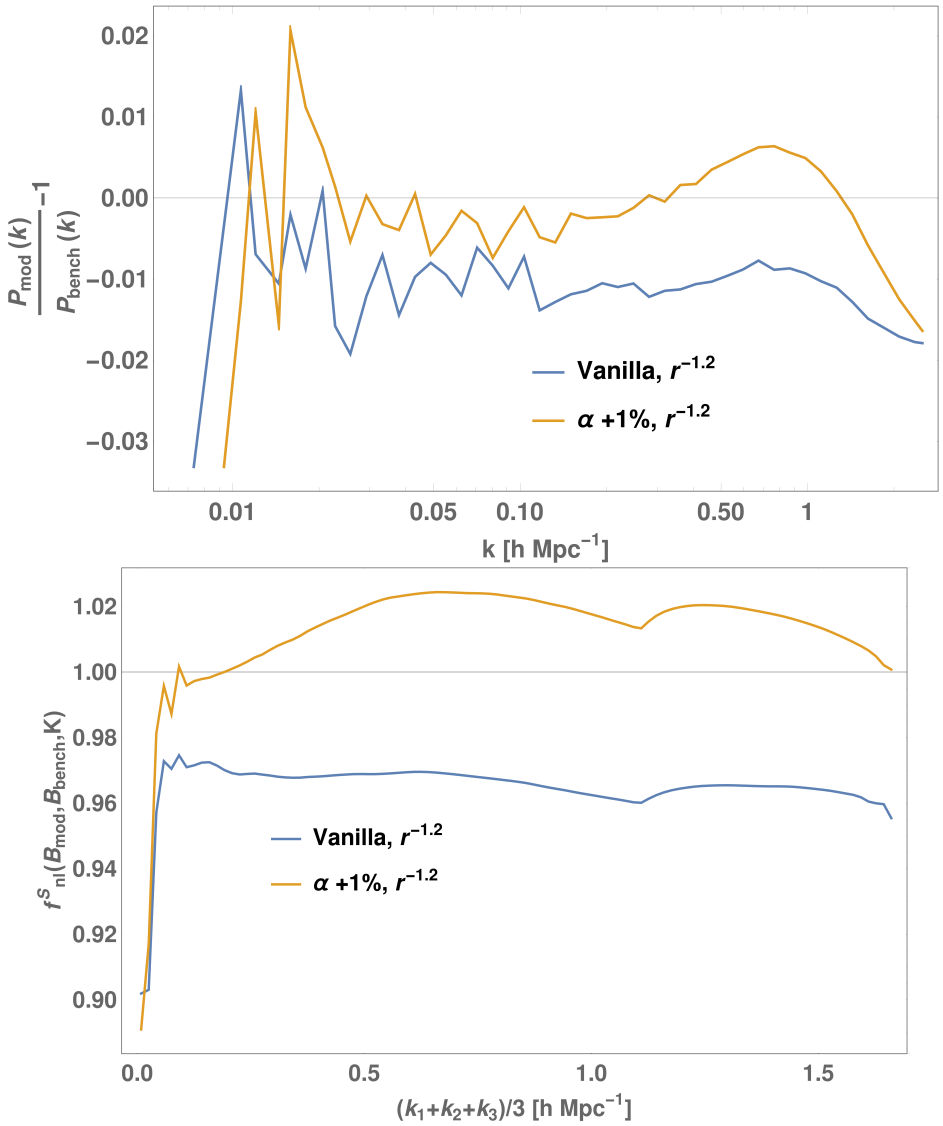

Fig. 4.27 Improvements to joint lognormal-Gaussian assembly bias model by boosting α.

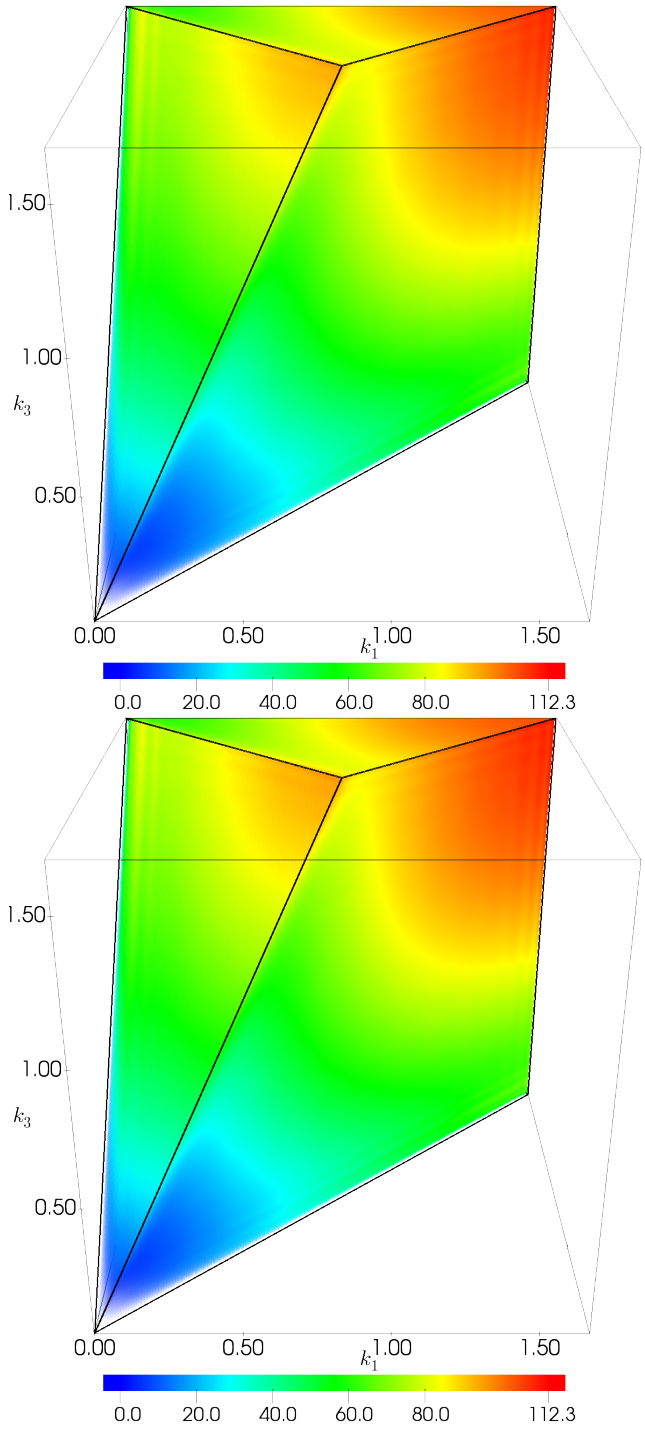

Fig. 4.28 Improvements to joint lognormal-Gaussian assembly bias model. The halo profile is radial with $\gamma = 1.2$. Top panel: Adding an extra galaxy to all parent halos with mass greater than $2 \times 10^{13}\, h^{-1} M_{\odot}$. Bottom panel: Boosting α by 1%.

4.5.1 Halo profile

An important ingredient in a phenomenological galaxy catalogue is the spatial distribution of the galaxies within a parent halo. The subhalo radial number density found for parent halos (separated into a number of mass bins) was not well matched by the average NFW dark matter profile found in the same halo mass range. On the other hand, as suggested, e.g., by [231] a power law profile of the form $\rho \propto r^{-\gamma}$, with $\gamma \sim 1$, works well as a universal profile across a wide range of halo masses spanning three orders of magnitude.

By randomising the solid angular distribution of the benchmark halos we have also quantified the power loss in the power spectrum and bispectrum if halo substructure and triaxiality are not preserved, that is, by fixing the original subhalo number and then retaining radial distances while randomising angular positions. The effect of this internal redistribution was modest with deviations less than 1% and 4% at $k, K/3 = 1\,h\mathrm{Mpc}^{-1}$ for the power spectrum and bispectrum correlator respectively. These lost correlations mean that the best fit power law profile near $\gamma \approx 1$ is necessarily power deficient at small scales. However, we have found that phenomenological values around $\gamma \approx 1.5$ apparently help to recover this power loss to less than 0.5% up to $k, K/3 = 2\,h\mathrm{Mpc}^{-1}$ in both power spectrum and bispectrum. Note that these profile modifications are constrained by using the original occupation numbers for individual halos, which is information generally only available from costly nonlinear simulations.

4.5.2 Halo occupation distribution

To statistically model the number of galaxies within a parent halo, we have investigated the popular practice of using an HOD that only depends on halo mass, $\bar{N}_g(M)$. We observed that using the measured mean number of galaxies for a halo of a given mass M to repopulate the parent halos leads to a power deficit of about 2% in the power spectrum at large scales where $k < 0.1\,h\mathrm{Mpc}^{-1}$, and greater differences at smaller length scales. The loss of power in the bispectrum is more pronounced with much poorer scaling, yielding deviations exceeding 10% by $k = 0.5\,h\mathrm{Mpc}^{-1}$. We found that the same effect can be reproduced if one shuffles the given halo occupation numbers within the mass bins (or by using a dispersion around the mean HOD value). Clearly this simple HOD prescription for populating halos destroys important correlations, so it suggests that other physical mechanisms are contributing to the number of galaxies per halo, rather than just the halo mass.

Nevertheless, we have attempted to recover this power loss by tuning the four-parameter HOD model given by (Equation (4.10)). The best fit parameters actually lead to further power loss at all scales, perhaps because the HOD fit is only accurate up to 10%, which suggests that

a better functional form should be adopted to match HODs from simulations. After tweaking the parameters while keeping galaxy number constant we found that boosting the power law exponent α by 4.5% raised the power spectrum to the correct level to $k = 0.5\,h\,\mathrm{Mpc}^{-1}$ irrespective of choice in the other parameter, but unfortunately this results in substantially over-boosting the bispectrum (overcompensating at around the 10% level). We infer that an HOD model which only depends on halo mass cannot accurately reproduce both the power spectrum and bispectrum of a benchmark mock catalogue.

4.5.3 Assembly bias

These investigations led us to incorporate further information in the HOD that takes into account the formation history of the halos to determine the halo occupation number. Motivated by other assembly bias studies in the literature such as [242–246], we have developed a new prescription using a joint probability distribution to model correlations between the halo occupation number N_g and concentration c found in the benchmark catalogue. Even an extension which just separates halos of a given mass into two concentration bins [144] - representing above and below median values for c - yields more accurate power spectra and bispectra with improved scaling.

We have found that the marginalised distribution for halo concentration is well described by a Gaussian distribution across the entire mass range of the benchmark, while taking care to impose an appropriate lower bound when drawing from the distribution. On the other hand the marginalised halo occupation number is well fitted with a lognormal distribution. Our assembly bias model is therefore a joint lognormal-Gaussian bivariate distribution which depends on halo mass, $P(N_g \cap c\,|M)$. A non-zero covariance between the two variables imply that halo concentration is correlated with halo occupation number, and we find the correlation coefficient is $r \approx -0.5$ for a mass range of $M = 10^{13} - 10^{14} h^{-1}\,M_{\odot}$. In terms of the assembly history within an N-body simulation, we can interpret higher halo concentration causing fewer subhalos because of earlier halo formation, that is, in this case there is more time for the merger of substructure (a factor which depends to some extent on our benchmark resolution). We were also able to obtain very similar results using a joint lognormal-lognormal distribution for the halo number and concentration.

4.5.4 Prescriptions for fast mock catalogue polyspectra

One of the key results of this Chapter is that our assembly bias model for populating halos can recover the benchmark power spectrum to within 1% and the bispectrum to within 4% across the entire range of scales of the simulation. In its most accurate form this involves

using a joint lognormal-Gaussian probability distribution for N_g and c, coupled with a radial power law halo profile with $\gamma = 1.2$, together with the concentrations found for individual halos. Without use of individual halo concentrations, we could assign both concentration and halo number statistically, obtaining good bispectrum scaling though with a 2% and 5% deficit emerging for the power spectrum and bispectrum respectively. These assembly bias prescriptions represent a considerable improvement over all the other methods we investigated in this Chapter and can be deployed with fast mock catalogue generators.

We also explored ways to phenomenologically reduce this small remaining power deficit. Modifying the index in the four-parameter HOD model, as before, encountered the problem of over-boosting the bispectrum. However, motivated by the dominant contributions of high mass halos, we considered enhancing this by adding an extra galaxy to all parent halos above a certain mass threshold $M > 2 \times 10^{14} h^{-1} M_{\odot}$. We were able to obtain a 1% fit to both the benchmark power spectrum and bispectrum in the range $0.04\,h\,\mathrm{Mpc}^{-1} < k < 1.1\,h\,\mathrm{Mpc}^{-1}$.

Finally we note a few caveats about the mock catalogue population methods we have proposed. Our assumption that galaxies can be identified with subhalos will have an important impact on both the spatial distribution and occupation number of the parent halos; clearly this approach can be developed further and made more realistic by increasing resolution and incorporating more physical mechanisms in the simulations. For example, our present mass resolution with a particle mass of $M_p = 2.093 \times 10^{10} h^{-1} M_{\odot}$ may be insufficient to ensure finer substructures are resolved and preserved during halo mergers; it would be prudent in future to expand these investigations by exploring the dependence on simulation resolution. We also note that our most accurate assembly bias model relies on concentration information for individual halos obtained from the mock catalogue simulation. This is not necessarily available from all fast simulation generators and halo finder codes, but algorithms such as PINOCCHIO can provide the merger history of dark matter halos, which in turn could be converted into halo concentrations. Nevertheless, by statistically sampling the Gaussian distribution for concentration we were still able to obtain a good power spectrum and bispectrum fit, and this model can be further fine-tuned with the galaxy boost.

In summary, we investigated various phenomenological schemes, including the halo profile, the Halo Occupation Distribution (HOD) algorithm, and assembly bias models, to generate three-dimensional mock galaxy catalogues. We apply the fast bispectrum estimator `MODAL-LSS` to these mock galaxy catalogues, comparing the results with the power spectrum and bispectrum obtained from `GADGET-3` N-body simulation data analysed with the phase space halo finder `ROCKSTAR`. Our goal is to make the high precision bispectrum a tractable diagnostic tool for analysing huge galaxy surveys (such as DES, DESI and Euclid), by proposing efficient methods to generate mock galaxy catalogues with the appropriate power

spectrum and bispectrum. We were able to show the effect of changing the halo profile on the power spectrum and bispectrum. Populating parent halos with subhalos using simple HOD models (depending only on halo mass) yielded results deficient in both the power spectrum (2%) and the bispectrum (>4%) at $k, K/3 \approx 0.2\,h\,\mathrm{Mpc}^{-1}$, where $K = k_1 + k_2 + k_3$. Efforts to match the power spectrum by modifying the standard four-parameter HOD model resulted in over-boosting of the bispectrum (creating about a 10% excess in the sliced bispectrum correlator). In contrast, populating halos with an assembly bias model which used halo concentration information allowed us to recover the benchmark power spectrum to within 1% and the bispectrum to within 4% across the entire range of scales of the simulation. In its most accurate form this involved using a joint lognormal-Gaussian probability distribution for the subhalo number and concentration, coupled with a radial power law halo profile with index -1.2, together with the concentrations found for individual halos. We could also phenomenologically reduce this small remaining power deficit by adding an extra galaxy to all parent halos above a certain mass threshold $M > 2 \times 10^{14}\,h^{-1} M_{\odot}$ to obtain a better than 1% fit to both the benchmark power spectrum and bispectrum in the range $0.04\,h\,\mathrm{Mpc}^{-1} < k, K/3 < 1.1\,h\,\mathrm{Mpc}^{-1}$. This robust statistical prescription for populating parent halos with subhalos should be applicable to fast dark matter codes, allowing us to rapidly generate and analyse mock catalogues which simultaneously reproduce both the halo power spectrum and bispectrum obtained from nonlinear N-body simulations. We anticipate that this approach can be adapted to match polyspectra obtained from more sophisticated N-body and hydrodynamic simulations. Combining this relatively simple methodology with fast estimators like `MODAL-LSS` should enable the bispectrum to become a key diagnostic tool, both for breaking degeneracies in cosmological parameter estimation and for quantitatively analysing gravitational collapse and other physical effects on highly nonlinear length scales.

Chapter 5

Conclusions

In the last few decades we have been ushered into the precision age of Cosmology, primarily because of highly successful CMB missions such as Planck, culminating in very tight measurements on the parameters of the ΛCDM model of the Universe. However, to make further progress in our understanding we must exploit the three-dimensional information available from the matter distribution in the Universe as opposed to two-dimensional CMB maps. The cross-correlation of these datasets, such as in CMB lensing studies, will provide additional opportunities to put independent constraints on cosmological parameters. While the matter power spectrum has been the primary source of cosmological information from LSS to date, at the mildly non-linear scales probed by galaxy surveys the three-point correlation function, or bispectrum, is expected to be one of the most important cosmological observable. Furthermore, the matter bispectrum may lead to a detection of primordial non-Gaussianity, on top of the usual gravitational contributions after decoupling, which will have profound implications for any primordial theories such as inflation. Nevertheless, it is not an easy task to trace the non-linear evolution of LSS, but it is essential if we are to make use of the wealth of cosmological information coming from near-future galaxy surveys. This requires accurate quantitative descriptions of the gravitational and halo bispectrum and the ability to efficiently analyse large numbers of mock galaxy catalogues, which necessitates advances in fast bispectrum estimation techniques. Here, we summarise the most important developments made in understanding and analysing the LSS bispectrum which are reported in this Thesis.

5.1 Bispectrum estimation

While the direct estimation of the bispectrum of a matter density field is numerically intractable, FFT-based methods are popular in the literature to enable its computation for a se-

lection of triangular configurations. In this thesis we present the newly rewritten MODAL-LSS algorithm which reduces the numerical intensity of bispectrum estimation into a series of FFTs through an eigenmode expansion. The MODAL-LSS methodology has previously been shown to be superior to other bispectrum estimators in terms of data compression, and we have further enhanced its capabilities in a number of ways. First, increased parallelisation and an improved choice of numerical libraries allowed us to analyse 2048^3 FFT grids with $\mathcal{O}(1000)$ eigenmodes and thus obtain an estimate of the bispectrum of a dark matter simulation with unprecedented accuracy and speed. Additionally, the incorporation of custom modes into our eigenmode basis, which were designed to capture the late-time matter bispectrum signal, led to rapid convergence and effective reconstruction of any matter bispectrum signal.

Through rigorous tests we have demonstrated the precision with which MODAL-LSS can be used to reconstruct all the theoretical 3D bispectrum shapes commonly mentioned in the literature, and to obtain the estimated bispectrum of large density grids. We have also investigated sources of systematic and random errors in bispectrum estimation, in particular writing down for the first time the covariance of the MODAL-LSS estimator. Interestingly, we have observed that the cutoff frequency for aliasing contributions in the MODAL-LSS estimator is the same as the Nyquist frequency for the power spectrum, i.e. at $k_{Ny} = \frac{1}{2}k_{max}$, contrary to the value of $\frac{1}{3}k_{max}$ that others have obtained.

5.2 Dark Matter Bispectrum

To be able to make comparisons between our theoretical models and observation we are reliant on large N-body simulations as non-linear gravitational interactions cannot be traced analytically at small scales. Furthermore, to infer constraints on cosmological parameters using observational data one needs a large number of simulation realisations to accurately estimate covariance matrices. Clearly the generation of thousands of high-precision N-body runs is impractical, and many have developed fast numerical methods to trade accuracy for computational efficiency. We have benchmarked some of these methods against the tree-PM code GADGET-3 with the power spectrum and bispectrum, and we have quantified the deficiencies that result. We have also shown how these effects can be ameliorated by a simple boosting technique for the bispectrum that exploits the measured power spectrum deficit.

We have estimated the covariance of the MODAL-LSS estimator using 10 COLA simulations, showing how it deviates from its Gaussian prediction at $k \sim 0.1\,h$Mpc and flattens towards 0.1% at large k. This has important consequences for forecasts using the galaxy surveys

because typically only the Gaussian contributions to the covariances have been considered, which may significantly inflate the ability to place constraints on cosmological parameters. As MODAL-LSS was developed to facilitate comparisons between theoretical and observational bispectra we have tested our dark matter simulations against the tree-level bispectrum at large scales, and have observed known transient modes and grid resolution effects that distort the initial bispectrum. Although these transient effects diminish for late redshifts they are still measurable on the very largest scales after averaging over many realisations, so they remain problematic and will need to be corrected using improved initial conditions.

5.3 Halo Bispectrum

After our work on the fast dark matter simulation codes, the logical progression towards observational data is the mapping between dark matter particles and dark matter halos, which in turn provides the gravitational framework in which baryons collapse to form visible galaxies. Although this mapping, more commonly known as 'halo finding' is typically less computationally expensive than dark matter N-body simulations, it nevertheless remains a bottleneck in the analysis of observational data. More importantly the detailed pathways by which dark matter and baryons interact to form galaxies remains to be adequately understood, so an important way to make progress is to try and construct galaxy mock catalogues phenomenologically with given observables. This will lend us some insight into the physical factors that are most relevant and, in our case, to determine the utility of the bispectrum in distinguishing between different galaxy formation pathways.

This is the approach we have adopted by attempting to reproduce the power spectrum and bispectrum of a benchmark galaxy mock catalogue. Through ROCKSTAR, a state-of-the-art phase space halo finder, we have obtained a benchmark halo catalogue from the GADGET-3 simulation of our previous work. This was then adopted in a benchmark galaxy catalogue by identifying galaxies with the subhalos. Our investigations have shown that the radial NFW profile, commonly used in the literature to populate halos with galaxies, is inappropriate, and that a power law profile should be used instead. Additionally, the occupation number of halos are typically modelled with an HOD algorithm which depends only on halo mass. We have seen that this leads to a power deficit at large scales in both the power spectrum and bispectrum, which hints at the necessity of a more sophisticated modelling of the halo occupation number. Following the examples of others we incorporated halo concentration information, which has shown to be correlated with the assembly history of the halos, to build assembly bias models of both the halo occupation number and halo concentration. Our joint lognormal-Gaussian assembly bias model, coupled with a radial power law halo

profile of $r^{-1.2}$, was shown to match the power spectrum and bispectrum of the benchmark catalogue far better than the alternatives we investigated. Furthermore, by boosting the occupation number of all parent halos with mass $M > 2 \times 10^{14}\, h^{-1} M_{\odot}$ by an extra galaxy, we were able to recover the benchmark power spectrum and bispectrum to 1% in the range $0.04\, h\,\mathrm{Mpc}^{-1} < k < 1.1\, h\,\mathrm{Mpc}^{-1}$.

5.4 Outlook

Using novel and highly efficient numerical methods employing separable eigenmodes, we have pioneered three-dimensional bispectrum estimation to characterise large-scale structure distributions with the aim of substantially increasing the cosmological information that can be extracted from near-future galaxy surveys like LSST and Euclid. The focus of the Thesis has been on direct estimation of the bispectrum from dark matter N-body simulations and fast dark matter codes, as well as dark matter configurations analysed to locate their halos (or galaxies). This has now created a high precision diagnostic tool capable of rapidly recovering the full 3D bispectrum to sub-percent accuracy across a wide range of scales. Our work on the dark matter bispectrum brought our attention to problematic transient modes in the initial conditions for N-body simulations, which may bias the estimation of cosmological parameters and their errors, and require further investigations. With `MODAL-LSS` we have systematically developed approximate methods to create mock galaxy catalogues with a realistic power spectrum and bispectrum, which is an essential prerequisite for the statistical analysis of huge galaxy surveys, i.e. for the estimation of covariance matrices, elimination of selection contributions to the bispectrum, and other systematic effects. Although additional observation effects must be incorporated in the present analysis, most notably a repetition of our investigations in redshift space while incorporating redshift space distortions (RSDs), this work represents an important step which will shortly enable a near-optimal estimate to be made of the full 3D bispectrum in publicly available galaxy survey data from the Sloan Digital Sky Survey and then the Dark Energy Survey. This programme of work should allow for the improved measurement of cosmological parameters (notably galaxy bias parameters and σ_8 where power spectrum degeneracies can be removed) as well as an initial search for bispectrum signatures predicted by competing early universe scenarios. These developments in tractable bispectrum estimation open a new non-Gaussian window on the Universe using large-scale structure observations which, in tandem and cross-correlated with CMB maps, should prove to be a valuable tool for cosmology on the largest scales, while also helping to quantitatively characterise nonlinear evolution on smaller galaxy and cluster scales.

References

[1] Johnathan Hung, James R. Fergusson, and E. P. S. Shellard. Advancing the matter bispectrum estimation of large-scale structure: a comparison of dark matter codes, 2019, arXiv:1902.01830.

[2] Johnathan Hung, Marc Manera, and E. P. S. Shellard. Advancing the matter bispectrum estimation of large-scale structure: fast prescriptions for galaxy mock catalogues, 2019, arXiv:1909.03248.

[3] ESA/Planck Collaboration. Planck's view of the cosmic microwave background, 208. [Online; accessed October 11, 2018].

[4] I. Zehavi, Z. Zheng, D. H. Weinberg, et al. Galaxy Clustering in the Completed SDSS Redshift Survey: The Dependence on Color and Luminosity. *The Astrophysical Journal*, 736:59, July 2011, 1005.2413.

[5] Edwin Hubble. A relation between distance and radial velocity among extra-galactic nebulae. *Proceedings of the National Academy of Sciences*, 15(3):168–173, 1929, https://www.pnas.org/content/15/3/168.full.pdf.

[6] Daniel Baumann. TASI Lectures on Inflation, 2009, arXiv:0907.5424.

[7] Daniel Baumann. TASI Lectures on Primordial Cosmology, 2018, arXiv:1807.03098.

[8] Planck Collaboration, Y. Akrami, F. Arroja, et al. Planck 2018 results. X. Constraints on inflation, 2018, arXiv:1807.06211.

[9] Antony Lewis, Anthony Challinor, and Anthony Lasenby. Efficient Computation of Cosmic Microwave Background Anisotropies in Closed Friedmann-Robertson-Walker Models. *The Astrophysical Journal*, 538(2):473, 2000.

[10] Max Tegmark, Michael R. Blanton, Michael A. Strauss, et al. The Three-Dimensional Power Spectrum of Galaxies from the Sloan Digital Sky Survey. *The Astrophysical Journal*, 606(2):702–740, may 2004.

[11] Andrei Lazanu, Tommaso Giannantonio, Marcel Schmittfull, and E. P. S. Shellard. Matter bispectrum of large-scale structure: Three-dimensional comparison between theoretical models and numerical simulations. *Phys. Rev. D*, 93:083517, Apr 2016.

[12] J. Jasche, F. S. Kitaura, and T. A. Ensslin. Digital Signal Processing in Cosmology, 2009, arXiv:0901.3043.

[13] Cullan Howlett, Marc Manera, and Will J. Percival. L-PICOLA: A parallel code for fast dark matter simulation, 2015, arXiv:1506.03737.

[14] Peter S. Behroozi, Risa H. Wechsler, and Hao-Yi Wu. The ROCKSTAR Phase-space Temporal Halo Finder and the Velocity Offsets of Cluster Cores. *The Astrophysical Journal*, 762(2):109, 2013.

[15] Asantha Cooray and Ravi Sheth. Halo models of large scale structure. *Physics Reports*, 372(1):1 – 129, 2002.

[16] Planck Collaboration. Planck 2015 results - XIII. Cosmological parameters. *Astronomy & Astrophysics*, 594:A13, 2016.

[17] Nuala McCullagh, Donghui Jeong, and Alexander S. Szalay. Toward accurate modelling of the non-linear matter bispectrum: standard perturbation theory and transients from initial conditions. *Monthly Notices of the Royal Astronomical Society*, 455(3):2945–2958, 2016.

[18] Martín Crocce, Sebastián Pueblas, and Román Scoccimarro. Transients from initial conditions in cosmological simulations. *Monthly Notices of the Royal Astronomical Society*, 373(1):369–381, 2006.

[19] Andrew R. Liddle. *An introduction to modern cosmology*. Wiley, Chichester, second edition. edition, 2003.

[20] A. Friedman. Über die Krümmung des Raumes. *Zeitschrift für Physik*, 10(1):377–386, Dec 1922.

[21] G. Lemaître. L'Univers en expansion. *Annales de la Société Scientifique de Bruxelles*, 53, 1933.

[22] H. P. Robertson. Kinematics and World-Structure. *The Astrophysical Journal*, 82:284, November 1935.

[23] A. G. Walker. On Milne's Theory of World-Structure. *Proceedings of the London Mathematical Society*, s2-42(1):90–127, 1937.

[24] Wei-Tou Ni. Solar-system tests of the relativistic gravity. *International Journal of Modern Physics D*, 25(14):1630003, 2016, https://doi.org/10.1142/S0218271816300032.

[25] LIGO Scientific and Virgo Collaborations. Tests of General Relativity with GW150914. *Phys. Rev. Lett.*, 116:221101, May 2016.

[26] Timothy Clifton, Pedro G. Ferreira, Antonio Padilla, and Constantinos Skordis. Modified gravity and cosmology. *Physics Reports*, 513(1):1 – 189, 2012. Modified Gravity and Cosmology.

[27] A. A. Penzias and R. W. Wilson. A Measurement of Excess Antenna Temperature at 4080 Mc/s. *The Astrophysical Journal*, 142:419–421, July 1965.

[28] Adam G. Riess, Alexei V. Filippenko, Peter Challis, et al. Observational Evidence from Supernovae for an Accelerating Universe and a Cosmological Constant. *The Astronomical Journal*, 116(3):1009, 1998.

[29] S. Perlmutter, G. Aldering, G. Goldhaber, et al. Measurements of Ω and Λ from 42 High-Redshift Supernovae. *The Astrophysical Journal*, 517(2):565, 1999.

[30] Steven Weinberg. *Cosmology*. Oxford University Press, Oxford, 2008.

[31] David N. Spergel. The dark side of cosmology: Dark matter and dark energy. *Science*, 347(6226):1100–1102, 2015, http://science.sciencemag.org/content/347/6226/1100.full.pdf.

[32] Planck Collaboration, Y. Akrami, F. Arroja, et al. Planck 2018 results. I. Overview and the cosmological legacy of Planck, 2018, arXiv:1807.06205.

[33] Planck Collaboration, N. Aghanim, Y. Akrami, et al. Planck 2018 results. VI. Cosmological parameters, 2018, arXiv:1807.06209.

[34] Peter Ade, James Aguirre, Zeeshan Ahmed, et al. The Simons Observatory: science goals and forecasts. *Journal of Cosmology and Astroparticle Physics*, 2019(02):056–056, feb 2019.

[35] R. Gualtieri, J. P. Filippini, P. A. R. Ade, et al. SPIDER: CMB Polarimetry from the Edge of Space. *Journal of Low Temperature Physics*, 193(5):1112–1121, Dec 2018.

[36] Hirokazu Ishino. LiteBIRD. *International Journal of Modern Physics: Conference Series*, 43:1660192, 2016, https://doi.org/10.1142/S2010194516601927.

[37] P. Daniel Meerburg, Daniel Green, Muntazir Abidi, et al. Primordial Non-Gaussianity, 2019, arXiv:1903.04409.

[38] N. Kaiser. On the spatial correlations of Abell clusters. *The Astrophysical Journal*, 284:L9–L12, September 1984.

[39] T. K. Chan, D. Kereš, J. Oñorbe, et al. The impact of baryonic physics on the structure of dark matter haloes: the view from the FIRE cosmological simulations. *Monthly Notices of the Royal Astronomical Society*, 454(3):2981–3001, 10 2015, http://oup.prod.sis.lan/mnras/article-pdf/454/3/2981/4038253/stv2165.pdf.

[40] Adam G. Riess, Stefano Casertano, Wenlong Yuan, et al. New Parallaxes of Galactic Cepheids from Spatially Scanning the Hubble Space Telescope : Implications for the Hubble Constant. *The Astrophysical Journal*, 855(2):136, 2018.

[41] The Dark Energy Survey Collaboration. The Dark Energy Survey, 2005, arXiv:astro-ph/0510346.

[42] H. T. Diehl et al. The Dark Energy Survey and operations: Year 1. *Proc.SPIE*, 9149, 2014.

[43] Z. Ivezic et al. LSST: from Science Drivers to Reference Design and Anticipated Data Products, 2008, arXiv:0805.2366.

[44] R. Laureijs et al. Euclid Definition Study Report, 2011, arXiv:1110.3193.

[45] Chris Bebek Brenna Flaugher. The Dark Energy Spectroscopic Instrument (DESI). *Proc.SPIE*, 9147, 2014.

[46] Tobias Baldauf, Mehrdad Mirbabayi, Marko Simonović, and Matias Zaldarriaga. LSS constraints with controlled theoretical uncertainties, 2016, arXiv:1602.00674.

[47] A. Einstein. Die Feldgleichungen der Gravitation. *Sitzungsberichte der Königlich Preußischen Akademie der Wissenschaften (Berlin), Seite 844-847.*, 1915.

[48] A. Einstein. Kosmologische Betrachtungen zur allgemeinen Relativitätstheorie. *Sitzungsberichte der Königlich Preußischen Akademie der Wissenschaften (Berlin), Seite 142-152.*, 1917.

[49] Sean M. Carroll. Lecture Notes on General Relativity, 1997, arXiv:gr-qc/9712019.

[50] D. N. Spergel et al. First year Wilkinson Microwave Anisotropy Probe (WMAP) observations: Determination of cosmological parameters. *Astrophys. J. Suppl.*, 148:175–194, 2003, astro-ph/0302209.

[51] Planck Collaboration, P. A. R. Ade, N. Aghanim, et al. Planck 2015 results - XVII. Constraints on primordial non-Gaussianity. *A&A*, 594:A17, 2016.

[52] Jason Kalirai. Scientific discovery with the James Webb Space Telescope. *Contemporary Physics*, 59(3):251–290, 2018, https://doi.org/10.1080/00107514.2018.1467648.

[53] M. Pierre, C. Adami, M. Birkinshaw, et al. The XXL survey: First results and future. *Astronomische Nachrichten*, 338(2-3):334–341, 2017, https://onlinelibrary.wiley.com/doi/pdf/10.1002/asna.201713352.

[54] G. P. Efstathiou, R. S. Ellis, J. E. Gunn, D. York, and Matthew Colless. First results from the 2dF Galaxy Redshift Survey. *Philosophical Transactions of the Royal Society of London. Series A: Mathematical, Physical and Engineering Sciences*, 357(1750):105–116, 1999, https://royalsocietypublishing.org/doi/pdf/10.1098/rsta.1999.0317.

[55] K. Abazajian, J. K. Adelman-McCarthy, M. A. Agüeros, et al. The First Data Release of the Sloan Digital Sky Survey. *The Astronomical Journal*, 126:2081–2086, October 2003, astro-ph/0305492.

[56] B. P. Abbott, R. Abbott, T. D. Abbott, et al. Observation of Gravitational Waves from a Binary Black Hole Merger. *Phys. Rev. Lett.*, 116:061102, Feb 2016.

[57] B. P. Abbott, R. Abbott, T. D. Abbott, et al. GW151226: Observation of Gravitational Waves from a 22-Solar-Mass Binary Black Hole Coalescence. *Phys. Rev. Lett.*, 116:241103, Jun 2016.

[58] B. P. Abbott, R. Abbott, T. D. Abbott, et al. GW170104: Observation of a 50-Solar-Mass Binary Black Hole Coalescence at Redshift 0.2. *Phys. Rev. Lett.*, 118:221101, Jun 2017.

[59] B. P. Abbott, R. Abbott, T. D. Abbott, et al. GW170814: A Three-Detector Observation of Gravitational Waves from a Binary Black Hole Coalescence. *Phys. Rev. Lett.*, 119:141101, Oct 2017.

[60] B. P. Abbott, R. Abbott, T. D. Abbott, et al. GW170817: Observation of Gravitational Waves from a Binary Neutron Star Inspiral. *Phys. Rev. Lett.*, 119:161101, Oct 2017.

[61] The LIGO Scientific Collaboration, the Virgo Collaboration, B. P. Abbott, et al. GW170608: Observation of a 19-solar-mass Binary Black Hole Coalescence, 2017, arXiv:1711.05578.

[62] Jonathan R Gair, Stanislav Babak, Alberto Sesana, et al. Prospects for observing extreme-mass-ratio inspirals with LISA. *Journal of Physics: Conference Series*, 840:012021, may 2017.

[63] Jonathan R. Gair. The Scientific Potential of Space-Based Gravitational Wave Detectors. In Carlos F. Sopuerta, editor, *Gravitational Wave Astrophysics*, pages 225–243, Cham, 2015. Springer International Publishing.

[64] G. Lemaître. Un Univers homogène de masse constante et de rayon croissant rendant compte de la vitesse radiale des nébuleuses extra-galactiques. *Annales de la Société Scientifique de Bruxelles*, 47:49–59, 1927.

[65] Adam G. Riess, Stefano Casertano, Wenlong Yuan, Lucas M. Macri, and Dan Scolnic. Large Magellanic Cloud Cepheid Standards Provide a 1% Foundation for the Determination of the Hubble Constant and Stronger Evidence for Physics beyond ΛCDM. *The Astrophysical Journal*, 876(1):85, may 2019.

[66] E. Di Valentino, E. V. Linder, and A. Melchiorri. Vacuum phase transition solves the H_0 tension. *Phys. Rev. D*, 97(4):043528, February 2018, 1710.02153.

[67] E. Di Valentino, C. Bœhm, E. Hivon, and F. R. Bouchet. Reducing the H_0 and σ_8 tensions with dark matter-neutrino interactions. *Phys. Rev. D*, 97(4):043513, February 2018, 1710.02559.

[68] Pablo Lemos, Elizabeth Lee, George Efstathiou, and Steven Gratton. Model independent H(z) reconstruction using the cosmic inverse distance ladder. *Monthly Notices of the Royal Astronomical Society*, 483(4):4803–4810, 11 2018, http://oup.prod.sis.lan/mnras/article-pdf/483/4/4803/27441127/sty3082.pdf.

[69] D. J. Fixsen. THE TEMPERATURE OF THE COSMIC MICROWAVE BACKGROUND. *The Astrophysical Journal*, 707(2):916–920, nov 2009.

[70] R.H. Dicke. *Gravitation and the universe*. Memoirs of the American Philosophical Society. American Philosophical Society, 1970.

[71] V. Mukhanov. *Physical Foundations of Cosmology*. Cambridge University Press, Oxford, 2005.

[72] R. Brandenberger. Alternatives to cosmological inflation. *Physics Today*, 61(3):44, 2008.

[73] A. A. Starobinskiĭ. Spectrum of relict gravitational radiation and the early state of the universe. *Soviet Journal of Experimental and Theoretical Physics Letters*, 30:682, December 1979.

[74] Alan H. Guth. Inflationary universe: A possible solution to the horizon and flatness problems. *Phys. Rev. D*, 23:347–356, Jan 1981.

[75] Andreas Albrecht and Paul J. Steinhardt. Cosmology for Grand Unified Theories with Radiatively Induced Symmetry Breaking. *Phys. Rev. Lett.*, 48:1220–1223, Apr 1982.

[76] C. P. Burgess and G. D. Moore. *The Standard Model: A Primer*. Cambridge University Press, 2006.

[77] Jérôme Martin, Christophe Ringeval, Roberto Trotta, and Vincent Vennin. The best inflationary models after Planck. *Journal of Cosmology and Astroparticle Physics*, 2014(03):039–039, mar 2014.

[78] Vladimir Shiltsev. Crystal Ball: On the Future High Energy Colliders, 2015, arXiv:1511.01934.

[79] Eiichiro Komatsu and David N. Spergel. Acoustic signatures in the primary microwave background bispectrum. *Phys. Rev. D*, 63:063002, Feb 2001.

[80] Planck Collaboration, Y. Akrami, F. Arroja, et al. Planck 2018 results. IX. Constraints on primordial non-Gaussianity, 2019, arXiv:1905.05697.

[81] Xingang Chen, Min xin Huang, Shamit Kachru, and Gary Shiu. Observational signatures and non-Gaussianities of general single-field inflation. *Journal of Cosmology and Astroparticle Physics*, 2007(01):002–002, jan 2007.

[82] Leonardo Senatore, Kendrick M Smith, and Matias Zaldarriaga. Non-Gaussianities in single field inflation and their optimal limits from the WMAP 5-year data. *Journal of Cosmology and Astroparticle Physics*, 2010(01):028–028, jan 2010.

[83] Paolo Creminelli, Alberto Nicolis, Leonardo Senatore, Max Tegmark, and Matias Zaldarriaga. Limits on non-Gaussianities from WMAP data. *Journal of Cosmology and Astroparticle Physics*, 2006(05):004–004, may 2006.

[84] Paolo Creminelli and Matias Zaldarriaga. A single-field consistency relation for the three-point function. *Journal of Cosmology and Astroparticle Physics*, 2004(10):006–006, oct 2004.

[85] Juan Maldacena. Non-gaussian features of primordial fluctuations in single field inflationary models. *Journal of High Energy Physics*, 2003(05):013, 2003.

[86] Xingang Chen. Primordial Non-Gaussianities from Inflation Models. *Adv. Astron.*, 2010:638979, 2010, 1002.1416.

[87] A. Challinor, R. Allison, J. Carron, et al. Exploring cosmic origins with CORE: Gravitational lensing of the CMB. *Journal of Cosmology and Astroparticle Physics*, 2018(04):018–018, apr 2018.

[88] M. Jarvis et al. The DES Science Verification weak lensing shear catalogues. *Monthly Notices of the Royal Astronomical Society*, 460(2):2245–2281, 2016.

[89] Dionysios Karagiannis, Andrei Lazanu, Michele Liguori, et al. Constraining Primordial non-Gaussianity with Bispectrum and Power Spectum from Upcoming Optical and Radio Surveys, 2018, arXiv:1801.09280.

[90] Román Scoccimarro, Emiliano Sefusatti, and Matias Zaldarriaga. Probing primordial non-Gaussianity with large-scale structure. *Phys. Rev. D*, 69:103513, May 2004.

[91] Emiliano Sefusatti and Eiichiro Komatsu. Bispectrum of galaxies from high-redshift galaxy surveys: Primordial non-Gaussianity and nonlinear galaxy bias. *Phys. Rev. D*, 76:083004, Oct 2007.

[92] Yong-Seon Song, Atsushi Taruya, and Akira Oka. Cosmology with anisotropic galaxy clustering from the combination of power spectrum and bispectrum. *Journal of Cosmology and Astroparticle Physics*, 2015(08):007, 2015.

[93] Matteo Tellarini, Ashley J. Ross, Gianmassimo Tasinato, and David Wands. Galaxy bispectrum, primordial non-Gaussianity and redshift space distortions. *Journal of Cosmology and Astroparticle Physics*, 2016(06):014, 2016.

[94] Planck Collaboration. Planck 2013 results. XX. Cosmology from Sunyaev–Zeldovich cluster counts. *A&A*, 571:A20, 2014.

[95] Christian Wagner, Licia Verde, and Lotfi Boubekeur. N-body simulations with generic non-Gaussian initial conditions I: power spectrum and halo mass function. *Journal of Cosmology and Astroparticle Physics*, 2010(10):022–022, oct 2010.

[96] D. M. Regan, M. M. Schmittfull, E. P. S. Shellard, and J. R. Fergusson. Universal non-Gaussian initial conditions for N-body simulations. *Phys. Rev. D*, 86:123524, Dec 2012.

[97] Héctor Gil-Marín, Christian Wagner, Frantzeska Fragkoudi, Raul Jimenez, and Licia Verde. An improved fitting formula for the dark matter bispectrum. *Journal of Cosmology and Astroparticle Physics*, 2012(02):047, 2012.

[98] M. M. Schmittfull, D. M. Regan, and E. P. S. Shellard. Fast estimation of gravitational and primordial bispectra in large scale structures. *Phys. Rev. D*, 88:063512, Sep 2013.

[99] Daniel J. Eisenstein et al. SDSS-III: Massive Spectroscopic Surveys of the Distant Universe, the Milky Way, and Extra-Solar Planetary Systems. *The Astronomical Journal*, 142(3):72, 2011.

[100] Kyle S. Dawson et al. The Baryon Oscillation Spectroscopic Survey of SDSS-III. *The Astronomical Journal*, 145(1):10, 2013.

[101] Héctor Gil-Marín, Jorge Noreña, Licia Verde, et al. The power spectrum and bispectrum of SDSS DR11 BOSS galaxies – I. Bias and gravity. *Monthly Notices of the Royal Astronomical Society*, 451(1):539–580, 2015.

[102] Héctor Gil-Marín, Licia Verde, Jorge Noreña, et al. The power spectrum and bispectrum of SDSS DR11 BOSS galaxies – II. Cosmological interpretation. *Monthly Notices of the Royal Astronomical Society*, 452(2):1914–1921, 2015.

[103] Héctor Gil-Marín et al. The clustering of galaxies in the SDSS-III Baryon Oscillation Spectroscopic Survey: RSD measurement from the power spectrum and bispectrum of the DR12 BOSS galaxies. *Monthly Notices of the Royal Astronomical Society*, 465(2):1757–1788, 2017.

[104] Daniel Baumann, Alberto Nicolis, Leonardo Senatore, and Matias Zaldarriaga. Cosmological non-linearities as an effective fluid. *Journal of Cosmology and Astroparticle Physics*, 2012(07):051–051, jul 2012.

[105] John Joseph M. Carrasco, Mark P. Hertzberg, and Leonardo Senatore. The effective field theory of cosmological large scale structures. *Journal of High Energy Physics*, 2012(9):82, Sep 2012.

[106] U. Seljak and M. Zaldarriaga. A Line-of-Sight Integration Approach to Cosmic Microwave Background Anisotropies. *The Astrophysical Journal*, 469:437, October 1996, astro-ph/9603033.

[107] Julien Lesgourgues. The Cosmic Linear Anisotropy Solving System (CLASS) I: Overview, 2011, arXiv:1104.2932.

[108] F. Bernardeau, S. Colombi, E. Gaztañaga, and R. Scoccimarro. Large-scale structure of the Universe and cosmological perturbation theory. *Physics Reports*, 367(1–3):1 – 248, 2002.

[109] R. Scoccimarro, S. Colombi, J. N. Fry, et al. Nonlinear Evolution of the Bispectrum of Cosmological Perturbations. *The Astrophysical Journal*, 496:586–604, March 1998, astro-ph/9704075.

[110] Ryuichi Takahashi. Third-Order Density Perturbation and One-Loop Power Spectrum in Dark-Energy-Dominated Universe. *Progress of Theoretical Physics*, 120(3):549–559, 09 2008, http://oup.prod.sis.lan/ptp/article-pdf/120/3/549/5203666/120-3-549.pdf.

[111] F. R. Bouchet, S. Colombi, E. Hivon, and R. Juszkiewicz. Perturbative Lagrangian approach to gravitational instability. *A & A*, 296:575, April 1995, astro-ph/9406013.

[112] Donghui Jeong. *Cosmology with high ($z > 1$) redshift galaxy surveys*. PhD thesis, The University of Texas at Austin, 2010.

[113] Tobias Baldauf. Advanced Cosmology, 2019.

[114] Nobuyoshi Makino, Misao Sasaki, and Yasushi Suto. Analytic approach to the perturbative expansion of nonlinear gravitational fluctuations in cosmological density and velocity fields. *Phys. Rev. D*, 46:585–602, Jul 1992.

[115] B. Jain and E. Bertschinger. Second-order power spectrum and nonlinear evolution at high redshift. *The Astrophysical Journal*, 431:495–505, August 1994, astro-ph/9311070.

[116] M. H. Goroff, B. Grinstein, S.-J. Rey, and M. B. Wise. Coupling of modes of cosmological mass density fluctuations. *The Astrophysical Journal*, 311:6–14, December 1986.

[117] Y. B. Zel'dovich. Gravitational instability: An approximate theory for large density perturbations. *Astronomy & Astrophysics*, 5:84–89, March 1970.

[118] T. Buchert and J. Ehlers. Lagrangian theory of gravitational instability of Friedman-Lemaitre cosmologies - second order approach: an improved model for nonlinear clustering. *Monthly Notices of the Royal Astronomical Society*, 264:375–387, 1993.

[119] T. Buchert. Lagrangian Theory of Gravitational Instability of Friedman-Lemaitre Cosmologies - a Generic Third-Order Model for Nonlinear Clustering. *Monthly Notices of the Royal Astronomical Society*, 267:811, April 1994, astro-ph/9309055.

[120] Andrei Lazanu, Tommaso Giannantonio, Marcel Schmittfull, and E. P. S. Shellard. Matter bispectrum of large-scale structure with Gaussian and non-Gaussian initial conditions: Halo models, perturbation theory, and a three-shape model. *Phys. Rev. D*, 95:083511, Apr 2017.

[121] R. E. Smith, J. A. Peacock, A. Jenkins, et al. Stable clustering, the halo model and non-linear cosmological power spectra. *Monthly Notices of the Royal Astronomical Society*, 341(4):1311–1332, 2003.

[122] Asantha Cooray and Ravi Sheth. Halo models of large scale structure. *Physics Reports*, 372(1):1 – 129, 2002.

[123] D.G. Figueroa, E. Sefusatti, A. Riotto, and F. Vernizzi. The effect of local non-Gaussianity on the matter bispectrum at small scales. *Journal of Cosmology and Astroparticle Physics*, 2012(08):036, 2012.

[124] Robert E. Smith, Ravi K. Sheth, and Román Scoccimarro. Analytic model for the bispectrum of galaxies in redshift space. *Phys. Rev. D*, 78:023523, Jul 2008.

[125] Valageas, P. and Nishimichi, T. Combining perturbation theories with halo models. *Astronomy & Astrophysics*, 527:A87, 2011.

[126] Valageas, P. and Nishimichi, T. Combining perturbation theories with halo models for the matter bispectrum. *Astronomy & Astrophysics*, 532:A4, 2011.

[127] H. Mo, F. van den Bosch, and S. White. *Galaxy Formation and Evolution*. Galaxy Formation and Evolution. Cambridge University Press, 2010.

[128] A.R. Liddle and D.H. Lyth. *Cosmological Inflation and Large-Scale Structure*. Cosmological Inflation and Large-scale Structure. Cambridge University Press, 2000.

[129] J. F. Navarro, C. S. Frenk, and S. D. M. White. The Structure of Cold Dark Matter Halos. *The Astrophysical Journal*, 462:563, May 1996, astro-ph/9508025.

[130] J. F. Navarro, C. S. Frenk, and S. D. M. White. A Universal Density Profile from Hierarchical Clustering. *The Astrophysical Journal*, 490:493–508, December 1997, astro-ph/9611107.

[131] J. F. Navarro, C. S. Frenk, and S. D. M. White. The assembly of galaxies in a hierarchically clustering universe. *Monthly Notices of the Royal Astronomical Society*, 275:56–66, July 1995, astro-ph/9408067.

[132] J. Einasto. On the Construction of a Composite Model for the Galaxy and on the Determination of the System of Galactic Parameters. *Trudy Astrofizicheskogo Instituta Alma-Ata*, 5:87–100, Jan 1965.

[133] Aaron D. Ludlow and Raul E. Angulo. Einasto Profiles and the Dark Matter Power Spectrum. *Mon. Not. Roy. Astron. Soc.*, 465(1):L84–L88, 2017, 1610.04620.

[134] W. H. Press and P. Schechter. Formation of Galaxies and Clusters of Galaxies by Self-Similar Gravitational Condensation. *The Astrophysical Journal*, 187:425–438, February 1974.

[135] Andrew R. Zentner. The Excursion Set Theory of Halo Mass Functions, Halo Clustering, and Halo Growth. *International Journal of Modern Physics D*, 16(05):763–815, 2007, https://doi.org/10.1142/S0218271807010511.

[136] R. K. Sheth and G. Tormen. Large-scale bias and the peak background split. *Monthly Notices of the Royal Astronomical Society*, 308:119–126, September 1999, astro-ph/9901122.

[137] Jeremy Tinker, Andrey V. Kravtsov, Anatoly Klypin, et al. Toward a Halo Mass Function for Precision Cosmology: The Limits of Universality. *The Astrophysical Journal*, 688(2):709–728, dec 2008.

[138] Thorsten Naab and Jeremiah P. Ostriker. Theoretical Challenges in Galaxy Formation. *Annual Review of Astronomy and Astrophysics*, 55(1):59–109, 2017, https://doi.org/10.1146/annurev-astro-081913-040019.

[139] J. A. Peacock and R. E. Smith. Halo occupation numbers and galaxy bias. *Monthly Notices of the Royal Astronomical Society*, 318:1144–1156, November 2000, astro-ph/0005010.

[140] R. Scoccimarro, R. K. Sheth, L. Hui, and B. Jain. How Many Galaxies Fit in a Halo? Constraints on Galaxy Formation Efficiency from Spatial Clustering. *The Astrophysical Journal*, 546:20–34, January 2001, astro-ph/0006319.

[141] A. A. Berlind and D. H. Weinberg. The Halo Occupation Distribution: Toward an Empirical Determination of the Relation between Galaxies and Mass. *The Astrophysical Journal*, 575:587–616, August 2002, astro-ph/0109001.

[142] Zheng Zheng, Idit Zehavi, Daniel J. Eisenstein, David H. Weinberg, and Y. P. Jing. HALO OCCUPATION DISTRIBUTION MODELING OF CLUSTERING OF LUMINOUS RED GALAXIES. *The Astrophysical Journal*, 707(1):554–572, nov 2009.

[143] Daniel J. Eisenstein, Lehman H. Garrison, and Sihan Yuan. Using galaxy pairs to investigate the three-point correlation function in the squeezed limit. *Monthly Notices of the Royal Astronomical Society*, 472(1):577–590, 08 2017.

[144] Daniel J Eisenstein, Lehman H Garrison, and Sihan Yuan. Exploring the squeezed three-point galaxy correlation function with generalized halo occupation distribution models. *Monthly Notices of the Royal Astronomical Society*, 478(2):2019–2033, 04 2018.

[145] M. Manera, R. Scoccimarro, W. J. Percival, et al. The clustering of galaxies in the SDSS-III Baryon Oscillation Spectroscopic Survey: a large sample of mock galaxy catalogues. *Monthly Notices of the Royal Astronomical Society*, 428:1036–1054, January 2013, 1203.6609.

[146] Noam I. Libeskind, Carlos S. Frenk, Shaun Cole, et al. The distribution of satellite galaxies: the great pancake. *Monthly Notices of the Royal Astronomical Society*, 363(1):146–152, 10 2005.

[147] Ben Moore, Joachim Stadel, and Jürg Diemand. Velocity and spatial biases in cold dark matter subhalo distributions. *Monthly Notices of the Royal Astronomical Society*, 352(2):535–546, 08 2004.

[148] Mr. Bayes and Mr. Price. An Essay towards Solving a Problem in the Doctrine of Chances. By the Late Rev. Mr. Bayes, F. R. S. Communicated by Mr. Price, in a Letter to John Canton, A. M. F. R. S. *Philosophical Transactions*, 53:370–418, 1763.

[149] Daniel Babich. Optimal estimation of non-Gaussianity. *Phys. Rev. D*, 72:043003, Aug 2005.

[150] Matthew B Wingate. The Standard Model, 2015.

[151] James Ahrens, Berk Geveci, and Charles Law. *ParaView: An End-User Tool for Large Data Visualization.* Visualization Handbook, Elsevier, 01 2005.

[152] B S Everitt and A Skrondal. *The Cambridge Dictionary of Statistics; 4th ed.* Cambridge University Press, Leiden, 2010.

[153] J. R. Fergusson, M. Liguori, and E. P. S. Shellard. General CMB and primordial bispectrum estimation: Mode expansion, map making, and measures of $F_{\rm NL}$. *Phys. Rev. D*, 82:023502, Jul 2010.

[154] Planck Collaboration, Ade, P. A. R., Aghanim, N., et al. Planck 2013 results. XII. Diffuse component separation. *A&A*, 571:A12, 2014.

[155] Z. Slepian and D. J. Eisenstein. Computing the three-point correlation function of galaxies in O(N^2) time. *Monthly Notices of the Royal Astronomical Society*, 454:4142–4158, December 2015, 1506.02040.

[156] Z. Slepian and D. J. Eisenstein. Accelerating the two-point and three-point galaxy correlation functions using Fourier transforms. *Monthly Notices of the Royal Astronomical Society*, 455:L31–L35, January 2016, 1506.04746.

[157] Roman Scoccimarro. Fast estimators for redshift-space clustering. *Phys. Rev. D*, 92:083532, Oct 2015.

[158] J.P. Briggs, S.J. Pennycook, J.R. Fergusson, J. Jäykkä, and E.P.S. Shellard. Separable projection integrals for higher-order correlators of the cosmic microwave sky: Acceleration by factors exceeding 100. *Journal of Computational Physics*, 310:285 – 300, 2016.

[159] Matteo Frigo and Steven G. Johnson. The Design and Implementation of FFTW3. *Proceedings of the IEEE*, 93(2):216–231, 2005. Special issue on "Program Generation, Optimization, and Platform Adaptation".

[160] Mark Galassi et al. *GNU Scientific Library Reference Manual*. Network Theory Ltd., S.l.], 3rd ed., for gsl version 1.12. edition, 2009.

[161] Gene H. Golub. *Matrix computations / Gene H. Golub, Department of Computer Science, Stanford University, Charles F. Van Loan, Department of Computer Science, Cornell University.* Johns Hopkins studies in the mathematical sciences. Johns Hopkins University Press, Baltimore ; London, third edition. edition, 1997.

[162] M. M. Schmittfull, D. M. Regan, and E. P. S. Shellard. Fast estimation of gravitational and primordial bispectra in large scale structures. *Phys. Rev. D*, 88:063512, Sep 2013.

[163] David Seery, Robert E. Smith, Alexander Eggemeier, Donough Regan, and Joyce Byun. Towards optimal cosmological parameter recovery from compressed bispectrum statistics. *Monthly Notices of the Royal Astronomical Society*, 471(2):1581–1618, 07 2017, http://oup.prod.sis.lan/mnras/article-pdf/471/2/1581/19407307/stx1681.pdf.

[164] P. J. E. Peebles. *The large-scale structure of the universe*. Princeton University Press, 1980.

[165] Y. P. Jing. Correcting for the Alias Effect When Measuring the Power Spectrum Using a Fast Fourier Transform. *The Astrophysical Journal*, 620(2):559, 2005.

[166] Licia Verde. A practical guide to Basic Statistical Techniques for Data Analysis in Cosmology, 2007, arXiv:0712.3028.

[167] Kwan Chuen Chan and Linda Blot. Assessment of the information content of the power spectrum and bispectrum. *Phys. Rev. D*, 96:023528, Jul 2017.

[168] I. Mohammed, U. Seljak, and Z. Vlah. Perturbative approach to covariance matrix of the matter power spectrum. *Monthly Notices of the Royal Astronomical Society*, 466:780–797, April 2017, 1607.00043.

[169] H. A. Feldman, N. Kaiser, and J. A. Peacock. Power-spectrum analysis of three-dimensional redshift surveys. *The Astrophysical Journal*, 426:23–37, May 1994, astro-ph/9304022.

[170] Joachimi, B., Shi, X., and Schneider, P. Bispectrum covariance in the flat-sky limit. *A&A*, 508(3):1193–1204, 2009.

[171] Raul E. Angulo and Andrew Pontzen. Cosmological N-body simulations with suppressed variance. *Monthly Notices of the Royal Astronomical Society: Letters*, 462(1):L1–L5, 2016.

[172] Andrew Pontzen, An že Slosar, Nina Roth, and Hiranya V. Peiris. Inverted initial conditions: Exploring the growth of cosmic structure and voids. *Phys. Rev. D*, 93:103519, May 2016.

[173] Weiguang Cui, Lei Liu, Xiaohu Yang, et al. An Ideal Mass Assignment Scheme for Measuring the Power Spectrum with Fast Fourier Transforms. *The Astrophysical Journal*, 687(2):738, 2008.

[174] E. Sefusatti, M. Crocce, R. Scoccimarro, and H. M. P. Couchman. Accurate estimators of correlation functions in Fourier space. *Monthly Notices of the Royal Astronomical Society*, 460(4):3624–3636, 2016.

[175] C. E. Shannon. Communication in the Presence of Noise. *Proceedings of the IRE*, 37(1):10–21, Jan 1949.

[176] P. Monaco, T. Theuns, G. Taffoni, et al. Predicting the Number, Spatial Distribution, and Merging History of Dark Matter Halos. *The Astrophysical Journal*, 564:8–14, January 2002, astro-ph/0109322.

[177] P. Monaco, E. Sefusatti, S. Borgani, et al. An accurate tool for the fast generation of dark matter halo catalogues. *Monthly Notices of the Royal Astronomical Society*, 433:2389–2402, August 2013, 1305.1505.

[178] M. White, J. L. Tinker, and C. K. McBride. Mock galaxy catalogues using the quick particle mesh method. *Monthly Notices of the Royal Astronomical Society*, 437:2594–2606, January 2014, 1309.5532.

[179] F.-S. Kitaura and S. Heß. Cosmological structure formation with augmented Lagrangian perturbation theory. *Monthly Notices of the Royal Astronomical Society*, 435:L78–L82, August 2013, 1212.3514.

[180] Svetlin Tassev, Matias Zaldarriaga, and Daniel J. Eisenstein. Solving large scale structure in ten easy steps with COLA. *Journal of Cosmology and Astroparticle Physics*, 2013(06):036, 2013.

[181] Davide Gualdi, Héctor Gil-Marín, Marc Manera, Benjamin Joachimi, and Ofer Lahav. Geometrical compression: a new method to enhance the BOSS galaxy bispectrum monopole constraints. *Monthly Notices of the Royal Astronomical Society: Letters*, 484(1):L29–L34, 01 2019, http://oup.prod.sis.lan/mnrasl/article-pdf/484/1/L29/27496796/sly242.pdf.

[182] Davide Gualdi, Marc Manera, Benjamin Joachimi, and Ofer Lahav. Maximal compression of the redshift-space galaxy power spectrum and bispectrum. *Monthly Notices of the Royal Astronomical Society*, 476(3):4045–4070, 01 2018, http://oup.prod.sis.lan/mnras/article-pdf/476/3/4045/24541764/sty261.pdf.

[183] Davide Gualdi, Héctor Gil-Marín, Robert L Schuhmann, et al. Enhancing BOSS bispectrum cosmological constraints with maximal compression. *Monthly Notices of the Royal Astronomical Society*, 484(3):3713–3730, 01 2019, http://oup.prod.sis.lan/mnras/article-pdf/484/3/3713/27723669/stz051.pdf.

[184] Alan F. Heavens, Elena Sellentin, Damien de Mijolla, and Alvise Vianello. Massive data compression for parameter-dependent covariance matrices. *Monthly Notices of the Royal Astronomical Society*, 472(4):4244–4250, Dec 2017, 1707.06529.

[185] Justin Alsing and Benjamin Wandelt. Generalized massive optimal data compression. *Monthly Notices of the Royal Astronomical Society: Letters*, 476(1):L60–L64, 02 2018, http://oup.prod.sis.lan/mnrasl/article-pdf/476/1/L60/24566044/sly029.pdf.

[186] R. Scoccimarro. Transients from initial conditions: a perturbative analysis. *Monthly Notices of the Royal Astronomical Society*, 299:1097–1118, October 1998, astro-ph/9711187.

[187] Román Scoccimarro, Lam Hui, Marc Manera, and Kwan Chuen Chan. Large-scale bias and efficient generation of initial conditions for nonlocal primordial non-Gaussianity. *Phys. Rev. D*, 85:083002, Apr 2012.

[188] R. W. Hockney and J. W. Eastwood. *Computer simulation using particles*. Bristol: Hilger, 1988.

[189] Martín Crocce, Sebastián Pueblas, and Román Scoccimarro. Transients from initial conditions in cosmological simulations. *Monthly Notices of the Royal Astronomical Society*, 373(1):369–381, 2006.

[190] A. Klypin and J. Holtzman. Particle-Mesh code for cosmological simulations. *ArXiv Astrophysics e-prints*, December 1997, astro-ph/9712217.

[191] S. Colombi, A. Jaffe, D. Novikov, and C. Pichon. Accurate estimators of power spectra in N-body simulations. *Monthly Notices of the Royal Astronomical Society*, 393:511–526, February 2009, 0811.0313.

[192] Jorge J. Moré. The Levenberg-Marquardt algorithm: Implementation and theory. In G. A. Watson, editor, *Numerical Analysis*, pages 105–116, Berlin, Heidelberg, 1978. Springer Berlin Heidelberg.

[193] Cora Uhlemann, Cornelius Rampf, Mateja Gosenca, and Oliver Hahn. A semiclassical path to cosmic large-scale structure, 2018, arXiv:1812.05633.

[194] N. Kaiser. On the spatial correlations of Abell clusters. *The Astrophysical Journal*, 284:L9–L12, September 1984.

[195] J. M. Gelb and E. Bertschinger. Cold dark matter. 1: The formation of dark halos. *The Astrophysical Journal*, 436:467–490, December 1994, astro-ph/9408028.

[196] J. S. Bullock, T. S. Kolatt, Y. Sigad, et al. Profiles of dark haloes: evolution, scatter and environment. *Monthly Notices of the Royal Astronomical Society*, 321:559–575, March 2001, astro-ph/9908159.

[197] Volker Springel, Simon D. M. White, Giuseppe Tormen, and Guinevere Kauffmann. Populating a cluster of galaxies – I. Results at z = 0. *Monthly Notices of the Royal Astronomical Society*, 328(3):726–750, 2001.

[198] J. G. Stadel. *Cosmological N-body simulations and their analysis*. PhD thesis, UNIVERSITY OF WASHINGTON, 2001.

[199] D. Aubert, C. Pichon, and S. Colombi. The origin and implications of dark matter anisotropic cosmic infall on ˜L_* haloes. *Monthly Notices of the Royal Astronomical Society*, 352:376–398, August 2004, astro-ph/0402405.

[200] S. P. D. Gill, A. Knebe, and B. K. Gibson. The evolution of substructure - I. A new identification method. *Monthly Notices of the Royal Astronomical Society*, 351:399–409, June 2004, astro-ph/0404258.

[201] M. C. Neyrinck, N. Y. Gnedin, and A. J. S. Hamilton. VOBOZ: an almost-parameter-free halo-finding algorithm. *Monthly Notices of the Royal Astronomical Society*, 356:1222–1232, February 2005, astro-ph/0402346.

[202] J. Weller, J. P. Ostriker, P. Bode, and L. Shaw. Fast identification of bound structures in large N-body simulations. *Monthly Notices of the Royal Astronomical Society*, 364:823–832, December 2005, astro-ph/0405445.

[203] J. Diemand, M. Kuhlen, and P. Madau. Early Supersymmetric Cold Dark Matter Substructure. *The Astrophysical Journal*, 649:1–13, September 2006, astro-ph/0603250.

[204] J. Kim and C. Park. A New Halo-finding Method for N-Body Simulations. *The Astrophysical Journal*, 639:600–616, March 2006, astro-ph/0401386.

[205] Jeffrey P. Gardner, Andrew Connolly, and Cameron McBride. Enabling Rapid Development of Parallel Tree Search Applications. In *Proceedings of the 5th IEEE Workshop on Challenges of Large Applications in Distributed Environments*, CLADE '07, pages 1–10, New York, NY, USA, 2007. ACM.

[206] L. D. Shaw, J. Weller, J. P. Ostriker, and P. Bode. The Bound Mass of Substructures in Dark Matter Halos. *The Astrophysical Journal*, 659:1082–1095, April 2007, astro-ph/0603150.

[207] S. Habib, A. Pope, Z. Lukić, et al. Hybrid petacomputing meets cosmology: The Roadrunner Universe project. In *Journal of Physics Conference Series*, volume 180 of *Journal of Physics Conference Series*, page 012019, July 2009.

[208] S. R. Knollmann and A. Knebe. AHF: Amiga's Halo Finder. *The Astrophysical Journal Supplement*, 182:608–624, June 2009, 0904.3662.

[209] M. Maciejewski, S. Colombi, V. Springel, C. Alard, and F. R. Bouchet. Phase-space structures - II. Hierarchical Structure Finder. *Monthly Notices of the Royal Astronomical Society*, 396:1329–1348, July 2009, 0812.0288.

[210] Yago Ascasibar. Estimating multidimensional probability fields using the Field Estimator for Arbitrary Spaces (FiEstAS) with applications to astrophysics. *Computer Physics Communications*, 181(8):1438 – 1443, 2010.

[211] S. Planelles and V. Quilis. ASOHF: a new adaptive spherical overdensity halo finder. *Astronomy and Astrophysics*, 519:A94, September 2010, 1006.3205.

[212] Y. Rasera, J.-M. Alimi, J. Courtin, et al. Introducing the Dark Energy Universe Simulation Series (DEUSS). In J.-M. Alimi and A. Fuözfa, editors, *American Institute of Physics Conference Series*, volume 1241 of *American Institute of Physics Conference Series*, pages 1134–1139, June 2010, 1002.4950.

[213] S. Skory, M. J. Turk, M. L. Norman, and A. L. Coil. Parallel HOP: A Scalable Halo Finder for Massive Cosmological Data Sets. *The Astrophysical Journal Supplement*, 191:43–57, November 2010, 1001.3411.

[214] P. M. Sutter and P. M. Ricker. Examining Subgrid Models of Supermassive Black Holes in Cosmological Simulation. *The Astrophysical Journal*, 723:1308–1318, November 2010, 1006.2879.

[215] Bridget L. Falck, Mark C. Neyrinck, and Alexander S. Szalay. ORIGAMI: Delineating Halos Using Phase-space Folds. *The Astrophysical Journal*, 754(2):126, 2012.

[216] H.-Y. Wu, A. R. Zentner, and R. H. Wechsler. The Impact of Theoretical Uncertainties in the Halo Mass Function and Halo Bias on Precision Cosmology. *The Astrophysical Journal*, 713:856–864, April 2010, 0910.3668.

[217] C. E. Cunha and A. E. Evrard. Sensitivity of galaxy cluster dark energy constraints to halo modeling uncertainties. *Physical Review D*, 81(8):083509, April 2010, 0908.0526.

[218] M. Davis, G. Efstathiou, C. S. Frenk, and S. D. M. White. The evolution of large-scale structure in a universe dominated by cold dark matter. *The Astrophysical Journal*, 292:371–394, May 1985.

[219] W. H. Press and P. Schechter. Formation of Galaxies and Clusters of Galaxies by Self-Similar Gravitational Condensation. *The Astrophysical Journal*, 187:425–438, February 1974.

[220] Alexander Knebe, Steffen R. Knollmann, Stuart I. Muldrew, et al. Haloes gone MAD14: The Halo-Finder Comparison Project. *Monthly Notices of the Royal Astronomical Society*, 415(3):2293–2318, 08 2011, http://oup.prod.sis.lan/mnras/article-pdf/415/3/2293/5972749/mnras0415-2293.pdf.

[221] N. Padmanabhan, D. J. Schlegel, U. Seljak, et al. The clustering of luminous red galaxies in the Sloan Digital Sky Survey imaging data. *Monthly Notices of the Royal Astronomical Society*, 378:852–872, July 2007, astro-ph/0605302.

[222] Roman Scoccimarro. The Bispectrum: From Theory to Observations. *The Astrophysical Journal*, 544(2):597–615, dec 2000.

[223] F.-S. Kitaura, S. Rodríguez-Torres, C.-H. Chuang, et al. The clustering of galaxies in the SDSS-III Baryon Oscillation Spectroscopic Survey: mock galaxy catalogues for the BOSS Final Data Release. *Monthly Notices of the Royal Astronomical Society*, 456:4156–4173, March 2016, 1509.06400.

[224] Jesús Vega-Ferrero, Gustavo Yepes, and Stefan Gottlöber. On the shape of dark matter haloes from MultiDark Planck simulations. *Monthly Notices of the Royal Astronomical Society*, 467(3):3226–3238, 02 2017, http://oup.prod.sis.lan/mnras/article-pdf/467/3/3226/10875743/stx282.pdf.

[225] Michael D Schneider, Carlos S Frenk, and Shaun Cole. The shapes and alignments of dark matter halos. *Journal of Cosmology and Astroparticle Physics*, 2012(05):030–030, may 2012.

[226] Carlos A. Vera-Ciro, Laura V. Sales, Amina Helmi, et al. The shape of dark matter haloes in the Aquarius simulations: evolution and memory. *Monthly Notices of the Royal Astronomical Society*, 416(2):1377–1391, 09 2011, http://oup.prod.sis.lan/mnras/article-pdf/416/2/1377/18594489/mnras0416-1377.pdf.

[227] Angrick, C. and Bartelmann, M. Triaxial collapse and virialisation of dark-matter haloes. *Astronomy & Astrophysics*, 518:A38, 2010.

[228] Anatoly A. Klypin, Sebastian Trujillo-Gomez, and Joel Primack. DARK MATTER HALOS IN THE STANDARD COSMOLOGICAL MODEL: RESULTS FROM THE BOLSHOI SIMULATION. *The Astrophysical Journal*, 740(2):102, oct 2011.

[229] A. Jenkins, G. De Lucia, S. D. M. White, and L. Gao. Galaxies and subhaloes in ΛCDM galaxy clusters. *Monthly Notices of the Royal Astronomical Society*, 352(2):L1–L5, 08 2004.

[230] L. Gao, S. D. M. White, A. Jenkins, F. Stoehr, and V. Springel. The subhalo populations of ΛCDM dark haloes. *Monthly Notices of the Royal Astronomical Society*, 355(3):819–834, 12 2004.

[231] Carlos S. Frenk, Jiaxin Han, Shaun Cole, and Yipeng Jing. A unified model for the spatial and mass distribution of subhaloes. *Monthly Notices of the Royal Astronomical Society*, 457(2):1208–1223, 02 2016, http://oup.prod.sis.lan/mnras/article-pdf/457/2/1208/2882862/stv2900.pdf.

[232] M. Branch, T. Coleman, and Y. Li. A Subspace, Interior, and Conjugate Gradient Method for Large-Scale Bound-Constrained Minimization Problems. *SIAM Journal on Scientific Computing*, 21(1):1–23, 1999, https://doi.org/10.1137/S1064827595289108.

[233] L. Anderson, É. Aubourg, S. Bailey, et al. The clustering of galaxies in the SDSS-III Baryon Oscillation Spectroscopic Survey: baryon acoustic oscillations in the Data Releases 10 and 11 Galaxy samples. *Monthly Notices of the Royal Astronomical Society*, 441:24–62, June 2014, 1312.4877.

[234] S. Gottlöber, A. A. Klypin, and A. V. Kravtsov. Halo evolution in a cosmological environment. In G. Giuricin, M. Mezzetti, and P. Salucci, editors, *Observational Cosmology: The Development of Galaxy Systems*, volume 176 of *Astronomical Society of the Pacific Conference Series*, page 418, Jun 1999, astro-ph/9810445.

[235] Andrey V. Kravtsov and Anatoly A. Klypin. The Origin and Evolution of Halo Bias in Linear and Nonlinear Regimes. *The Astrophysical Journal*, 520(2):437–453, aug 1999.

[236] R. G. Mann, J. A. Peacock, and A. F. Heavens. Eulerian bias and the galaxy density field. *Monthly Notices of the Royal Astronomical Society*, 293(3):209–221, 01 1998, http://oup.prod.sis.lan/mnras/article-pdf/293/3/209/3881609/293-3-209.pdf.

[237] Vincent Desjacques, Donghui Jeong, and Fabian Schmidt. Large-scale galaxy bias. *Physics Reports*, 733:1 – 193, 2018. Large-scale galaxy bias.

[238] Ciyou Zhu, Richard H. Byrd, Peihuang Lu, and Jorge Nocedal. Algorithm 778: L-BFGS-B: Fortran Subroutines for Large-scale Bound-constrained Optimization. *ACM Trans. Math. Softw.*, 23(4):550–560, December 1997.

[239] Richard H. Byrd, Peihuang Lu, Jorge Nocedal, and Ciyou Zhu. A Limited Memory Algorithm for Bound Constrained Optimization. *SIAM Journal on Scientific Computing*, 16(5):1190–1208, 1995.

[240] Francesco Pace, Marc Manera, David J. Bacon, Robert Crittenden, and Will J. Percival. The importance of the cosmic web and halo substructure for power spectra. *Monthly Notices of the Royal Astronomical Society*, 454(1):708–723, 09 2015, http://oup.prod.sis.lan/mnras/article-pdf/454/1/708/3938653/stv2019.pdf.

[241] Robert E. Smith, Ravi K. Sheth, and Román Scoccimarro. Analytic model for the bispectrum of galaxies in redshift space. *Phys. Rev. D*, 78:023523, Jul 2008.

[242] Mohammadjavad Vakili and ChangHoon Hahn. How Are Galaxies Assigned to Halos? Searching for Assembly Bias in the SDSS Galaxy Clustering. *The Astrophysical Journal*, 872(1):115, feb 2019.

[243] L. Gao, V. Springel, and S. D. M. White. The age dependence of halo clustering. *Monthly Notices of the Royal Astronomical Society*, 363:L66–L70, October 2005, astro-ph/0506510.

[244] T. Sunayama, A. P. Hearin, N. Padmanabhan, and A. Leauthaud. The scale-dependence of halo assembly bias. *Monthly Notices of the Royal Astronomical Society*, 458:1510–1516, May 2016, 1509.06417.

[245] A. P. Hearin, A. R. Zentner, F. C. van den Bosch, D. Campbell, and E. Tollerud. Introducing decorated HODs: modelling assembly bias in the galaxy-halo connection. *Monthly Notices of the Royal Astronomical Society*, 460:2552–2570, August 2016, 1512.03050.

[246] Risa H. Wechsler, Andrew R. Zentner, James S. Bullock, Andrey V. Kravtsov, and Brandon Allgood. The Dependence of Halo Clustering on Halo Formation History, Concentration, and Occupation. *The Astrophysical Journal*, 652(1):71–84, nov 2006.

[247] D. H. Zhao, H. J. Mo, Y. P. Jing, and G. Börner. The growth and structure of dark matter haloes. *Monthly Notices of the Royal Astronomical Society*, 339:12–24, February 2003, astro-ph/0204108.

[248] D. H. Zhao, Y. P. Jing, H. J. Mo, and G. Börner. Accurate Universal Models for the Mass Accretion Histories and Concentrations of Dark Matter Halos. *The Astrophysical Journal*, 707:354–369, December 2009, 0811.0828.

[249] A. S. Villarreal, A. R. Zentner, Y.-Y. Mao, et al. The immitigable nature of assembly bias: the impact of halo definition on assembly bias. *Monthly Notices of the Royal Astronomical Society*, 472:1088–1105, November 2017, 1705.04327.

[250] Risa H. Wechsler, James S. Bullock, Joel R. Primack, Andrey V. Kravtsov, and Avishai Dekel. Concentrations of Dark Halos from Their Assembly Histories. *The Astrophysical Journal*, 568(1):52–70, mar 2002.

[251] Yao-Yuan Mao, Andrew R Zentner, and Risa H Wechsler. Beyond assembly bias: exploring secondary halo biases for cluster-size haloes. *Monthly Notices of the Royal Astronomical Society*, 474(4):5143–5157, 12 2017, http://oup.prod.sis.lan/mnras/article-pdf/474/4/5143/23126779/stx3111.pdf.

[252] Kyle R. Stewart, James S. Bullock, Elizabeth J. Barton, and Risa H. Wechsler. GALAXY MERGERS AND DARK MATTER HALO MERGERS IN *Lambda*CDM: MASS, REDSHIFT, AND MASS-RATIO DEPENDENCE. *The Astrophysical Journal*, 702(2):1005–1015, aug 2009.

[253] Morris L Eaton. *Multivariate statistics : a vector space approach*. Wiley series in probability and mathematical statistics. Wiley, New York ; Chichester, 1983.

[254] P. Monaco, E. Sefusatti, S. Borgani, et al. An accurate tool for the fast generation of dark matter halo catalogues. *Monthly Notices of the Royal Astronomical Society*, 433(3):2389–2402, 06 2013, http://oup.prod.sis.lan/mnras/article-pdf/433/3/2389/4061631/stt907.pdf.

[255] Aaron D. Ludlow, Julio F. Navarro, Raúl E. Angulo, et al. The mass–concentration–redshift relation of cold dark matter haloes. *Monthly Notices of the Royal Astronomical Society*, 441(1):378–388, 04 2014, http://oup.prod.sis.lan/mnras/article-pdf/441/1/378/2996980/stu483.pdf.

[256] Camila A. Correa, J. Stuart B. Wyithe, Joop Schaye, and Alan R. Duffy. The accretion history of dark matter haloes – III. A physical model for the concentration–mass relation. *Monthly Notices of the Royal Astronomical Society*, 452(2):1217–1232, 07 2015, http://oup.prod.sis.lan/mnras/article-pdf/452/2/1217/18505290/stv1363.pdf.

[257] Aaron D. Ludlow, Sownak Bose, Raúl E. Angulo, et al. The mass–concentration–redshift relation of cold and warm dark matter haloes. *Monthly Notices of the Royal Astronomical Society*, 460(2):1214–1232, 05 2016, http://oup.prod.sis.lan/mnras/article-pdf/460/2/1214/8115724/stw1046.pdf.

[258] Andrew J Benson, Aaron Ludlow, and Shaun Cole. Halo concentrations from extended Press–Schechter merger histories. *Monthly Notices of the Royal Astronomical Society*, 485(4):5010–5020, 03 2019, http://oup.prod.sis.lan/mnras/article-pdf/485/4/5010/28249774/stz695.pdf.